Cranfield UNIVERSITY

School of Industrial and Manufacturing Science

Giancarlo Bussu

Damage Tolerance of Welded Aluminium Aircraft Structures

PhD THESIS

Cranfield UNIVERSITY

School of Industrial and Manufacturing Science

PhD THESIS

Academic Year 2000-2001

Giancarlo Bussu

Damage Tolerance of Welded Aluminium Aircraft Structures

Supervisor: Professor P. E. Irving

November 2000

This thesis is submitted to fulfil the requirements for the degree of Doctor of Philosophy

Patri et Matri

magistribus vitae ac doctrinae

ABSTRACT

Riveting is a traditional joining technique mostly used in the manufacturing of aircraft structures. Manufacturing studies on the next generation of wide body commercial aircraft have indicated that the achievement of acceptable cost/benefit goals would require the application of highly cost-effective joining processes. Although riveting provides good structural performance, it is expensive and time consuming. Welding is a candidate process to be used to manufacture large aircraft structures allowing sensible cost reductions and structural efficiency.

Welded aluminium 2024-T351 structural joints produced with a new generation of welding processes, such as Friction Stir Welding (FSW) and Plasma welding were characterised in terms of microstructure, hardness and weld residual stress. Tensile properties and stress-strain behaviour of the FSW joints was investigated and discussed using simple mechanical models. The investigation of the fatigue properties of the FSW and Plasma welded structural joints revealed the superior behaviour of the FSW joints. It was found that fatigue strength in FSW joints is dominated by surface irregularities produced by the welding process. Weld surface skimming greatly improved fatigue strength by removing surface stress concentrations. Initiation in skimmed joints occurred at locations of minimum hardness. Fatigue endurance behaviour of skimmed joints was equal or superior to that reported in riveted aluminium joints. Fatigue crack propagation studies were carried out on FSW 2024-T351 joints for cracks parallel and orthogonal to the weld direction. Crack propagation behaviour was sensitive to both weld orientation and the distance of the crack from the weld line. Growth rates both faster and slower than in the parent material were observed, depending on the crack orientation and distance from the weld. Residual stress was mechanically relieved and the effects on crack propagation observed. A comparative analysis of the results associated with crack closure measurements indicated that crack growth behaviour in the FSW joints was generally dominated by the weld residual stress. Possible design solutions for damage tolerant welded aircraft structural components were identified and discussed in the light of the experimental results.

ACKNOWLEDGEMENTS

I would like to thank the UK Department of Trade and Industry for Sponsorship of this work under the CARAD extra mural research scheme and British Aerospace Airbus for the provision of samples. I would like to acknowledge Professor P. E. Irving for supervising this work.

CONTENTS

1. INTRODUCTION

Page

1.1 Why weld an aircraft? 1

1.2 The damage tolerance issue 2

1.3 Design aspect 3

1.4 The research objectives 4

1.5 Work contained in the present thesis 4

2. LITERATURE OVERVIEW

2.1 Fatigue behaviour of metallic materials 6

2.2 The fracture mechanics approach to fatigue 8

2.3 High strength aluminum alloys 14

2.4 Welding of high strength aluminium alloys 16

2.5 The friction stir welding process 19

2.6 Previous work on the characterization of FSW joints 22

2.6.1 Macrostructure and microstructure characterization 22

2.6.2 Mechanical properties 24

2.6.3 Application of FSW on aluminium primary structures 26

2.7 Plasma welding of aluminium alloys 28

2.8 Factors affecting the fatigue strength of welded components 30

2.9 Crack propagation in welded joints: effect of residual stress 38

2.10 Crack propagation in welded joints: effect of microstructure and hardness 41

2.11 Design of welded aluminium aerospace structures 42

3. EXPERIMENTAL PROCEDURES

3.1 Parent material 2024-T351 45

3.2 Welding procedures 46

3.3 Specimen preparation for metallography 46

3.4 Hardness profile measurement 47
3.5 Preparation of tensile specimens 49
3.6 Tension testing procedures 52
3.7 Fatigue test specimen design and preparation 53
3.8 Residual stress measurements 55
3.9 Fatigue testing procedures 57
3.10 Crack propagation test: specimen design and preparation 58
3.11 Experimental procedures: crack propagation tests 61
3.12 The DCPD crack length measurements system 66
3.13 The crack length versus potential difference relationship 69
3.14 DCPD crack length measurement system evaluation 71
3.15 Measurement of fatigue crack opening loads (COL) 73

4. EXPERIMENTAL RESULTS

4.1 Joint characterization 76
4.1.1 Weld macrostructure 76
4.1.2 Weld microstructure 79
4.1.3 Hardness profiles 87
4.1.4 Friction stir weld residual stress 88
4.1.5 Tensile proprieties of friction stir welds 90
4.1.6 Tensile properties of plasma welds 96

4.2 Fatigue properties of welded joints 97
4.2.1 Friction stir welded joints 97
4.2.2 Effect of weld orientation on fatigue of FSW joints 99
4.2.3 Effect of surface skimming on fatigue life of FSW joints 99
4.2.4 Plasma welded joints versus FSW joints 100
4.2.5 Fatigue crack initiation 101
4.2.6 Fatigue crack initiation and hardness distribution 108

4.3 Fatigue crack propagation 113

4.3.1 Parent plate 2024-T351 113
4.3.2 Propagation of cracks orthogonal to the weld 113
4.3.3 Propagation of cracks parallel to the weld 118
4.3.4 Effect of residual stress relief on crack propagation 120
4.3.5 SEM examination of cracks orthogonal to the weld 126
4.3.6 SEM examination of cracks parallel to the weld 129
4.3.7 Measurement of crack opening loads during fatigue of welded specimens 137

5. DISCUSSION OF RESULTS

5.1 Structure and hardness in friction stir and plasma welded joints 141
5.2 Residual stresses in friction stir welded joints 144
5.3 Tensile testing of friction stir welded joints 147
5.4 Tensile properties - observations 151
5.5 Fatigue endurance properties 154
5.6 Crack propagation in friction stir welded joints 157
5.6.1 Effect of residual stress on crack propagation 159
5.6.2 Residual stress and crack closure 163
5.6.3 Effect of microstructure and hardness on crack propagation 165
5.6.4 Crack propagation at higher crack growth rates 166

6. DESIGN CONSIDERATIONS

6.1 Have FSW joints the right fatigue lives for aircraft structures? 168
6.2 FSW joints S-N data: the durability aspect 171
6.3 Damage tolerance considerations on FSW joint initial defects 171
6.4 Damage tolerant aircraft welded structures: which design philosophy? 174
6.5 Welded wing structure: proposed solutions 175
6.5.1 The outer wing stiffened panel 176
6.5.2 Spars 178
6.5.3 Ribs 178
6.6 Damage tolerance evaluation of aircraft welded structures 179

7. CONCLUSIONS AND RECOMMANDATIONS FOR FUTURE WORK

7.1 Welded joint characterization 185

7.2 Fatigue properties 186

7.3 Crack propagation 187

7.4 Design considerations 189

7.5 Recommendations for future work 189

8. REFERENCES 191

APPENDIX

Design of high load capacity grips 200

LIST OF FIGURES

		Page
2.1	Typical S-N curves for metallic materials representing the effect of mean stress and stress amplitude on fatigue strength.	7
2.2	Typical fatigue crack propagation curves da/dn vs ΔK for metallic materials.	11
2.3	The crack closure phenomenon.	12
2.4	The effect of age hardening on the 0.2% proof stress of an Al-4Cu alloy.	15
2.5	Comparison of mechanical properties between 2024-T351 and 7075-T651 plate alloys.	16
2.6a	A Typical microstructure and phases in an Al-Cu-Mg age hardened alloy after fusion welding.	18
2.6b	Correspondence between hardness and microstructure in an Al-Cu-Mg age hardened alloy after fusion welding.	19
2.7	Principle of operation of the friction stir welding process.	30
2.8	The typical microstructure of a FSW joint.	23
2.9	Plasma arc welding torch with temperature distribution.	29
2.10	Comparison of the fatigue properties of 6005-T4 and T6 base metal and welded joints obtained using different welding techniques.	31
2.11	Fatigue design curves from BS 8118 for aluminium welded joints.	32
2.12	Typical residual stress distribution in a welded plate.	34
2.13	Effect of residual stress on the mean stress of CA fatigue cycles.	36
2.14	Mechanical stress relief of longitudinal weld residual stress.	37
2.15a	Crack closure through an initial tensile residual stress field.	41
2.15b	Crack closure through an initial compressive residual stress field.	41
2.16	A proposed welded design solution for a wing skin panel joint of a transport aircraft.	44
3.1a	Microstructure in LT plane of the 2024-T351 6.35 mm rolled plates.	47
3.1b	Microstructure in TS plane of the 2024-T351 6.35 mm rolled plates.	48
3.1c	Microstructure in LS plane of the 2024-T351 6.35 mm rolled plates.	48
3.2	Locations of hardness transverse measurements carried out in the FSW	49

	cross sections.	
3.3	Longitudinal and transverse welded and parent plate specimen geometry for the tensile tests.	50
3.4	Strain gauges position on the transverse FSW specimen for the tensile test.	51
3.5	Strain gauges position and the transverse hardness values on the transverse FSW specimen before the tensile test.	52
3.6	Longitudinal and transverse welded specimen geometry for the fatigue tests.	54
3.7	Residual stress positions referred to the plate joint line.	57
3.8a	The SCT specimen arrangement and principal dimensions.	58
3.8b	The C T specimen arrangement and principal dimensions.	59
3.9	The surface semicircular flaws introduced on the SCT specimens.	60
3.10	Position and orientation of the initial surface defect for the SCT	61
3.11	Position and orientation of the CT specimens in respect to the weld.	62
3.12	Plots of K/K_o as functions of the crack length for the SCT specimens.	65
3.13	Correction factors for crack offset used to calculate the stress intensity values for the SCT specimens.	67
3.14	The schematic of the DCPD system.	68
3.15	The locations of the electrical potential probes on the CT and SCT specimens.	69
3.16a	The experimental data points and the respective calibration curve obtained for the CT specimens.	71
3.16b	The experimental data points and the respective calibration curves obtained for the SCT specimens.	72
3.17	Definition of compliance on the crack mouth displacement vs load curve.	74
3.18	Extensometer positioning in the CT specimens for the measurement of the fatigue crack opening load.	75
4.1a	The friction stir weld bead.	77
4.1b	The friction stir weld back surface.	77
4.1c	The typical friction stir weld macrostructure on a plane orthogonal to	78

	the weld direction.	
4.2	The typical friction stir weld macrostructure on the plane parallel to the weld on the plate joint line.	78
4.3	The "lip", delimiting on one side the weld bead.	79
4.4	The typical cross section of a plasma welded plate on a plane orthogonal to the weld direction.	80
4.5a	The microstructure of the weld nugget of a FWS joint in the plane orthogonal to the weld direction.	81
4.5b	The typical microstructure of the weld nugget of a FWS joint in the plane parallel to the weld direction.	82
4.6	The superficial layer of the weld top surface.	82
4.7	Microstructure, in the plane normal to the weld, of the the thermo-mechanically affected region next to the nugget.	83
4.8a	The microstructure in the thermo-mechanically affected region, at 6 mm from the plate joint line, on a plane normal to the weld.	83
4.8b	The microstructure in the thermo-mechanically affected region, at 6 mm from the plate joint line, on a plane parallel to the weld.	84
4.9a	The typical microstructure in the HAZ, at 28 mm from the plate joint line, on a plane normal to the weld.	84
4.9b	The microstructure in the HAZ, at 28 mm from the plate joint line, on a plane parallel to the weld.	85
4.10	The grain structure in the centre of the plasma weld in a section normal to the weld.	85
4.11	The transition in grain structure on the boundaries between the melted region and the HAZ in a cross section of a plasma welded joint.	86
4.12	The typical microstructure that characterised the dark bands on the HAZ in the plasma welded joints (plane normal to the weld).	86
4.13	The typical hardness profiles of the friction stir welded joints.	87
4.14	The typical hardness profile of the plasma welded joints.	88
4.15	The stress-strain curves from the transverse FSW joint during the tensile test.	92
4.16	The strain distribution in the direction of the stress axis measured during	94

	the tensile test on the transverse FSW joint.	
4.17a	The longitudinal section of a transverse FSW joint failed in the tensile test.	94
4.17b	Typical location of failure in the transverse FSW joints and the position of minimum hardness values.	95
4.18	The stress-strain curves from the tension test on the longitudinal FSW joint.	96
4.19	S-N curves (R = 0.1) for parent plates and FSW joints in as-welded conditions.	98
4.20	S-N curves (R = 0.1) for parent plates and FSW joints in surface skimmed conditions.	101
4.21	Optical cross section of a FSW joint.	102
4.22	S-N curves of transverse plasma welded (skimmed) and transverse FSW joints (skimmed) under constant load amplitude (R = 0.1).	103
4.23	SEM picture of the initiation area in the transverse FSW specimens.	103
4.24	View of the initiation area in a transverse FSW specimen revealing fatigue initiation from an oxide inclusion.	104
4.25	Picture of a tested longitudinal FSW specimen in as-welded conditions.	105
4.26	SEM picture of the initiation area in a FSW specimen.	105
4.27	Near-surface defect on a transverse skimmed FSW joint.	106
4.28	Fatigue initiation locations in the transverse skimmed FSW joints.	107
4.29	Multiple fatigue initiation observed on a transverse skimmed FSW joint.	108
4.30a	The initiation area in a transverse skimmed plasma welded specimen.	109
4.30b	Fracture surface with pores from which the crack initiated.	109
4.31	Defects corresponding to of the plate joint line in the transverse skimmed plasma welded joints.	110
4.32	Location of the fatigue initiation sites on the transverse skimmed plasma joints.	110
4.33	Defect size and distribution in the transverse skimmed FSW and plasma joints.	111
4.34	Position of fatigue initiation sites and hardness distribution in the transverse skimmed FSW joints.	111

4.35	Positions of fatigue initiation sites and hardness distribution in the transverse skimmed plasma welded joints.	112
4.36	Crack propagation curves from tests performed on the 2024-T351 parent plate.	114
4.37a	Crack propagation curves from test carried out on the SCT specimens with cracks orthogonal to the weld.	115
4.37b	Crack propagation curves from test carried out on the SCT specimens with cracks orthogonal to the weld.	116
4.38	Crack front positions propagating from the flaw at 11 mm from the weld microstructure.	117
4.39	Crack front position propagating from the flaw on the PJL and the weld microstructure.	117
4.40	Crack propagation curves from tests performed on the CT specimens with cracks parallel to the weld.	119
4.41	Procedure used to obtain 2% permanent deformation in the SCT specimens.	121
4.42a	Typical microstructure of tie thermo-mechanically affected zone in a 2% stretched specimen.	122
4.42b	Typical hardness profile in a 2% stretched specimen.	123
4.43	Crack propagation curves from test carried out on 2% plastically deformed SCT specimens with cracks orthogonal to the weld.	124
4.44	Crack propagation curves from test carried out on 2% plastically deformed CT specimens with cracks parallel to the weld.	126
4.45	Representation of the areas shown in the SEM pictures of the SCT specimens fracture surfaces.	128
4.46	Fracture surface of the crack at 25 mm from the PJL in a tested SCT specimen (near-threshold regime).	131
4.47	Fracture surface of the crack at 25 mm from the PJL in the 2% stretched SCT specimen (near-threshold regime).	131
4.48	Fracture surface of the crack at 11 mm from the PJL in a tested SCT specimen (near-threshold regime).	132
4.49	Fracture surface of the crack at 11 mm from the PJL in the 2% stretched	132

	SCT specimen (near-threshold regime).	
4.50	Fracture surface observed in the crack on the weld of a tested SCT specimens (near-threshold regime).	133
4.51	Fracture surface in the weld of the 2% stretched SCT specimens (near-threshold regime).	133
4.52	Fracture surface at 6 mm from the PJL on a CT specimen (near-threshold regime).	134
4.53	Fracture surface at 6 mm from the PJL in the 2% stretched CT specimens (near-threshold regime).	134
4.54	Fracture surface on the weld of a CT specimen (near-threshold regime).	135
4.55	Picture of the tested CT specimens with the crack on the plate joint line.	135
4.56	Fracture surface on the weld of the 2% stretched CT specimens (near-threshold regime).	136
4.57	Fracture surface at 28 mm from the PJL on a CT specimen (near-threshold regime).	136
4.58	Fracture surface at 28 mm from the PJL in the 2% stretched CT specimens (near-threshold regime).	137
4.59a	Stress intensity factor as a function of the compliance offset values for the CT specimens with crack at 6mm from the PJL.	138
4.59b	Stress intensity factor as a function of the compliance offset values for the CT specimens with crack at 28mm from the PJL.	139
4.59c	Stress intensity factor as a function of the compliance offset values for the CT specimen (stretched) with crack on the weld.	139
5.1	The mechanism of formation of transverse residual stress in a welded plate.	146
5.2	The stress-strain models representing the tensile behaviour of the transverse and longitudinal welded joints.	148
5.3	Definition of A_w and A_p with respect to the joint hardness profile.	149
5.4	Predicted and measured yielding of the longitudinal welded joint.	151
5.5a	Simplified strain distribution in a transverse FSW joint.	152
5.5b	Calculated elongation plotted as a function of the reference length.	153
5.6	Simplified geometrical representation of the lip for the estimation of the	155

stress concentration factor.

5.7 Stress-strain cycles in the transverse joint following the 2% nominal stretching. 163

5.8 The effect of stretching on the propagation of the crack at 6 mm from the PJL interpreted applying the crack closure model. 164

6.1 Longitudinal splice stringer bolted wing skin joint. 169

6.2 S-N curves on FSW skimmed joints compared with riveted joints endurance data (R = 0.1). 170

6.3 Defect size and distribution in the FSW and plasma skimmed compared with defect size and statistical distribution in riveted joints. 173

6.4 Two skin-skin welded joint solutions for a lower wing panel. 177

6.5 Possible design for a welded lower wing panel: skin-stringer web welded solution. 179

6.6 Welded spar solution compared with a traditional mechanically fastened one. 180

6.7 Comparison between a welded and a traditional machined rib. 181

6.8 Damage tolerance evaluation of aircraft welded structures. 182

6.9 Determination of inspection intervals in damage tolerant structures. 183

LIST OF TABLES

		Page
3.1	Specified chemical composition for 2024-T351 aluminium alloy.	45
3.2	Mechanical properties for 2024-T351 aluminium alloy.	45
3.3	Standard plasma autogenous welding parameters (vertical-up).	46
3.4a	Resolution values of the DCPD system in the CT and SCT specimen tests.	72
3.4b	Accuracy values of the DCPD system in the CT and SCT specimen tests.	73
4.1a	Residual stresses measured on the as-welded plate.	89
4.1b	Residual stresses measured on the dog-bone as-welded specimen.	89
4.1c	Residual stresses measured on the dog-bone specimen after surface skimming.	89
4.2	Tensile properties measured for the FSW joints and parent plate specimens.	91
4.3	Degradation of the tensile properties due to the FSW process.	91
4.4	Monotonic test results performed on transverse plasma welded joints and degradation values of the parent plate properties.	97
4.5	Comparison of tensile properties between transverse plasma and FSW joints.	97
4.6	Near-threshold stress intensity factor values of cracks growing at 90° with respect to the weld direction (SCT specimens).	118
4.7	Near-threshold stress intensity factor values of cracks growing parallel to the weld direction (CT specimens).	120
4.8	Results of the residual stress measurements on the plastically deformed specimens and a comparison with the residual stress values measured in the undeformed specimens at similar locations.	124
4.9	Results of the crack propagation test carried out on the 2% plastically deformed SCT specimens.	125
4.10	The near-threshold ΔK values measured in the 2% plastically deformed SCT specimens.	127
4.11	Numerical results of the COL measurements on the CT specimens.	140
5.1a	Comparison of residual stress, hardness, grain size and near-threshold stress intensity factor values in the SCT specimens.	158

5.1b Comparison of residual stress, hardness, grain size and near-threshold stress intensity factor values in the CT specimens. 158

5.2 ΔK values corresponding to the transition near-threshold regime to the intermediate stage for orthogonal and parallel cracks. 167

NOMENCLATURE

Symbol/ Abbreviation	Description	Unit
a	Crack length	mm
a_i	Initial crack length	mm
a_f	Final crack length	mm
A_i	Cross sectional area of the generic element in the welded joint mechanical model	mm^2
A_w	Cross sectional area of weld in the welded joint mechanical model	mm^2
A_p	Cross sectional area of parent plate in the welded joint mechanical model	mm^2
CA	Constant Amplitude	
da/dn	Crack growth rate	mm/cycle
C_n	Eccentricity coefficient	
COL	Crack Opening Load	
CT	Compact Tension	
DCPD	Direct Current Potential Drop	
ΔK	Stress intensity factor range	MPa $m^{1/2}$
ΔK_{eff}	Effective stress intensity factor range	MPa $m^{1/2}$
ΔK_{NT}	Stress intensity factor range measured at $5 \cdot 10^{-10}$ m/cycle	MPa $m^{1/2}$
ΔK_{th}	Threshold stress intensity factor range (measured at 10^{-11} mm/cycle)	MPa $m^{1/2}$
$\Delta\sigma$	Stress range	MPa
ΔV	Difference in electrical potential	V
ΔV_x	Difference in electrical potential on the test specimen	V
$(\Delta V_x/\Delta V_y)_0$	Reference electrical potential ratio	
ΔV_y	Difference in electrical potential on the test	V

	control specimen	
E	Young's Modulus	GPa
EA	Normal stiffness	kN
EDM	Electric Discharge Machine	
EDX	Energy Dispersive X-Ray Analysis	
ε_{ult}	Elongation	
$f(a/W)$	Specimen geometry function	
FSW	Friction Stir Welding	
GAG	Ground-Air-Ground	
HAZ	Heat Affected Zone	
I	In-plane moment of inertia	mm^4
K	Stress intensity factor	MPa $m^{1/2}$
K_c	Critical stress intensity factor	MPa $m^{1/2}$
K_f	Fatigue stress concentration factor	
k_i	Elastic constant of the generic element in the	GPa
K_{max}	Maximum stress intensity factor	MPa $m^{1/2}$
K_{min}	Minimum stress intensity factor	MPa $m^{1/2}$
$K_{min, eff}$	Minimum effective stress intensity factor	MPa $m^{1/2}$
K_{op}	Crack opening stress intensity factor	MPa $m^{1/2}$
K_{offset}^{outer}	Stress intensity factor for an eccentric crack at the tip close to the plate edge	MPa $m^{1/2}$
K_{offset}^{inner}	Stress intensity factor for an eccentric crack at the tip close to the plate centre line	MPa $m^{1/2}$
k_p	Elastic constant of the parent plate in the welded joint mechanical models	GPa
k_{pi}	Work hardening coefficient of the generic element in the welded joint mechanical models	GPa
k_{pp}	Work hardening coefficient of the parent plate in the welded joint mechanical models	GPa
K_t	Stress concentration factor	
k_w	Elastic constant of the weld in the welded joint mechanical models	GPa

k_{wp}	Work hardening coefficient of the parent plate in the weld mechanical models	GPa
K_0	Stress intensity factor for a crack in an infinite plate	MPa $m^{1/2}$
L	Longitudinal	
LS	Longitudinal Short	
LT	Longitudinal Transverse	
MIG	Metal Inert Gas	
N	Fatigue life	cycle
N_I	Cycles to initiate a fatigue crack	cycle
N_P	Propagation period	cycle
P	Load	kN
PAW	Plasma Arc Welding	
P_i	Load in the generic element of the welded joint mechanical model	kN
PJL	Plate Joint Line	
P_{max}	Maximum load	kN
P_p	Load in the parent plate of the welded joint mechanical model	kN
$P_{res,p}$	Load in the parent plate due to the weld residual stress in the welded joint mechanical model	kN
$P_{res,w}$	Load in the weld due to the weld residual stress in the welded joint mechanical model	kN
P_w	Load in the generic element of the welded joint mechanical model	kN
R	Stress ratio	
S_n	Fatigue limit	MPa
SCT	Surface-Crack Tension	
SEM	Scanning Electron Microscopy	
S-N	Stress-Life	
ST	Short Transverse	
σ	Stress	MPa

σ_ϕ	Stress acting on the plane oriented at ϕ with respect to the principal plane	MPa
σ_{op}	Crack opening stress	MPa
σ_{long}	Residual stress in the direction of the weld	MPa
σ_m	Mean stress	MPa
σ_{max}	Maximum stress	MPa
σ_{min}	Minimum stress	MPa
σ_{prop}	Proportional limit	MPa
σ_{transv}	In-plane residual stress orthogonal to the weld welded joint mechanical models	MPa
σ_{ult}	Tensile strength	MPa
σ_{yi}	Yield stress of the generic element in the welded joint mechanical models	MPa
σ_{yw}	Yield stress of the weld in the welded joint mechanical models	MPa
$\sigma_{0.2}$	0.2% proof stress	MPa
σ_1	Stress acting on the first principal plane	MPa
σ_2	Stress acting on the second principal plane	MPa
t	Thickness	mm
TEM	Transmission Electron Microscopy	
TIG	Tungsten Inert Gas	
TL	Transverse Longitudinal	
V_{off}	Electrical potential measured with current off	V
V_{on}	Electrical potential measured with current on	V
VPPA	Variable Polarity Plasma Arc	
W	Width	mm
W_p	Parent plate width of a welded joint	mm
W_w	Weld width of a welded joint	mm
x_p	Strain parallel to the main stress axis in the parent plate	
x_w	Strain parallel to the main stress axis in the weld	

1. INTRODUCTION

1.1 Why weld an aircraft?

Reduction of manufacturing costs of civil aircraft structures is a key requirement to enhance the competitiveness of the civil aircraft industry [18, 69, 102]. Increasing manufacturing cost effectiveness becomes a vital condition for the commercial success of the next generation of large wide body aircraft. In this light, aircraft industry has extended its interest from the traditional fastening process to alternative more cost-effective joining processes. Welding is a candidate process to be used in manufacturing of large aircraft structures allowing sensible cost reductions and structural efficiency. The main advantages of welding process compared to mechanical fastening are:

Manufacturing benefits:

- Welding is a single-step operation whereas riveting is a multi-step operation (drilling, hole cold working, shimming and riveting are generally required) [40]
- Welding is a continuous process therefore can be more easily automated reducing assembly cost and time
- Large extruded components can be welded reducing machining and material scrapping
- Welding allows limitation of the number of parts, reducing structural complexity.

Design benefits:

- Welding allows sensible weight reduction avoiding overlapped regions, high density rivets and sealant typical of mechanical fastened joints
- Design can be simplified using simpler and more efficient solutions
- Design and structural efficiency can be improved
- Continuous joints improve stiffness in structures
- Absence of fretting phenomenon
- Potentially leakage-free structures.

Typical disadvantages of welding compared to mechanical fastening are:

- Parent material properties degradation
- Residual stresses are introduced in the structure
- Distortion can cause assembly and jigging problems and interfere with aerodynamics requirements
- Fail-safe limitations typical of monolithic structures
- Reparability of welded structures.

Current research aims to develop welding processes suitable for production of high integrity welds in high strength heat-treatable aluminium alloys. Most recent advances are represented by the novel Friction Stir Welding (FSW) process. This is a solid-state process capable of producing high quality joints of aerospace aluminium alloys, such as 2024 and 7075. FSW is one of the most promising processes to be used in manufacturing of aluminium aircraft structures. To date a relatively limited amount of information has been published on FSW. Research, initially focused on the understanding of the process mechanisms and the material physical and metallurgical modifications, has recently moved to characterisation of the mechanical performances of the joints. For evident airworthiness implications, the application of any new technology to aircraft construction can only be made after that a robust knowledge of the mechanical behaviour of the structure has been generated. In order to set the foundation of this knowledge it is important to characterise the tensile, fatigue and crack propagation behaviour of FSW joints.

1.2 The damage tolerance issue

An essential part of airworthiness of large commercial aircraft is the requirement to demonstrate damage tolerance of major structural elements. Airworthiness authorities require aircraft manufacturers to provide evidence that the structure can operate safely until partial damage becomes readily detectable and the structure is repaired [48]. A damage tolerant structure must be demonstrated in both riveted and welded aircraft structures. A regime of repeated inspections ensures crack detection before the growth of the crack to a critical size, for which catastrophic failure will occur under design limit load.

In addition to data on service loads and non-destructive inspection capabilities, analytical determinations of damage tolerance will require data on crack growth characteristics of the material, the initial defect size and distributions, and the factors which will control the crack growth behaviour. Changing the manufacturing process from riveting to welding will change the material crack growth behaviour profoundly, as well as introducing a number of new variables determining crack behaviour. Many of the new variables such as residual stress distribution, heat affected zone extension and microstructure modifications will be controlling the crack propagation through the welded joints. In addition, the starting defect size and distribution in the welded structures could be significantly changed from that in riveted structures. Furthermore, a welded structure is in effect an integral structure. From this follows that a crack that initiates from a local defect can potentially propagate through the entire structure. The effects and consequences of this aspect will have a large impact on the actual damage tolerance design philosophy based instead on fastened structures.

1.3 Design aspects

Current designs of civil transport aircraft reflect the fatigue and damage tolerance performance of mechanically fastened joints. Structures have to evolve in order to optimize damage tolerance performance. Fail-safe multiple load path solutions could contemplate the use of welds together with riveted joints. All this will require re-examination of the current design roles in order to maximize crack detectability and residual strength.

The best location for welds are not necessarily those currently used for mechanically fastened joints. New design solutions where welds are located away from stress concentrations, and characterised by high strength-to-weight values would be possible. In the identification of the structural solution of minimum weight, the choice of important parameters such as stringer pitch, stringer cross sectional area and shape is currently limited by manufacturing restrictions also related to the riveting process. The use of welding together with extruded elements, such as integrally stiffened panels, can reduce these manufacturing limitations allowing higher degree of freedom in the choice

of the structural optimum solution. Use of different alloys in different parts of the structure, joined by welding is a further possibility to achieve high structural efficiency.

1.4 The research objectives

(1) To characterize FSW joints in terms of microstructure, hardness variations and residual stress

(2) To investigate tensile mechanical properties of FSW joints and failure mechanisms

(3) To evaluate fatigue strength of FSW joints in relation to design variables such as weld orientation to the stress axis and weld surface skimming

(4) To investigate fatigue initiation mechanisms

(5) To characterise crack propagation behaviour of FSW joints in relation to design variables such as weld orientation to the stress axis

(6) To identify dominating factors influencing crack propagation behaviour

(7) To identify possible damage tolerant structural solutions of welded wing structures.

1.5 Work reported in the present thesis

The work is focussed on large civil aircraft wing panels on a single alloy choice 2024-T351 and maximum thickness of 6.35 mm. The majority of mechanical testing has been performed on welds made using the solid state FSW. A subsidiary test program has been performed on Variable Polarity Plasma Arc (VPPA) welded 2024 T-351 joints in order to provide a term of comparison with joints obtained with fusion welding process. Macrostructure, microstructure and hardness distribution in FSW and VPPA welded joints have been characterized. Residual stresses have been measured in FSW plates and joints. Tensile tests have been carried out on FSW longitudinal and transverse orientation joints and compared with plasma transverse joints.

S-N data of FSW longitudinal and transverse orientation joints in as-welded and skimmed surface state have been experimentally evaluated. Fatigue test results have been compared with S-N data obtained from transverse plasma welded joints (skimmed condition). Weld defects responsible for fatigue initiation have been characterised in size and distribution. Fatigue crack growth properties of FSW joints for crack

propagation in the direction parallel and orthogonal to the weld have been investigated. The contribution of residual stresses, HAZ and microstructure to crack growth behaviour particularly in the near threshold regime have all been characterised. Possible damage tolerant welded and riveted-welded structural solutions for a wing panel have been identified and discussed in the light of the experimental results.

2. LITERATURE OVERVIEW

2.1 Fatigue behaviour of metallic materials

Fatigue is a failure mechanism that occurs as a result of a large number of load applications. A single load, which does not cause any damage to the material or the structure, may cause fatigue failure if applied a large number of times. At relatively low cyclic loads (i.e. low as compared with the static failure load), fatigue crack nucleation involves cyclic slipping of crystallographic planes within the single grains of the metal [98]. During this stage, a microcrack is produced on the free surface of the element, where crystallographic plane slipping is easier. The microcrack growth is dominated by the local shear stress. As the microcrack grows reaching the length of a few grains, the direction of propagation becomes orthogonal to the maximum tensile stress direction. Crack propagation follows this stage and ends with the fatigue failure of the component.

The fatigue behaviour of a structural element is influenced by several factors such as loading (stress range, mean stress, loading history and frequency), material properties (i.e. static strength and microstructure) and geometry (stress concentrations). During a constant amplitude (CA) loading, the stress (σ) varies between a maximum (σ_{max}) and a minimum (σ_{min}) value. Fatigue strength of an element subjected to CA loading is influenced by stress range $\Delta\sigma$ and mean stress σ_m, defined as:

$$\Delta\sigma = \sigma_{max} - \sigma_{min} \qquad \textit{Eqn. 2.1}$$

and

$$\sigma_m = \frac{(\sigma_{max} + \sigma_{min})}{2} \qquad \textit{Eqn. 2.2}$$

The influence of stress range and mean stress on fatigue can be represented by plotting the stress values versus the corresponding fatigue lives. The plot, known as an S-N curve, can be obtained for constant mean stress or constant stress ratio (R), defined as $\sigma_{min}/\sigma_{max}$. Figure 2.1 shows typical S-N curves for metallic materials, corresponding to

two different mean stress values. Large stress range values have a detrimental effect on the fatigue strength: as the stress range increases, fatigue life is reduced [98, 50]. The points A and B, intersections of the line $\Delta\sigma$ = const with the S-N curves, show that for constant stress range an increment in the mean stress determines a reduction in fatigue life. The points C and D, intersections of the line N = const with the curves, shows that at higher stress range the mean stress has to be reduced in order to obtain the same fatigue life [50]. As Figure 2.1 shows, for long fatigue lives the S-N curve tends to approach a horizontal asymptote defined as the fatigue limit. The fatigue limit is a stress level below which no fatigue failure occurs. Some metals, i.e. aluminium alloys, do not exhibit a real fatigue limit [25, 50]. In this case, a fatigue limit is arbitrarily defined specifying the corresponding fatigue cycles (typically 10^7 or 10^8 cycles).

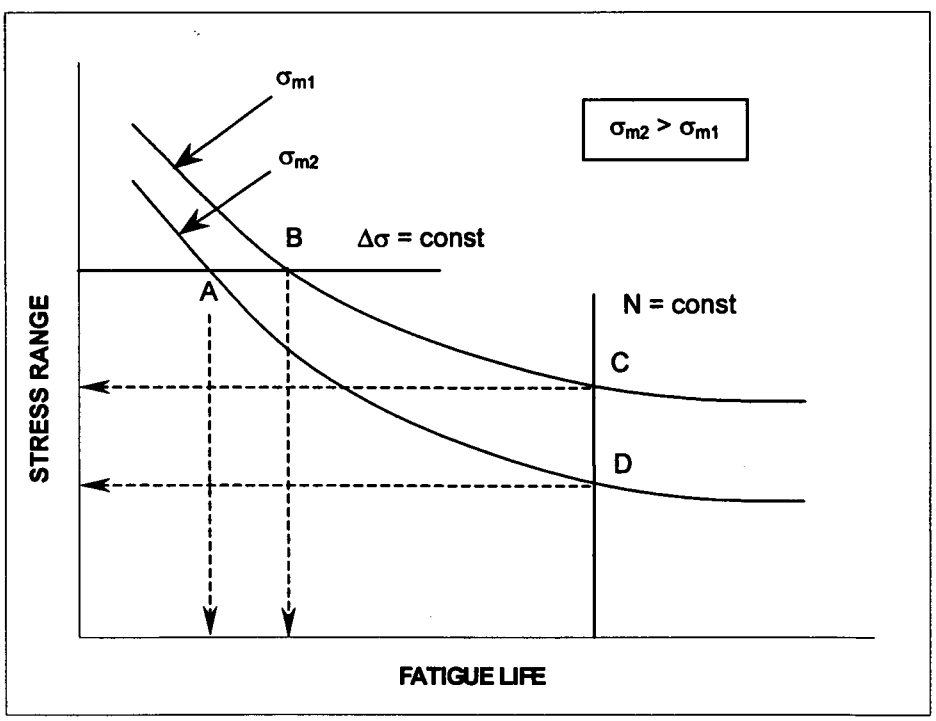

Figure 2.1 Typical S-N curves for metallic materials representing of the effect of mean stress and stress range on fatigue strength.

Fatigue strength depends on the material characteristics such as tensile strength and microstructure. In general, it is found that materials with high strength and hardness exhibit higher fatigue strength than materials with lower strength [64, 50]. Empirical correlations between the tensile strength and fatigue limit have been proposed [50, 98],

however only a first estimate of the fatigue limit is obtained. In metals, a fine grain structure gives higher fatigue strength than a coarse microstructure [25, 50]. Heat treatment and cold working, modifying the grain size and microstructure, can increase the fatigue strength in metals [64].

Stress concentrations, associated with the presence of notches or material defects such as inclusions, reduce the fatigue strength of a structural element. The severity of a stress concentration is typically expressed using the definition of the stress concentration factor (K_t). Assuming that the material behaves elastically, the maximum value of the stress (σ_{max}) in the vicinity of a stress concentration is

$$\sigma_{max} = K_t \sigma \qquad \textit{Eqn. 2.3}$$

where σ is the nominal stress value. The effect of stress concentrations on fatigue strength is expressed introducing the definition of fatigue stress concentration factor (K_f) [98, 50]. The fatigue stress concentration factor is defined as

$$K_f = \frac{S_n}{S_n'} \qquad \textit{Eqn. 2.4}$$

where S_n and S_n' are the fatigue limits for the smooth specimen and the notched specimen, respectively. Generally $K_f > 1$, and $K_f \leq K_t$. This is due to the fact that a plastic zone always develops in the proximity of the notch, reducing locally the severity of stress concentration [50]. In metals, K_f is found to be a function of the notch sensitivity (q) of the material which depends upon the notch geometry and the hardness of the material. Materials of high hardness values and strength generally exhibit higher notch sensitivity than softer and more ductile materials [25, 50].

2.2 The fracture mechanics approach to fatigue

In aircraft structures fatigue cracks do occur in service. For this reason it is important to predict and control initiation and propagation of fatigue cracks. Fracture mechanics provides the tools to predict the time (cycles) for an initial crack to reach a critical

length, to determine the residual strength of a structure with existing cracks and the dimension of allowable defects present in the structure when introduced into service. Linear Elastic Fracture Mechanics (LEFM) relies on the assumption that fatigue crack growth can be described in terms of the stress intensity factor concept. The stress intensity factor (K) gives an indication of the severity of the stress field around the crack tip. The stress intensity factor depends on the geometry of the component, the shape and size of the crack and the load applied.

Assuming that the crack under load is opened perpendicular to the fracture surface (Mode I) and the equilibrium equations of stresses and the compatibility equation of strains are valid [27], a general form for the stress intensity factor for a component of finite dimensions is:

$$K = C\sigma\sqrt{\pi a} \qquad \textit{Eqn. 2.5}$$

where σ is the nominal stress, a the crack length and C a dimensionless factor, a function of the crack length and of the component geometry [27, 98].

Let us consider a cracked component subjected to a remote stress that varies cyclically between a constant minimum value (σ_{min}) and maximum value (σ_{max}). The stress range $\Delta\sigma$ is defined as $\sigma_{max} - \sigma_{min}$, and from Equation 2.5 a stress intensity factor range may be defined as:

$$\Delta K = K_{max} - K_{min} = C\,\Delta\sigma\sqrt{\pi a} \qquad \textit{Eqn. 2.6}$$

As the stress cyclically varies Δn times, the crack length increases of Δa, and a fatigue crack propagation rate can be defined as $\Delta a/\Delta n$. The crack propagation rate $\Delta a/\Delta n$ in the limit can be written as the differential da/dn. It has been found experimentally that, for constant stress ratio $R = \sigma_{min}/\sigma_{max}$, ΔK correlates fatigue crack growth rates in components with different stress ranges, crack lengths and different geometry, i.e.

$$\frac{da}{dn} = f(\Delta K, R) \qquad \textit{Eqn. 2.7}$$

This correlation is shown schematically in Figure 2.2, where da/dn is plotted against ΔK on a double logarithmic diagram. In region I, Figure 2.2, cracks do not propagate below a threshold stress intensity factor value of ΔK_{th}. This threshold value is defined in terms of crack growth rate (10^{-11}m/cycle), however an operational definition is commonly used and can be based on the accuracy of the crack monitoring system and the number of elapsed cycles [25, 98].

In region I, crack propagation is typically influenced by the mean stress value, the environment and the material microstructure, particularly the grain size [27, 98]. Region II in Figure 2.2 is often characterised by a linear log-log relation between da/dn and ΔK. This relation can be described with different semi or wholly empirical models. The most widely used is the Paris equation [98]:

$$\frac{da}{dn} = \alpha\,(\Delta K)^m \qquad \textit{Eqn. 2.8}$$

where α and m are constants obtained by fitting the experimental data. In region II, crack propagation is typically influenced by the mean stress, environmental conditions and microstructure, depending on the material. Region III is characterised by fast crack propagation. The plot approaches a vertical asymptote where the maximum stress intensity factor, K_{max}, in the fatigue stress cycle becomes equal to the critical stress intensity factor, K_c. In this region a large influence of the mean stress, thickness and microstructure of the material is typically observed [98].

In general, fatigue crack growth resistance of a material is influenced by the strength level. The 7075-T6 aluminium alloy has an inferior crack growth behaviour compared with the lower strength 2024-T3 alloy [25]. Similarly, artificial ageing of the 2024 alloy (T8 condition) gives a 25% higher yield stress, however, the crack growth rate becomes approximately two times higher than that in the naturally aged condition [25].

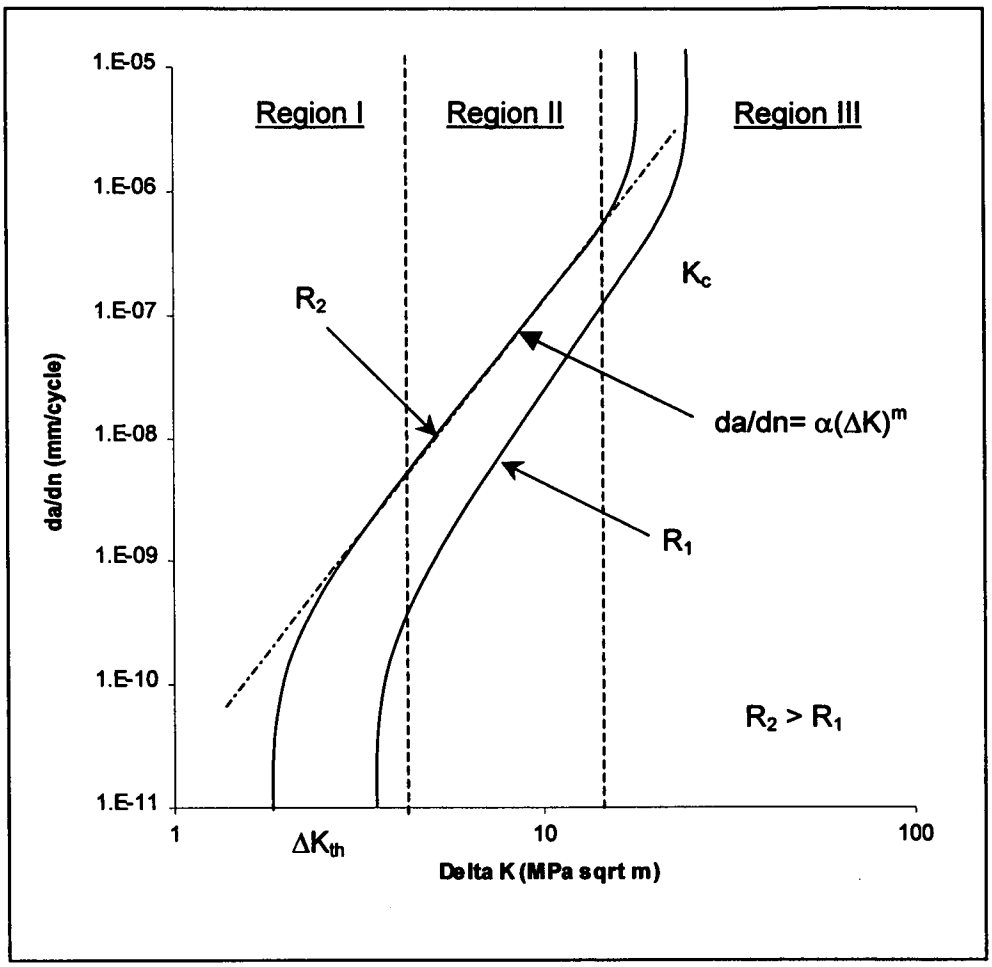

Figure 2.2 Typical fatigue crack growth curves da/dn against ΔK for metallic materials.

Figure 2.2 also shows the influence of the stress ratio on fatigue crack growth behaviour. Crack growth rates at the same ΔK value are generally higher for greater R values. The influence of the stress ratio on crack growth behaviour can be explained applying the crack closure concept. The term crack closure refers to the phenomenon by which the fracture surfaces of a crack come into contact during the unloading portion of a load cycle and load is transferred through the crack.

When reloading from minimum load, some increment of load must be applied before the crack is again fully open. Consequently, the closure phenomenon provides a mechanism by which the effective cyclic stress intensity factor range at the crack tip (ΔK_{eff}) differs from the nominally applied value (ΔK). This is illustrated in Figure 2.3. Figure 2.3a shows the variation of the applied stress intensity factor K with the applied

stress σ. Figure 2.3b shows the variation of the effective stress intensity K_{eff} with the applied stress and also the important concept of crack opening stress σ_{op}.

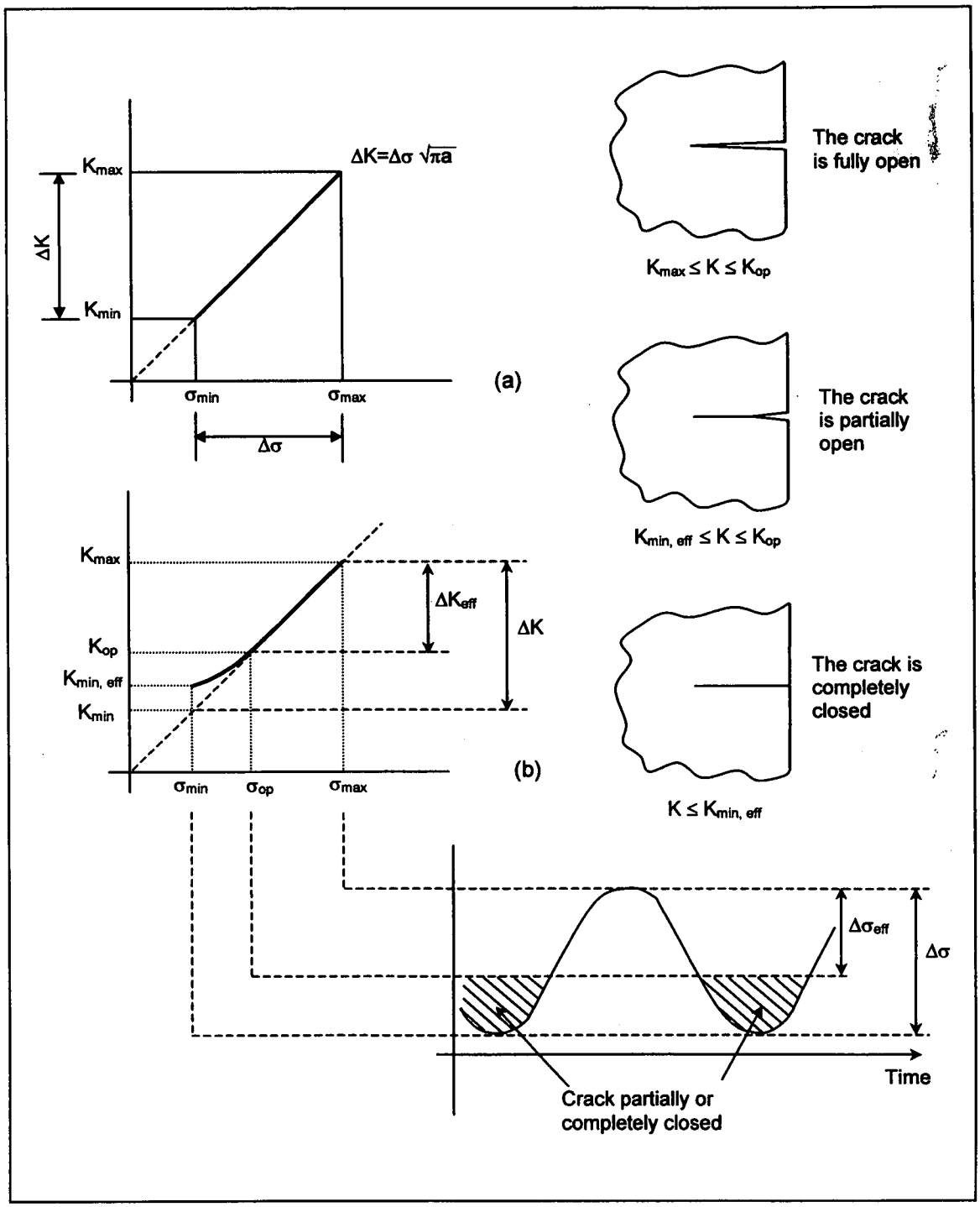

Figure 2.3 The crack closure phenomenon.

This has been defined by Elber [23, 89] as the minimum value of applied stress for which the crack is fully open. The value of σ_{op} can be determined experimentally from the change in compliance of the specimen. In fact, crack closure results in an increase in stiffness and a decrease in compliance [27].

The crack closure mechanism was proposed by Elber [23] in order to provide an explanation for some crack growth retardation effects experimentally observed in materials even under constant amplitude cyclic loading. This approach is based on the fundamental assumption that a crack cannot propagate while being closed. On this basis, the crack growth driving force is represented by ΔK_{eff} instead of ΔK. Physically, crack closure can occur as a consequence of crack tip plasticity (plasticity-induced crack closure).

As the crack grows under load cycling, a zone of reversed plasticity develops along the crack flanks [27, 98]. This plastic deformation can result in contact between the crack surfaces even under tensile externally applied loads. In general, crack closure can result from any cause of physical contact between the two crack surfaces such as crack surface roughness (roughness-induced crack closure), crack surface oxidation (oxide-induced crack closure) or the presence of a viscous medium (viscous-induced crack closure). A review of the role of microstructure and environment on crack closure can be found in Ref. [84].

High R values result in less crack closure, i.e. ΔK_{eff} becomes nearly equal to ΔK. This can be represented with different empirical relationships. For the 2024-T3 aluminium alloy the following relationship has been proposed [27]:

$$\frac{\Delta K_{eff}}{\Delta K} = U = 0.55 + 0.35R + 0.1R^2 \qquad \textit{Eqn. 2.9}$$

This relationship provides a good correlation between crack growth rates and ΔK_{eff} for R values between –0.5 and 0.33.

2.3 High strength aluminium alloys

Aluminium is a lightweight metal with a density of 2.7 Mg/m^3, one third of the density of steel. Although pure aluminium has relatively low tensile properties compared with steel, it responds readily to strengthening mechanisms. Based on the type of strengthening mechanism, aluminium alloys can be classified in age hardenable and non-age hardenable alloys. The former are typically aluminium-copper (2xxx series) alloys, aluminium-magnesium-zinc (7xxx series) alloys and aluminium-magnesium-silicon (6xxx series) alloys. The latter are aluminium-manganese (3xxx series) alloys, aluminium-magnesium (5xxx series) alloys and aluminium-silicon (4xxx series) alloys.

In the age hardenable alloys, the strengthening effect is obtained by producing a uniform dispersion of a fine hard coherent precipitate in a softer, ductile matrix. The coherent precipitates create a widespread disruption of the matrix lattice interfering with the movement of dislocations in the alloy† [2]. In age hardening the alloy is heated to a temperature above the solvus temperature to obtain a homogeneous solid solution, quenched to obtain a non-equilibrium supersaturated solid solution, and finally, held at a temperature below the solvus temperature. At this ageing temperature, atoms diffuse and precipitates form and grow at numerous nucleation sites. A typical example of this is the ageing of an aluminium-copper alloy. At the start of ageing, from the α supersaturated solid solution a very thin precipitate, the Guinier-Preston I (GP-I), forms. As ageing continues, more copper atoms diffuse to the precipitates and the GP-I zones coarsen into the S" (or GP-II) form. With continued diffusion, the precipitates grow to the S' phase [93]. The non-equilibrium precipitates GP-I, S" and S' are coherent precipitates. Figure 2.4 shows the effect of ageing on the yield strength of an Al-4Cu alloy [2]. The strength of the alloy increases as the coherent precipitates grow in size. When these coherent phases are present, the alloy is in the aged condition. When the stable non-coherent S phase precipitates the strength of the alloy decreases and the alloy is in the overaged condition.

† The slip process in a metal can be explained by the movement of dislocations. Slip is the process by which a metal deforms in a ductile manner. Slip determines the mechanical properties of metals [2].

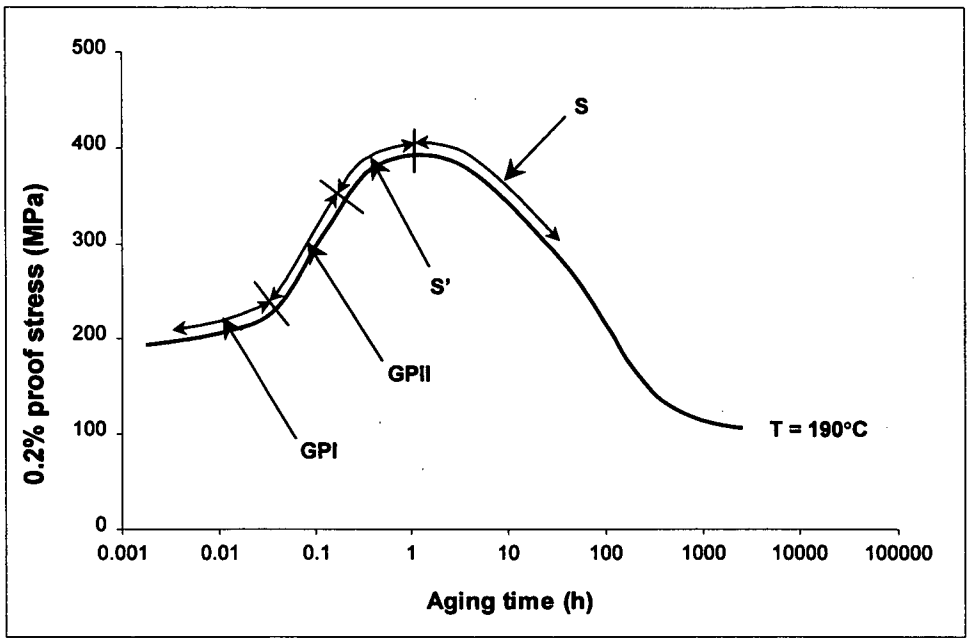

Figure 2.4 The effect of age hardening on the 0.2% proof stress of an Al-4Cu alloy, Ref. [2].

In the non-age hardenable alloys 3xxx, 5xxx and 4xxx, strengthening is obtained by strain hardening, grain size control and solid solution strengthening. In the solid solution strengthened alloys the substitutional atoms of the alloying elements produce local lattice disruptions interfering with the dislocation movement [2]. The solid solution strengthening mechanism is less effective than the age hardening because the interference with the dislocation movement is limited to the substitutional atom areas. For this reason, age hardenable alloys generally have higher mechanical properties than solid solution strengthened alloys. The former can be 3 times stronger than the latter and 30 times stronger than pure aluminium [1].

In aerospace structural applications, where high strength and low density are of primary importance, only the strongest 2xxx and 7xxx alloys are used. Figure 2.5 shows a comparison, in terms of 0.2% proof stress and fracture toughness K_{IC}, between 2024-T351 (solution heat-treated, controlled stretched and naturally aged) and 7075-T651 (solution heat-treated and artificially aged) aluminium alloys, widely used in aircraft primary structures. It can be noticed that the 7075-T651 alloy has higher strength than 2024-T351 but lower fracture toughness. The 2xxx alloys exhibit a crack propagation

behaviour generally superior to the 7xxx alloys. Fatigue crack growth rates in 2xxx alloys are close to one-third of those observed in the 7xxx alloys [81].

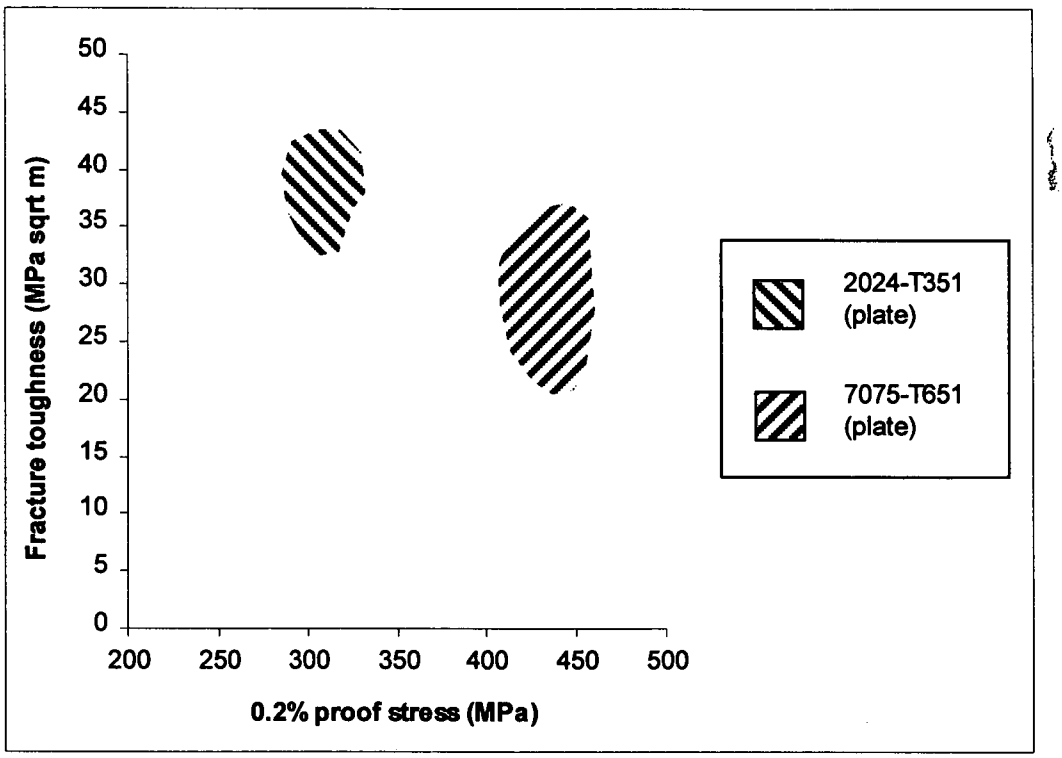

Figure 2.5 Comparison of mechanical properties between 2024-T351 and 7075-T651 plate alloys, Ref. [64].

The 2024-T351 alloy, having good fracture toughness, fatigue strength and stress-corrosion susceptibility lower than the 7075-T651 alloy, is typically used in high strength tension structural applications [64]. These applications include lower wing skin and stringers where fatigue and stress-corrosion cracking are particularly severe [72]. The 7075-T651 alloy finds its typical applications in the upper wing skin and stringers, in spars and ribs elements where high tensile strength is required.

2.4 Welding of high strength aluminium alloys

High strength precipitation hardened aluminium alloys are traditionally considered not easily weldable. During the welding process aluminium reacts in the presence of oxygen producing alumina (Al_2O_3), an oxide with high melting point (2066°C) and higher specific weight. The fragments of brittle alumina from the pool surface tend to sink into

the melted metal generating detrimental oxide inclusions within the weld. Weld cracking that typically affects the heat-treatable alloys is due to the wide melting range of the aluminium alloys. High porosity levels are caused by the high solubility of hydrogen in molten aluminium [21]. In the phase transition liquidus-solidus the aluminium specific volume is reduced by 6% [2]. This variation in specific volume is the primary cause for the formation of high residual stresses in welded joints, as will be discussed later.

As discussed in Section 2.3, high strength aluminium alloys are typically obtained by age hardening. During fusion welding, the metal in the weld exceeds the liquidus temperature eliminating the effect of age hardening. The same effect is observed in the regions where the temperature exceeds the solvus temperature. The lower temperature zone near the unaffected base metal is exposed to temperatures just below the solvus and may overage. In this case precipitates coarsen, transforming into a stable non-coherent phase, and the strength of the alloy decreases. Microstructural modifications, presence of precipitates and the effect on age hardening for a fusion TIG welded 2024 aluminium joint have been described by Norman [74]. Figure 2.6a shows the typical microstructure and phases in an Al-Cu-Mg age hardened alloy after fusion welding.

In the fusion zone (Fig. 2.6a) complete melting and re-solidification takes place. The microstructure is typically dendritic with the grains elongated in the direction of the maximum thermal gradient during cooling. Cu and Mg are rejected into the inter-dendritic regions. The lack of solute in the dendrite arms produces a low hardness value (Fig. 2.6b). In the partially melted region (Fig. 2.6a), the solute elements diffuse to the grain boundaries where they form the eutectic phase (α-Al + Al_2Cu + Al_2CuMg). During cooling, the eutectic phase solidifies in a continuous film. A precipitate-free zone is produced adjacent to the grain boundaries.

In the solution treated zone (Fig. 2.6a) the maximum temperature locally exceeds the solvus temperature. Under these circumstances, any precipitate is dissolved and a homogeneous solution is produced. If the cooling rate is sufficiently high, the solute

remains in solution. This supersaturated solid solution, containing excess of Cu and Mg naturally ages giving rise to a local increase in hardness of the material (Fig. 2.6b).

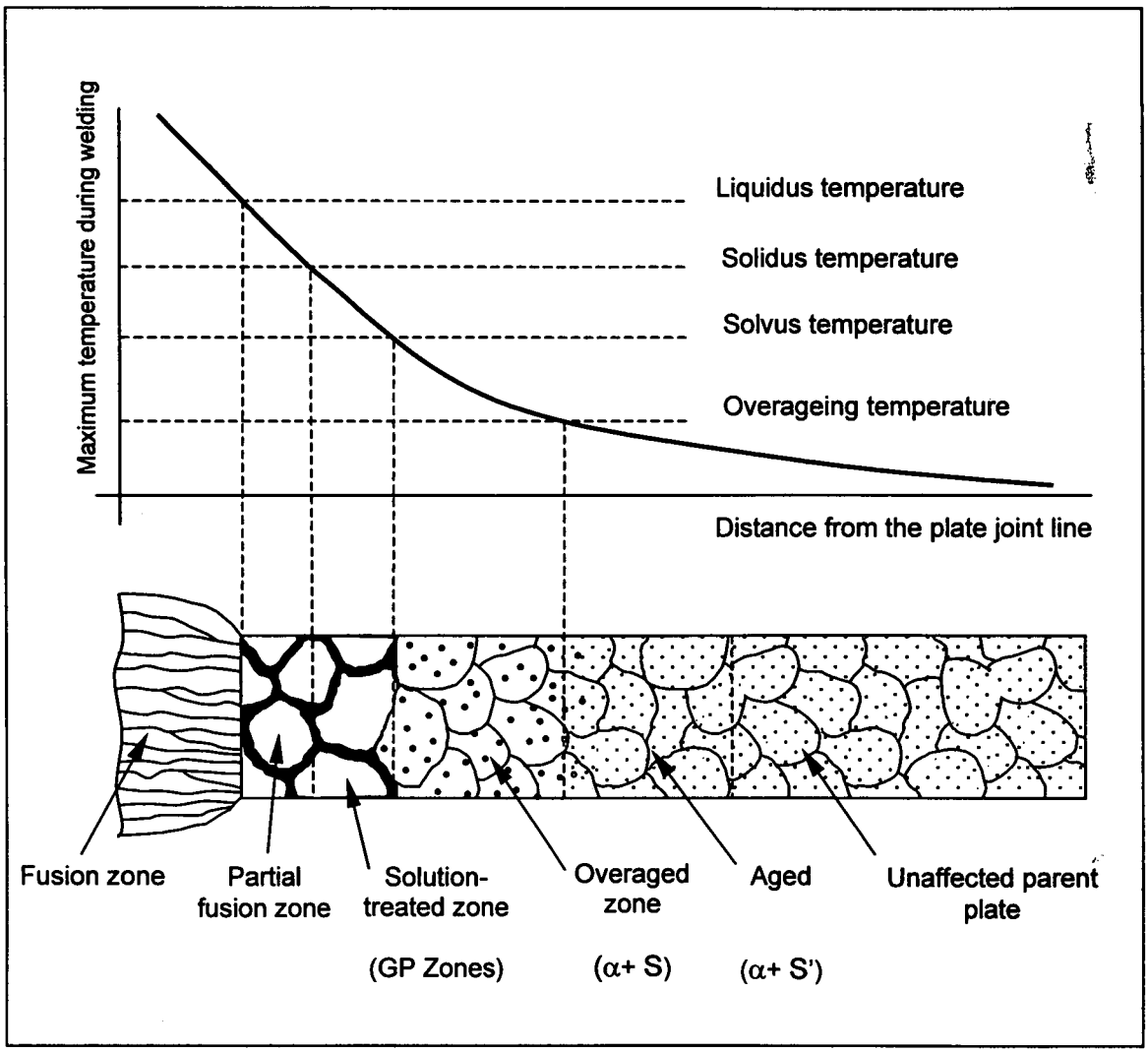

Figure 2.6a Typical microstructure and phases in an Al-Cu-Mg age hardened alloy after fusion welding.

In the overaged zone (Fig. 2.6a), the maximum temperature during welding falls below the solvus temperature of the S' phase [93]. Under these conditions, the precipitates present in the matrix coarsen into the S phase and an overaged zone is produced. The overageing produces a local drop in hardness (Fig. 2.6b). Further out in the HAZ (Fig. 2.6a), it is possible that, in the regions where the peak temperature was below 200 °C, the precipitation of the main strengthening phase S' occurs. If the original material has

the capacity to be given an artificial ageing treatment (i.e. produced in a naturally aged condition), the hardness will exhibit an increase above the parent plate value (Fig. 2.6b).

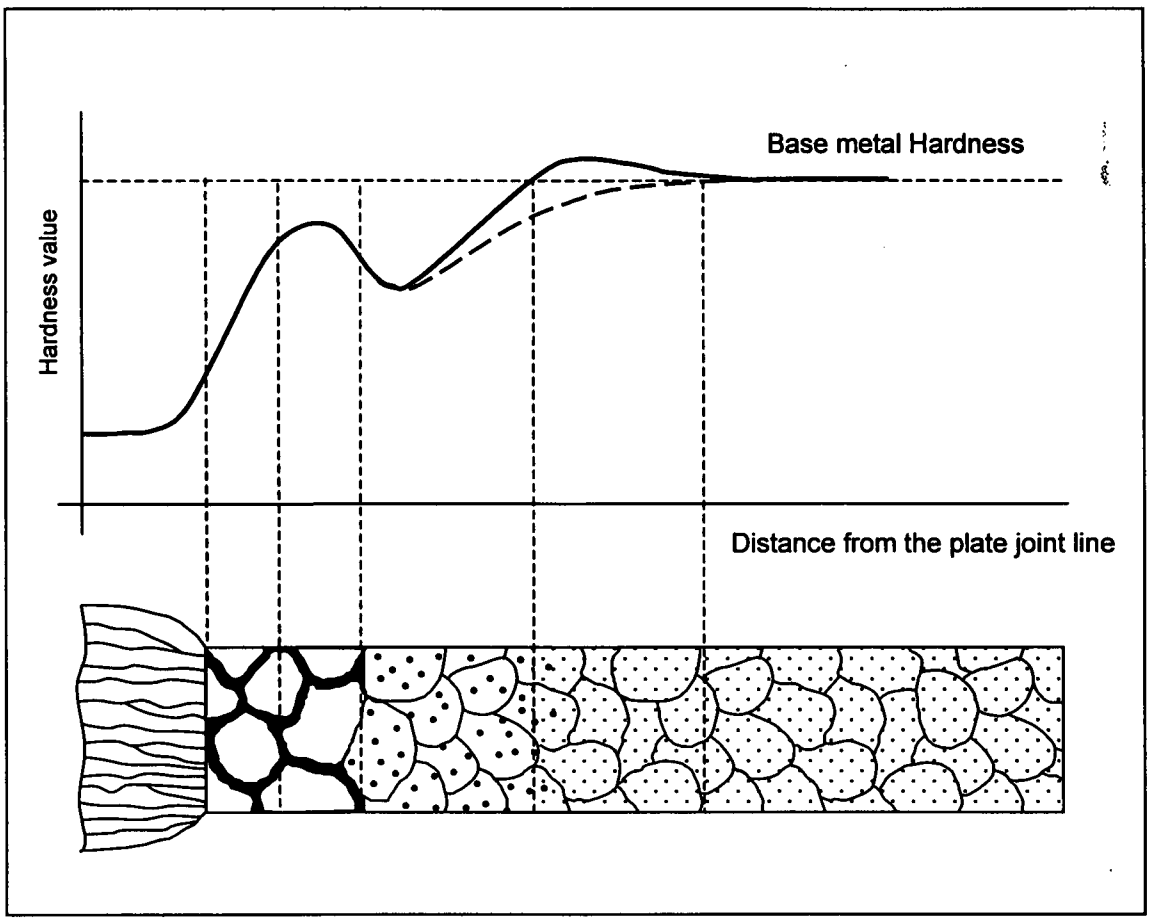

Figure 2.6b Correspondence between hardness and microstructure in an Al-Cu-Mg age hardened alloy after fusion welding.

2.5 The friction stir welding process

Friction Stir Welding (FSW) is a novel solid-phase welding process [103]. FSW was invented and patented in 1991 by The Welding Institute (TWI). The process, capable of welding high-strength aluminium alloys, is attracting the interest of the major aerospace industries. A rotating non-consumable tool is forced between two plates and moved along their contact line. During this operation, frictional heat, generated by contact between tool and plates, softens the material. The plasticised material is stirred and forced to the back of the tool where it is consolidated and produces a continuous joint. The principle of operation is illustrated in Figure 2.7.

The principal characteristic of FSW is the fact that is a solid state process. The energy required to join the plates is introduced in the workpiece in a dual form: frictional heat and mechanical action by the tool pin. The solid state weld formation avoids the major problems related to fusion welding of aluminium alloys. Formation of cracks, principally during solidification, is avoided both because the material does not melt and because the plasticised material is intimately stirred and mixed by the tool [20].

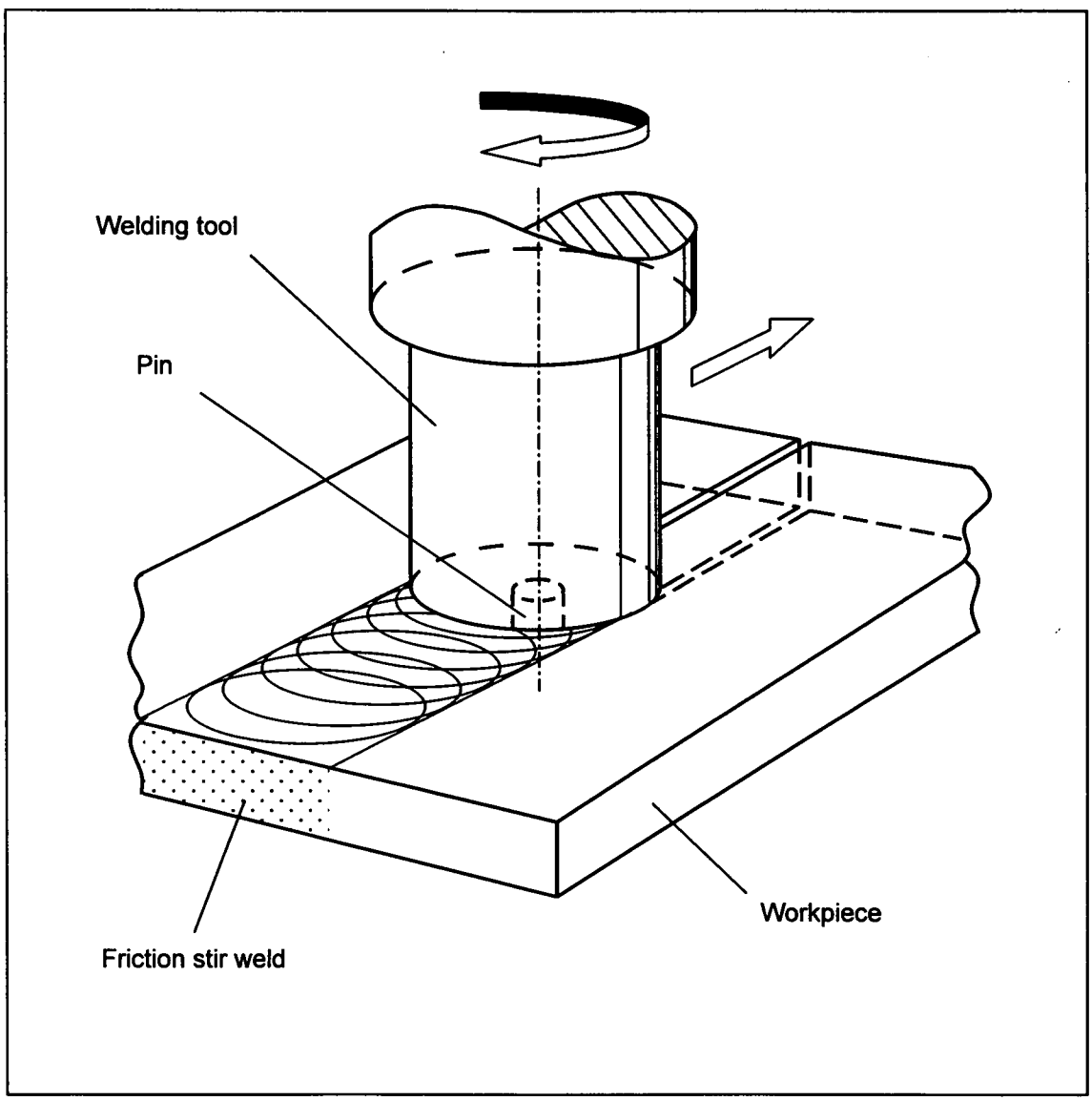

Figure 2.7 Principle of operation of the friction stir welding process.

Absence of melting and mechanical action interferes with the formation of porosity and solidification defects in the weld. Absence of weld metal evaporation allows no loss of

alloying elements guaranteeing the preservation of the alloy composition. No formation of aluminium oxide during friction stir welding has been observed. It is reasonable to believe that the below-melting-point welding temperature and the tool stirring action would prevent the formation of oxides during the process. For this reason the process does not require any shielding gas and oxide removal.

The tool stirs the material breaking up the oxide film that covers the plates. The oxide film is crushed and recombined within the joint. No detailed studies have been carried out in order to characterise the size and distribution of the crushed oxide fragments within the joint. Within the weld nugget, inclusions between 10 and 20 μm have been observed, however their composition and origin has not been investigated [52]. Al(Fe-Mn) inter-metallic particles, containing some Si and Cu, have been observed in 2014-T6 and 7075-T6 FSW joints. Their mean size, approximately of 3 μm in the parent plate, is less than 1 μm within the nugget [96]. This reduction in size has been explained as an effect of the mechanical break-up exerted by the tool. The described advantages allow production of nominally void and crack free welds of high strength aluminium alloys such as 2xxx and 7xxx series that are notoriously difficult to weld [104, 105]. It has been found that the most critical parameter in the FSW process is the pressure between the welding tool and the aluminium plate, as it is directly proportional to the heat delivered to the material [67]. If the pressure provided by the tool generates less heat than that required to plasticise the material, a weld characterised by internal defects and regions with lack of adhesion ("kissing bonds") between the plates is produced [67].

The FSW operation is simple and could potentially lead to advantages in terms of manufacturing costs. Although no cost analysis of the application of FSW to the fabrication of large aluminium structure has been published in open literature, some of the potential advantages have been discussed [20]. Energy delivery is not affected by the high reflectivity of aluminium and the tool is driven by an efficient electromechanical machine making FSW a highly energy efficient process. No filler metal, gas shielding and joint edge profiling are required. Single pass FSW travelling speed (75 cm/min to single-pass-weld a 6 mm 6082-T6 plate) can be greater than speed values for an automated single pass TIG or plasma welding (54 cm/min to weld a 1.6

mm 6013-T4 plate) [55, 112]. These characteristics simplify the automation of the FSW operations [49]. Aluminium plates can be single-pass friction stir welded up to 38mm in thickness [100].

Although FSW is a solid phase process, sharp changes in microstructure, a softened heat affected zone and residual stresses are also produced as in the traditional fusion welds. During welding substantial forces are developed between tool and workpiece. In order to counterbalance these forces the plates need to be rigidly clamped against a backing bar. As the welding operation finishes the tool pin is withdrawn from the plates and a hole is left at the end of the run. Studies in order to develop a retractable pin tool in order to overcome to this limitation are in progress [22].

2.6 Previous work on the characterization of FSW joints

FSW is a novel process that only in the last four years has attracted the interest of the aerospace industry. For this reason, a limited amount of literature data has been published so far. The majority of the works refer to the process and manufacturing technique development [4, 67, 104]. The applications were initially limited to the 5xxx and 6xxx series aluminium alloys. Preliminary microstructural assessments and tensile properties have been carried out.

2.6.1 Macrostructure and microstructure characterization

Several studies have been carried out in order to characterise the microstructure and hardness profile in FSW joints. Figure 2.8 shows the typical macrostructure of a FSW joint. Regardless of the specific aluminium alloy composition, FSW joints have a core (Fig. 2.8, a) characterised by equiaxed grains much finer than the parent plate, typically equal or smaller than 10 μm [52, 100, 105]. Within this region, the grains are generally separated by high angle boundaries, indicating that they are not subgrains and that recrystallization takes place during welding [105]. A typical onion ring appearance characterises the nugget of FSW joints. Their dimensions and density vary depending on the process parameters. The onion rings extend following a three-dimensional pattern within the entire nugget. No variation in microstructure or hardness has been observed within the rings [52].

The hardness within the nugget varies depending on the alloy and its initial heat treatment. For 2024-T351, 2219-T87, 2014-T6 and 7075-T351 alloys, hardness profiles in the weld nugget show local maximum values at the plate joint line [15, 52, 106]. The hardness value in the nugget has been correlated with the size of the precipitates present in the region. In the nugget of 7075-T351welded joints, two types of intragranular precipitate (60-80 nm) have been observed. The same types of precipitate have been found in the parent plate, although of slightly smaller size (50-75 nm). Other smaller precipitates of unspecified composition, intragranular (10 nm) and intergranular (30 nm), have been observed in the parent plate only.

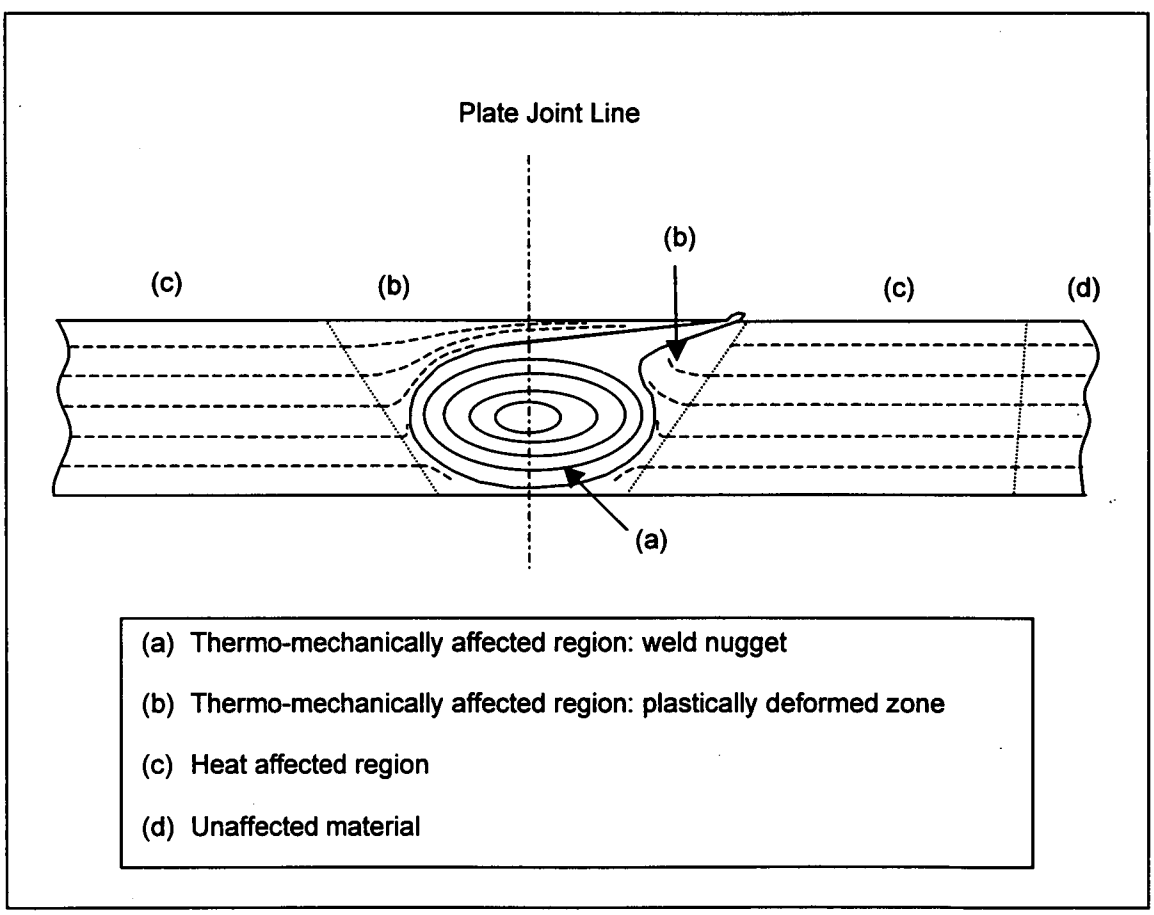

Figure 2.8 The typical microstructure of a FSW joint.

These differences in size and distribution of precipitates between parent plate and nugget suggest that solution heat treatment takes place to a certain degree in the nugget during welding. Reprecipitation occurs during cooling causing the hardness to increase

locally [105, 96]. Similar observations were made on 2014-T6 joints by the same authors. These have been confirmed by Transmission Electron Microscopy (TEM) observations on 2024-T351 FSW joints [8].

External to the nugget and within the thermo-mechanically affected region (Fig. 2.8, b), all the observations have indicated the presence of an elongated grain structure suggesting that severe plastic deformation takes place during welding. In this region, partial recrystallisation of the grains has been observed by several authors [14, 105, 52]. In the 2xxx and 7xxx series heat treatable alloys, this region is characterised by hardness minima. TEM observations conducted on FSW 7075-T651 joints have shown that at the locations of minimum hardness the Mg-Zn precipitates are generally coarser (between 30 and 40 nm) than in the parent plate (between 15 and 30 nm) [63]. Most recent investigations on 2014-T6 and 7075-T6/T651 FSW joints, have shown that the precipitates within the regions of minimum hardness are the equilibrium precipitates phase θ and η, respectively. This indicates that complete overageing is responsible for the lowest hardness values [96].

Next to the thermo-mechanically affected region is the Heat Affected Zone (HAZ), Figure 2.8, c. This region is not affected by the mechanical action of the tool, but the mechanical properties are influenced by the heat flow from the weld. Hardness profiles show an increase in the direction of the parent plates. Secondary hardness maxima and minima have been observed next to the parent metal in 2024-T351, 6061-T651 and 6082-T6 [14, 59, 100]. No detailed studies have been carried out to date in order to explain these hardness variations.

2.6.2 Mechanical properties

FSW aluminium 6xxx series alloys have been tested by different authors [4, 56, 109]. Results of the investigations indicated reductions in the parent plate properties of 25-30% for the yield stress, 10-20% for the tensile strength and 30-60% for the elongation. A direct comparison with the tensile properties of Metal Inert Gas (MIG) welded joints indicated that FSW joints exhibited better tensile performance than the MIG joints. For the MIG joints, the yield stress was 30% lower than in the FSW joints [56]. The tensile

strength and elongation were respectively 20% and 10% lower than in the FSW joints [56]. In all the cases, fracture was reported to occur at locations of minimum hardness.

Several studies have been recently conducted in order to investigate the tensile properties of FSW joints in 2xxx and 7xxx series aluminium alloys [8, 54, 109]. FSW 2024-T351 joints have generally exhibited a reduction in the parent plate properties of 23-28% for the 0.2% proof stress, 13-17% for the ultimate stress and 50-73% for the elongation. Tests carried out on FSW aluminium-lithium 2195-T8 joints have shown degradations in the 0.2% proof stress of 30% of the parent plate value and reductions in tensile strength of 19% of the parent plate. These values have indicated a degradation of the tensile properties in line with the more traditional 2024 alloy [54]. Results of tests performed on FSW 7020-T6 joints have indicated degradation levels in the parent plate properties of 26% for the 0.2% proof stress, 16% for the ultimate stress and 67% for the elongation [109]. No complete evaluation of the tensile properties of FSW 7075 joints has been found in the literature.

Endurance data (S-N curves) have been obtained recently for different types of FSW joints and compared with the performance of fusion welded joints. The recent interest in the fatigue properties of FSW joints is due to the fact that the assessment of the mechanical performance, conducted in support of weld process optimisation, have been exclusively made through the evaluation of tensile properties. Results of Constant Amplitude (CA) fatigue tests have been carried out on 2024-T351 joints [8].

Transverse FSW joints, obtained from 1.6 mm sheets, exhibited at 10^5 cycles a degradation in fatigue strength of 25% compared with the parent plate strength in the same orientation. Fatigue strength increased with the ratio tool rotational speed/travel speed reaching the parent plate fatigue strength. Initiation took place at locations of minimum cross sectional area on the weld nugget. For 4 mm FSW joints, fatigue strength at 10^7 cycles was 20% less than in the parent plate. In this case, failures took place at profile irregularities on the weld top surface. This was due to the notch effect associated with the weld profile.

Comparative studies of CA fatigue performance have been carried out between FSW and fusion welded joints in 6N01-T5 alloy (equivalent to 6005-T5) [39, 56]. Test results have indicated that FSW joints performed equally or better than laser and MIG welded joints. At 10^7 cycles, MIG and laser welded joints showed a reduction in fatigue strength of 20-25% compared to the FSW joints. At 10^7 cycles, the fatigue strength of FSW joints was 75% of the parent plate strength.

Fatigue endurance data obtained testing plasma-keyhole welded 6005-T4/T6 joints have been compared with fatigue test results of FSW joints [4]. FSW joints always performed better than plasma welded joints. At 10^6 cycles, FSW joints exhibited fatigue strength 30% higher than the plasma joints. A comparison between S-N curves obtained for 2024-T3 FSW joints and fastened joints has indicated that the former performed better than the latter [77]. FSW joints at 10^7 cycles exhibited fatigue strength 50% higher than the mechanical joints. First fatigue crack initiation studies on FSW joints have been carried out by Bussu and Irving [15]. As will be discussed later, it has been shown that hardness and weld bead surface quality are dominant factors initiating fatigue cracks.

2.6.3 Application of FSW on aluminium primary structures

FSW aluminium aerospace structural components have not yet been introduced in service. However, several feasibility studies are being conducted by aerospace manufacturers such as Lockheed Martin and Airbus [49, 77]. A full-scale demonstrator of a barrel section of the external tank for the National Aeronautics and Space Administration (NASA) Space Transport System (Space Shuttle) has been assembled using an automated FSW process [49]. The barrel section (8.25 m in diameter and 4.5 m high) has been assembled by friction stir welding Al-Li 2196-T8 integrally stiffened panels and a longeron subassembly.

The panels, previously formed, have been welded along the longitudinal edges where the local thickness was 8.1 mm. The longeron subassembly has been obtained by welding forged 2219 elements. In this case, a variable thickness weld (from 16.5 to 8.1 mm) has been obtained using a two side welding technique with retractable pin tools

[22]. The mechanical properties of the full-scale structure confirmed the test results conducted on laboratory specimens.

BAe Airbus is considering and evaluating the application of FSW in the manufacturing of primary structures for large civil aircraft in order to reduce airframe assembly costs and improve structural efficiency [77]. Feasibility studies have considered the friction stir welding of wing integrally stiffened panels, obtained by either machining or extrusion. Welding these panels would reduce the number of parts and simplify the design. Detailed design solutions considered the replacement of traditional bolted joints with simpler FSW joints, making due allowance as necessary for any reductions in the static strength associated with the weld. This would produce sensible weight reductions avoiding fasteners and eliminate the stress concentrations associated with the fastener holes.

Irregularly or complex shaped components generally require the machining of large billets of material from which only a fraction is required to produce the part. FSW has been considered in order to reduce the waste of extra material, machining smaller billets of materials and joining any additional grow-outs that may be required. Welding dissimilar aluminium alloys such as 2024/7075 has been also considered in order to improve structural efficiency.

FSW has found so far its largest application in the shipbuilding and automotive industry. These applications have generally involved welding of 5000, 6000 series aluminium alloys structural components. In the maritime sector, FSW has been applied in the assembly of the hull panels of 24 m high speed vessels [37]. Assembly of large deck and side wall integrally stiffened panels for catamarans and cruise liners has been carried out by friction stir welding pre-extruded 12×2.8 m elements [67]. The application of FSW extended to the assembly of 25% of the entire structure allowed cost reductions of 4-5% compared with alternative joining methods.

FSW has also been applied in the production of floor panels for high speed aluminium trains. The panels were obtained by welding integrally stiffened extruded elements.

FSW, used to replace MIG and laser welding, showed advantages in static and fatigue strength of the panels and higher quality of the welds [56, 39].

2.7 Plasma welding of aluminium alloys

In plasma arc welding (PAW) heat is generated by the current flow between a non-consumable tungsten electrode and the workpiece [75]. Plasma welding differs from the ordinary Tungsten Inert Gas (TIG) welding in the fact that the welding arc is constrained in an orifice (Fig. 2.9). Plasma (a gas in a highly ionised and conductive state) generated from the electrode is forced to flow through a small orifice. The arc constraint produces a highly concentrated plasma flow (pinch effect) with a distribution of temperature between 8000 and 25000 °C and arc jet speeds between 300 and 2000 m/sec.

The vigorous flushing action of the plasma jet allows welding with the "keyhole" technique [108]. In this case, the flow penetrates completely the workpiece and the metal is melted in a cylindrical region around the keyhole. As the torch translates, the melted metal solidifies behind the hole leaving a continuous weld. Plasma keyhole welding has several advantages over unconstrained TIG welding. Plasma welding is less sensitive to contamination of the workpiece because the plasma gas, flowing through the open keyhole, entrains gases that, under other circumstances, would be trapped as porosity in the melted alloy. From this it follows that joint preparation is simpler and less expensive than traditional TIG welding. A more symmetrical fusion zone is produced. This tends to reduce substantially the joint distortion. The greater penetration allows a reduction in the number of passes required for a given joint. Aluminium alloy plates up to 15 mm in thickness can be welded with a single pass. Variable polarity plasma arc (VPPA) welding is generally used to weld aluminium alloys in order to reduce and control the high tendency of oxide formation responsible for poor joint quality [75, 108].

Studies on the application of the keyhole VPPA technique to assemble the Space Shuttle external fuel tank have been carried out by NASA [16, 75]. Aluminium 2219-T87 plates up to 13 mm in thickness were single-pass-welded. Tensile tests indicated that the

ultimate strength of the joints were approximately 70% of the parent plate at room temperature. The joints had ultimate strength values 12% higher than that of the TIG welded joints obtained with the same material. Aluminium 2219-T87 plates up to 12.7 mm in thickness were double-pass welded obtaining similar values of tensile strength.

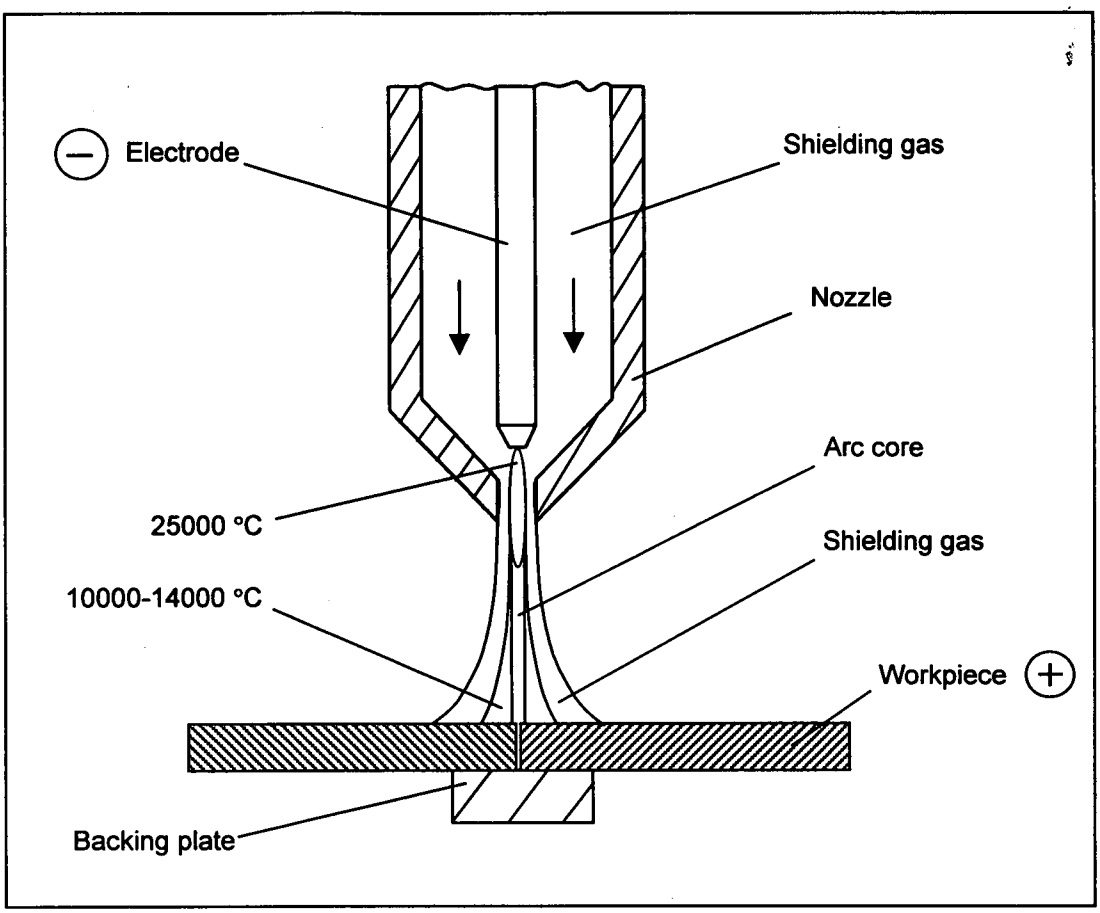

Figure 2.9 Plasma arc welding torch with temperature distribution.

An investigation of the mechanical properties of 2024-T351 aluminium alloy joints welded with an optimised keyhole VPPA welding process was conducted in Ref. [111]. Hardness measurements on 6.35 mm thick plates, welded using 2319 filler wire, showed that the minimum hardness was 68% of that in the parent plate. Through thickness measurements on the plate joint line exhibited variations in hardness of less than 5% of hardness minima. This indicated a uniform energy delivery through the plate thickness during the welding process. Hardness values were compared with those measured in TIG welded joints obtained with similar base material and filler. The HAZ in the plasma

joints was 25% smaller than that in TIG joints, whereas TIG welds exhibited hardness minima 6% higher than that of the plasma welds. This indicated that during plasma welding, the energy density was higher than in TIG welding.

Tensile tests were carried out on as-welded and surface skimmed autogenous keyhole VPPA welded 2024-T351 aluminium joints [111, 112]. Results indicated that surface skimming increased the ultimate strength by 7%. As-welded joints showed an ultimate strength of 333 MPa, 31% lower than that in the parent plate. The skimmed joints exhibited an ultimate strength of 310 MPa, 35% lower than the parent plate.

Results of a comparative study on the fatigue performance of 6005-T4/T6 parent plate and welded joints were reported in Ref. [4]. Figure 2.10 shows the above results obtained testing transverse butt welded joints in as-welded conditions. The data show a comparison between parent plate and welded joints as well as a comparison among different welding processes. It can be noticed that keyhole plasma welded joints exhibits better fatigue strength than MIG welded joints. Degradation in fatigue strength of the plasma welds is 33% of the parent plate strength at $2 \cdot 10^6$ cycles.

2.8 Factors affecting the fatigue strength of welded components

Welds are traditionally considered critical in terms of fatigue performance. Figure 2.10 shows an example of degradation in fatigue strength of welded joints with respect to the parent plate properties. Porosity, lack of penetration, weld undercutting, inclusions and hot cracking are the most important causes for often poor fatigue strength [61]. Joint geometry is a primary factor influencing fatigue strength. Longitudinal butt joints perform generally better than fillet joints and joint misalignment in transverse welds can reduce fatigue strength [61, 87, 14]. In transverse butt welded joints, the bead profile is an important factor that influences fatigue strength [53]. Fatigue cracks typically initiate at toes of the weld, that is at the junction of the plate surface and the weld, where a stress concentration is associated with the local change in geometry [71, 66].

The mechanical and physical properties of the parent metal have a significant effect on the fatigue strength of unwelded aluminium (Section 2.1). However, in welded

aluminium, the presence of a stress concentration or weld defects significantly alters that behaviour [87]. This characteristic fatigue behaviour of welded joints is reflected in the British Standards BS 8118 design curves for aluminium welded joints [14]. Figure 2.11 shows the fatigue S-N design curves from BS 8118 for longitudinal welded joints, transverse butt welded joints and unwelded aluminium structural elements. The curves are based on the assumption that joint geometry and manufacturing procedure are the dominant factors to determine the fatigue resistance of the joint, and they apply to any weldable structural aluminium alloy.

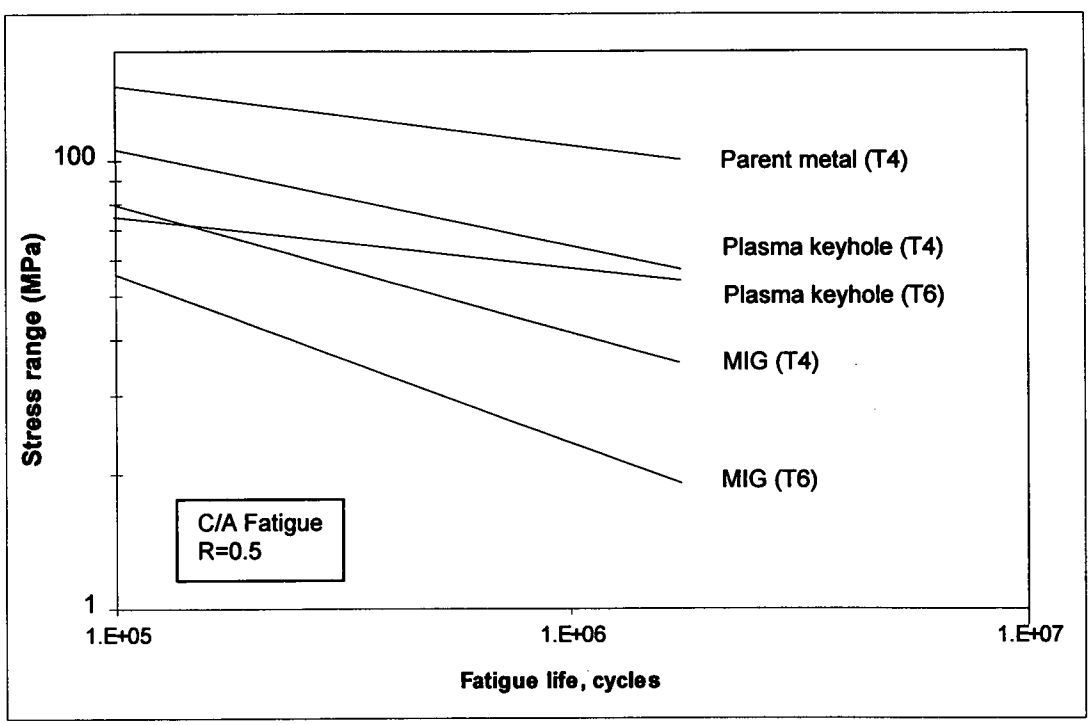

Figure 2.10 Comparison of the fatigue properties of 6005-T4 and T6 base metal and transverse welded joints. The curves have been obtained using different welding techniques, Ref. [4].

Residual stress plays an important rule in influencing fatigue performance of welded joints [38, 61, 65, 105]. Residual stresses in welded components arise from the local heating introduced by the weld heat source in the workpiece. The thermal expansion of the material close to the weld is inhibited by the restraining effect of the surrounding material. This causes plastic deformation to take place in the weld. During cooling, the longitudinal contraction of the weld metal is resisted and tensile residual stresses are

thus introduced in the weld [31]. These tensile residual stresses are balanced by compressive stresses in the regions far from the weld.

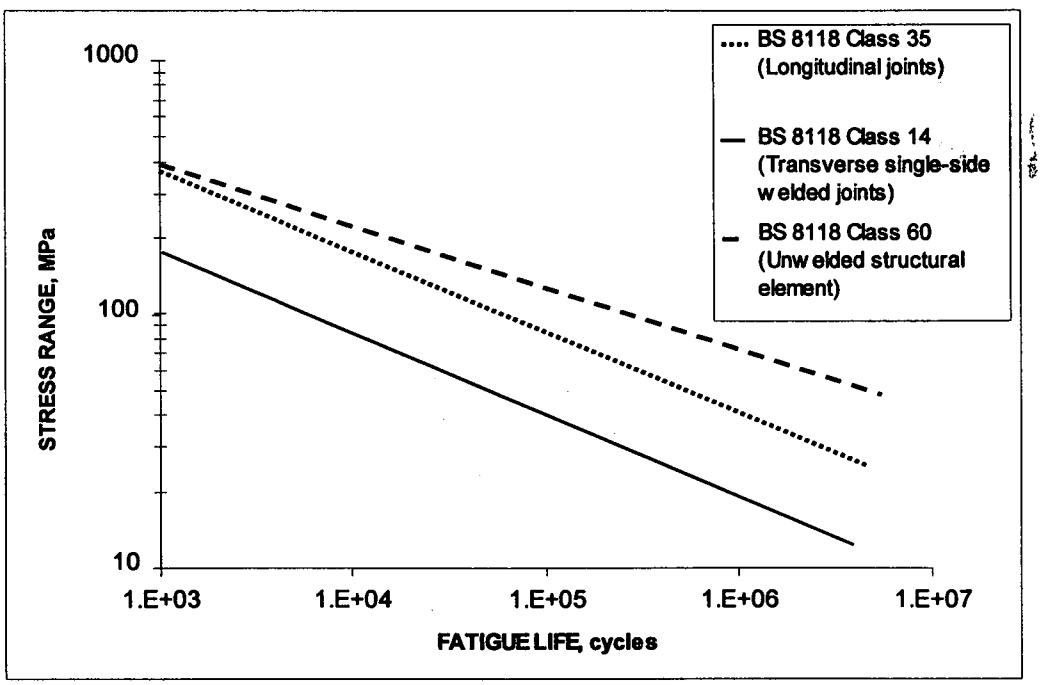

Figure 2.11 Fatigue design curves from BS 8118 for longitudinal and transverse aluminium welded joints compared with that of an unwelded structural element.

The typical residual stress distribution in a welded plate is shown in Figure 2.12 [61]. The longitudinal residual stress distribution (Fig. 2.12, a) is not in equilibrium for in-plane rotations. A transverse residual stress distribution (Fig. 2.12, b) arises to balance the in-plane rotation of the two half-plates. A through thickness transverse residual stress (Fig. 2.12, c), generally negligible for small plate thickness, is introduced too. The dependence of residual stress on plate thickness and number of passes was investigated by Kelsey. As can be observed from Fig. 2.12, the weld bead is in tension whereas regions near the weld are in compression. The size of the tensile residual stress in the weld can often approach the yield strength of the weld material, depending also on the boundary conditions during welding [38]. Leggatt found longitudinal residual stress peaks in the weld metal to be between 50 and 100% of the weld metal proof strengths in 5456-H116, 6061-T651, 5083-O and 2219-T87 welded plates.

The effect of weld residual stress on fatigue life of aluminium longitudinal joints has been investigated by Hill. Residual stress and yield stress were measured in longitudinal 5456-H321 welded joints. The joints were tested under CA fatigue loads at different stress ratios (R). Results in the form of S-N data were compared with those obtained from similar joints after that residual stresses were relieved by thermal treatment. The fatigue strength of the as-welded joints was at 10^7 cycles, 35% higher than the stress relieved samples for R =-0.5. For R = 0 the difference was 25% and for R = 0.5 it was less than 10%. This indicated that weld residual stress reduced the fatigue strength of the joints and that the reduction was higher at low stress ratios. The same dependence was observed for different joint geometries and different materials [94, 33].

This effect is generally explained considering the modification of the mean stress of the applied fatigue loads by the tensile residual stress in the weld [61]. During the first cycle when the maximum applied stress σ_{max} is reached, yielding takes place in the weld metal due to the presence of high residual stress. The yielding causes a redistribution of the residual stresses so that as the following cycles are applied, the effective fatigue stress cycles will range between the weld yield stress (σ_{yw}) and $\sigma_{yw} - \Delta\sigma_{appl}$, Figure 2.13. Thus, the effective fatigue cycles will have equal stress range but different mean stress.

Under compressive fatigue loading, i.e. from zero to $-\sigma_{max}$ (Fig. 2.13), the effective fatigue loading will range between σ_{yw} and $\sigma_{yw} - \sigma_{max}$. These imply that fatigue failure can occur under loading conditions which normally would not cause fatigue failure, such as compressive loading. Moreover, the fatigue strength of welds in the presence of residual stresses is generally dominated by the applied stress range regardless of the applied stress ratio [33].

The effect of residual stress on fatigue strength is influenced by the maximum loads of the applied cycles as mechanical residual stress relief can occur. This interaction between residual stress and load history is extremely important when overloads or variable amplitude loading are involved. The effect of single tensile loads on weld residual stress has been described in detail by Gray [31]. Figure 2.14 shows the stress-

strain behaviour of a longitudinal welded plate loaded in tension under uniform strain (this is typically the case of a specimen during a tensile test). The constitutive behaviour of the material has been represented as elastic-linear plastic ignoring the work hardening behaviour.

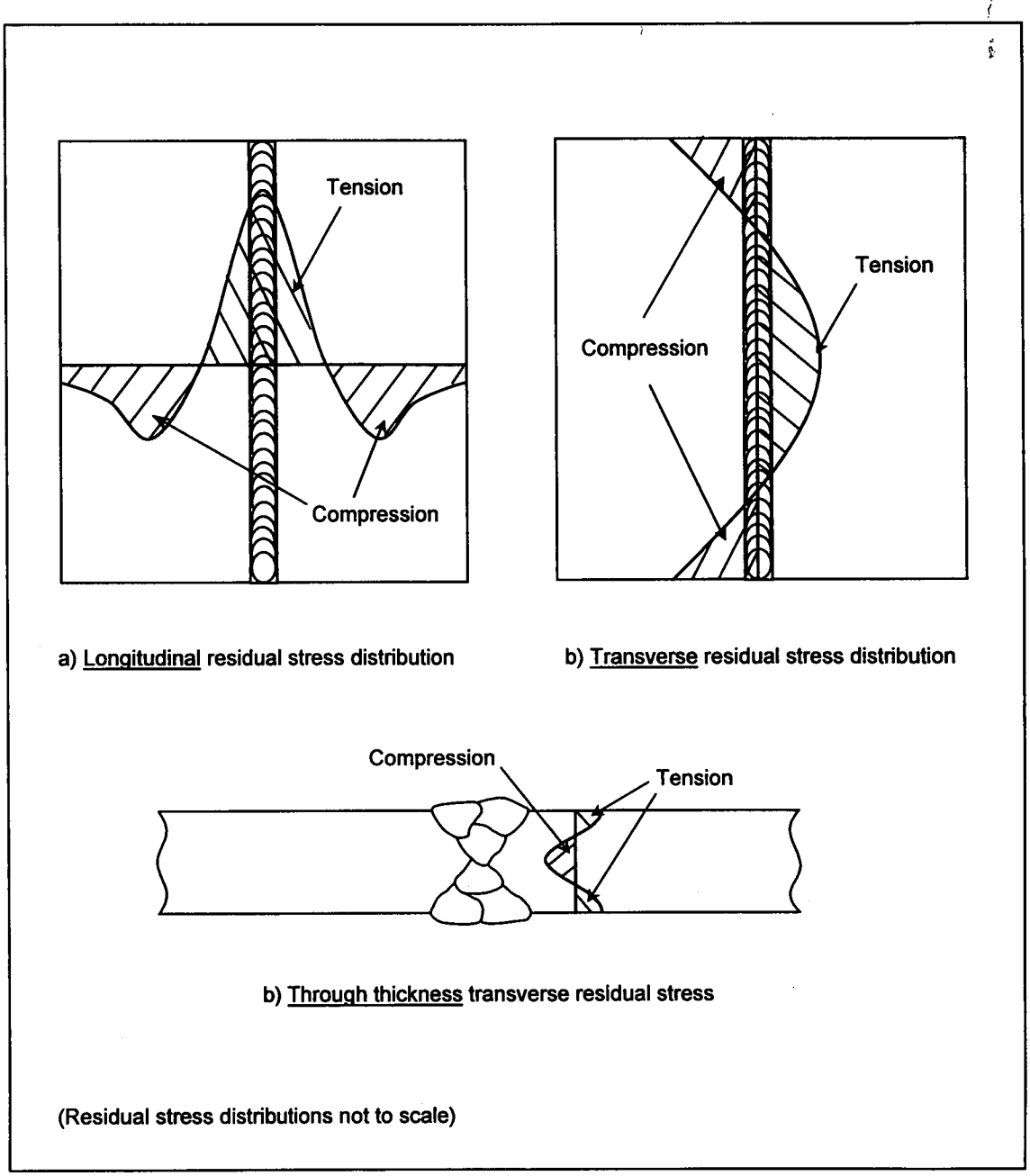

Figure 2.12 Typical residual stress distribution in a welded plate.

When the load is applied to position (1) and removed to (1'), the tensile residual stress at A and the compressive residual stress at B are reduced. At the same time, a tensile residual stress has been generated at C. Obviously, for equilibrium the algebraic summation of the areas delimited by the residual stress distribution plots has to be zero. Loading to position (2) and unloading to (2'), produces a more severe stress relief. If the joint is loaded to position (3), all of the plate has reached tensile yield and the residual stress after unloading must be zero since the plate is now behaving like a large tensile specimen. Any load that exceeds (3) does not produce further residual stress modification

This analysis showed that weld residual stress is reduced by any tensile loading in the direction of the residual stress component, provided that sufficient ductility is available to allow the necessary deformation.

The total fatigue life (N) of a structural component is typically subdivided in the initiation and propagation periods. The former (N_I) is scientifically defined as the number of fatigue cycles to nucleate a flaw along persistent slip bands [98]. From an engineering viewpoint, N_I can be defined as the number of cycles for a crack to be detectable within specified values of probability and confidence. The propagation period (N_P) is the number of fatigue cycles to grow the nucleated flaw or the detectable crack to fatigue failure. It is defined as $N = N_I + N_P$. S-N curves represent the total fatigue life and no distinction is explicitly made between initiation and propagation.

An important issue in the fatigue analysis of welded structural components is the evaluation of the initiation and propagation periods. In welded joints, small crack-initiating defects are typically present in the fusion zone of the weld. For this reason, the fatigue life of welded joints is often considered to be dominated by crack propagation and in this light initial defect size is important in determining fatigue life. Fracture mechanics is applied to provide a conservative estimate of the total life. However, it has been also shown that the number of cycles required to initiate, from pre-existing defects, a crack large enough to be detected and treated by linear fracture mechanics as a "large crack", can be significant (up to 10-40% of the total life) [7]. The initiation period is

generally longer for low stress fatigue failures and shorter for high stress fatigue failures [7]. Investigations carried out on aluminium and steel weldments have shown that fatigue initiation typically takes place from local defects at the weld toe of transverse joints and at ripples of the weld surface in longitudinal joints [61, 62, 76]. This is generally explained as an effect of the stress concentration K_t associated with the weld toe profile [61].

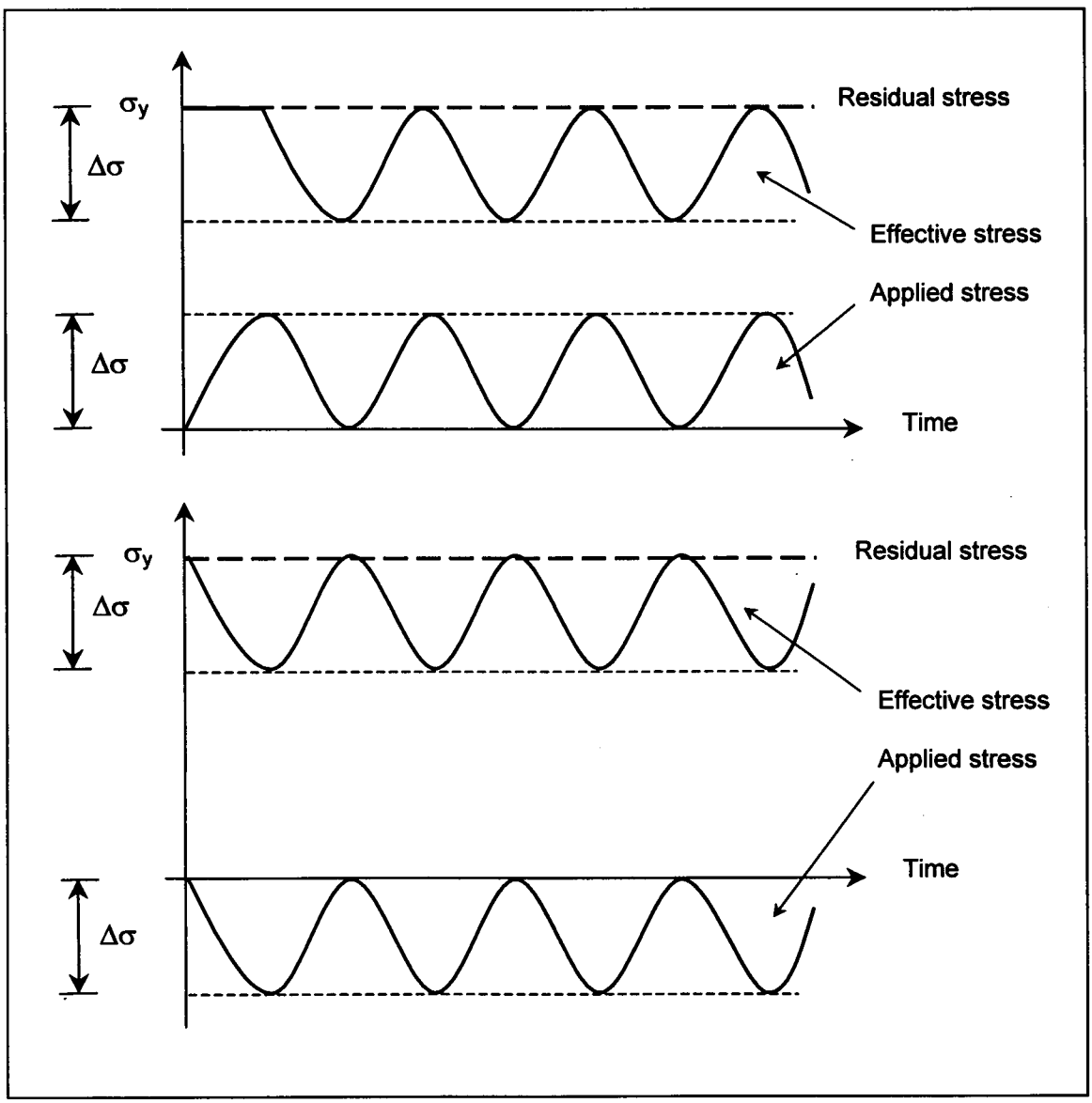

Figure 2.13 Effect of residual stress on the mean stress of CA fatigue cycles, Ref. [61]. The fatigue behaviour of welded joints in the presence of residual stresses is dominated by the stress range of the applied load cycles.

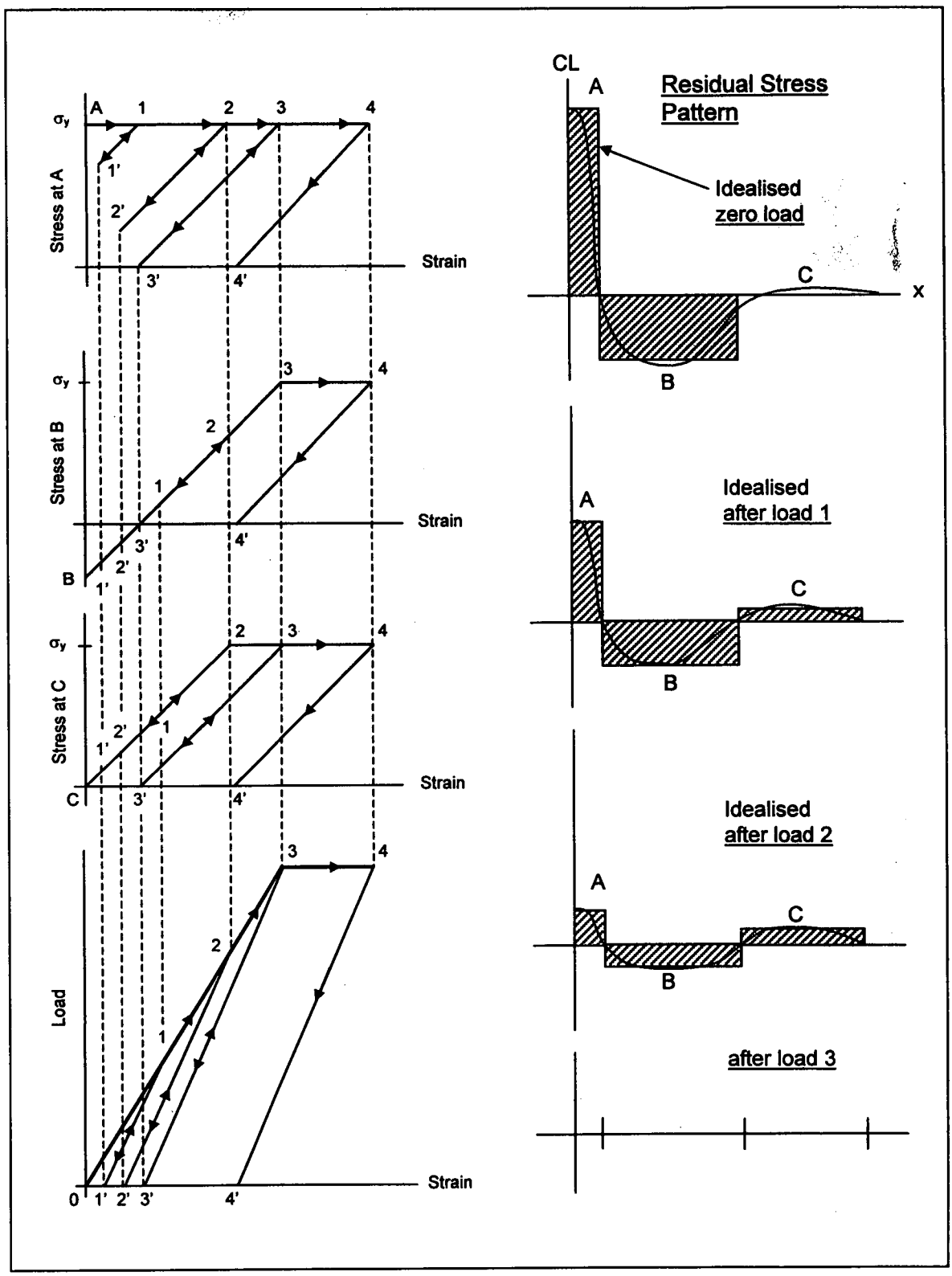

Figure 2.14 Mechanical stress relief of longitudinal weld residual stress.

Typical weld defects are inter-metallic inclusions, porosity and lack of penetration. These defects if located internally to the weld and acceptable from a static point of view, do not affect the joint fatigue strength. This can be explained by the fact that the stress intensity factor of an internal crack is generally lower than that associated with a surface crack of similar geometry [86]. Quality of weld surface is a primary factor affecting joint fatigue performance. It has been observed that fatigue strength in transverse joints can be reduced by 40% by poor surface quality [61].

2.9 Crack propagation in welded joints: effect of residual stress

Crack propagation properties in welds are typically affected by the modifications during welding of the parent plate characteristics. The modifications are the introduction of a residual stress field, changes in microstructure and softening of the parent metal. Several authors have observed strong interactions between residual stress and crack propagation in aluminium alloy and steel welded plates [24, 42, 53, 70].

Cracks have been introduced into plates with tensile residual stresses of maximum values between 0.5 and 1 times yield. Cracks starting from the weld centre line and growing orthogonal to the weld direction exhibited, in the first stage of the propagation, growth rates between 3 and 7 times greater than in the parent material. In the subsequent stage of the growth, the crack propagation rates decreased gradually reaching the crack growth rate measured in the parent plate at similar stress intensity factor values (ΔK). These observations indicated that the longitudinal tensile residual stress present in the weld was responsible for the initial fast growth. In the second stage of the propagation, the tensile residual stress was gradually relieved as the crack extended through the weld and the difference in growth rate reduced [24, 42].

Cracks orthogonal to the weld were initiated in the HAZ where maximum longitudinal compressive residual stresses between 0.25 and 0.5 times the yield stress of the parent material were measured. The cracks exhibited growth rates up to 5 times slower than in the parent material. The crack growth rates decreased and in some cases crack arrest was observed [42]. This was believed to be caused by a redistribution of compressive residual stresses following crack extension. The redistribution increased the

compressive residual stress peak in front of the crack causing a decrease in the crack propagation rate. The increase of the compressive residual stresses following the crack propagation is necessary in order to preserve the balance [42, 110]. In the works previously mentioned, no evidence was found that the transverse residual stress distribution in the weld influenced the propagation of cracks orthogonal to the weld.

In their works, El-Soudani and Ignat'eva observed changes in threshold stress intensity factor ranges (ΔK_{th}) [24, 42]. Cracks that initiated in the compressive residual stress regions exhibited near-threshold ΔK values approximately twice those of the parent plate. Cracks that initiated in the weld exhibited threshold ΔK values close to the parent plate ones, indicating that the tensile residual stress field marginally affected the near-threshold ΔK values [24, 42]. No explanation was proposed for these latter experimental observations.

Several investigations have been conducted on cracks propagating parallel to the weld. The cracks were introduced both in the weld and in the HAZ and results compared with the parent plate properties. Experimental results did not indicate a common behaviour. Crack propagation tests carried out on 7005-T6 welded plates showed that cracks which were initiated within the weld exhibited crack growth rates comparable to the parent plate and 5 times higher than in the HAZ [24]. The cracks propagating in the HAZ exhibited near-threshold ΔK values approximately 1.8-2.0 times the values observed both in the weld and in the parent plate. Deviation of the crack paths in the direction of the parent plate was explained as the effect of the longitudinal residual stress gradient in the direction orthogonal to the weld.

Similar tests conducted on welded C-Mn micro-alloyed steel plates showed that cracks growing in the weld had a better behaviour than in the parent plate. Crack growth rates in the weld were approximately 13 times lower than in the parent metal, and the near-threshold ΔK values were between 2 and 3 times the parent plate values. Residual stress measurements indicated a distribution similar to the transverse residual stress showed in Figure 2.12. The tensile peak was 10% of the parent plate yield stress and compressive minimum values in modulus 30% of the yield stress of the parent metal [5, 6]. The

effective stress intensity factor (ΔK_{eff}), defined in the crack closure model [23, 89], was estimated via two numerical methods (Finite Element Analysis and Weight Function methods). The crack propagation curves coincided when re-plotted versus ΔK_{eff}. This fact indicated that crack propagation occurred in the weld and in the parent plate under similar ΔK_{eff} values. The through thickness transverse residual stress in thick plates affected the front shape of cracks orthogonal to the weld but did not affect its overall growth rate [53]. In cracks parallel to the weld the through thickness transverse residual stress induced crack branching and mid-thickness shear topography [24].

The crack closure model (Section 2.2) can be applied to evaluate the effect of residual stress on crack propagation in a welded plate [9, 41, 51]. Variation of the crack opening stress σ_{op} of cracks growing through a weld residual stress field has been experimentally observed by different authors [5, 8, 73]. σ_{op} and the relative stress intensity factor K_{op} is influenced by the residual stress in the region of propagation. For a crack growing through a tensile residual stress region, σ_{op} should be lower than for a crack growing through a compressive residual stress region [70].

For residual stress values greater than the one that is enough to cause the crack opening stress to drop below applied σ_{min}, the crack growth rate should not be influenced by variations in residual stress. This concept is illustrated in Figure 2.15a. Differently, for a crack growing through a compressive residual stress region, σ_{op} varies as a function of the compressive residual stress values (Fig. 2.15b). If the compressive residual stress is large enough to cause σ_{op} to approach σ_{max}, the crack propagation may be arrested [42].

The model can be used to predict crack growth rates in welded joints if K_{op} (ΔK_{eff}) is known (generally from elastic-plastic finite element analysis), or to evaluate the effect of residual stress on crack propagation when σ_{op} is experimentally determined [9, 41, 51]. The crack closure approach has the advantage of providing the mechanics to account for the effects of weld residual stress modifications due to overloads and crack growth [57]. However, prediction of crack growth rates usually requires the application of elastic-plastic fracture mechanics, and calculations must be repeated as the crack grows.

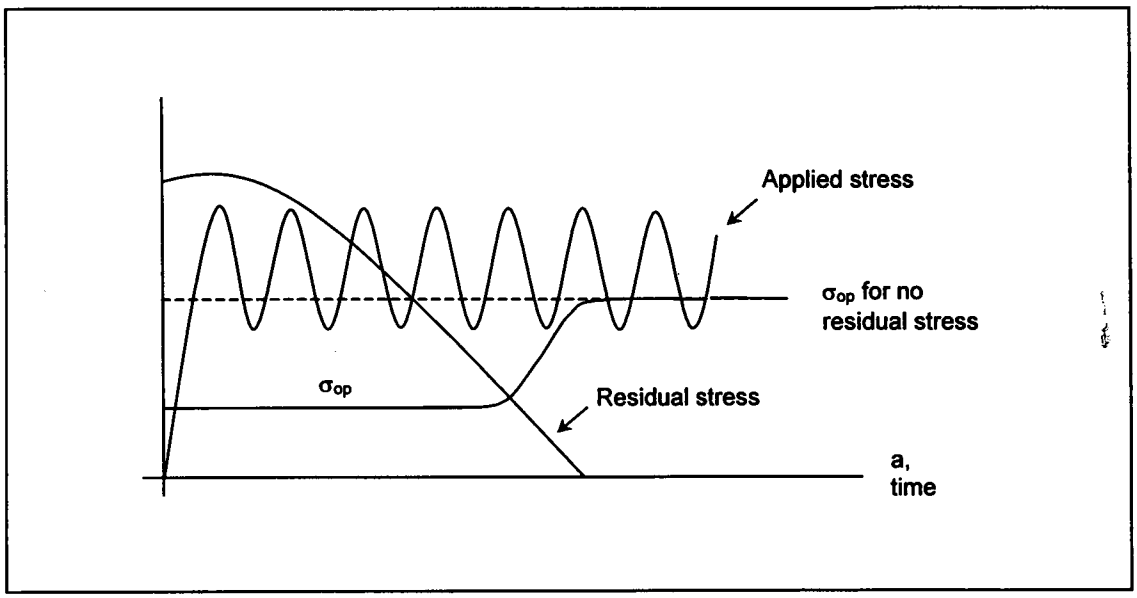

Figure 2.15a Crack closure through an initial tensile residual stress field.

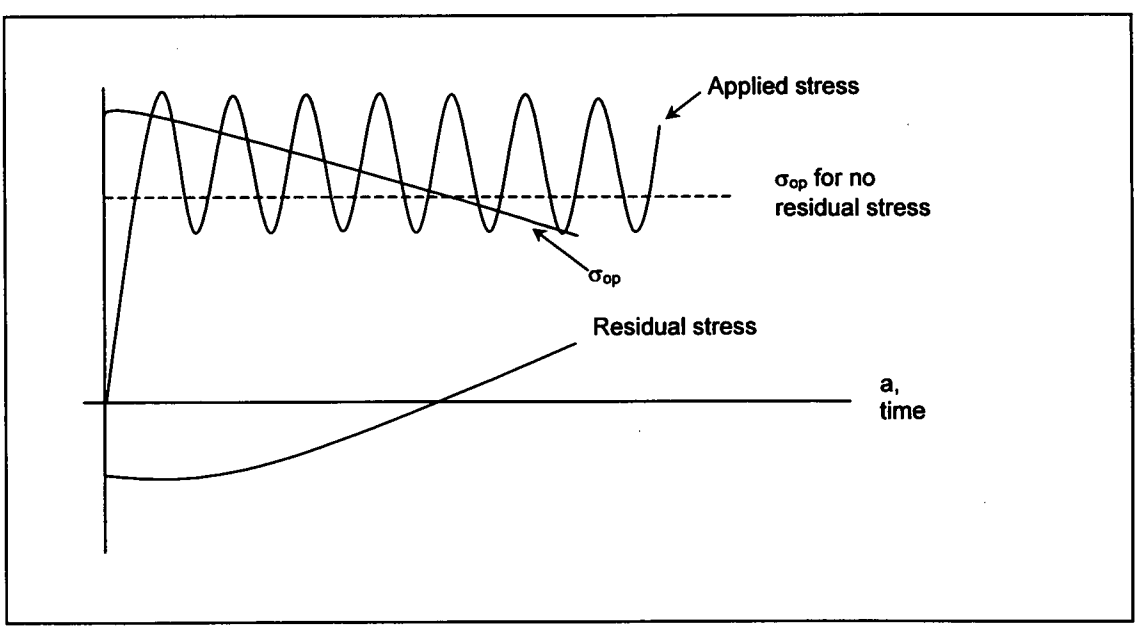

Figure 2.15b Crack closure through an initial compressive residual stress field.

2.10 Crack propagation in welded joints: effect of microstructure and hardness

Several studies on crack propagation in aluminium and steel welds have shown that the effect of microstructure and hardness is small compared with the effect of residual stress [24, 80, 107]. Fatigue crack growth rates measured in the weld, characterised by a cast

columnar structure, were similar to those in the respective 7005-T6 base alloy indicating that crack propagation in the weld was marginally affected by the different microstructure [24]. A decrease in fatigue crack growth rates associated with crack branching towards the regions of lower hardness was observed by the same author. This suggested a role of hardness in reducing the crack growth rates in the HAZ.

Crack growth rates in the HAZ 4 times lower than in the parent plate were observed in Al-4.5Zn-2.5Mg alloy welded samples [80]. Crack branching was observed in the HAZ. The reduction in crack growth rates was attributed by the authors to a combined effect of hardness and microstructure, residual stresses being small. Similar studies were conducted on EH36 steel welds after being tempered in order to release the residual stresses originated during welding [107]. Crack growth rates in the HAZ were 2 times lower than in the parent plate. This behaviour was attributed to the difference in microstructure between the HAZ and base metal. However, the changes in hardness due to the heat treatment and their effect on crack propagation were not investigated.

2.11 Design of welded aluminium aerospace structures

Although welded structural components have been used in airframes since 1920s [43], a limited amount of data has been published in the open literature regarding design approach and methodologies for welded aerospace structures.

Welded joints and fastened joints have different mechanical properties. Riveted joints bear loads by shear stresses acting on rivets [72]. Stress concentrations, secondary bending moments and the need of edge overlapping make the mechanism of bearing loads in riveted joints very different from that in a simple butt welded joint. These differences produce different design requirements in both cases. Although replacing riveted joints with welds could appear the simplest approach to the problem, this is not likely to be an efficient design methodology.

Welds differ from riveting because of the degradation of properties that takes place in welds. An appropriate choice of materials will tend to minimise the degradation caused by the welding process. In this direction, studies have been carried out in order to

develop guidelines for materials choice. The method consisted in selecting the material in order to minimise the weight of the welded component [11, 12].

The same studies have indicated that design of welded airframes should consider a panel-structures approach. This approach consists of the design of welded structural panels in flat form. The panels are subsequently shaped with the required geometrical accuracy (for example, in the super-plastic condition of the metal) and heat-treated if possible. The final structure is obtained by assembling the individual panels. This method allows controlling residual stresses and deformation due to welding and facilitates the automation of the welding process. The previous method considered frequent use of fillet welded joints, allowing higher design flexibility [11, 12]. However, it should be observed that the fillet welded joints have generally lower fatigue strength and lower level of inspectability than butt welded joints (Section 2.8).

The design of friction stir welded aircraft structures and their benefits have been investigated by British Aerospace Airbus [77]. The design approach uses welding in order to reduce manufacturing costs and achieve weight savings, not so much from the increase in stress levels and improved fatigue strength, but from the reduction of fastened joints. A possible design solution for welded wing skin panels was discussed, Fig. 2.16.

In conventional fastened wings, the skin panels are typically jointed in the span-wise direction via a butt strap joint incorporating a stringer, Fig. 2.16, a. The introduction of welding allows the elimination of the butt strap and sealant film. The skin panels are jointed via a span-wise butt weld located away from other geometric stress concentration features, such as bolted and riveted stringers, to improve the joint durability, Figure 2.16, b. No methodology of design for damage tolerance of welded structures has been proposed by the authors.

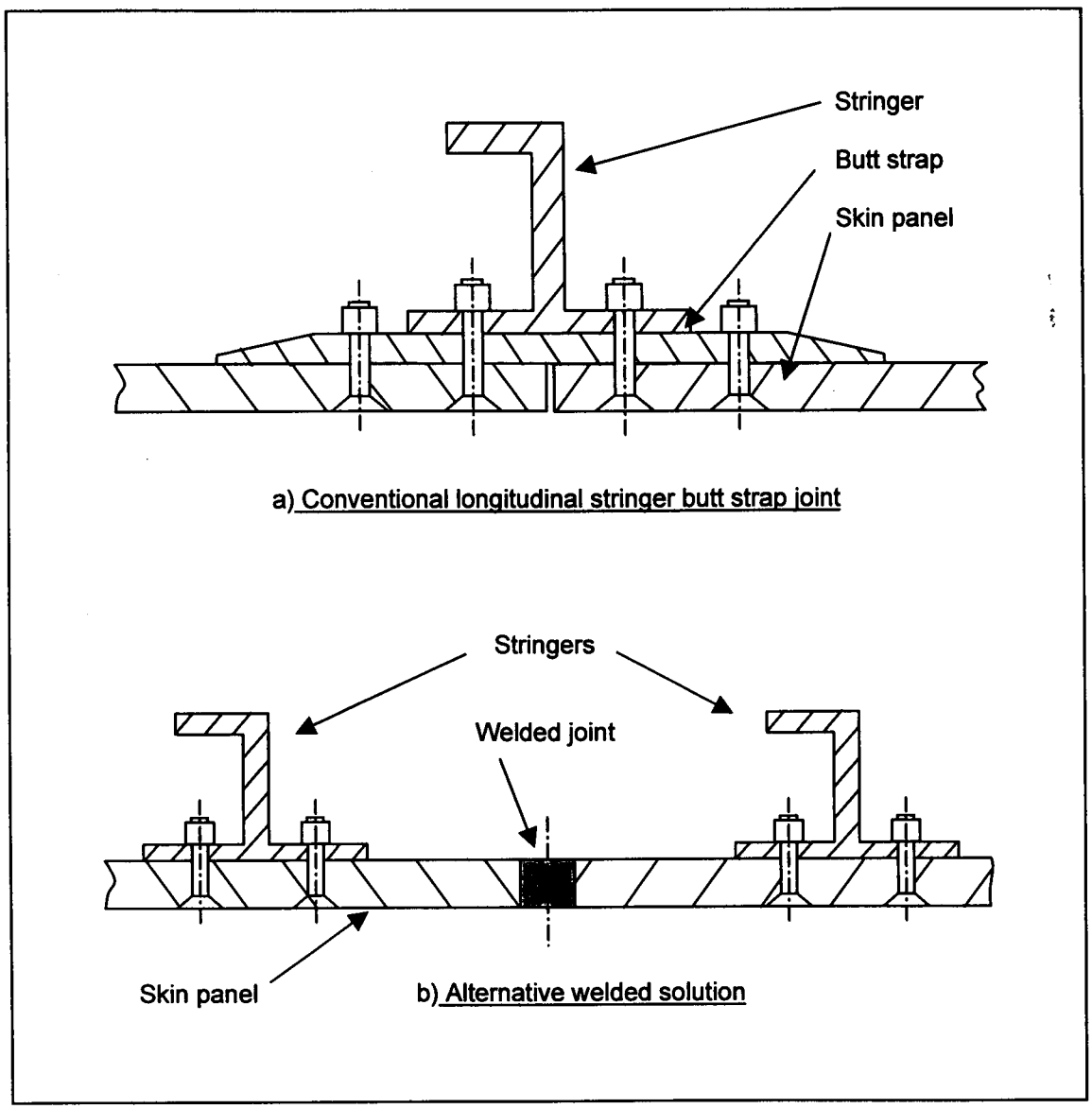

Figure 2.16 A proposed welded design solution for a wing skin panel joint of a transport aircraft.

3. EXPERIMENTAL PROCEDURES

3.1 Parent material 2024-T351

The 2024-T351 alloy has been selected being the standard alloy used to manufacture lower wing panels of the actual generation of large commercial aircraft [72]. The alloy 2024 is a Copper-Magnesium based age hardenable aluminum alloy. Copper allows the strengthening of the alloy through the age hardening process and Magnesium reduces the embrittling effect caused by iron impurities [2]. The 2024-T351 aluminium alloy is an Al-Cu-Mg alloy which has been solution heat-treated, control stretched and naturally aged. The specified chemical composition is given in Table 3.1.

Cu	Mg	Mn	Fe	Si	Zr	Cr	Ni	Others	Al
3.8 4.9	1.2 1.8	0.3 0.9	0.5	0.5	0.2	0.1	0.05	Pb 0.05 Sn 0.05 Ti+Zr 0.2	Rem.

Table 3.1 Specified chemical composition for 2024-T351 aluminium alloy (wt %), Ref. [1].

The 2024-T351 alloy was supplied in the form of plate (6.35 mm of thickness). Table 3.2 shows the mechanical properties of the 2024-T351 (plate) material.

Orientation	0.2 % Proof Stress (min)	Ultimate Stress (min)	Elongation on 50 mm (min)
L	310 MPa	430 MPa	12%
L-T	280 MPa	420 MPa	–

Table 3.2 Mechanical properties for 2024-T351 aluminium alloy, Ref. [1].

Figures 3.1a, 3.1b and 1.1c show the grain structure of the 2024-T351 plate in the three planes LT, TS and LS. Samples of the material were cut, embedded in epoxy resin and cured at room temperature. The polishing operation was carried out up to 5 μm finishing grade using automatic polishing machines. The samples were etched in a saturated solution of molybdic acid in 5% fluoridric acid for 20 seconds. The etching operation was repeated in alternation with the polishing procedure with a colloidal silica solution in order to obtain a better surface quality. Grains, evidenced by the etching, showed the typical elongation in the plate rolling direction.

3.2 Welding procedures

The friction stir welding to produce samples was carried out by BAe Airbus Ltd. Welding parameters were kept confidential to them. The welded plates were obtained by welding two 378 × 130 × 6.35 mm parent plates along their long edge. The weld direction was parallel to the L orientation in the parent metal. The plasma welding process was performed with no filler metal (autogenous plasma welding) using the "keyhole" technique [111]. The plasma welding operation was carried out by the Cranfield Welding Group. Table 3.3 shows the welding conditions.

Polarity 70% -e.n./(e.n. + e.p.) time	Orfice Diam. 2.25 mm
Frequency 50Hz -e.n. + e.p. cycle	Electr. Set-Back 3.0 mm
Balance 60% -e.p. amplitude	Plasma Flow rate 1.4 l/min Ar
Stand-Off 3.9 mm	Shield Gas Flow rate 10 l/min Ar/He

Table 3.3 Standard plasma autogenous welding parameters (vertical-up).

3.3 Specimen preparation for metallography

Friction stir and plasma welded plates were sectioned in the direction normal to the weld line and 100 × 30 × 6.35 mm samples extracted. Other samples were obtained by sectioning friction stir welded plates in the direction of the weld line. The samples were cut and polished as for metallographic examination (Section 3.1).

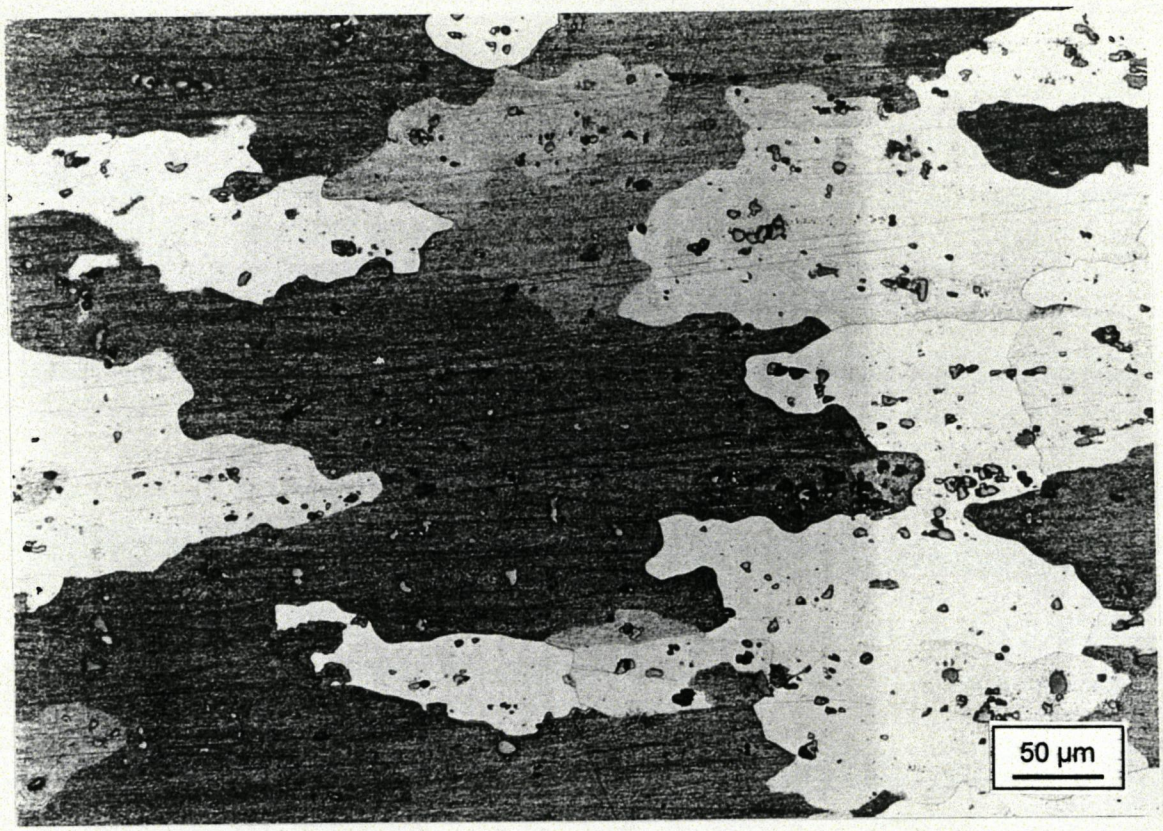

Figure 3.1a Microstructure in LT plane observed in the 2024-T351 6.35 mm rolled plates.

3.4 Hardness profile measurement

Samples were cut and polished as for metallographic examination. Hardness tests were performed in full accordance with the standard test method for Vickers hardness test ASTM E 92-82 (1989) using a Matsuzawa Seiki Vickers micro-hardness test machine.

Indentations were carried out applying 1.0 kg force for 15 seconds. Indentations on two FSW samples were preformed on the weld transverse sections at constant intervals of 1.0 mm on the mid-thickness line, at 2.0 mm from it, and on the weld upper and lower surfaces, as shown in Figure 3.2. Hardness tests on two plasma welds were carried out using the same procedure. The measurements were performed on the mid-thickness line and at constant intervals of 1.0 mm.

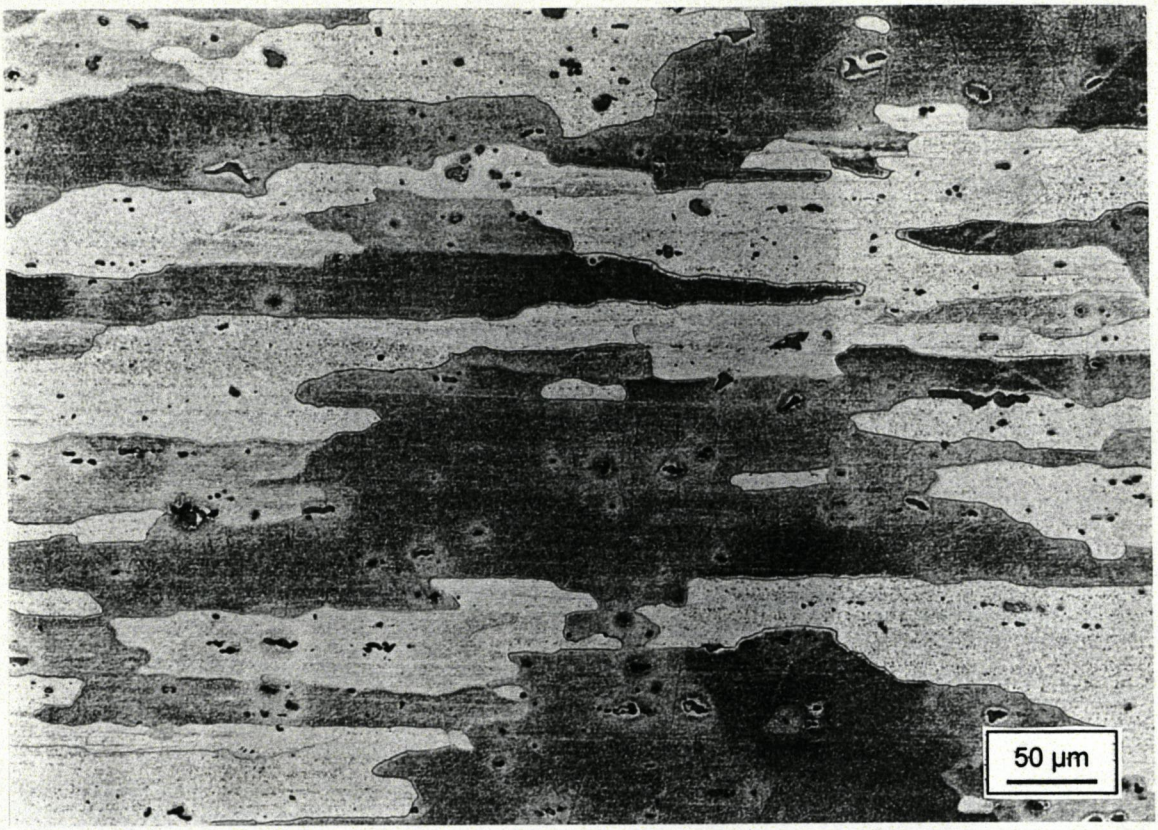

Figure 3.1b Microstructure in TS plane observed in the 2024-T351 6.35 mm rolled plates.

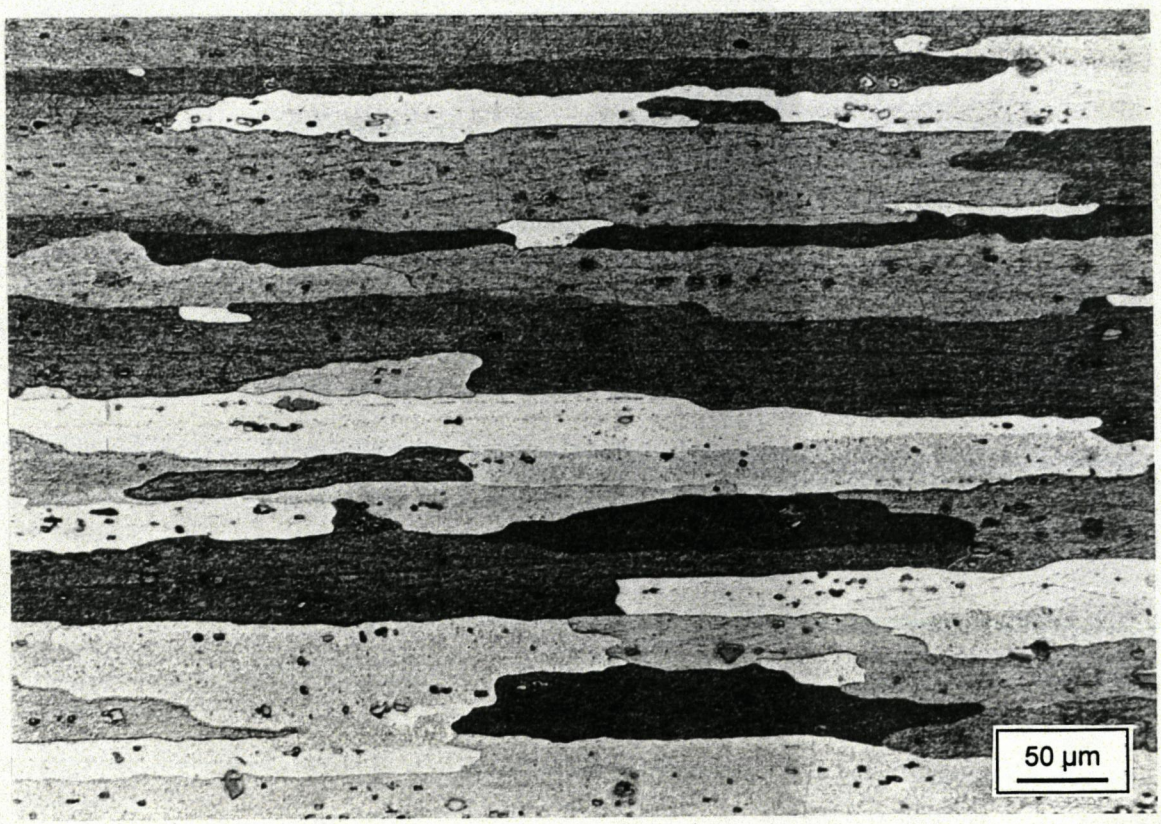

Figure 3.1c Microstructure in LS plane observed in the 2024-T351 6.35 mm rolled plates.

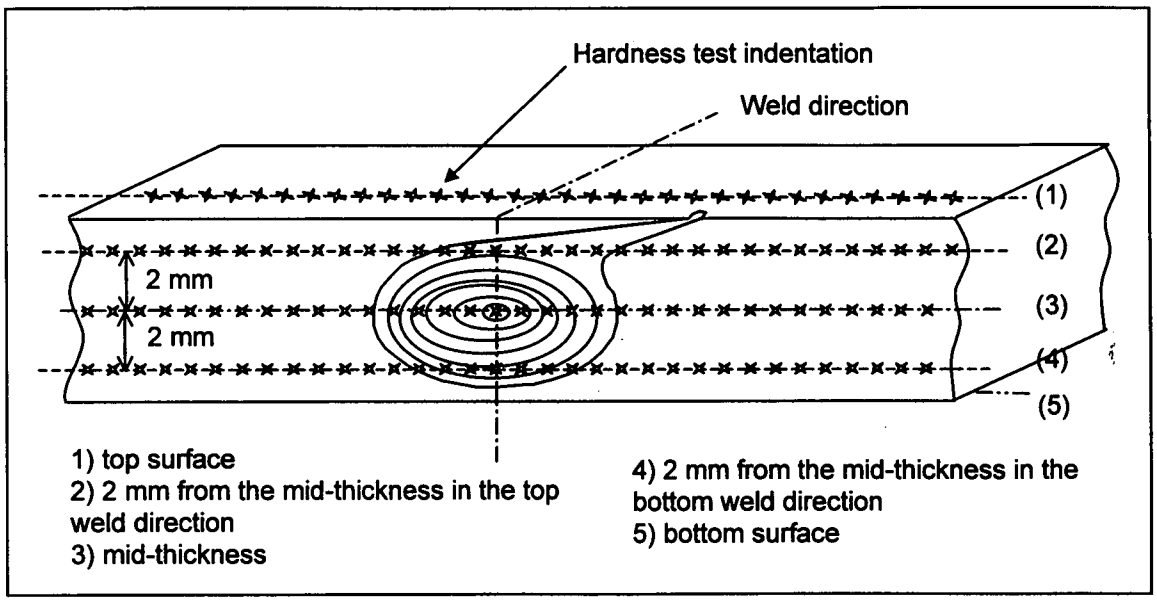

Figure 3.2 Locations of hardness transverse measurements carried out in the friction stir weld cross sections.

3.5 Preparation of tensile specimens

Material, initial plate dimensions and welding procedures were as described in Sections 3.1 and 3.2. Two different configurations of specimen were machined from the welded plates. The longitudinal specimen had its principal axis parallel to the weld axis. The transverse specimens had its principal axis perpendicular to the weld axis. The two specimen configurations and their principal dimensions are shown in Figure 3.4.

Specimen dimensions were chosen in accordance with ASTM E 8M (1997) standard requirements for tension testing of metallic materials. The definition of the specimen dimensions was made in respect of the limitations imposed by the welded plate dimensions and testing equipment operational limits. Specimen test gauge sections were always positioned far from weld start and stop areas in order to guarantee uniformity to the weld properties within the test sections. Plasma welded specimens were machined in the transverse configuration using the same geometry and dimensions as for the transverse FSW joints (Fig. 3.3).

One longitudinal and one transverse specimen were surface skimmed removing 0.5 mm from both specimen surfaces. In order to reduce distortion arising from residual stress relief during the skimming operation, a special jig and cutting procedure were developed. A vacuum chuck holder was built to hold the specimen in flat position during cutting. A 0.1 mm layer was removed with a fly-cut tool at each cut alternately on the top and bottom surface until 0.5 mm of material had been removed.

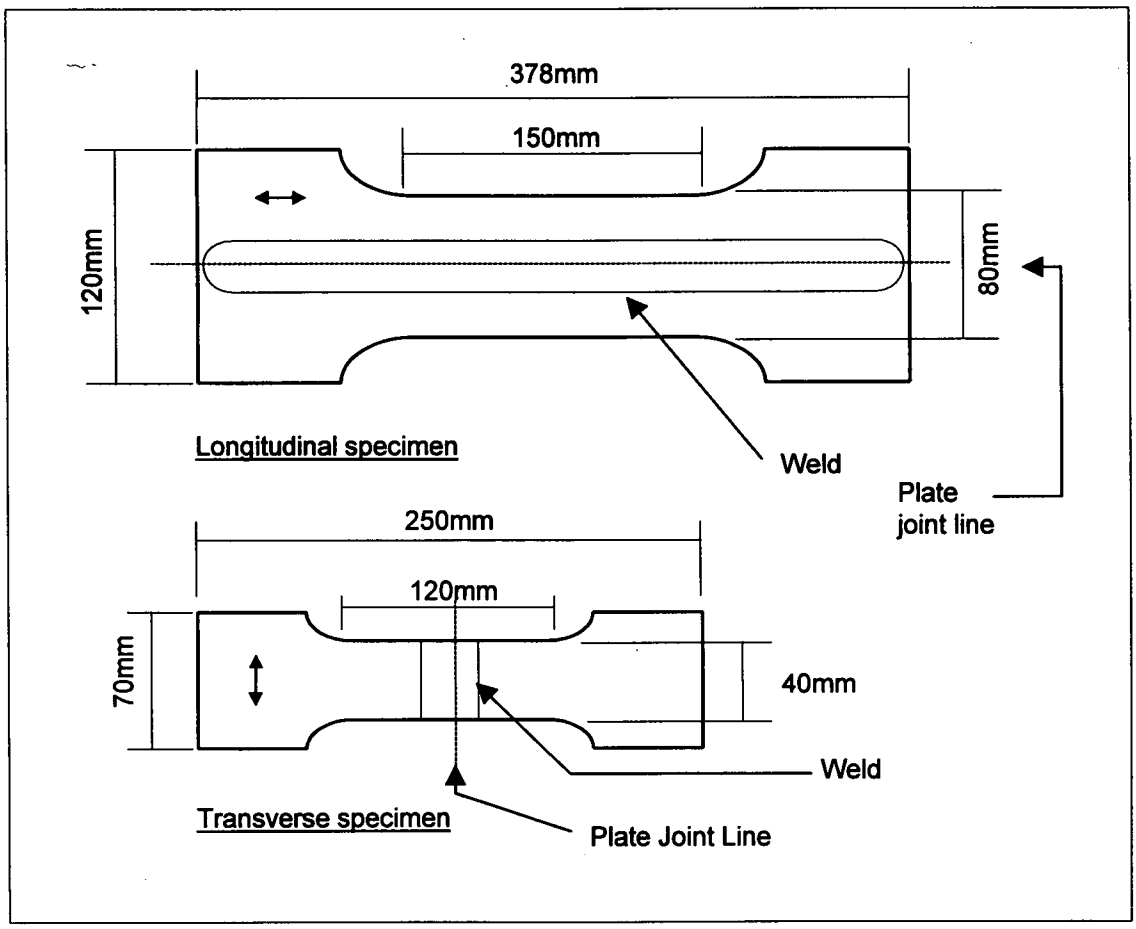

Figure 3.3 Longitudinal and transverse welded specimen geometry. The parent plate rolling directions are also indicated in the two cases.

The two skimmed specimens were strain-gauged in order to establish the local stress-strain behaviour. It was recognised that hardness distribution would have played a fundamental role in the distribution of strain within the transverse welded specimens,

whereas hardness and residual stresses would have affected the stress distribution within the longitudinal specimens.

Figure 3.4 shows the position of the strain gauges for the transverse welded specimen. Seven strain gauges were positioned at several distances from the plate joint line (PJL) on the top and bottom surface of the joint. Each of them was located at the relative minima and maxima of the hardness distribution curves, as shown in Figure 3.5. All the strain gauges were positioned on the specimen longitudinal line of symmetry in order to avoid any interference in the strain measurements by any unpredicted in-plane secondary bending moment.

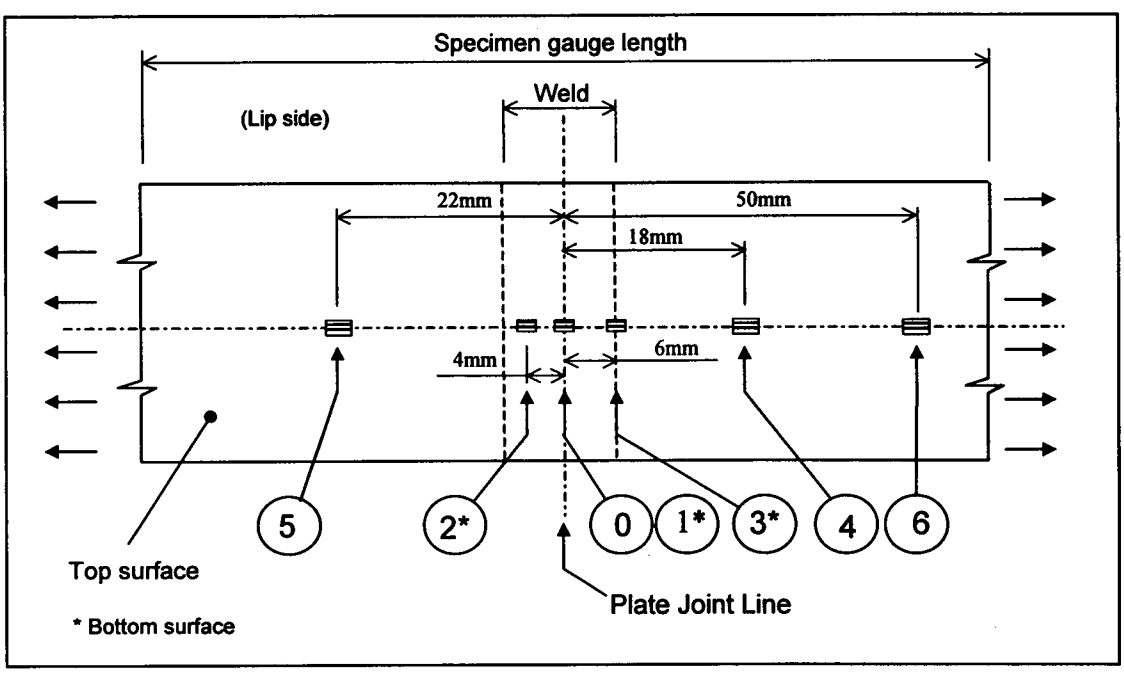

Figure 3.4 Strain gauge positions on the transverse FSW specimen in the monotonic tensile test.

Because of the rapid variation in the hardness values within the central area of the weld, strain gauges with 0.2 mm active gauge length (TML FLG-02-11) were applied in this region (gauges 0, 1, 2 and 3). Strain gauges 4, 5 and 6 had instead 3.05 mm active gauge length (MM EA-13-120LZ-120). Strain gauge 1 was positioned on the bottom weld

surface corresponding to the minimum hardness value on the PJL. Strain gauge 0 was positioned on the top weld surface in order to check for possible secondary bending. All the strain gauges were self-temperature-compensated.

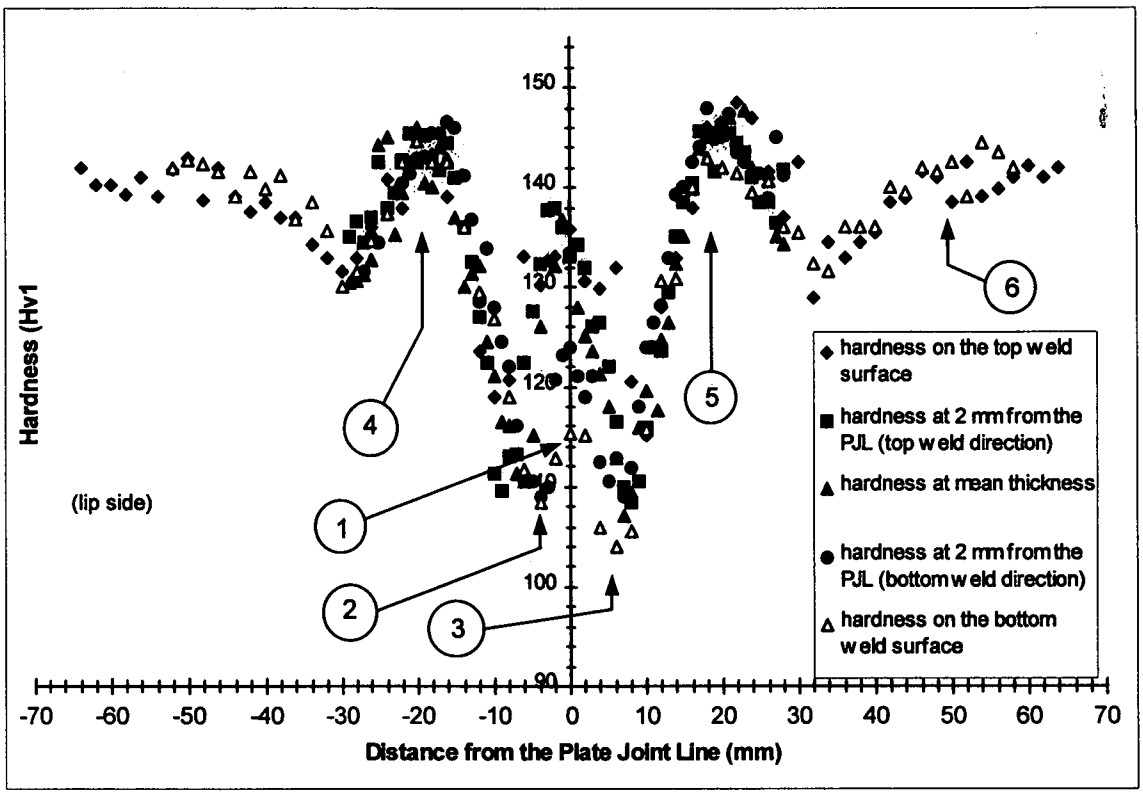

Figure 3.5 Strain gauges position compared with the transverse hardness values measured on the transverse FSW specimen before the tensile test. The hardness profiles were measured as described in Section 3.4.

The FSW longitudinal specimen was strain gauged on the specimen transverse line of symmetry and at different distances from the PJL. All the strain gauges (TML FLG-02-11) had 1.25 mm grid width and active gauge length of 0.2 mm. The self-temperature-compensated strain gauges were installed on the specimens using M-Bond 200/ Catalyst-C cyanoacrylate adhesive. Transverse and longitudinal specimens were tested under ambient laboratory conditions.

3.6 Tension testing procedures

The longitudinal and transverse specimens were tested using an Instron 8500 digitally controlled test machine capable of 250 kN as maximum load fitted with a 0.5 class load cell (±0.44% accuracy, 0.01% resolution). The load cell was calibrated in accordance with EURONORM EN 10002-2: 1991.

The tests were performed in accordance with ASTM E 8M (1997) standard. The specimens were clamped in the grips and the strain gauge signals were amplified, monitored and recorded via a Strawberry Tree multi-channel data acquisition system. The Strawberry Tree system is composed of a Mini-16 analog input and output board for IBM compatible PCs and a QuickLog PC data acquisition and control software [97]. The Mini-16 board is capable of attaining 16 bit resolution. The Load output signal from the load cell of the test machine was also recorded. The load was applied during the tests in position control mode and with a displacement rate of 1 mm/min, up to the failure of the specimens. The stress values were calculated with reference to the nominal specimen cross section. Yield strength was calculated with the 0.2% offset method, as recommended in ASTM E 8M (1997). Resolution and accuracy in the recorded strain values were 0.0004 strain (%) and ±2.7% of the nominal values, respectively. Using the above described procedure, six friction stir welded joints (three longitudinal and three transverse) and three transverse plasma welded joints were tested. Six parent plate 2024-T351 specimens, three longitudinal (L) and three transverse (LT), were also tested in order to compare the tensile behaviour with the welded joints.

3.7 Fatigue test specimen design and preparation

Material and welding procedures were as described in Sections 3.1 and 3.2. Two different configurations of specimen were machined out from the welded plates. The longitudinal specimen had its principal axis parallel to the weld axis. The transverse specimen had its principal axis perpendicular to the weld axis. The two specimen configurations and their principal dimensions are shown in Figure 3.6.

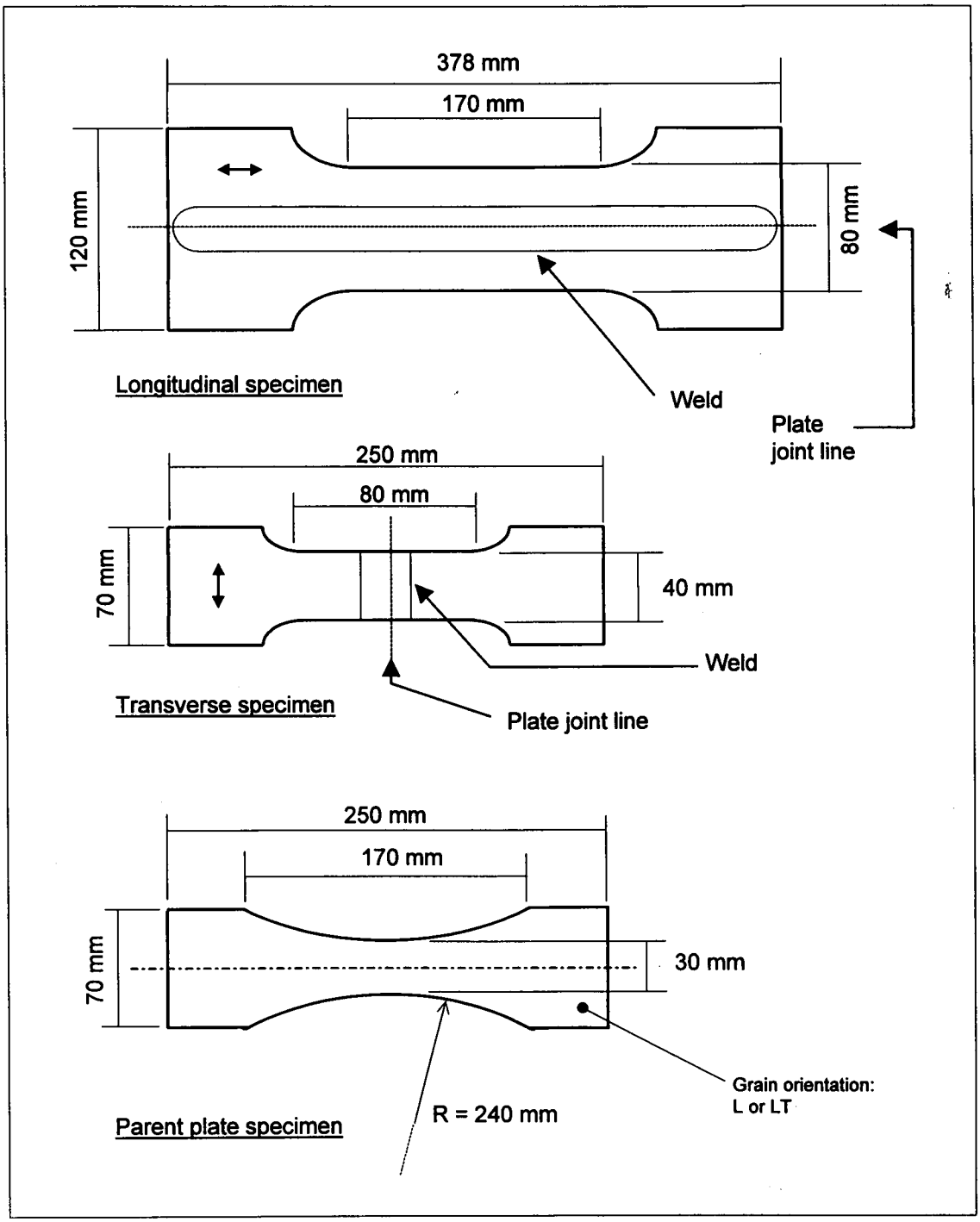

Figure 3.6 Longitudinal and transverse welded and parent plate specimen geometry. The parent plate rolling directions are indicated.

The longitudinal specimens were made as large as could be tested in order to minimise the residual stress relief, which typically affects small specimens. Previous work from

the literature [38, 53, 88] was also considered as further general guidelines. Specimen test gauge sections were in all cases, kept far from the plate weld-start and stop areas in order to guarantee uniformity of properties within the test gauge lengths.

Plasma welded specimens were machined only in the transverse configuration. Parent plate specimens were machined in the L and LT grain direction. The specimens had a continuous radius between ends (Fig. 3.6). This geometry was chosen in order to avoid failures at the end of the test gauge length as would occur during testing in fatigue dog-bone specimens of homogeneous material. Specimen dimensions were in accordance with ASTM E 466 (1997).

Samples were tested in two surface conditions, as welded and surface skimmed. The surface skimming operation was carried out as described in Section 3.5.

3.8 Residual stress measurements

Residual stresses were measured in a 2024-T351 6.35 × 250 × 330 mm friction stir welded plate using the Hole-drilling Strain-gauge method in accordance with ASTM E 837-95 (1998). The measurements were performed by Stress Engineering Ltd (UK). Three equiangular strain gauge rosettes (CEA-06-062UM-120) were positioned at different distances from the plate joint line (locations 1, 2, 3, in Figure 3.7) on an as-welded plate. The measurements were carried out at probable locations of maximum and minimum longitudinal residual stress. The choice of the locations was based on geometrical similarity with residual stress distributions measured in rectangular welded plates reported in Ref. [38, 58, 106].

A 2 mm nominal diameter hole was drilled at each location with a carbide tipped inverse cone flat bottom drill driven at 300,000 rpm by an air turbine. High rotational speed was required in order to minimise residual stress due to drilling. The holes were drilled at increments of 0.125 mm to a depth of 2 mm. Measurements of the strain values around the holes were made at each increment. The principal residual stresses σ_1

and σ_2 and their orientation β, positive if clockwise with respect to the weld, were calculated at each depth value using the following relationship:

$$\sigma_1, \sigma_2 = \frac{\varepsilon_1 + \varepsilon_2}{4A} \pm \frac{\sqrt{2}}{4B}\sqrt{(\varepsilon_1 - \varepsilon_2)^2 + (\varepsilon_2 + \varepsilon_3)^2}$$

Eqn. 3.1

$$\tan 2\beta = \frac{\varepsilon_3 - 2\,\varepsilon_2 + \varepsilon_1}{\varepsilon_3 - \varepsilon_1}$$

where ε_1, ε_2 and ε_3 are the strain values measured with the equiangular strain gauge rosettes. A and B are constants which are given in ASTM E 837-95 (1998) and are functions of the material Young's modulus, Poisson's ratio and the geometry of the problem.

A longitudinal welded specimen, of geometry and dimensions as described in Section 3.7, was machined out from the same plate. The residual stresses were measured with the above procedure at locations 1', 2', 3' (Figure 3.7). The specimen was subsequently surface skimmed removing a layer of 0.5 mm from each of the top and bottom surfaces, as described in Section 3.5. Residual stress measurements were finally repeated at locations 1", 2", 3" (Figure 3.7).

Stress values were originally expressed in terms of longitudinal and transverse components, the former parallel to the weld axis the latter normal to the weld axis. The following Mohr's circle relationship [50] was used to calculate longitudinal and transverse residual stress:

$$\sigma_\phi = \frac{\sigma_1 + \sigma_2}{2} + \frac{\sigma_1 - \sigma_2}{2}\cos 2\phi \qquad \textit{Eqn. 3.2}$$

where σ_ϕ is the stress acting on a plane oriented at any angle ϕ measured from the first principal plane positive if clockwise. As discussed in ASTM E 873-95, the error

associated with the method may vary significantly from case to case depending on the intensity of residual stress gradients and magnitude. In this case, the error will usually tend towards an underestimation of the maximum residual stress. As discussed in ASTM E 873 (2000), no round-robin exercise for welded plates has been carried out in order to estimate the error associated with the measurements. However, it is reasonable to believe that the error should be approximately ±15 MPa [82].

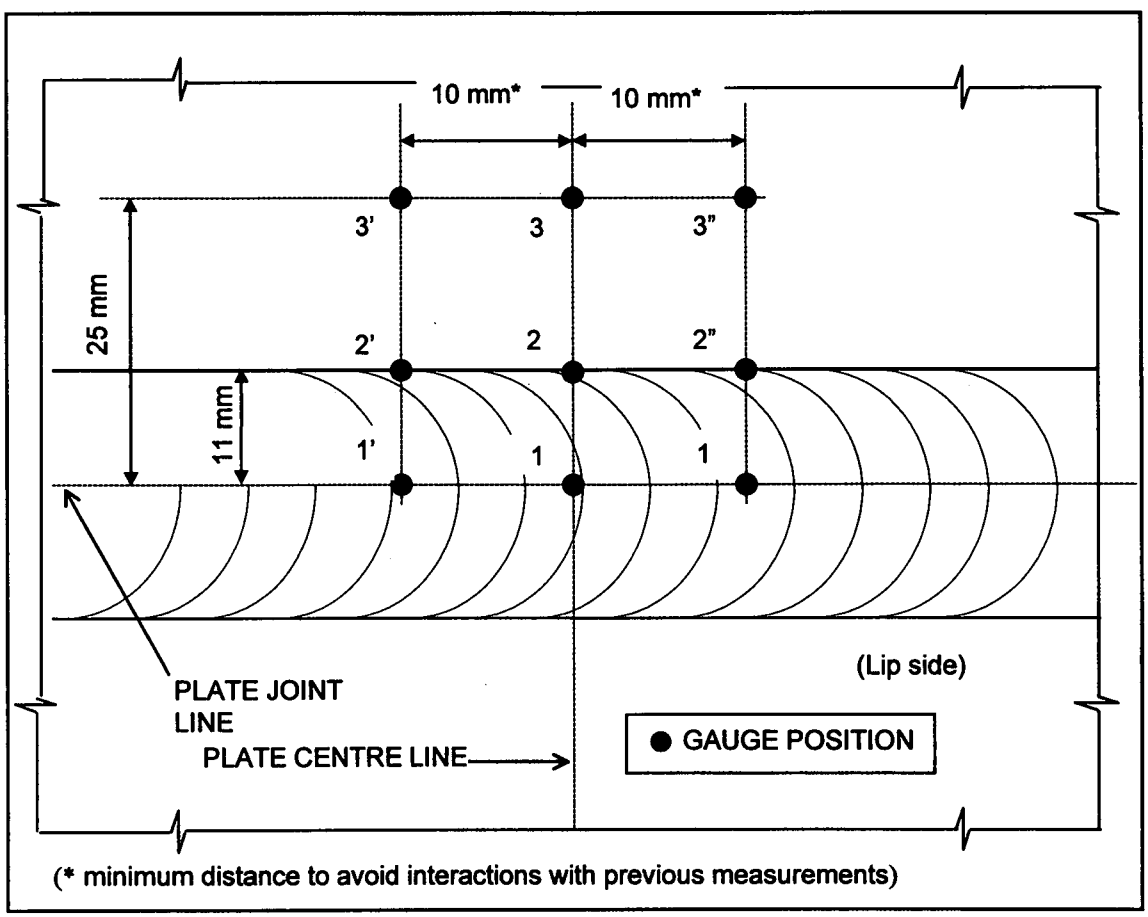

Figure 3.7 Residual stress positions referred to the plate joint line.

3.9 Fatigue testing procedures

All the fatigue tests were performed in accordance with ASTM E 466 (1997). The specimens were deburred on the edges to prevent crack initiation from irregular edge profiles. The tests were carried out at constant load amplitude, constant frequency of 15 Hz. Tests were conducted for a stress ratio R of 0.1. This is more representative of the

highly damaging load fluctuations that a wing panel experiences during its operative life [60]. More significantly, constant amplitude and low stress ratio cycles can be reasonably representative of the Ground-Air-Ground (GAG) cycles.

The specimens were tested using an Instron 8500 digitally controlled test machine of 250 kN capacity fitted with a 0.5 class load cell (±0.44% accuracy, 0.01% resolution). The load cell was calibrated in accordance with Euronorm EN 10002-2: 1991. Fatigue test results were plotted as stress range versus life (S-N). Cost/time limitations on testing imposed a limit on fatigue life of 10^7 cycles. Best-fit curves were plotted through the experimental data points for clarity.

3.10 Crack propagation test: specimen design and preparation

Two specimen designs were used: the Surface-Crack Tension specimen (SCT) and the Compact Tension specimen (CT). Figures 3.8a and 3.8b show the two specimen arrangements and principal dimensions.

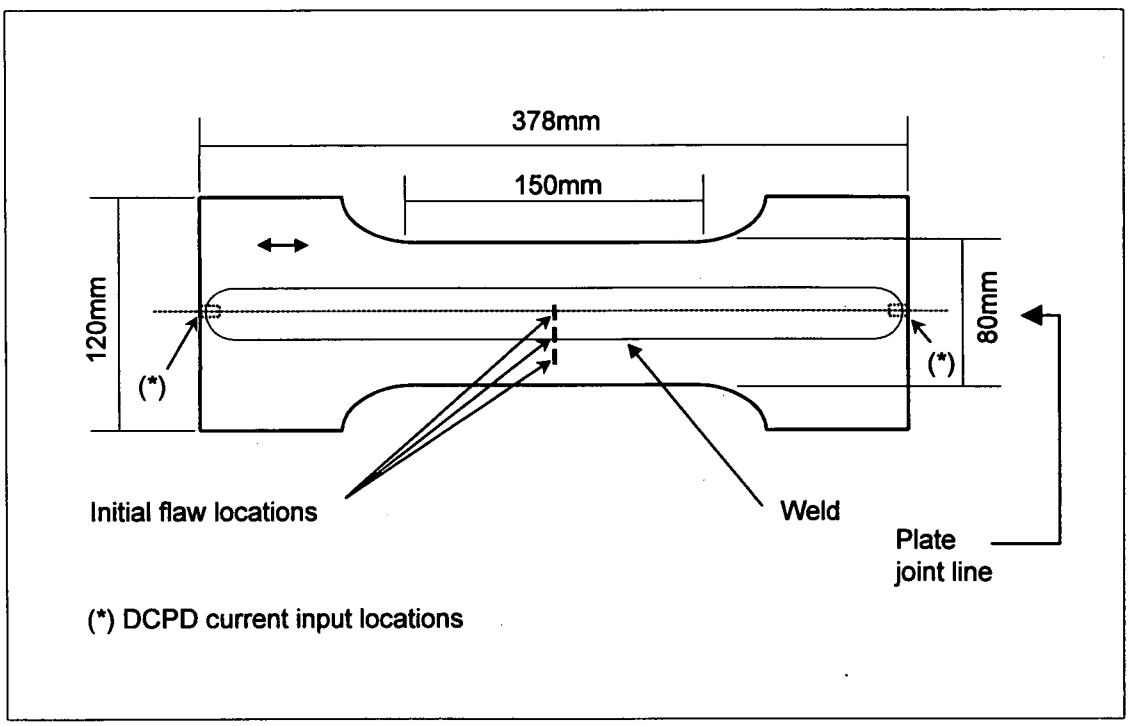

Figure 3.8a The Surface-Crack Tension specimen (SCT) arrangement and principal dimensions.

In the SCT test specimens the cracks were initiated and grown always at 90° to the weld line. In the CT test specimens the cracks were always parallel to the weld line. The SCT specimens were nominally similar to the longitudinal welded specimens tested in fatigue.

To initiate a surface crack, a semicircular flaw of 1 mm nominal radius was introduced in the specimens using the Electric Discharge Machining technique (EDM). During this operation, a specially manufactured copper alloy tool was made with nominal radius of 1.0 mm, thickness of 0.2 mm. Figure 3.9 shows the surface semicircular flaw obtained with this technique. Dimensional tolerances on the radius of the crack starters were ±0.2 mm.

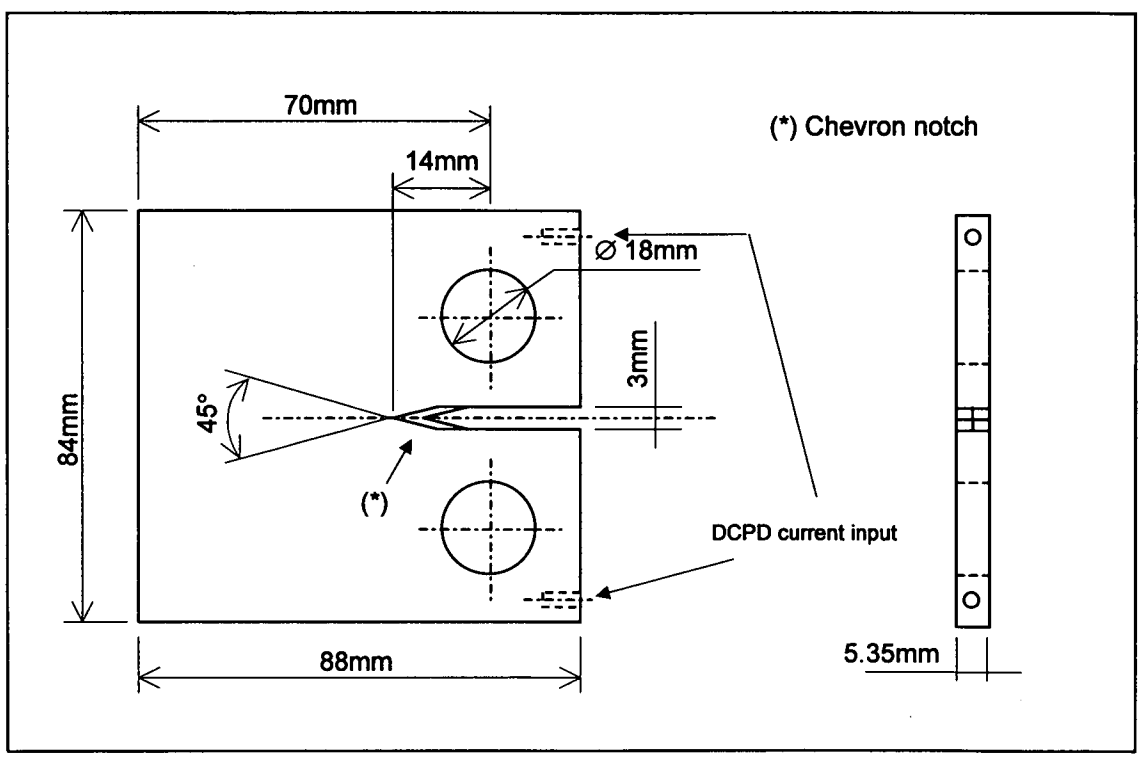

Figure 3.8b The Compact Tension specimen (CT) arrangement and principal dimensions.

The value of the surface flaw radius was small compared with the plate thickness in order to be able to observe the crack propagation during the through-thickness growth stage. Radii smaller then 1.00 mm were discarded because of difficulties encountered in

the manufacturing of the copper alloy tool. The 1 mm radius surface flaw was smaller than the initial surface flaw dimensions specified in the USAF Damage Tolerant Design Handbook [28]. Figure 3.10 shows the orientation and the positions with respect to the weld, at which the surface flaws were introduced. The flaws were introduced at the same locations at which residual stresses were measured on a similar specimen (Section 3.8). Moreover, the locations corresponded to regions characterised by different microstructures within the friction stir welded joint.

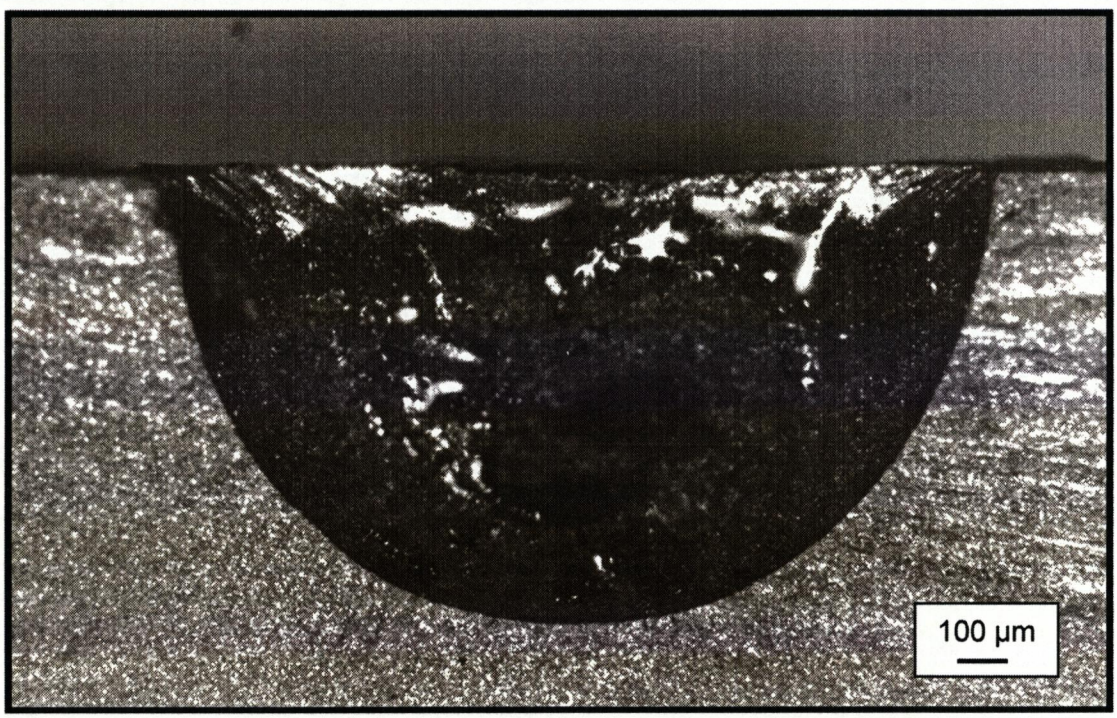

Figure 3.9 The surface semicircular flaws were introduced on the SCT specimens by Electric Discharge Machining (EDM).

The CT specimens were in accordance with ASTM E 647-95a (1997). From each friction stir welded plate, three CT specimens were machined from the central area of the plate, avoiding the weld start and stop areas and guaranteeing uniformity of properties within the specimens. The skimming operations were carried out according to the procedures described in Section 3.7.

The CT specimens were machined according to three different positions with respect to the weld. The notches were always parallel to the weld and were positioned on the plate joint line (PJL), at 6 mm and at 28 mm from the plate joint line on the side opposite to the lip. Figure 3.11 shows the three cases. These positions corresponded to local minima of hardness transverses (6 mm and 28 mm) and to different grain structure characteristics. CT and SCT specimens were polished with 0.5 μm diamond paste on the surfaces corresponding to the expected crack path in order to improve the crack tip optical detectability.

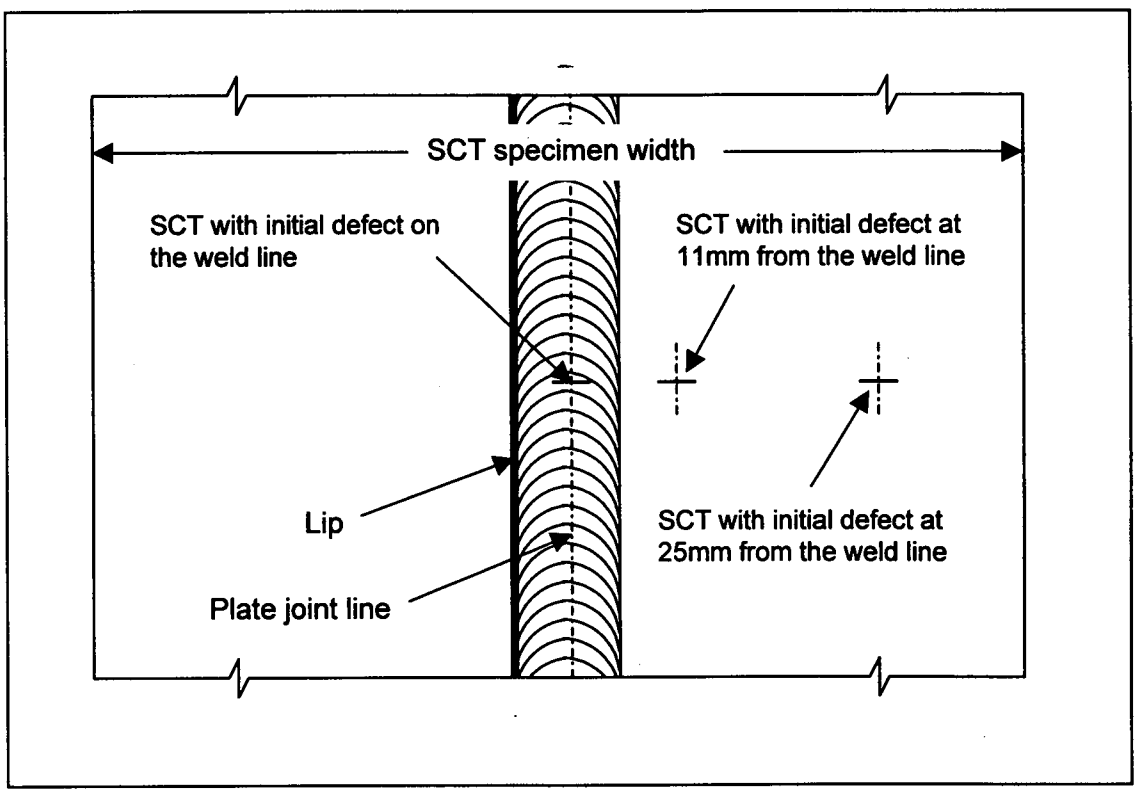

Figure 3.10 Position and orientation of the initial surface defect with respect to the weld for the SCT specimens.

3.11 Experimental procedures: crack propagation tests

All crack propagation tests were performed in accordance with the standard test methods for measurement of fatigue crack growth rates described in ASTM E 647 (1997). The tests were carried out at constant load amplitude, constant frequency of 15

Hz and constant stress ratio of R = 0.1. Specimens were tested under load control in ambient laboratory conditions using two Instron 8500 digitally controlled test machines of 100 kN and 250 kN load capacity. These machines were fitted with 0.5 class load cells (±0.44% accuracy, 0.01% resolution). The CT specimens were pre-cracked to an initial crack length of 18.0 mm. The pre-cracking load sequence was carried out in accordance with the recommended procedure as in ASTM E 647 (1997).

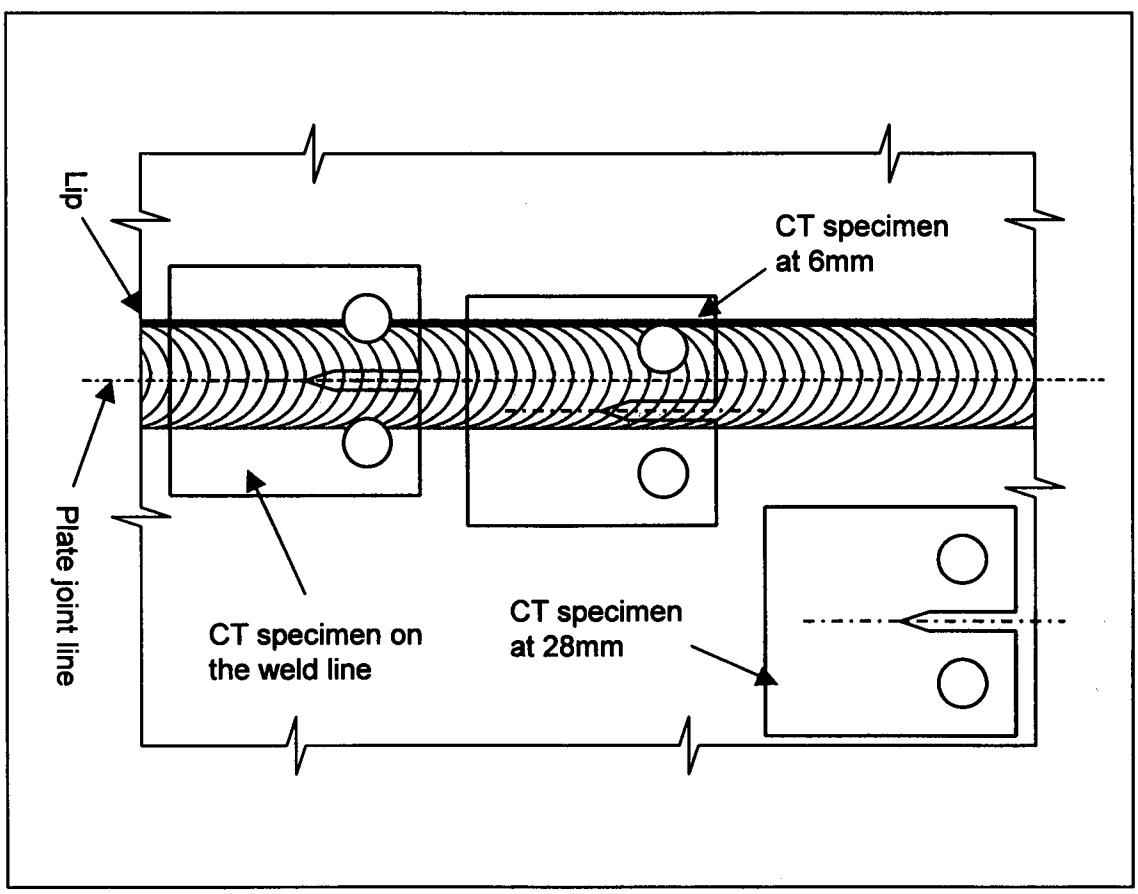

Figure 3.11 Position and orientation of the CT specimens with respect to the weld.

The stress intensity factor (K) values for the CT specimens were calculated using the expression (ASTM E 647 (1997)):

$$K = \frac{P}{t\,W^{1/2}} \cdot f(a/W) \qquad \textit{Eqn 3.3}$$

where:

$$f(a/W)=\frac{(2+a/W)\left[0.886+4.64(a/W)-13.32(a/W)^2+14.72(a/W)^3-5.6(a/W)^4\right]}{(1-a/W)^{3/2}}$$

a is the crack length, W the specimen width (70 mm), t the specimen thickness (5.35 mm) and P the applied load. The formulation for $f(a/W)$ is valid for $a/W \geq 0.2$.

In the case of the SCT specimens, the expression for the stress intensity factor depended on the crack front geometry. Two expressions for the stress intensity factor were used. During the first part of the tests the cracks propagated from semicircular surface flaws. For crack depths (c) less than t, the cracks were assumed to propagate as semicircular flaws (a/c = 1, where a is the half crack surface length). This assumption was based on the experimental evidence that the thumbnail cracks on breaking through the plate thickness (c = t) exhibited a/c values between 1.02 and 1.07. The stress intensity factor expression was [3]:

$$K=\frac{P}{tW}\cdot\frac{1}{\pi/2}\cdot f(a/t,a/W) \qquad \textit{Eqn 3.4}$$

where:

$$f(a/t,a/W)=\left[1.04+0.20(a/t)^2-0.11(a/t)^4\right]\left[1.1+0.35(a/t)^2\right]\left[\sec(\pi a/W)(a/t)^{1/2}\right]^{1/2}$$

a is half the crack surface length, t the specimen thickness (5.35 mm) and W the specimen width (80.0 mm). The formulation for $f(a/t, a/W)$ is valid for $a/t < 0.5$, and refers to the stress intensity factor on the crack tip at the plate surface. For $a > t$, the cracks breaking through the plate thickness, the stress intensity factor was calculated using the expression for a centre cracked plate [3]:

$$K=\frac{P}{tW}(\pi a)^{1/2} f(a/W) \qquad \textit{Eqn 3.5}$$

where:

$$f(a/W)=1+0.256(a/W)-1.152(a/W)^2+12.200(a/W)^3$$

a half the crack length, t the specimen thickness and W the specimen width. These assumptions involved a certain degree of error particularly at the stage when the surface crack became a through crack. However, the majority of the observed crack growth behaviour referred to the stage when the crack was a surface crack and the transformation into a through crack, followed by the through crack growth occupied only the very last part of the test. Tests conducted on the parent plate generated data were in good agreement with crack propagation data published in ESDU 81031 [25] (Section 4.12). This confirms that the test procedures, the criteria and the assumptions used for the calculation of experimental data led to representative results.

The formulations used for the stress intensity factors did not take into account contributions from the residual stress field. The stress intensity formulations were corrected for crack eccentricity in the SCT specimens with the semicircular flaws at 11 and 25 mm from the plate joint line. The corrections were based on the case of an eccentric through crack in a finite width plate subjected to a uniform uniaxial tensile stress [86]:

$$K_{offset}^{outer}/K_0 = 1+\sum_{n=2}^{19} C_n(2a/W)^n \qquad \textit{Eqn. 3.6a}$$

at the outer crack tip and:

$$K_{offset}^{inner}/K_0 = 1 + \sum_{n=2}^{19} (-1)^n C_n (2a/W)^n \qquad \textit{Eqn. 3.6b}$$

at the inner crack tip. K_0 is the stress intensity factor obtained as W tends to infinity and is given by $\sigma (\pi a)^{1/2}$. The coefficients C_n, functions of the eccentricity, are tabulated in Ref. [44].

Figure 3.12 shows the plots of Equation 3.6a and 3.6b, for the through crack at 11 and 25 mm from the plate joint line, and on the plate joint line. The plots show that stress intensity in the eccentric cracks is lower than in centre cracks and higher at the crack tip which is closer to the plate edge (outer crack tip).

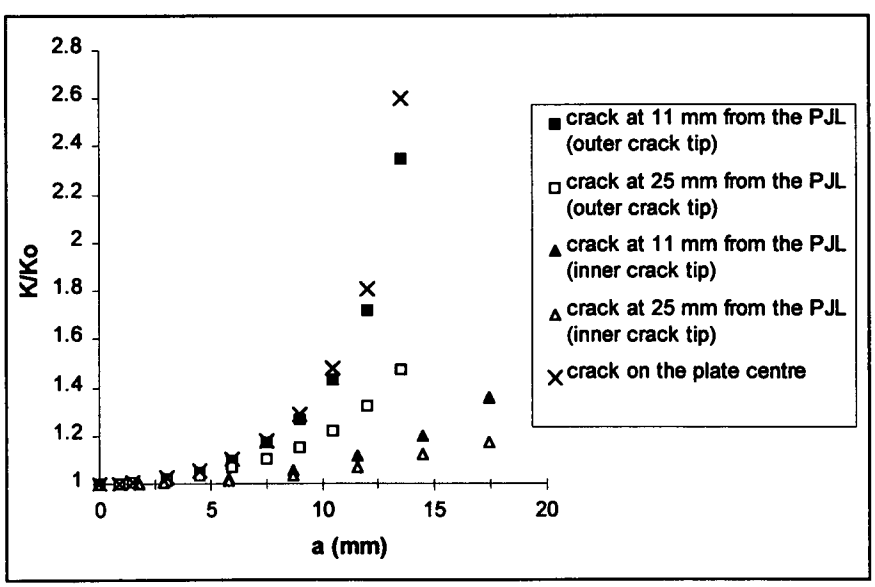

Figure 3.12 Plots of K/K_O versus crack length for the through crack at 11 and 25 mm from the plate joint line, and on the plate joint line (SCT apecimens).

No specific corrections for eccentric semielliptical flaws were available therefore the previous correction was also applied to the semicircular crack geometry. The stress intensity value associated with a semicircular surface crack is generally less than the

stress intensity value associated with a through crack of the same crack length, as can be observed by plotting together Equation 3.4 and 3.5. This is due to the "binding action" exerted by the material between the front of the semicircular crack and the back of the plate. It is reasonable to believe that the same binding action would reduce the effect of the offset on the semicircular crack with respect to the through crack. On this basis, the correction factor for eccentricity of through cracks represents an overestimation of the real correction factor for semicircular surface cracks. A quantitative estimation of the influence of the crack offset on the stress intensity factors in semicircular flaws could be obtained applying finite element analysis methods.

The correction factors used for the SCT specimens are plotted in Figure 3.13. It can be noticed that the eccentricity correction values, within the test crack lengths, were between 0.1% (for the initial crack lengths) and 24% (for final crack lengths between 9 and 10 mm) of the uncorrected values. Stress intensity values reported in the test results refer to the stress intensity value calculated at the crack tip on the plate surface nearest to the specimen edge.

3.12 The DCPD crack length measurement system

The Direct Current Potential Difference (DCPD) method allows the determination of the crack size in a conducting specimen by measurement of the electrical potential drop across the crack plane in the presence of a current flow. This method relies on the principle that the electrical field in a cracked specimen is a function of the specimen geometry and therefore of the crack size. The electrical potential increases as the crack size increases. The changes in electrical potential can be correlated with the physical crack length through empirical or analytical relationships. A detailed review of the method can be found in Ref. [29, 32, 99].

Figure 3.14 shows the schematic of the DCPD system. A Howden DCPD apparatus was used during the tests. In this apparatus a direct current of 15 A was pulsed through the specimen at the maxima of the applied loading. The synchronisation allowed elimination of errors in potential measurements associated with shorting across the

fracture surfaces due to crack closure at minimum load. At each reading, two electrical potential measurements were taken: the first with the current on (V_{on}) and the second with the current off (V_{off}). The difference ΔV between the two values was calculated. This procedure allowed elimination of errors associated with thermoelectric electromotive forces (emf).

Drifts in the measured voltage associated with changes in resistivity of the test specimen, DCPD circuits and connections were avoided by normalising the electrical potentials measured in the test specimen (ΔV_x) with the electrical potentials (ΔV_y) simultaneously measured on an identical dummy specimen. Figure 3.15 shows the locations of the electrical potential probes on the CT and SCT specimens.

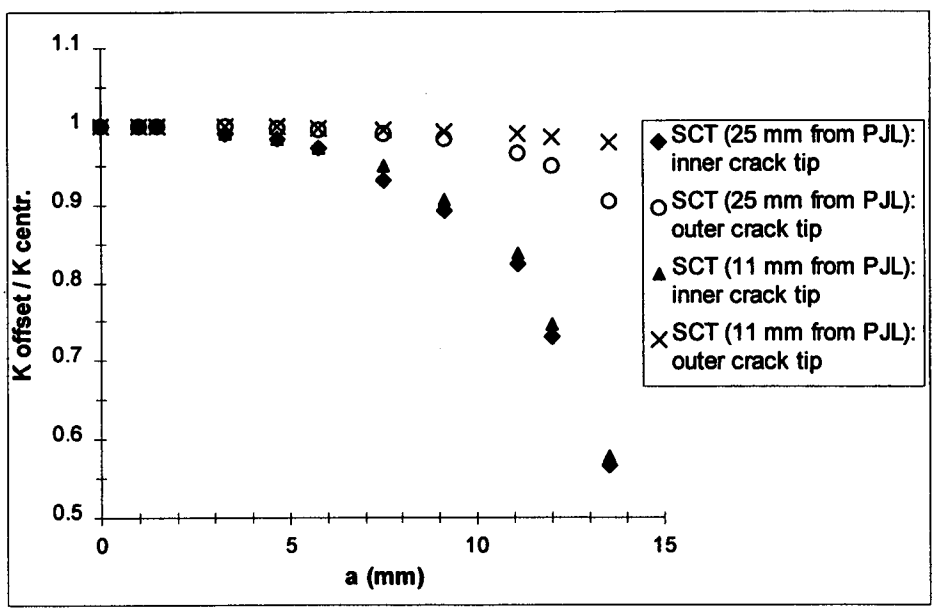

Figure 3.13 Correction factors for the crack offset used in the calculation of the stress intensity values in cracks on the SCT specimens.

The two analogue outputs ΔV_x and ΔV_y, generated by the DCPD apparatus, were received by the Strawberry Tree data acquisition system (Section 3.6). The operation $\Delta V_x/\Delta V_y$ was digitally performed within the Strawberry Tree system. The values were averaged over 50 readings and recorded every 500 cycles. A Model 488-PC2 IEEE

488.2 General Purpose Interface Card (GPIB) [68] was installed on a 486 personal computer in order to set the event detectors within the Instron 8500 digital control tower and the digital outputs to send a signal after each load cycle was completed. The digital output signal variations, received by the data acquisition system, were counted and recorded as number of load cycles.

The tests were carried out using a new set of grips, which were designed *ad hoc* by the author for testing large specimens and to allow the use of the DCPD technique when conducting fatigue crack propagation tests. Specific requirements and design procedure of the grips are described in the Appendix.

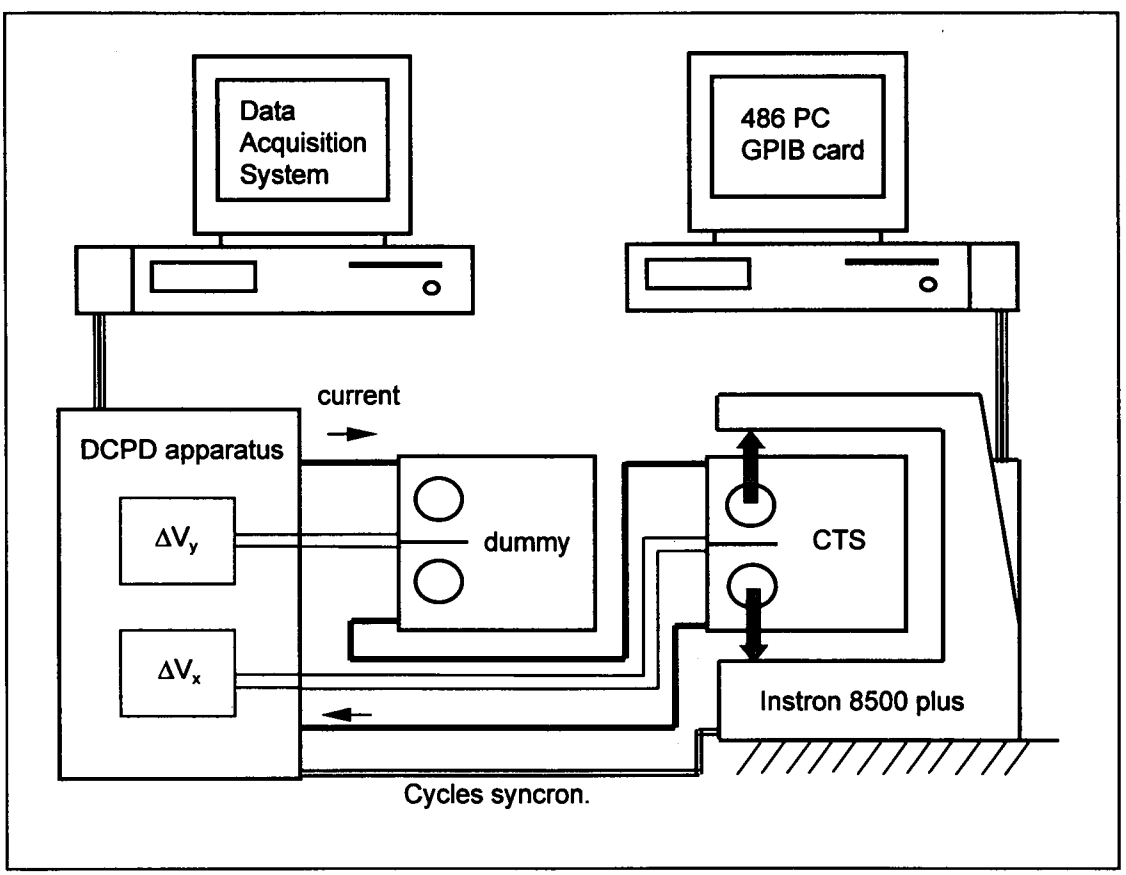

Figure 3.14 The schematic of the DCPD system.

3.13 The crack length versus potential difference relationship

Empirical relationships between the normalised electrical potential ratio $(\Delta V_x/\Delta V_y)/(\Delta V_x/\Delta V_y)_0$ and crack length a/W were developed in each case, with the potential ratio $(\Delta V_x/\Delta V_y)_0$ measured on the un-cracked specimen. The former normalisation was made in order to reduce errors due to differences in positioning the probes between similar specimens. In order to determine the crack length versus potential difference relationships optical surface measurements were made with a travelling microscope of 10 μm resolution and the crack length values were plotted versus the corresponding test electrical potential values. For the CT specimens, a third order polynomial curve was fitted to the experimental data points using a least squares fitting routine. Some of the CT specimens exhibited oblique crack fronts.

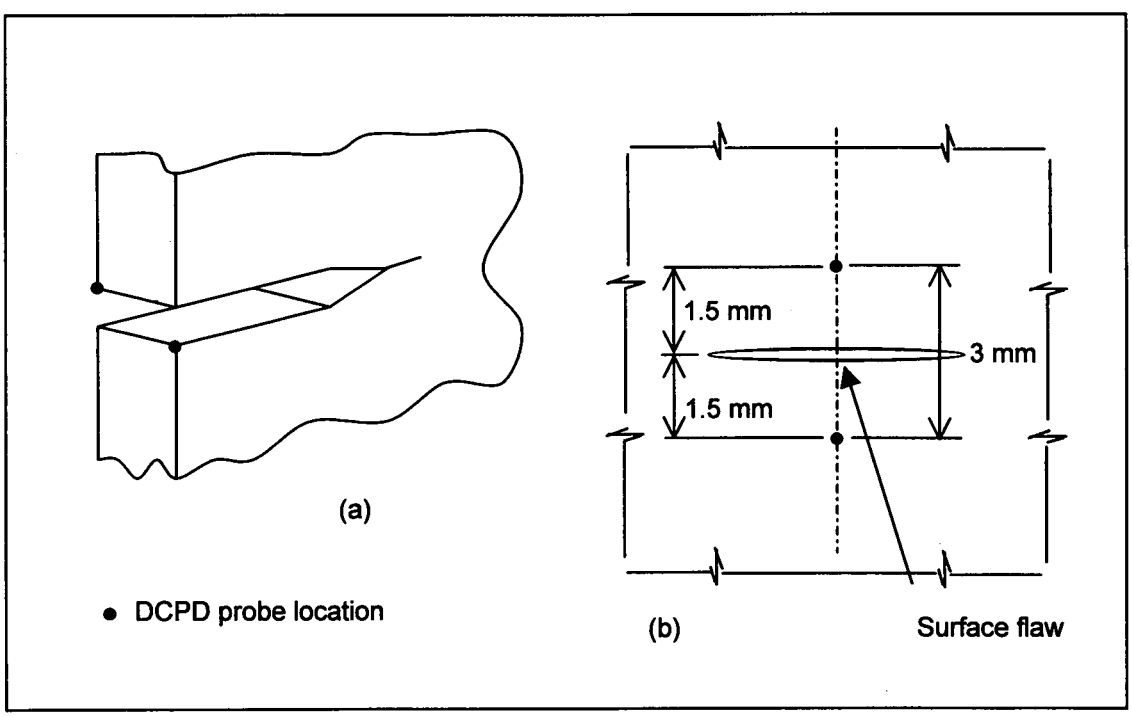

Figure 3.15 The locations of the electrical potential probes on the CT (a) and SCT specimens (b).

For those specimens, the two surface crack lengths were optically measured and their averaged values were plotted versus the corresponding potential differences. The

analytical expression of the calibration curve for the CT specimens with the respective least squares fit residual is shown below:

$y = -0.0034\ x^3 - 0.1705\ x^2 + 1.0809\ x - 0.7396;\ (R^2=0.998)$

with $y = a/W$ and $x = (\Delta V_x/\Delta V_y)/(\Delta V_x/\Delta V_y)_0$.

For the SCT specimens, a different calibration curve was obtained for each specimen configuration (initial flaw on the weld line, at 11 and 25 mm from it). In these cases the experimental data points were fitted in two sets. The first set contained the data points of the crack during its first stage of growth as a surface thumbnail crack. The second set contained the data points of the crack in its second stage of growth as a through crack. Two first order polynomial curves were fitted to each set of data points using a least squares fitting routine. The analytical expressions of the calibration curves for the CT specimens with the respective least squares fit residuals are shown below:

SCT specimens with crack on the Plate Joint Line:

$y = 0.0696\ x - 0.0401;\ (R^2 = 0.989)$ for $a < t$

$y = 0.0231\ x + 0.0192;\ (R^2 = 0.989)$ for $a > t$

SCT specimens with crack at 11 mm from the Plate Joint Line:

$y = 0.0439\ x - 0.0307;\ (R^2 = 0.994)$ for $a < t$

$y = 0.015\ x + 0.0272;\ (R^2 = 0.989)$ for $a > t$

SCT specimens with crack at 25 mm from the Plate Joint Line:

$y = 0.051\ x - 0.039;\ (R^2 = 0.999)$ for $a < t$

$y = 0.0149\ x + 0.04;\ (R^2 = 0.997)$ for $a > t$

with $y = a/W$ and $x = (\Delta V_x/\Delta V_y)/(\Delta V_x/\Delta V_y)_0$. Figure 3.16a and Figure 3.16b show the experimental data points and the calibration curves obtained for the CT and the SCT specimens.

3.14 DCPD crack length measurement system evaluation

The performance of the DCPD system was evaluated in terms of resolution and accuracy in the determination of the crack length. The effective resolution of the system was defined as the smallest change in crack size that can be detected in actual test operation. The resolution of the system depended on several factors. Voltmeter and amplifiers resolution, current magnitude, specimen geometry and electrical conductivity, probe and current input wire locations were the most important [29].

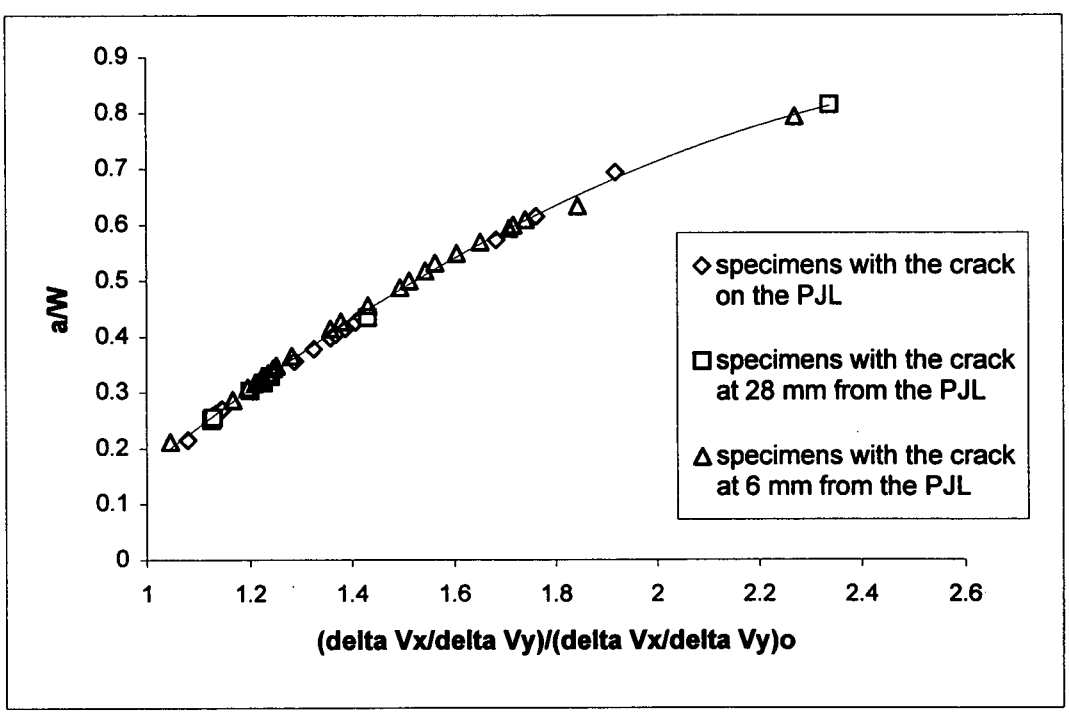

Figure 3.16a The experimental data points and the respective calibration curve obtained for the CT specimens.

Table 3.4a reports the values of the resolution of the DCPD system for the CT and SCT specimens under the specified test conditions and at the beginning of the tests. Table 3.4b contains the estimated accuracy of the DCPD system for CT and SCT specimens. The accuracy was estimated during constant-crack-length tests carried out under below-threshold ΔK conditions. The tests were representative of the long-term stability of the

DCPD system. Accuracy was calculated as the standard deviation of the recorded crack length values over the period of testing.

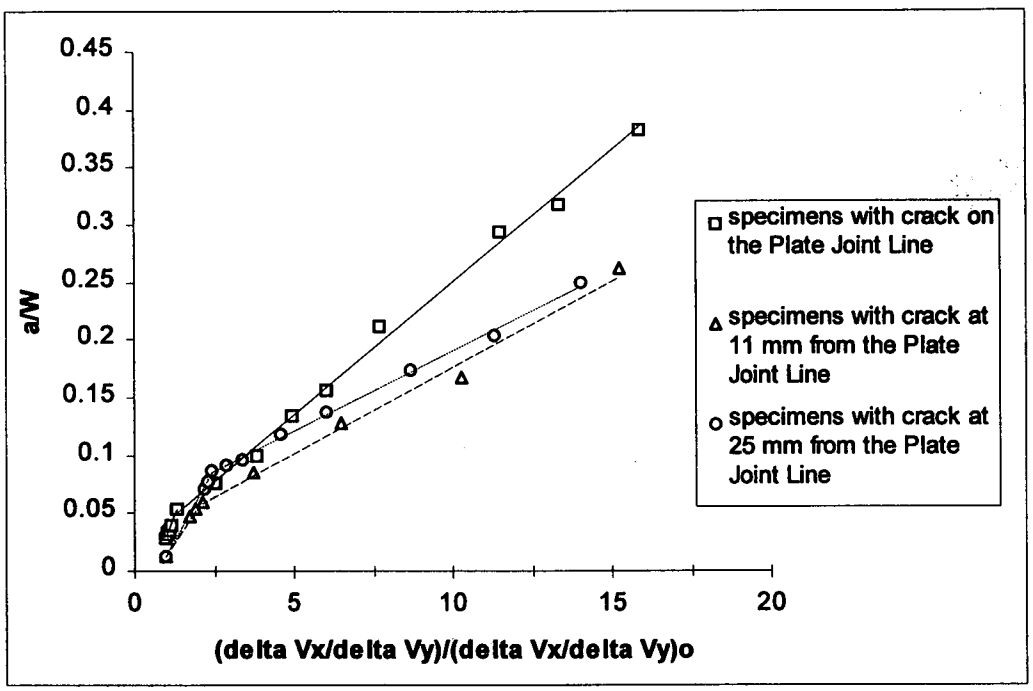

Figure 3.16b The experimental data points and the respective calibration curves obtained for the SCT specimens.

SPECIMEN CONFIG.	RESOLUTION	Crack size (mm)
CT	between 10 and 18 μm	18.04 ≤ a ≤18.20
SCT (crack on PJL)	between 10 and 20 μm	0.98 ≤ a ≤1.02
SCT (crack at 11 mm from PJL)	between 6 and 10 μm	0.99 ≤ a ≤1.01
SCT (crack at 25 mm from PJL)	between 10 and 18 μm	0.98 ≤ a ≤1.00

Table 3.4a Estimated resolution values of the DCPD system in the CT and SCT specimen tests.

SPECIMEN CONFIG.	DURATION	SAMPLE COUNT	MEAN (mm)	MAX. (mm)	MIN. (mm)	ACCURACY
CT	24 hours	500	16.053	16.100	15.887	±0.091 mm (±0.6%)
SCT (*)	24 hours	500	0.991	1.015	0.967	±0.009 mm (±0.9%)

(*) Crack at 25 mm from the plate joint line.

Table 3.4b Estimated accuracy values of the DCPD system in the CT and SCT specimen tests.

3.15 Measurement of fatigue crack opening loads (COL)

The crack opening load is defined as the minimum applied load for which a fatigue crack, present in the loaded specimen, is fully open. Measurements of fatigue crack opening loads were carried out on the CT specimens in order to observe any evidence of the crack closure phenomena [5, 8, 23, 73]. Crack opening loads were determined from the measurement of compliance. This method, as described in ASTM E 647 (1997) Appendix A4, is based on the observation that the compliance (slope of the strain or displacement against load curve for the specimens) attains a characteristic value and remains constant for those load values at which the crack is fully open, as shown in Figure 3.17. Upon unloading, the compliance changes from the characteristic value of the fully open crack (open crack compliance) to lower and load-dependent values. In order to reduce scatter in the opening load results [3], the opening load is typically defined as the load corresponding to a compliance that is offset from the fully open crack value:

$$\text{Compliance offset} = \frac{(\text{open crack compliance}) - (\text{compliance})}{\text{open crack compliance}} \times 100 \qquad \textit{Eqn. 3.7}$$

The measurements of the crack mouth displacements were carried out under constant load amplitude (R = 0.1) and a loading frequency of 0.2 Hz, with a class 0.2 Instron 10 mm gauge length extensometer (resolution 0.1%, accuracy 0.2%) positioned on the CT specimens, as shown in Figure 3.18. The measurements were carried out at the beginning of each crack propagation test. This condition corresponded to measured crack propagation rates between $5 \cdot 10^{-10}$ and $2 \cdot 10^{-9}$ m/cycle. Crack mouth displacements measured with the extensometer and load values were recorded with a Strawberry Tree multi-channel data acquisition system. The compliance values were calculated from the crack mouth displacement versus load curves using an incremental polynomial routine. Compliance offset values were calculated using Equation 3.7 and plotted in terms of stress intensity factor values.

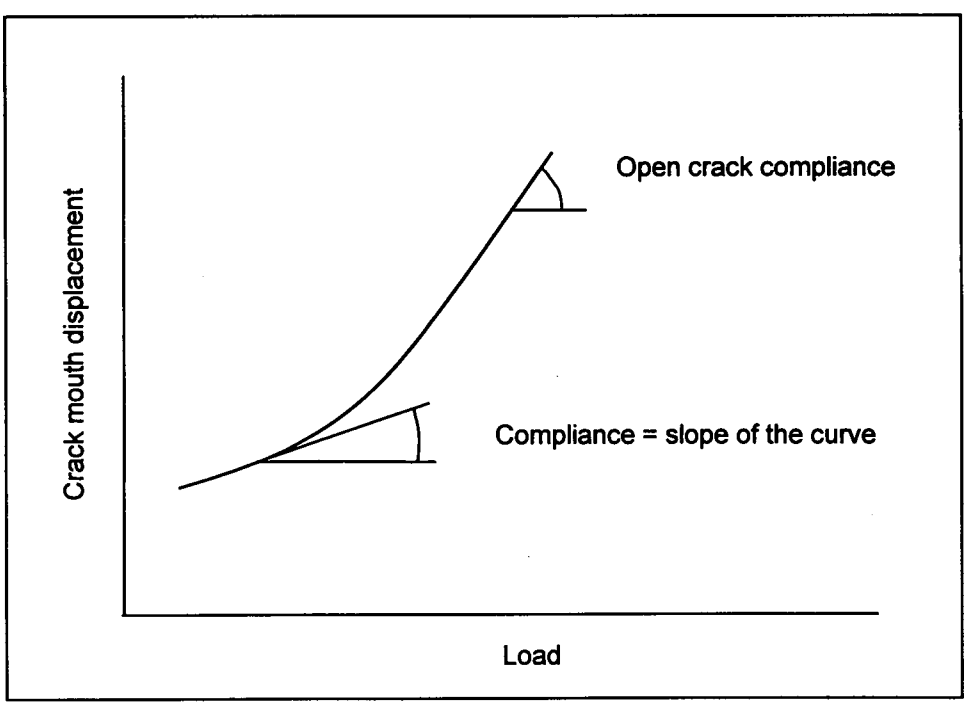

Figure 3.17 Definition of compliance on the crack mouth displacement versus load curve.

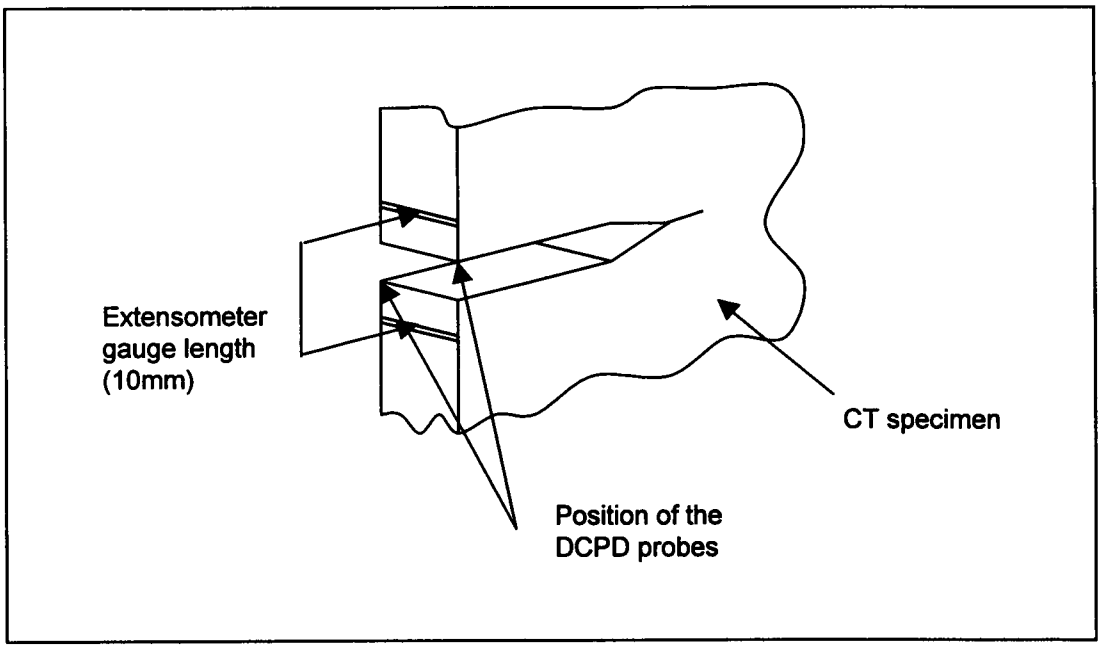

Figure 3.18 Extensometer positioning in the CT specimens for the measurement of the fatigue crack opening load from compliance.

4. EXPERIMENTAL RESULTS

4.1 Joint characterization

4.1.1 Weld macrostructure

Figure 4.1a shows the characteristic appearance of the friction stir weld bead. Concentric semicircular marks characterised the portion of the top weld surface where the physical contact between plates and welding tool took place. The weld back surface appears more regular and flat as shown in Figure 4.1b. Figure 4.1c shows a typical transverse macrosection from the FSW plates. The most evident feature is represented by the well-defined nugget, in the centre of the weld. The nugget dimensions generally extend between the pin and the shoulder diameter of the friction stir welding tool [105]. The area corresponds to the thermo-mechanically affected region. In this region the synergic effects of the heat input and the stirring action of the tool affected the structure and the properties of the material. The oval nugget contains smaller concentric rings typically resembling an onion ring structure. The concentric rings developed according a three-dimensional pattern which extends along all the weld. These characteristics can also be observed in Figure 4.2 which shows a typical longitudinal section of the weld corresponding to the plate joint line. It has been found that the size of the nugget depends on the plate thickness, the welding tool geometry and the welding parameters [67].

The nugget appears to be linked to the top weld surface via an appendage. This umbilical cord, characterised by the same microstructure as the nugget, ends on the weld bead in the direction of a protruding element, which is indicated by the term of "lip", Figure 4.3. The lip, bordering on one side the weld bead, is formed by a curl of metal partially overlapping the plate surface. Immediately out of the nugget the weld structure is characterised by highly oriented grain structure which bounds the thermo-mechanically affected region. The external regions, which were not directly affected by the mechanical action of the welding tool, represent the heat affected zone (HAZ) of the weld.

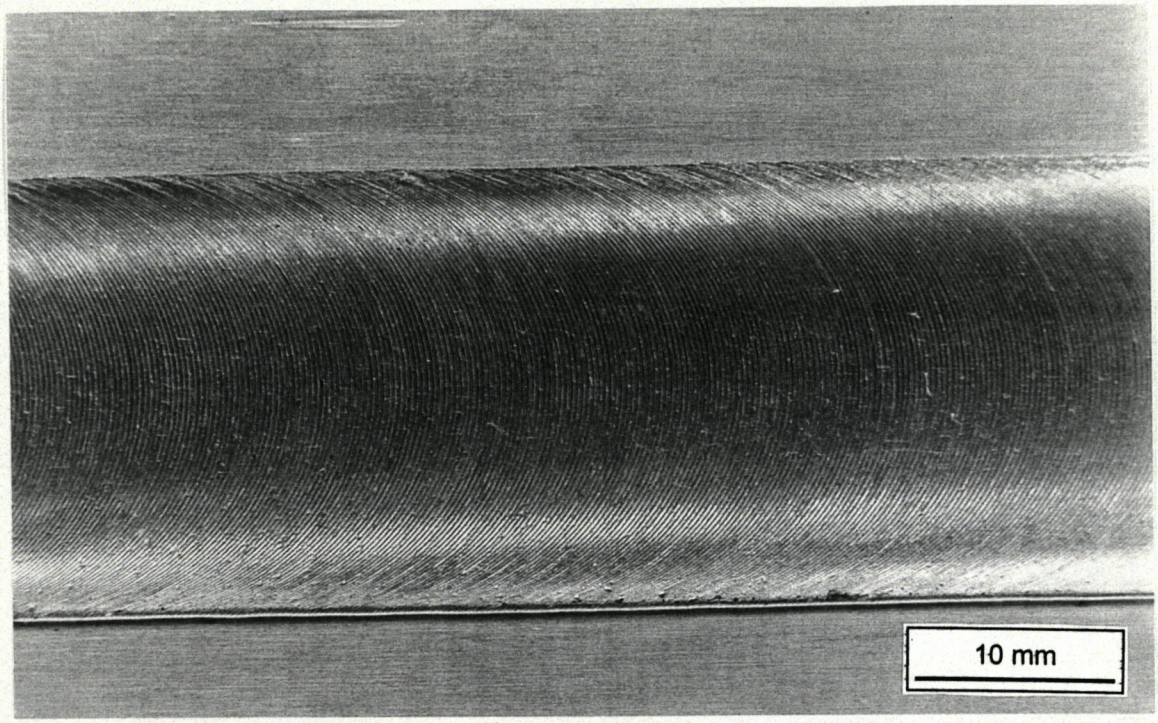

Figure 4.1a The friction stir weld bead. The typical circular tool marks are visible on the top surface.

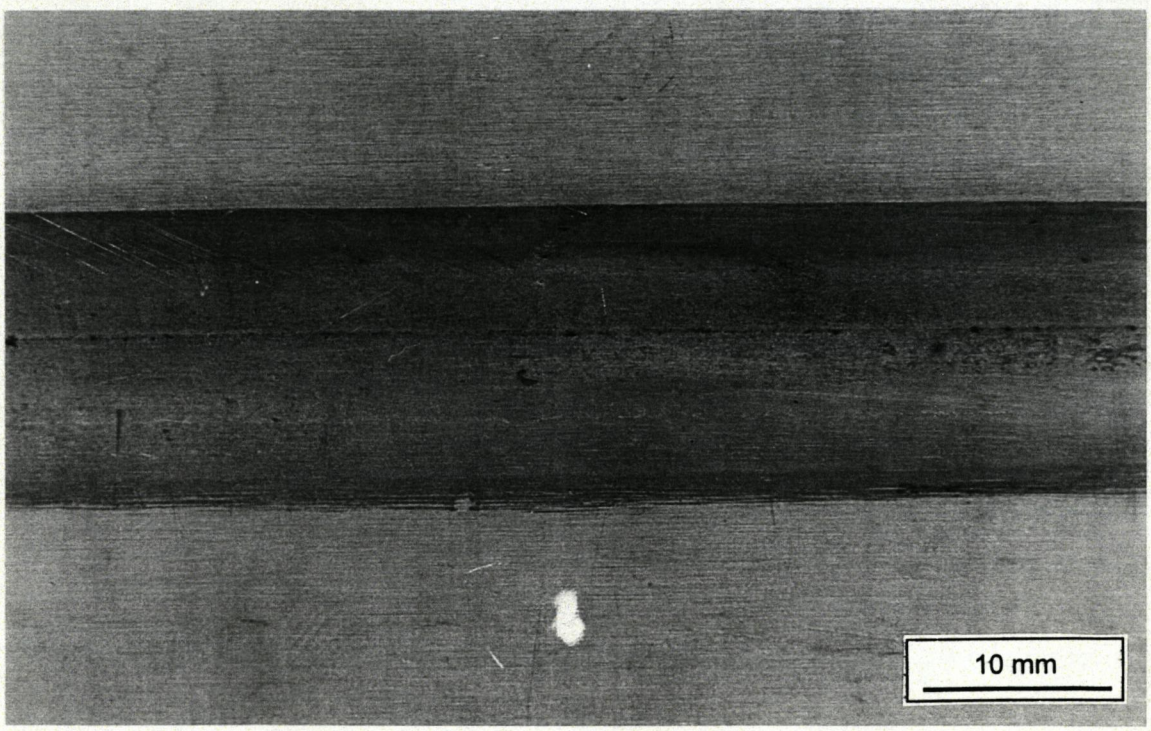

Figure 4.1b The friction stir weld back surface. It appears quite smooth and regular.

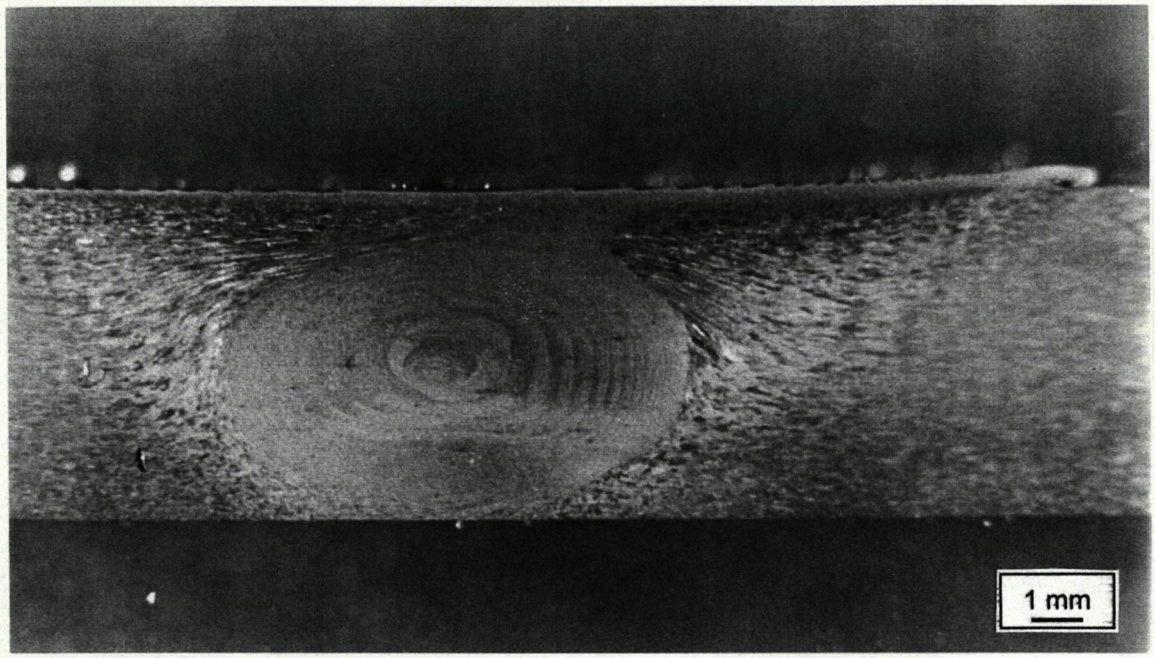

Figure 4.1c The typical friction stir weld macrostructure on a plane orthogonal to the weld direction.

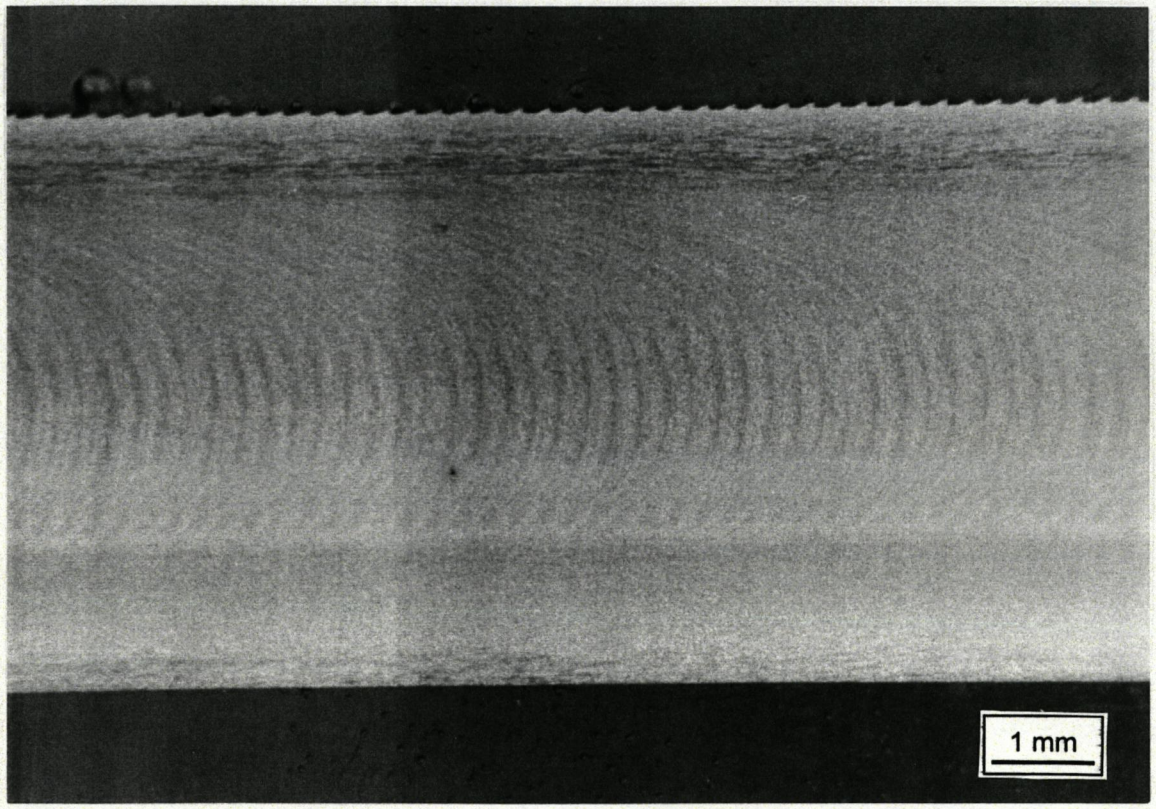

Figure 4.2 The typical friction stir weld macrostructure on the plane parallel to the weld on the plate joint line.

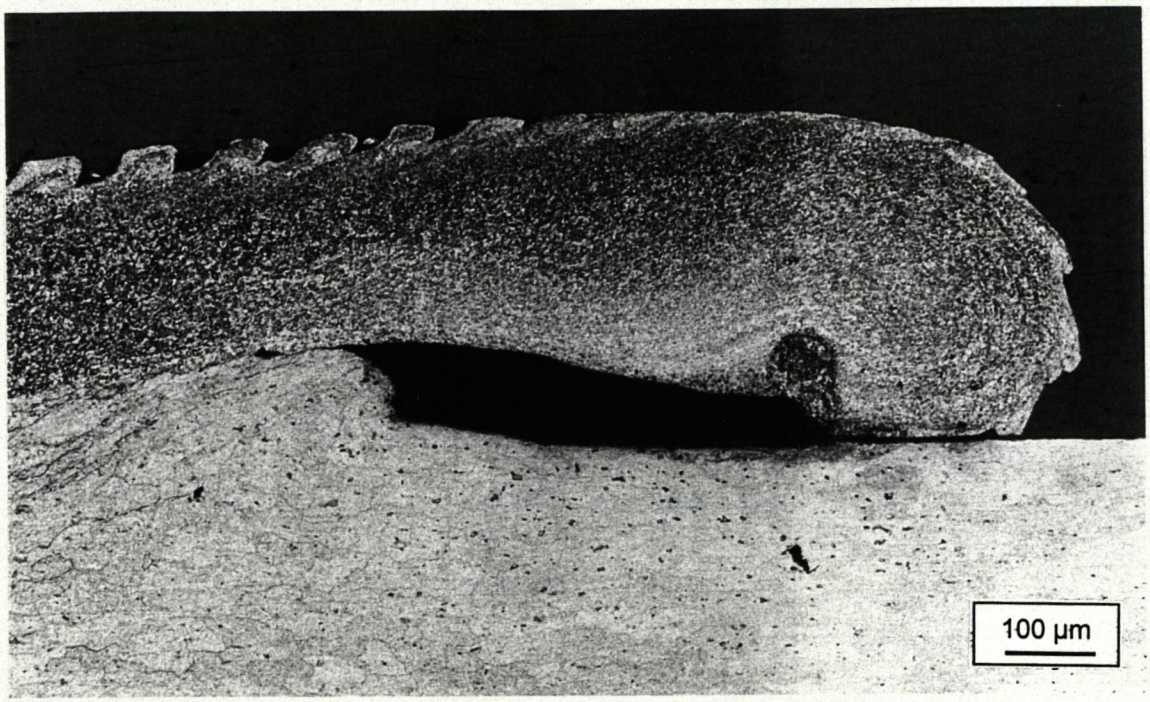

Figure 4.3 The "lip", bordering on one side the weld bead, is formed by a curl of metal partially overlapped to the plate surface. The section was taken on a plane normal to the weld.

Figure 4.4 shows a typical cross section from the plasma welded plates. In this case, the weld profile is less regular and slight undercuts characterise the weld beads. The weld core is characterised by a dark appearance that during the process undergoes complete melting. Slightly oblique and darker boundaries separate the melted region from the HAZ. The HAZ in the proximity of the weld is characterised by two light grey bands.

4.1.2 Weld microstructure

Figures 4.5a and 4.5b show detailed views of the typical microstructure of the nugget in a FSW plate on a plane normal and parallel to the weld direction, respectively. The grain structure appears to be very fine and equiaxed. Typical grain dimensions are between 5 and 10 µm. This fine grain structure characterises the appendage and constitutes the superficial layer of the weld top surface, as shown in Figure 4.6. The picture shows the profile of the tool marks.

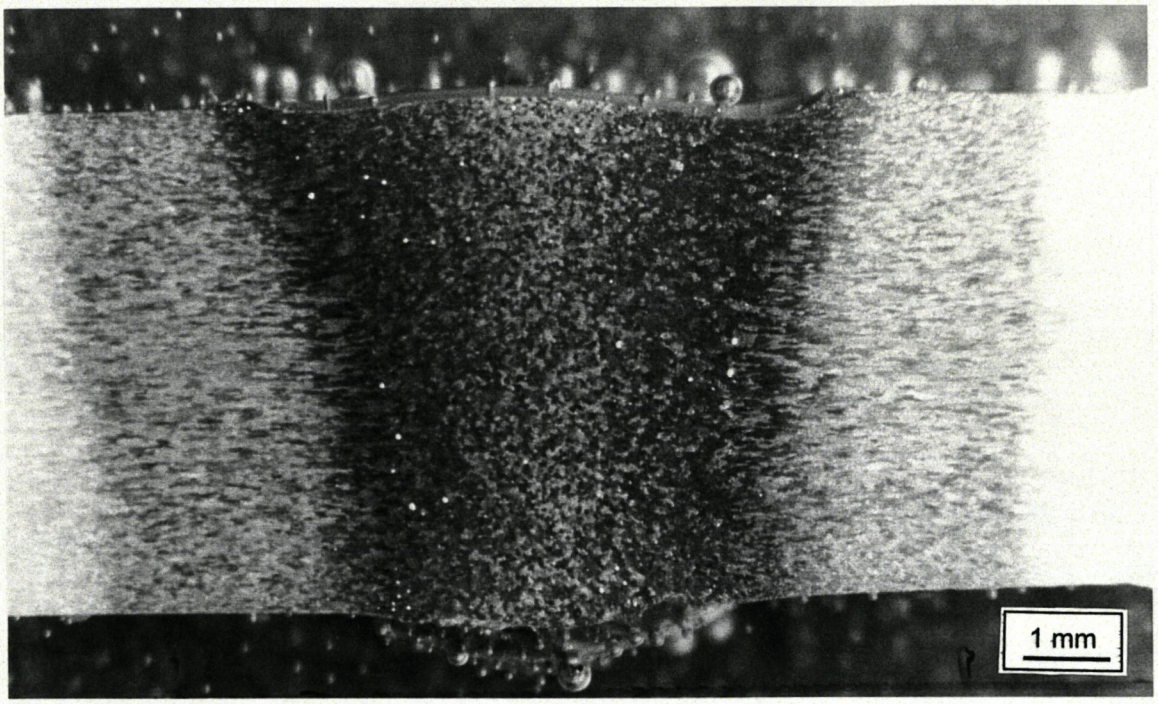

Figure 4.4 The typical cross section of a plasma welded plate on a plane orthogonal to the weld direction.

Within the thermo-mechanically affected region at the nugget boundaries, the grain structure is characterised by sharp and highly elongated grains. These grains are generally orientated according curves that end tangentially to the local nugget boundary. Figure 4.7 shows in detail the microstructure of the grains on the plane normal to the weld direction. Figures 4.8a and 4.8b show the typical microstructure that characterised the thermo-mechanically affected region, at 6 mm from the plate joint line (opposite the lip) on the planes normal and parallel to the weld direction, respectively. This location is characterised by severe changes in the local grain direction as an effect of the mechanical action exerted by the welding tool. The grains in the mid-lower area appear quite elongated, whereas near the top weld surface the structure is similar to the very refined structure observed in the nugget.

Figures 4.9a and 4.9b represent the microstructure in the HAZ, at 28 mm from the weld joint line (opposite the lip) on the planes normal and parallel to the weld direction, respectively. The grain structure appears very similar to that observed in the parent plate (Fig. 3.1b and 3.1c).

Figures 4.10, 4.11 and 4.12 represent the typical microstructure features observed in plasma welded plates. Figure 4.13 shows the grain structure at the centre of the weld. This area is characterised by the complete fusion and re-solidification of the material. The coarse and segregated microstructure, typical of aluminium castings [2], is characterised by 180-200 μm grains containing fine dendrite cells. The presence of defects was observed in this region of the joint. Figure 4.11 shows the transition in grain structure on the boundaries between the melted region and the HAZ. Columnar grains orientated in the direction orthogonal to the fusion-no fusion line characterise this area. On the left of the picture, the elongated grains of the rolled plate appears to be enlarged. Figure 4.12 shows the typical grain structure within the dark band in the HAZ. The grains, although less marked by the different etching response, have an elongated structure similar to the parent plate (TS).

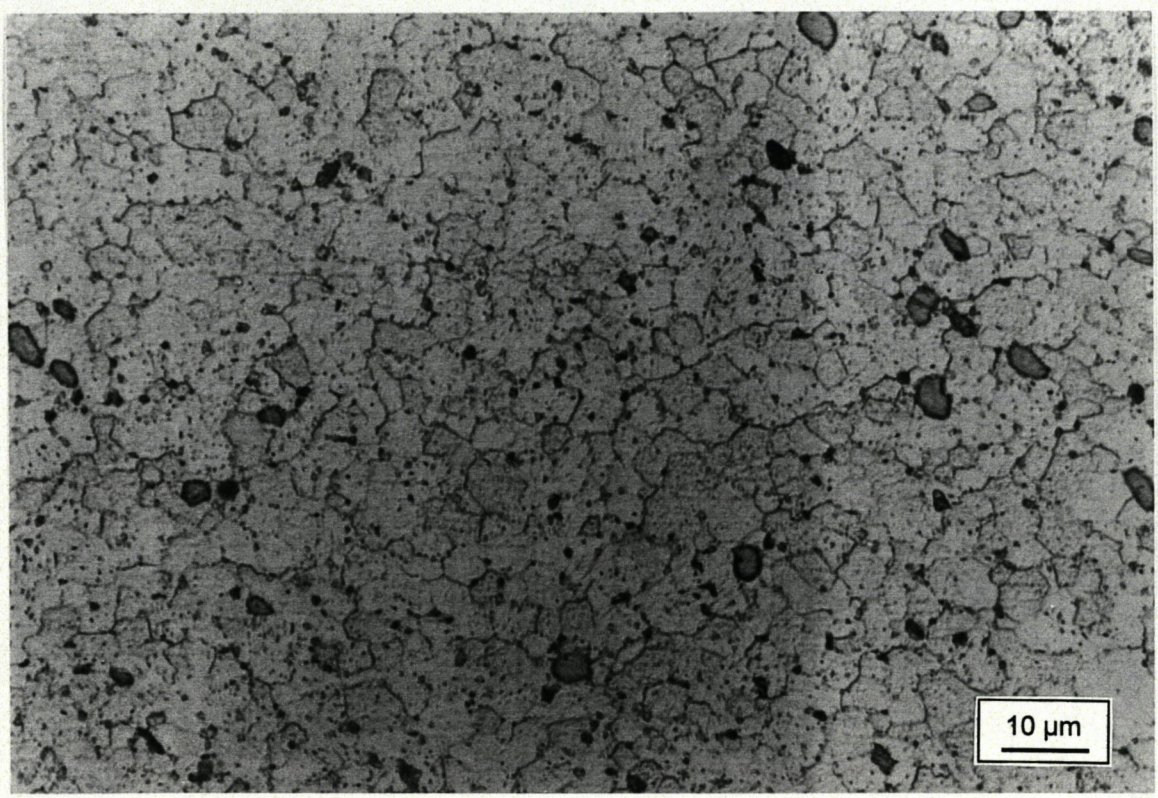

Figure 4.5a The typical microstructure of the weld nugget of a FWS joint on the plane orthogonal to the weld direction.

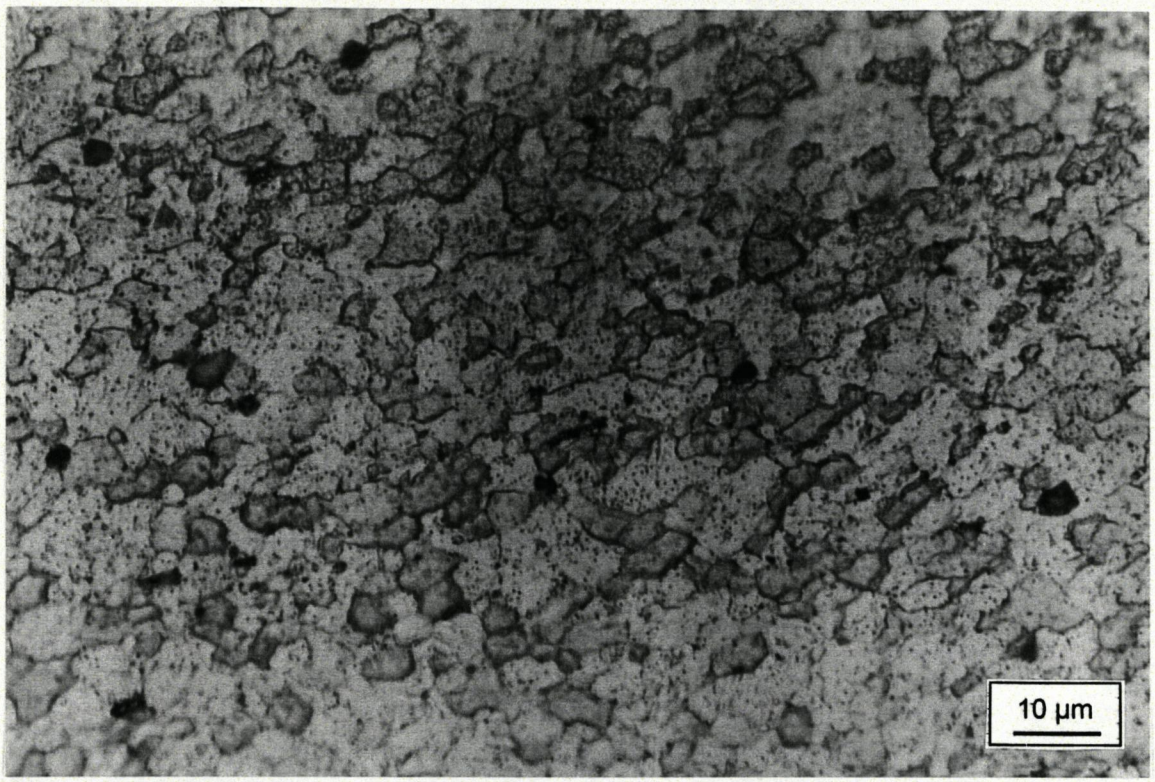

Figure 4.5b The typical microstructure of the weld nugget of a FWS joint on the plane parallel to the weld direction.

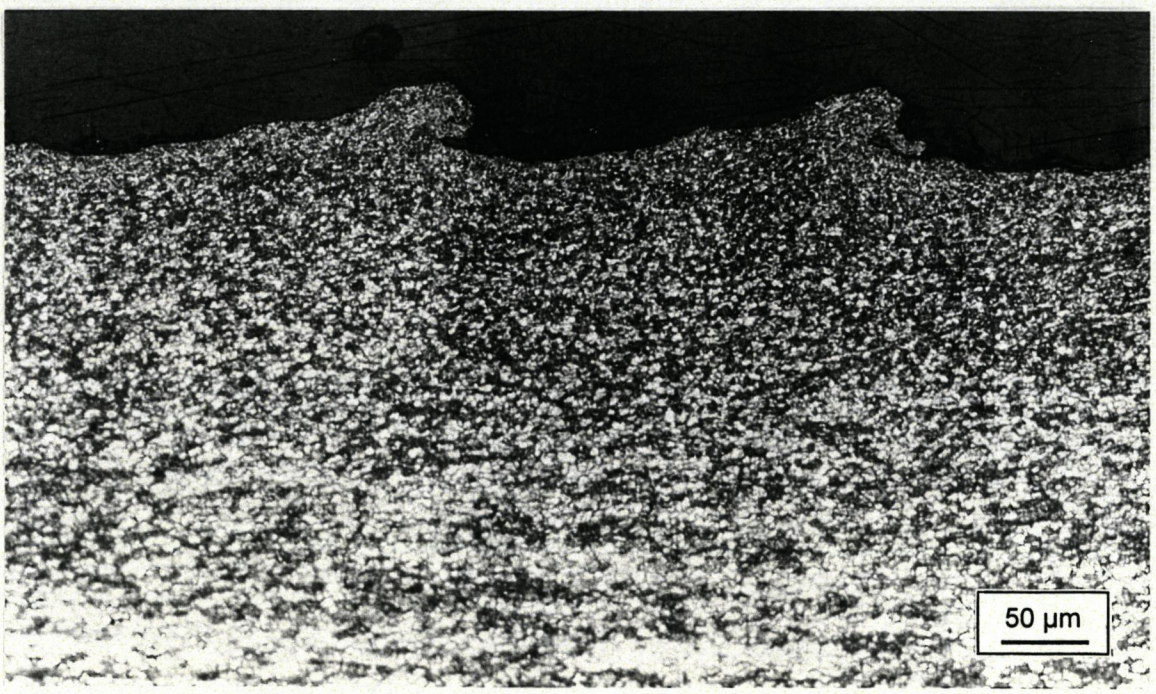

Figure 4.6 The superficial layer of the weld top surface characterised by a microstructure similar to that of the nugget. The picture shows the profile of the tool marks on a section parallel to the weld on the plate joint line.

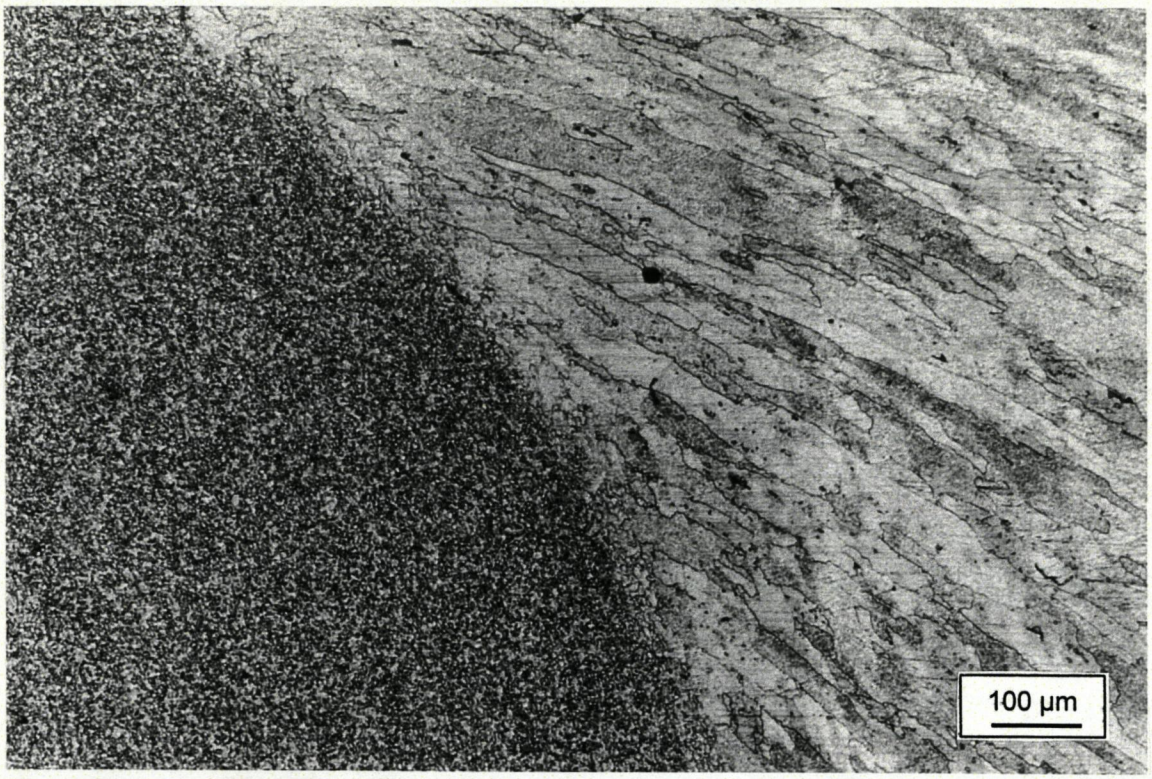

Figure 4.7 A detailed view, on the plane normal to the weld, of the local grain direction in the thermo-mechanically affected region next to the nugget.

Figure 4.8a The typical microstructure in the thermo-mechanically affected region, at 6 mm from the plate joint line, on a plane normal to the weld.

Figure 4.8b The typical microstructure in the thermo-mechanically affected region, at 6 mm from the plate joint line, on a plane parallel to the weld.

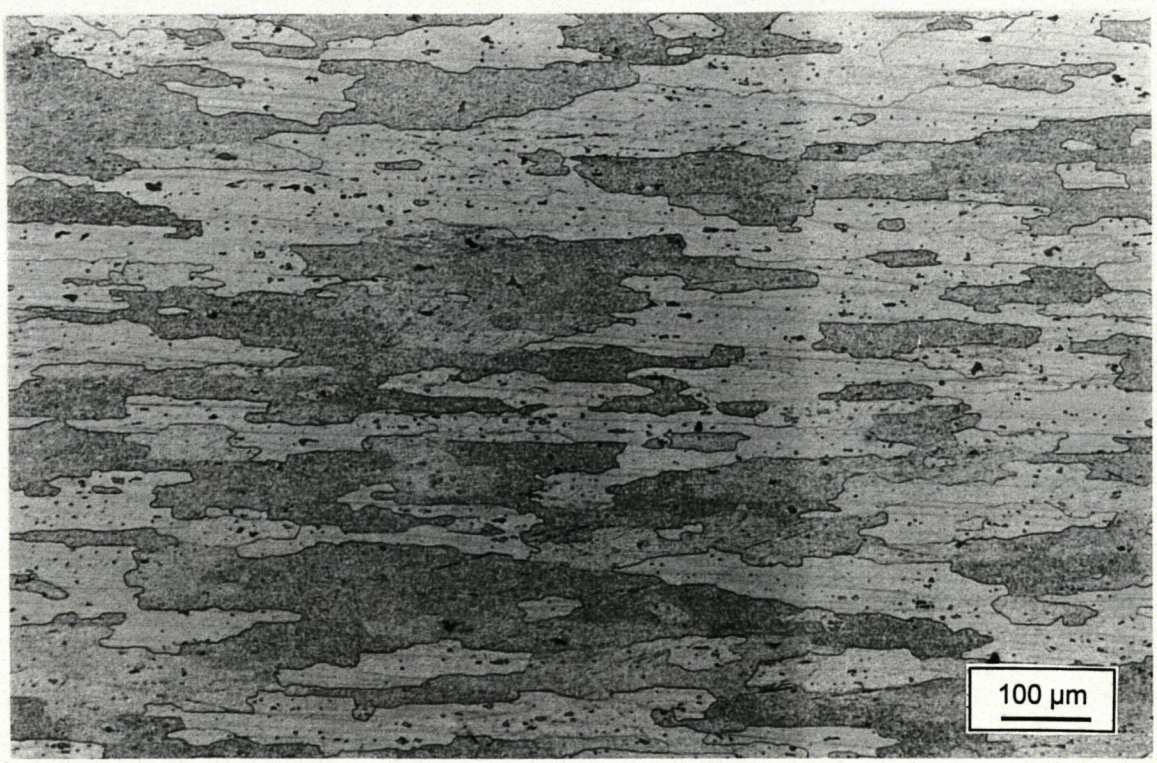

Figure 4.9a The typical microstructure in the HAZ, at 28 mm from the plate joint line, on a plane normal to the weld.

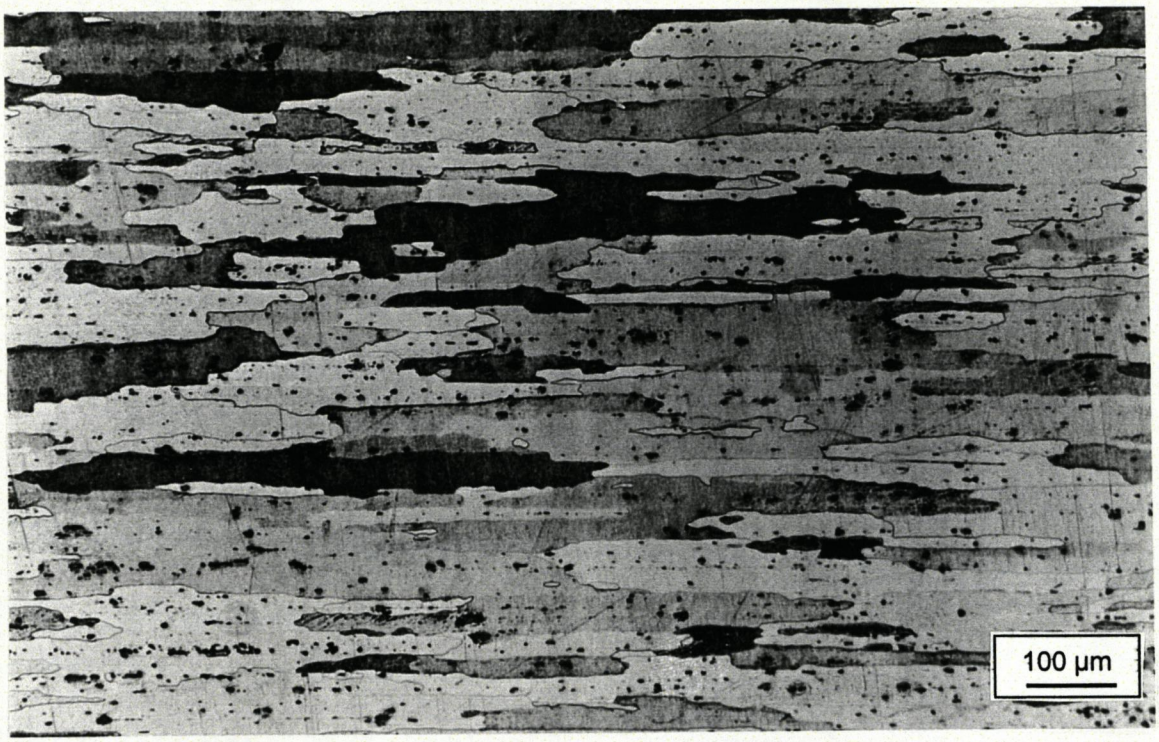

Figure 4.9b The typical microstructure in the HAZ, at 28 mm from the plate joint line, on a plane parallel to the weld.

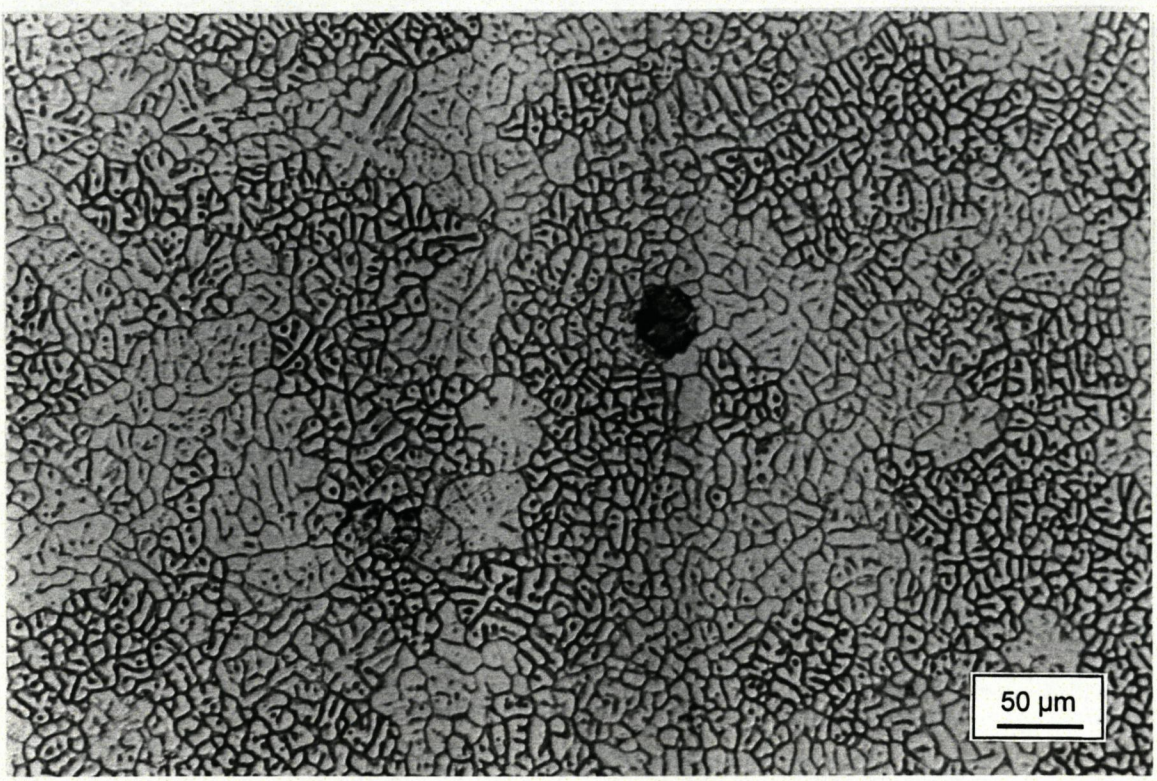

Figure 4.10 The grain structure in the centre of the plasma weld on a section normal to the weld.

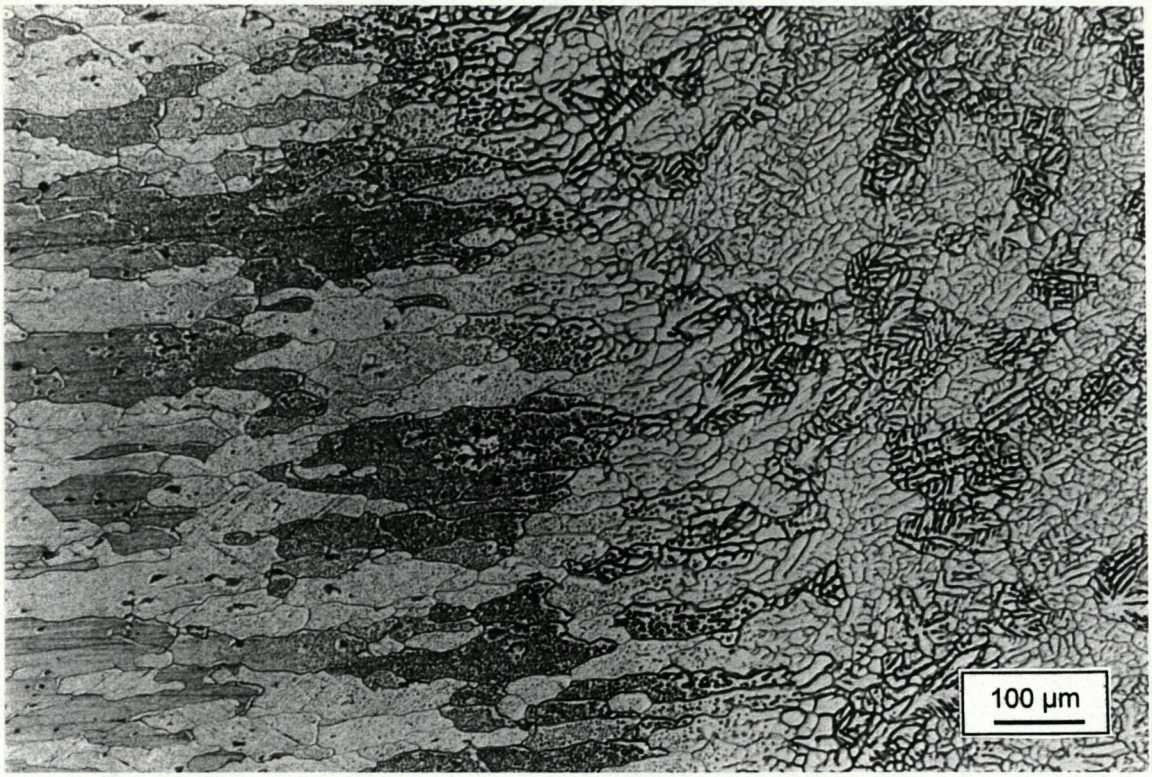

Figure 4.11 The transition in grain structure in the boundaries between the melted region and the HAZ on a cross section of a plasma welded joint.

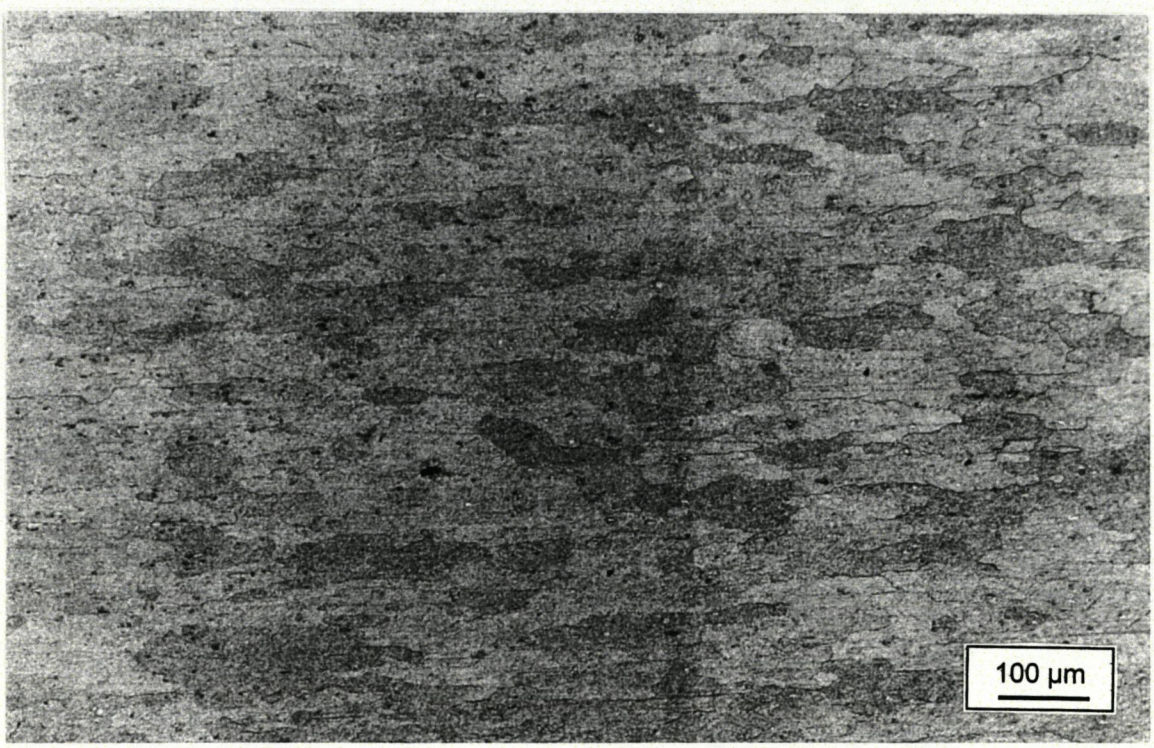

Figure 4.12 The typical microstructure characterising the dark bands on the HAZ in the plasma welded joints (plane normal to the weld).

4.1.3 Hardness profiles

Figure 4.13 shows typical hardness profiles obtained from the hardness tests carried out on a friction stir welded specimen. Hardness values on the plate joint line exhibit the largest variation through the plate thickness. The maximum value was measured on the top weld surface (137 Hv1) and the minimum on the bottom weld surface (117 Hv1). At 6 mm from the plate joint line in the direction opposite to the lip, the hardness values reached the absolute minimum of 103 Hv1 on the bottom weld surface. The through-thickness hardness variations were significantly reduced when moving sidewise from the centre of the weld. In the regions external to ±11 mm from the plate joint line, the through-thickness variation was particularly small, and the profiles were almost overlapped.

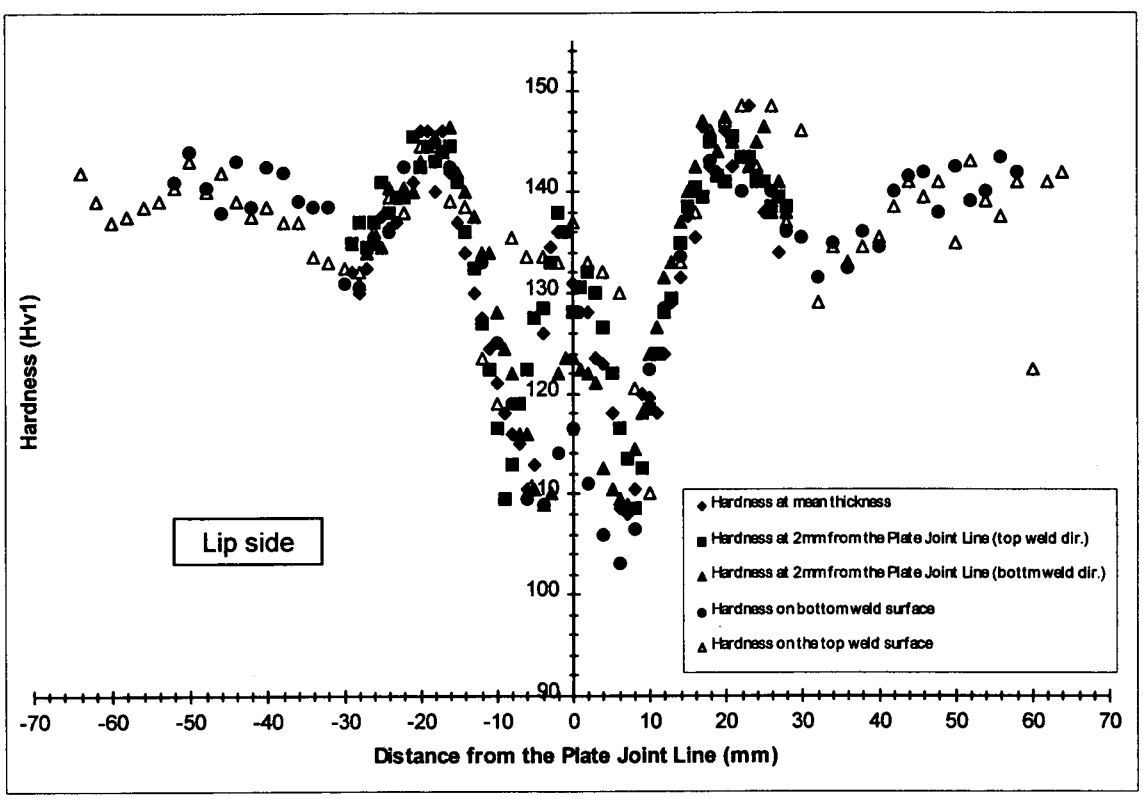

Figure 4.13 The typical hardness profiles of the friction stir welded joints.

At 22 mm from the weld on the side opposite the lip, the hardness value reaches its absolute maximum. The peak hardness value (149 Hv1) is greater than that of the parent metal (142 Hv1). Similarly, on the lip side at 19 mm from the weld, the hardness values

reach a local maximum of 146 Hv1. At 32 mm from the weld opposite the lip side, the hardness profiles reach a local minimum of 129 Hv1. On the opposite side and at 28 mm from the weld, the hardness values exhibit a local minimum value of 132 Hv1. Corresponding parent plate hardness values are reached at 52 mm (opposite lip side) and at 44 mm (lip side) from the weld. This indicates a heat affected zone width of 96 mm.

Figure 4.14 shows the typical hardness values measured in a plasma welded specimen. These reach the absolute minimum value on the weld centre-line (93 Hv1), and a peak (142 Hv1) at 6 mm from the weld. A point of local minimum (102 Hv1) is exhibited at 11 mm from the weld. The typical parent plate hardness values are eventually reached after 30 mm from the centre of the weld. The HAZ is about 60 mm in width.

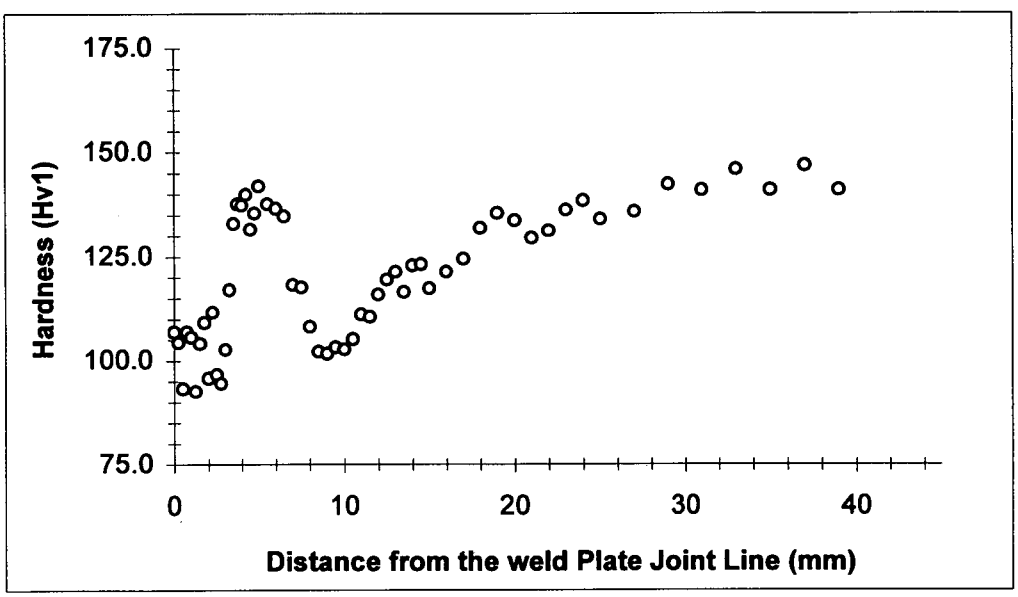

Figure 4.14 The typical hardness profile of the plasma welded joints.

4.1.4 Friction stir weld residual stress

Tables 4.1a, 4.1b and 4.1c show the longitudinal and transverse in-plane residual stresses obtained from the measurements carried out on the as-welded plate, the longitudinal welded specimen and the same specimen after being surface skimmed. The surface skimming operation was carried out as described in Section 3.5.

RESID. STRESS	ON PL. JNT. LN	AT 11mm	AT 25mm
LONGITUDINAL	104MPa	146MPa	14MPa
TRANSVERSE	21MPa	-3MPa	11MPa

Table 4.1a Residual stresses measured on the as-welded plate.

RESID. STRESS	ON PL. JNT. LN	AT 11mm	AT 25mm
LONGITUDINAL	33MPa	73MPa	-51MPa
TRANSVERSE	-7MPa	-14MPa	-2MPa

Table 4.1b Residual stresses measured on the longitudinal specimen (as-welded condition).

RESID. STRESS	ON PL. JNT. LN	AT 11mm	AT 25mm
LONGITUDINAL	8MPa	264MPa	-13MPa
TRANSVERSE	174MPa	5MPa	-192MPa

Table 4.1c Residual stresses measured on the longitudinal specimen after surface skimming.

The longitudinal residual stress in the as-welded plate was tensile in the central region. The greatest value was 11 mm from the weld and it corresponded to 47% of the nominal parent plate 0.2% proof stress (L). The longitudinal residual stress on the as-welded longitudinal specimen showed that the weld and the nearest regions were subjected to tensile residual stress, whereas compressive stresses were present in the external regions. Transverse residual stresses measured in the as-welded plate and longitudinal specimen were small enough to be within experimental error.

Skimming the sample resulted in a reduction in the longitudinal residual stress at the weld and in a very large increase in this stress at 11 mm from the weld. The longitudinal residual stress measured in the weld was tensile with the external regions subjected to compressive residual stress. The maximum tensile residual stress at 11 mm from the weld was 85% of the parent 0.2% proof stress (L). Transverse residual stresses became markedly tensile in the weld, being 56% of the parent 0.2% proof stress (L) and 22 times greater than the longitudinal component, and markedly compressive at 25 mm, being 62% of the parent 0.2% proof stress (L). The residual stress measurements in the three cases were broadly in agreement with values measured in previous works [38, 53, 70].

4.1.5 Tensile properties of friction stir welded joints

Table 4.2 shows values for the proportional limit, the 0.2% proof stress, the ultimate stress and the elongation measured in the tension tests performed on transverse and longitudinal FSW joints. The ultimate properties are the arithmetical mean of the test results. The degradation values of the previous properties are reported in Table 4.3. The definitions used to evaluate the degradation values are also indicated. The tensile properties measured in FSW joints were generally in good agreement with the values reported in Ref. [36, 109].

Figure 4.15 shows the stress-strain plots from the tensile test carried out on a transverse FSW specimen. The stress-strain curves for the FSW joint were obtained by recording the stress versus strain values at each strain gauge location. Figure 4.16 represents the strain distribution across the transverse joint measured at the strain gauge locations and at fixed stress levels. The minima and maxima of the strain distribution curves describe the formation of the first yielded region and its gradual extension to the surrounding areas of the joint.

When the load was applied to the specimen, all the strain values responded linearly until the specimen started yielding. Within this first stage of the test, the overall joint behaved elastically. Slight differences in slope among the stress-strain curves were noticed (Fig. 4.15). This has been attributed to the scatter effect in the constants of proportionality

involved in the calculation of the stress-strain curves (higher level of accuracy would have been required for the determination of the Young's modulus, as prescribed in ASTM E 111- 82 (1997)).

JOINT CONFIGURATION	σ_{prop} (MPa)	$\sigma_{0.2}$ (MPa)	σ_{ult} (MPa)	Elongation (%)
FSW LONGITUDINAL	110	316	425	7.2 [1]
PARENT PLATE (L)	265	449	490	19.8 [1]
FSW TRANSVERSE	154	243	409	7.1 [2]
PARENT PLATE (LT)	175	330	484	19.6 [2]

(1) measured over a gauge length of 170 mm; (2) measured over a gauge length of 84 mm.

Table 4.2 Tensile properties measured for the friction stir welded joints and parent plate specimens.

DEFINITION OF DEGRADATION	PROPERTY	DEGRADATION (%)
$\frac{FSWL - FSWT}{FSWL} \times 100$	σ_{prop}	-40
	$\sigma_{0.2}$	23
	σ_{ult}	4
	Elongation	1
$\frac{PARENT\ (LT) - FSWT}{PARENT\ (LT)} \times 100$	σ_{prop}	12
	$\sigma_{0.2}$	26
	σ_{ult}	15
	Elongation	64
$\frac{PARENT\ (L) - FSWL}{PARENT\ (L)} \times 100$	σ_{prop}	58
	$\sigma_{0.2}$	30
	σ_{ult}	13
	Elongation	64

Table 4.3 Values of the degradation due to the friction stir welding process for each tensile property (FSWL = longitudinal FSW joint, FSWT = transverse FSW joint).

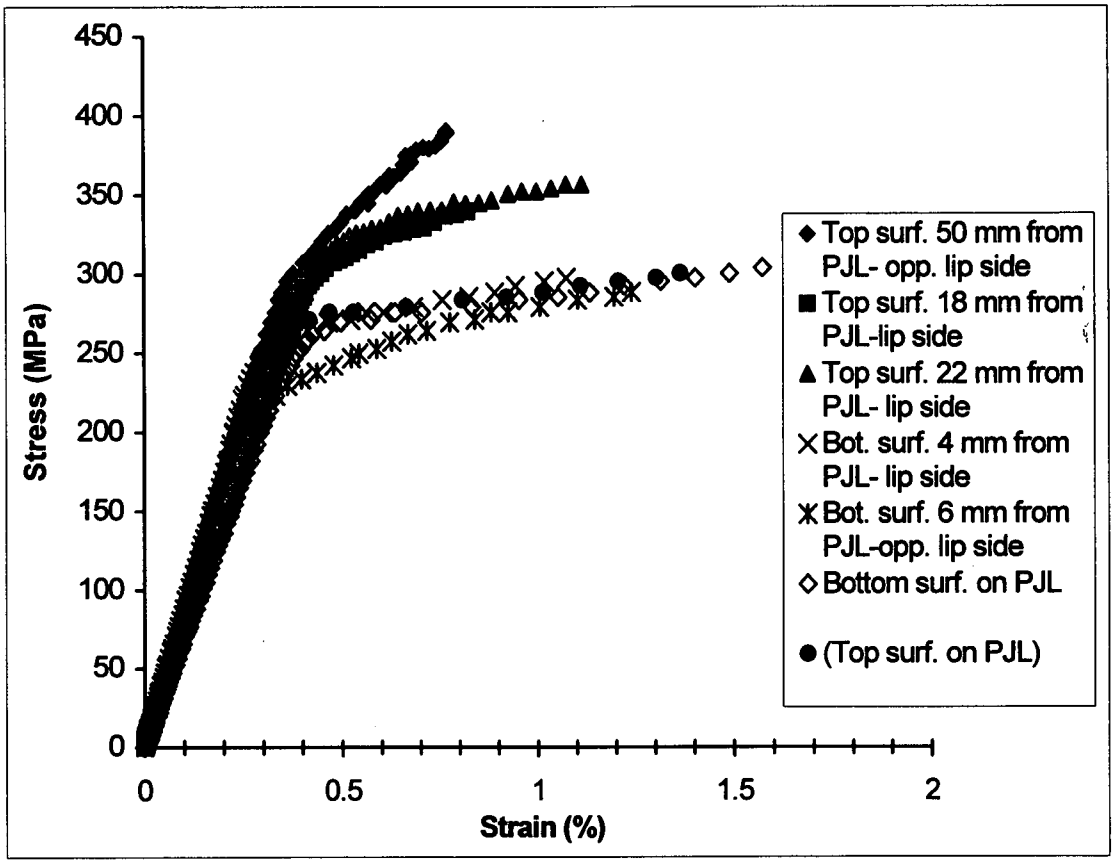

Figure 4.15 The stress-strain curves exhibited by the transverse FSW joint during the tensile test.

The joint started to yield at location 3, 6 mm from the PJL opposite the lip side. The stress-strain curve deviated from linear behaviour (Fig. 4.15) and strain distribution exhibited a maximum at the same location (Fig. 4.16). This corresponds to one of the point of lowest hardness of the joint (104 Hv1). The 0.2% proof stress of the joint was 243 MPa, reached at the former location. As the load increased, the next region to yield was the one at 4 mm from the plate joint line, but on the other side of the weld (on the lip side). At this location the yield strength was 273 MPa. This is the location where the hardness reached the second lowest value of the joint (108 Hv1). Gradually, the yielding extended to the centre of the weld. At this location the 0.2% proof stress was 276 MPa.

At 330 MPa, yield was reached at 18 mm from the PJL on the side opposite the lip. At 336 MPa, yielding was reached at 22 mm from the PJL on the same side of the weld,

and finally extended out of the heat affected region, on the parent metal at 50 mm from the weld (360 MPa). In the next stage all the stress-strain curves exhibited different slopes according the different rates of work hardening. Failure of the adhesive between the strain gauges and the specimen surface took place at strain values between 0.7 and 1.6% strain and the test could not be monitored up to the failure.

The transverse welded joint failed at 409 MPa. Failure took place at 6 mm from the plate joint line on the side opposite the lip, corresponding to the location of minimum hardness of the joint. Figure 4.17a shows a longitudinal section of a failed transverse joint. Failure surfaces were orientated at 45° to the specimen axis according to the maximum shear plane. Fracture planes coincided with the minimum hardness locations as showed in Figure 4.17b. The elongation was measured on 84 mm gauge length in order to include as much of the weld heat affected zone as possible. The elongation compared to the former length is 7.1%.

Figure 4.18 shows the stress-strain curves obtained from the tension test carried out on the longitudinal FSW joint. In this case all the curves from the different strain gauges are overlapped. The joint behaved linearly until 110 MPa. For higher load values, the curves slowly started to deviate from the linear behaviour reaching 0.2% strain offset at 316 MPa. Strain gauges started to de-bond from the specimen surface between 2.3 and 3% strain. The specimen failed after reaching an ultimate stress of 425 MPa. The failure took place within the test gauge length. Fracture surfaces were generated at ±45° on maximum shear planes. The elongation measured on an initial gauge length of 170 mm was 7.2%.

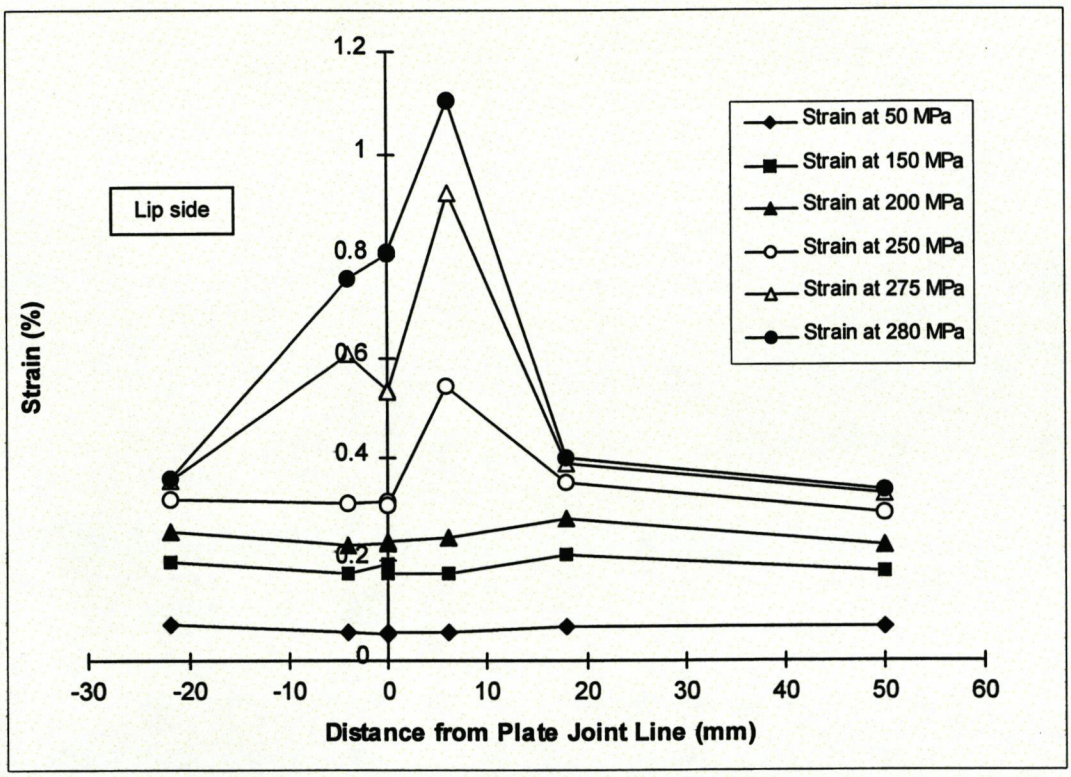

Figure 4.16 The distribution of strain, at fixed stress values, in the direction of the principal stress axis measured at each strain gauge location during the tensile test on the transverse FSW joint. The negative abscissas correspond to the lip side of the joint.

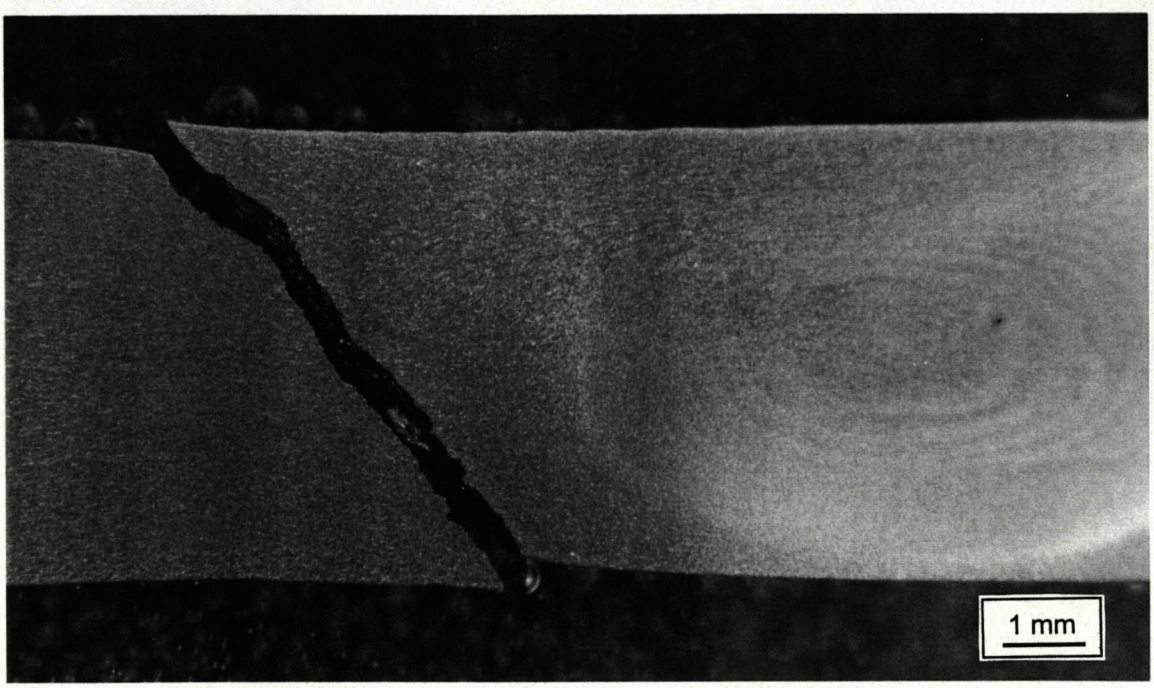

Figure 4.17a A longitudinal section of the transverse FSW joint failed in the tensile test.

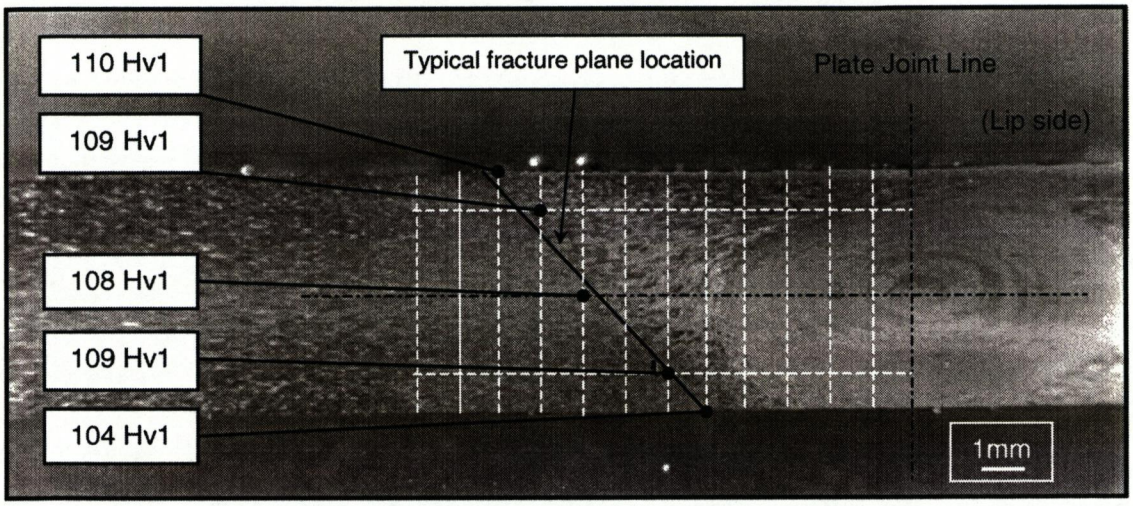

Figure 4.17b Typical location of failure, observed in the transverse friction stir welded joints, and the position of minimum hardness values. Hardness measurements were taken at each intersection point of the dotted lines (Section 3.4).

Under the specified testing conditions, the transverse joints exhibited 0.2% proof stress values 23% lower than the longitudinal ones. Much lower differences were observed in the ultimate stress and strain values. The transverse FSW joints showed ultimate stress and ultimate strain values of 4% and 1% less than the longitudinal joints, respectively.

An exception to the superior performance of the longitudinal joint was found in the measured proportional limits (σ_{prop}). Although the longitudinal joints have better performance, the transverse FSW joints generally exhibit the lowest degradation values in tensile properties. In fact, the 0.2% yield strength was reduced to 26% of the parent plate (LT) value, whereas the degradation observed in the longitudinal direction was 30% of the parent plate (L) value. The ultimate properties of the transverse and longitudinal joints exhibit similar differences with respect to the parent plate values. The longitudinal welded joint exhibits the largest degradation for σ_{prop} (58%) with respect to the parent plate.

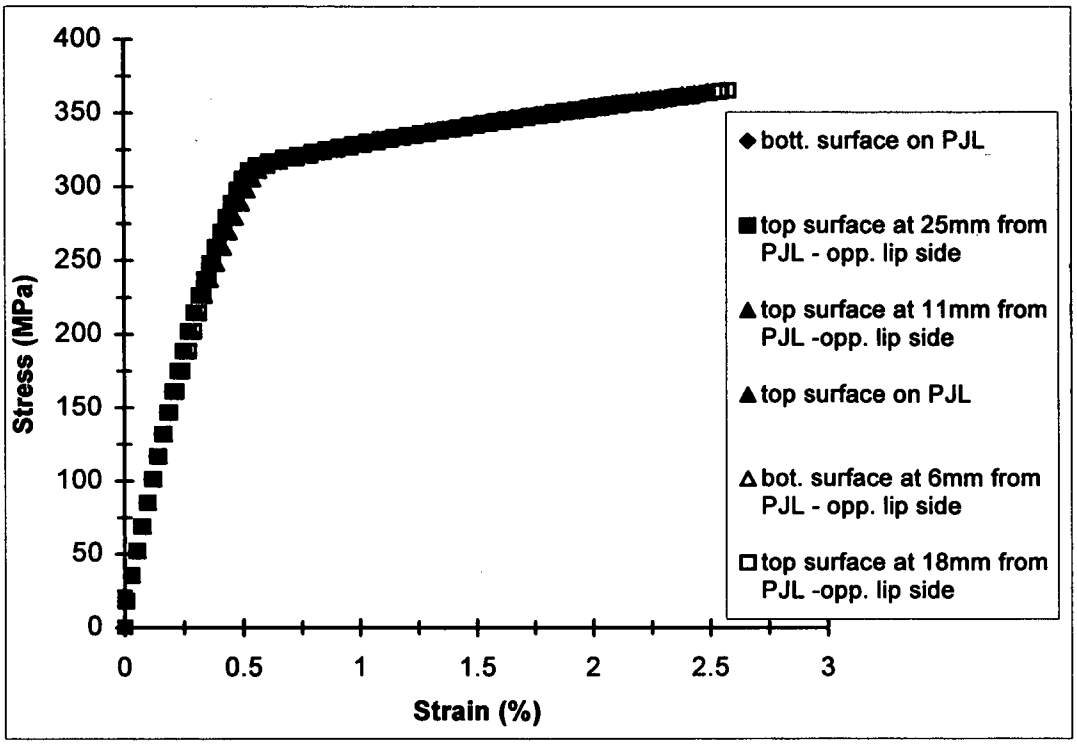

Figure 4.18 The stress-strain curves obtained from the tension test carried out on the longitudinal friction stir welded joint.

4.1.6 Tensile properties of plasma welds

Table 4.4 reports the results of the static tests performed on the plasma transverse welded joints. All the tensile tests were performed by the Cranfield Welding Group [107]. No measurements of strain values were carried out during the tests. The ultimate properties are the arithmetical mean of the test results. Table 4.4 reports the values of the reduction of the initial parent plate tensile properties (LT) due to the plasma welding process. Table 4.5 shows a comparison between the tensile properties of the transverse plasma welded joints and those measured for the transverse FSW joints.

As it can be noticed from Table 4.5, transverse FSW joints exhibit better ultimate properties than plasma welded joints. The difference between the elongation values is particularly high (7% for the FSW and only 2.4% for the plasma welds).

JOINT CONFIGURATION	σ_{prop} (MPa)	$\sigma_{0.2}$ (MPa)	σ_{ult} (MPa)	Elongation (%)
PLASMA TRANSVERSE	–	–	334	2.4[1]
$\frac{(PARENT\ (LT) - PLAS.) \times 100}{PARENT\ (LT)}$	–	–	31%	88%

(1) measured over a gauge length of 84 mm

Table 4.4 Results from the monotonic tests performed on transverse plasma welded joints and degradation values of the parent plate properties.

JOINT CONFIGURATION	$\frac{\sigma_{prop}(Plasma)}{\sigma_{prop}(FSW)}$	$\frac{\sigma_{0.2}\ (Plasma)}{\sigma_{0.2}\ (FSW)}$	$\frac{\sigma_{ult}\ (Plasma)}{\sigma_{ult}\ (FSW)}$	$\frac{Elong.(Plasma)}{\varepsilon_{ult}\ (FSW)}$
TRANSVERSE	–	–	0.82	0.34

Table 4.5 Comparison of tensile properties between transverse plasma and FSW joints.

4.2 Fatigue properties of welded joints

4.2.1 Friction stir welded joints

Figure 4.19 summarises the results of constant amplitude load fatigue tests performed on parent plate and FSW specimens in as-welded condition. All the S-N curves of friction stir welded joints are characterised by a quite pronounced "knee" in the region between 10^5 and 10^6 cycles. With the exception of the failure at the longest life which occurred on a transverse welded specimen at $2 \cdot 10^6$ cycles, no other failures were observed between 10^6 and 10^7 cycles.

A comparison between the parent plate and the weld data gives an indication of the degradation in fatigue properties due to the welding process. A correct evaluation can be made comparing the parent plate (L) data with the longitudinal FSW joints, and the parent plate (LT) data with the transverse friction stir welded joints. This comparison guarantees that the grain direction in the parent metal of the welded joints has the same orientation with respect to the normal stress as in the weld-free specimens.

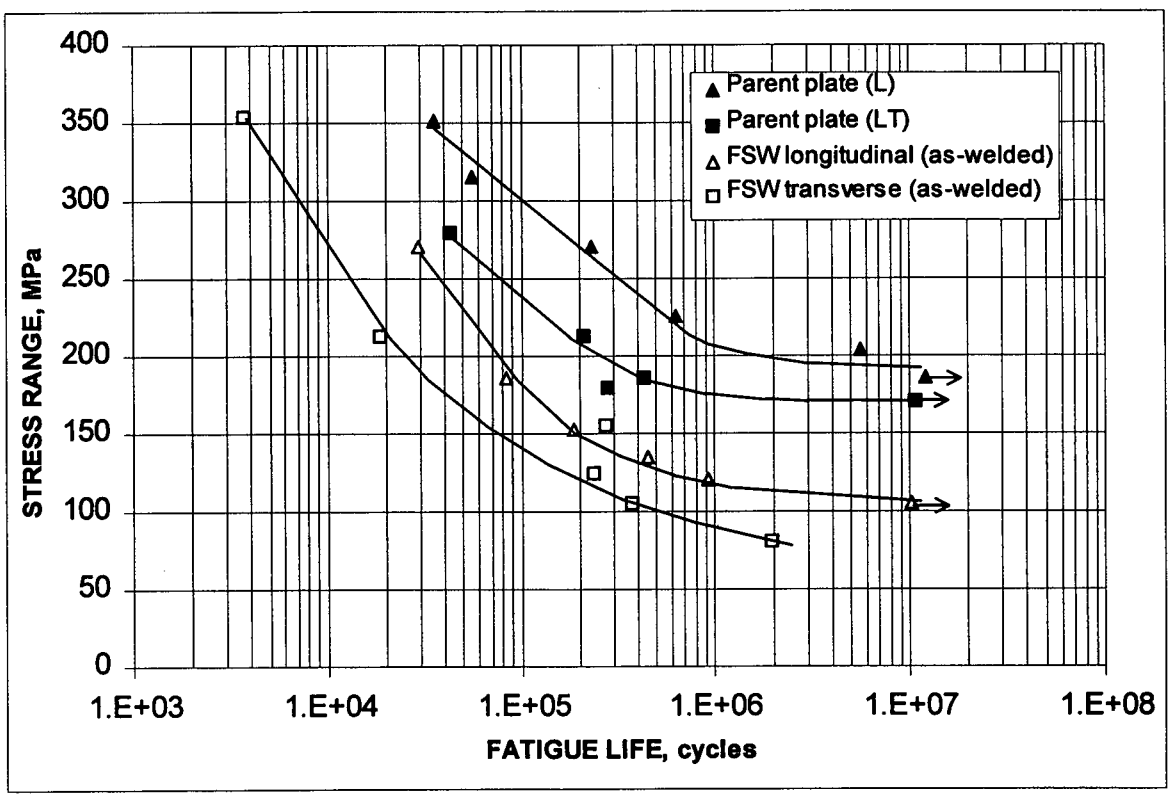

Figure 4.19 S-N experimental data (R = 0.1) for parent plates and FSW joints in as-welded conditions.

With reference to the parent plate data (L) and the longitudinal FSW joints data, four specimens (one for each condition) were tested at similar stress range values of 270 MPa and 185 MPa. In the former case the fatigue life of the welded joint was of 29186 cycles, 13% of the life exhibited by the parent plate. In the latter case, the welded joint failed after 82749 cycles whereas the parent plate exceeded the run-out threshold of 10^7 cycles. In the region of 10^5 cycles, the curves indicate for the welded joints a degradation of 36% of the parent stress range value. The endurance limit (at 10^7 cycles)

has been estimated to be between 121 and 105 MPa. This is approximately 42% less than for the parent plate (L) which is between 185 and 203 MPa.

Comparing the parent plate in the LT grain orientation with the FSW joints, between 10^5 and $2 \cdot 10^5$ cycles, the welded joints exhibited a degradation in stress range of 40% of the parent plate values. In the region of run-outs (10^7 cycles) the best-fit curves indicate a degradation in stress range greater than 50%.

4.2.2 Effect of weld orientation on fatigue life of FSW joints

Figure 4.19 shows that almost all the longitudinal joints perform better than the transverse joints. In fact only the transverse welded specimen tested at 155 MPa exhibited a longer life by a factor of 4.7 with respect to the longitudinal welded specimen tested at the same maximum stress level. In the region of short lives, the fatigue performance of the transverse joints was 30% of that exhibited by the longitudinal joints. In the region between 10^5 and 10^6 cycles, this difference was reduced to less than 10%.

While the longitudinal joints exhibited one run-out datum (10249338 cycles and stress range of 105 MPa), no run-outs were observed for the transverse welded joints. For the latter the longest observed life was of 19544870 cycles at 81 MPa of stress range. This result was the only failure to occur between 10^6 and10^7 cycles. In the region of run-outs, the best-fit curves indicate that the transverse joints exhibit stress range values 30% lower than those of the longitudinal joints.

4.2.3 Effect of surface skimming on fatigue life of FSW joints

Figure 4.20 shows the results of fatigue tests on surface skimmed longitudinal and transverse specimens. Figure 4.21 shows the extent of material removed during the surface skimming process. It can be noticed that all the profile irregularities of the weld surface i.e. tool marks, thickness variation and the overlapped weld toe (lip) have been completely removed by the process. The results show a beneficial effect on fatigue performance both in longitudinal and transverse specimens.

Fatigue performance of FSW joints was similar to the parent plate in the long-transverse direction. Marginal differences in results were observed between the skimmed longitudinal and transverse joints particularly in the region between 10^4 and 10^5 cycles. In the run-out region the transverse skimmed joints performed even slightly better than the longitudinal skimmed ones. The transverse skimmed specimens failed at different locations within the Heat Affected Zone (HAZ). The longitudinal skimmed joints failed in the parent metal and at the ends of the gauge test length.

A comparison between Figure 4.19 and Figure 4.20 indicates that the transverse skimmed joints exhibited the greatest beneficial effect from the skimming operation. For these joints, at short lives (between 10^4 and 10^5) and in the run-out region the skimmed transverse joints exhibited fatigue performance comparable to the parent plate (LT). In the region between 10^5 and 10^6 cycles, the degradation was generally less than 10% of the parent plate strength.

Skimming of the longitudinal joints had a minor beneficial effect on fatigue lives. In the region of short lives (between 10^4 and 10^5), the degradation was 20% of the parent plate (L) stress range values. For $2 \cdot 10^5$ cycles, the degradation was 30% of the parent plate (L) values. In the run-out region, the joints exhibited fatigue performance 20% less of the parent plate (L).

4.2.4 Plasma welded joints versus FSW joints

Figure 4.22 shows a comparison of fatigue performance between plasma welded transverse specimens and friction stir welded transverse specimens. All the specimens were surface skimmed. In the case of plasma welded specimens a heavier skimming operation was required in order to remove all the surface irregularities present on the weld bead. In this case, 1.00 mm was removed from each plate surface.

In the region of short lives (up to $2 \cdot 10^5$ cycles) fatigue performances of the two sets were comparable. A premature failure of a plasma welded joint tested with a maximum stress of 348 MPa (the sample failed during the first loading cycle) did not allow the

investigation of the fatigue performance in the region of short lives, with the limited number of specimens available.

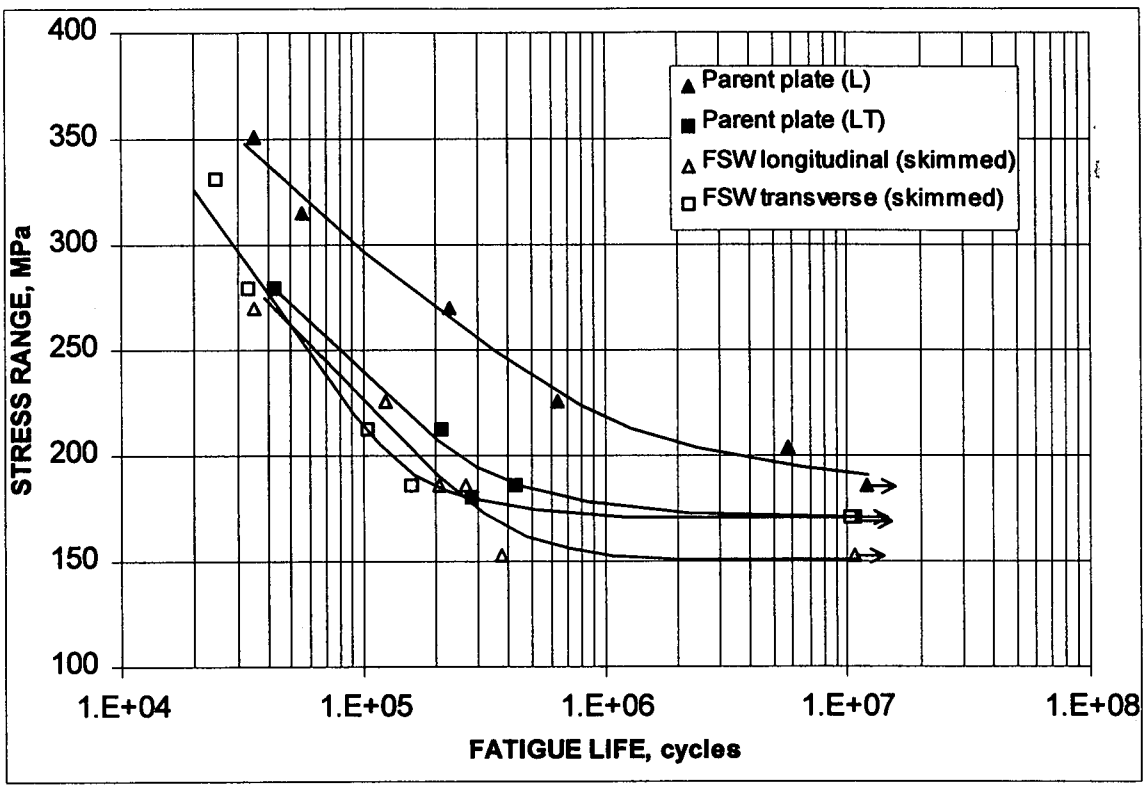

Figure 4.20 S-N experimental data (R = 0.1) for parent plates and FSW joints in surface skimmed conditions.

In the region of fatigue lives equal or greater than $2 \cdot 10^5$ cycles, the superiority of the friction stir welded joint over the plasma welded ones became more evident. In this region of lives, plasma welds exhibited stress range values approximately 17% less than the friction stir welds. For fatigue lives of 10^7 cycles, the estimated fatigue strength of plasma welds was 144 MPa, approximately 20% less than the transverse friction stir welded joints.

4.2.5 Fatigue crack initiation

Fatigue cracks in transverse as-welded joints typically initiated on the top weld surface at the lip on the weld toe. This location is shown in Figure 4.21. A detailed view of the lip is shown in Figure 4.3. The two SEM pictures in Figures 4.23 and 4.24 show the

typical appearance of the fracture surfaces observed on the FSW transverse specimens tested in as-welded conditions. In Figure 4.23, the lip and its characteristic tool marks are visible in the lower part of the picture. The thumbnail crack front, visible in the upper part of the picture, indicates that the crack initiated underneath the lip on the boundary line with the plate. The cracks grew on the plane orthogonal to the specimen main axis (coplanar to the view plane in Fig. 4.23).

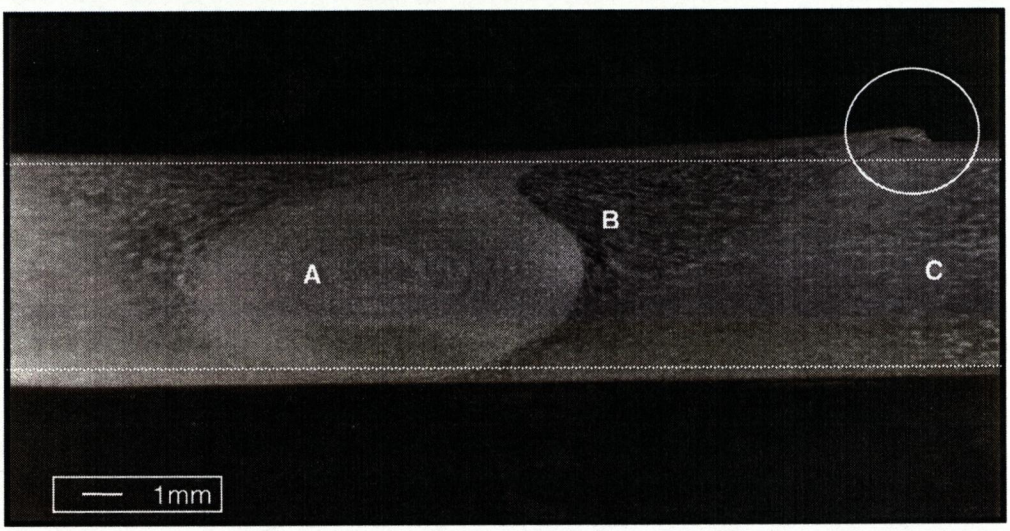

Figure 4.21 Optical cross section of a FSW joint. The dotted lines delimit the amount material removed in the skimmed specimens. The "lip", origin of fatigue cracks (indicated with a circle) was removed during the surface skimming operation. All the characteristic regions of a FSW joint are visible: A) dynamically recrystallized area, B) thermo-mechanically affected area, C) heat affected zone.

Figure 4.24 shows a typical example of initiation from a local defect on the boundary line between the lip and the plate. Initiations were generally caused by inclusions, as the picture shows. A quantitative microanalysis of initiation areas on the fracture surfaces was carried out using the Energy Dispersive X-Ray Analysis method (EDX) [10]. A Cambridge 250 scanning electron microscope was used to generate the incident electron beam. The analysis revealed the presence of aluminium only. Measurement of the initiating defect dimensions was carried out on the failed specimens. In all cases the defect size varied between 20 and 70 μm in diameter.

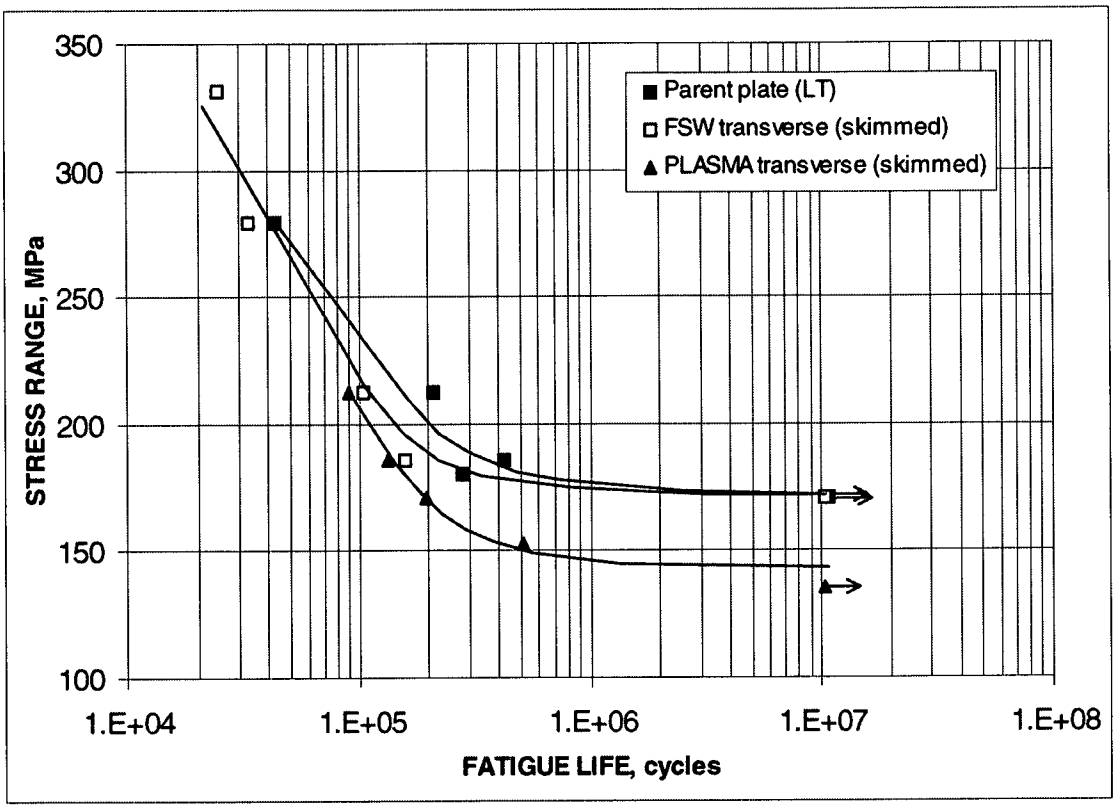

Figure 4.22 Fatigue tests results of transverse plasma welded (skimmed) and transverse friction stir welded joints (skimmed) under constant load amplitude (R = 0.1).

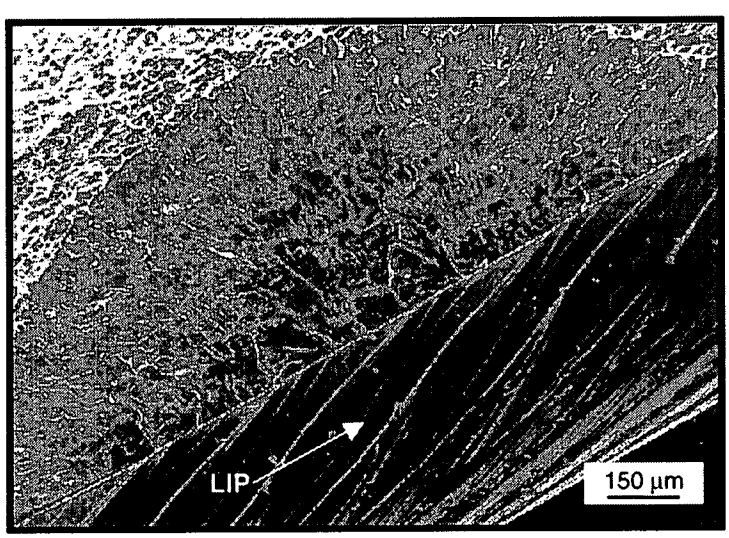

Figure 4.23 Typical SEM picture of the initiation area in the transverse FSW specimens. The crack started from underneath the "lip". The tool marks are visible on the lip surface.

For all longitudinal as-welded specimens, the fatigue cracks initiated from defects at the semicircular tool marks present on the top weld surface. These tool marks originated during the welding process and typically characterised the top weld surface of the FSW joints (Fig. 4.1a). In the early stage of the propagation, cracks generally grew on curved surfaces apparently following the contour of the tool marks as it can be observed from Figure 4.25. Figure 4.26 shows the typical appearance of the initiation area observed in the longitudinal specimens tested in fatigue. The defects from which these cracks initiated had similar size to those observed in the transverse joints. These defects were typically oxide inclusions.

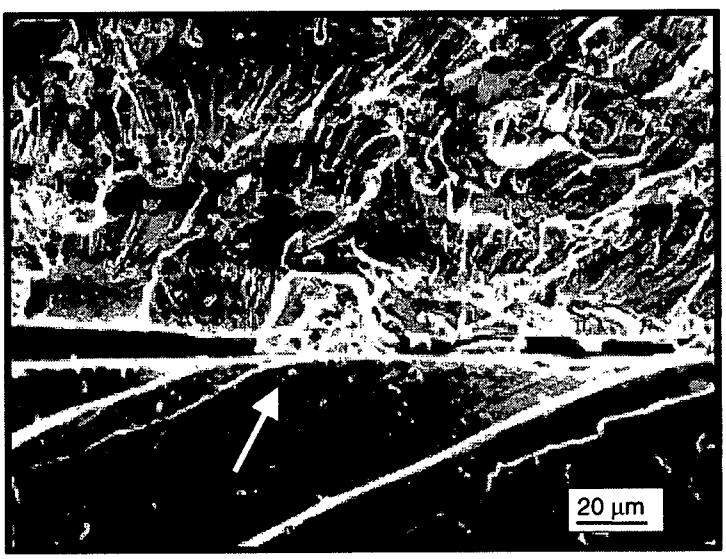

Figure 4.24 A detailed view of the initiation area in a transverse FSW specimen reveals that the crack initiated from an oxide inclusion underneath the lip ($\Delta\sigma$ = 180 MPa).

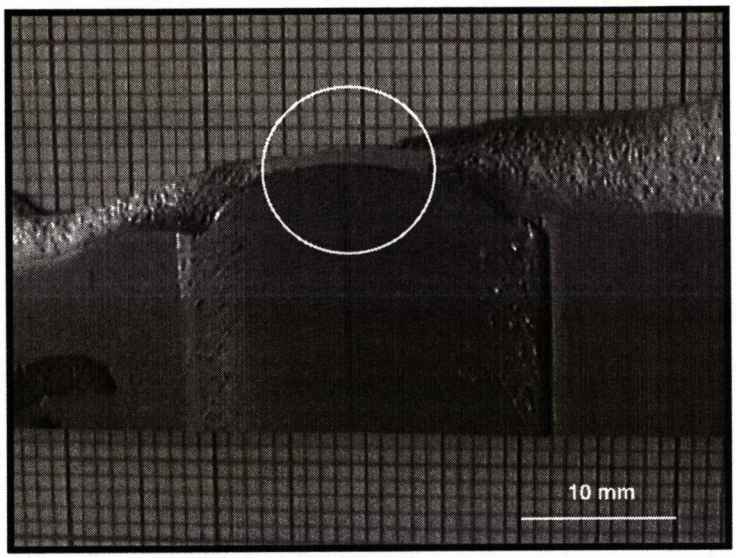

Figure 4.25 Optical picture of a tested longitudinal FSW specimen in as-welded conditions. The circle indicates the initially curved crack surface and the semicircular tool marks. On the right side of the weld toe is visible the lip, evidenced by the shadow.

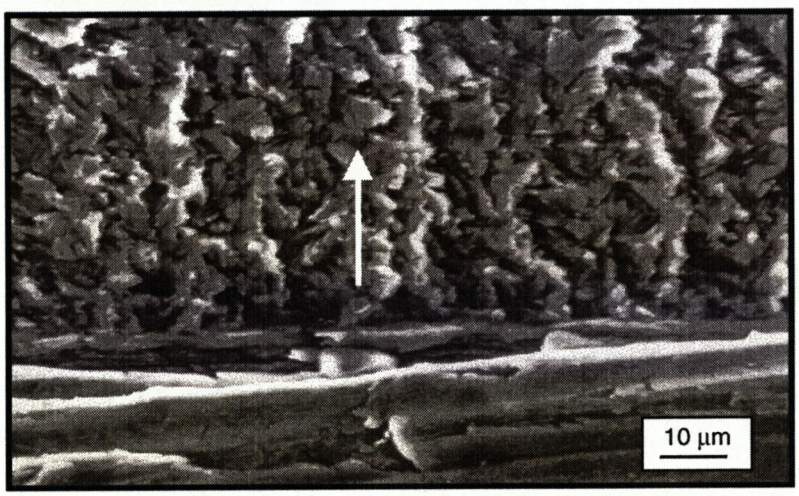

Figure 4.26 SEM picture of the initiation area in the same specimen showed in Fig. 4.25. The crack initiated from the top weld surface visible in the lower part of the picture with the characteristic tool marks. The faceted aspect of the crack surface is due to the refined grain structure within the weld nugget (Section 4.1.2). The arrow indicates the crack growth direction.

In the transverse skimmed joints fatigue initiation occurred at near-surface defects. Figure 4.27 shows a typical example of the defects from which fatigue cracks initiated. Lines on the fracture surface indicate the direction of crack propagation. Figure 4.28 shows the location of the fatigue initiation sites, observed on the failed specimens, with respect to the weld. Multiple initiation sites were observed on most of the joints. Figure 4.29 shows a case where fatigue initiated from two different locations near the joint surface. Figure 4.30a shows a typical SEM picture of one of the initiation areas observed in the transverse skimmed plasma welded specimens. The direction of crack propagation is evidenced by the "sun rise" marks on the fracture surface. These marks point to a circular defect next to the specimen surface. Similar defects are visible on the fracture surface. Figure 4.30b shows that the defects present in Figure 3.30a are pores.

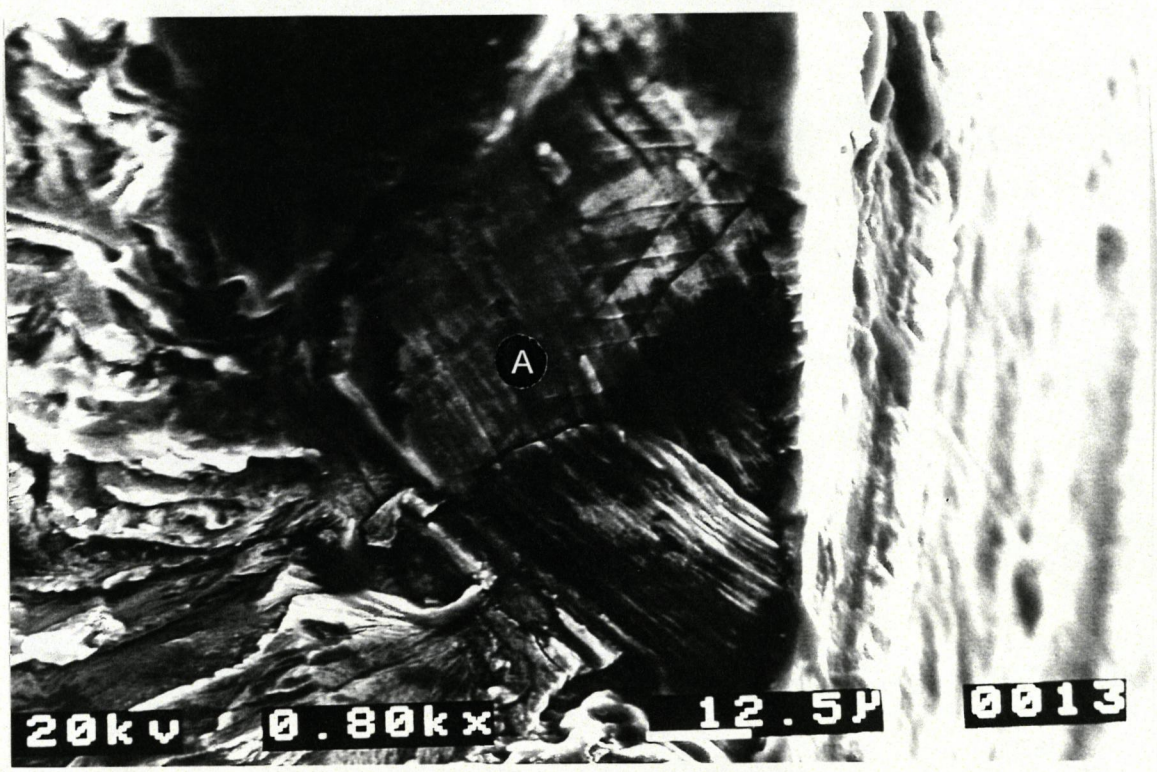

Figure 4.27 Near-surface defect on a transverse skimmed FSW joint ($\Delta\sigma$ = 279 MPa). The lines, on the left of the picture, indicate that the fatigue crack initiated from the defect (A).

SEM observation revealed other sources of fatigue crack initiation that characterised fatigue failure of plasma welded joints. Figure 4.31 shows an example. The defects resemble cavities containing an articulated structure. This appearance, typically

indicated as interdendritic shrinkage [2], suggests that the defects originated during the cooling phase of the welding process. Figure 4.32 shows the location, with respect to the weld, of the fatigue initiation sites observed on the transverse skimmed plasma joints.

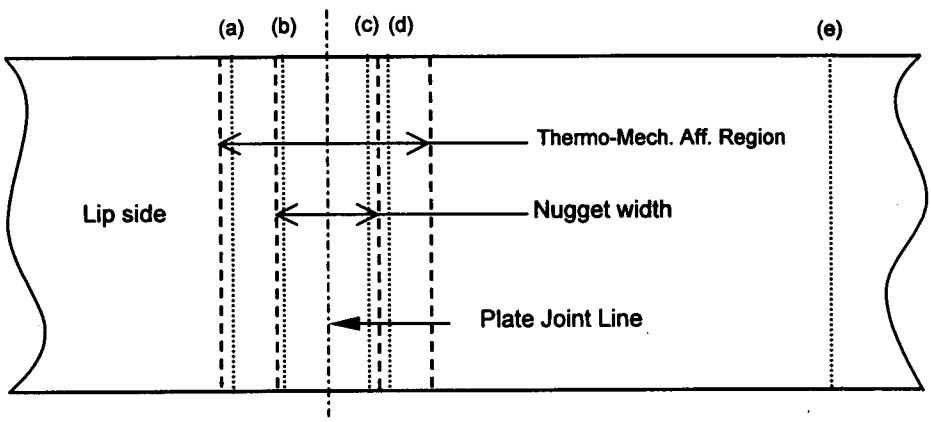

(a) failure at 9 mm from PJL top surf.; initiation from 1 sites, defects dim: 30 μm, (180 MPa, 281162 cycles)

(b) failure at 5 mm from PJL bottom surf.; initiation from 2 sites, defects dim: 50, 70 μm, (279 MPa, 33211 cycles)

(c) failure at 5 mm from PJL top surf.; initiation from 1 sites, defects dim: 50 μm, (212 MPa, 103749 cycles)

(d) failure at 7 mm from PJL bottom surf.; initiation from 2 sites, defects dim: 20, 30 μm, (185 MPa, 425854 cycles)

(e) failure at 28 mm from PJL top surf.; initiation from 3 sites, defects dim: 7, 50 μm, (331 MPa, 24550 cycles)

Figure 4.28 Fatigue initiation and failure locations in the transverse skimmed FSW joints.

All the defects responsible for fatigue initiation in the transverse skimmed FSW and plasma welded joints were measured using the SEM. Defect size and occurrence are shown in Figure 4.33. The measurements were carried out on 5 FSW and 5 plasma welded joints tested in fatigue. Defects in FSW joints were between 7 and 70 μm but more likely to be between 20 and 50 μm. Defects in plasma welded joints were between 20 and 200 μm.

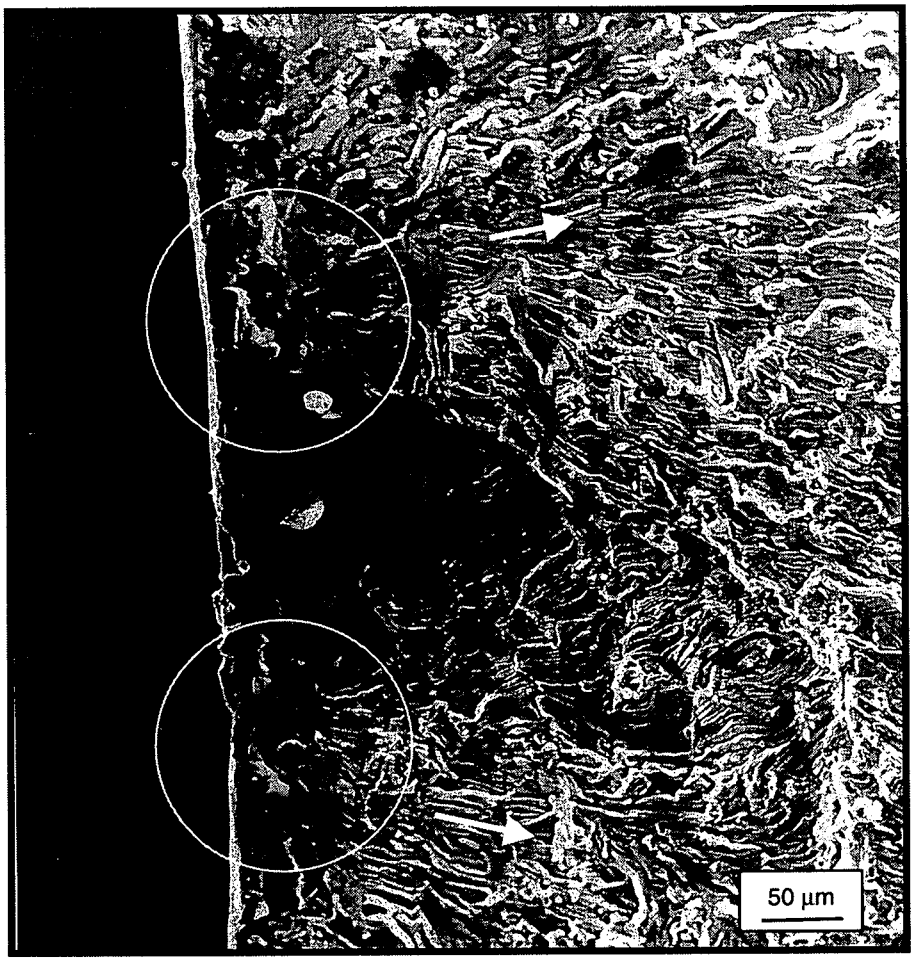

Figure 4.29 An example of multiple fatigue initiation observed on a transverse skimmed FSW joint ($\Delta\sigma$ = 185 MPa). The two initiation sites and the direction of propagation have been indicated for clarity.

4.2.6 Fatigue crack initiation and hardness distribution

An interesting correlation between fatigue initiation and hardness distribution was observed in the transverse skimmed FSW specimens. Positions of fatigue initiation sites, described in Figure 4.28, are plotted on the hardness-distance diagram obtained in Section 4.3. Figure 4.34 shows the correlation between the hardness distribution and the positions of the fatigue initiation sites. A similar correlation was observed in the transverse skimmed plasma welded joints. Figure 4.35 shows the correspondence between hardness profile, obtained in Section 4.1.3, and the locations of fatigue initiation sites.

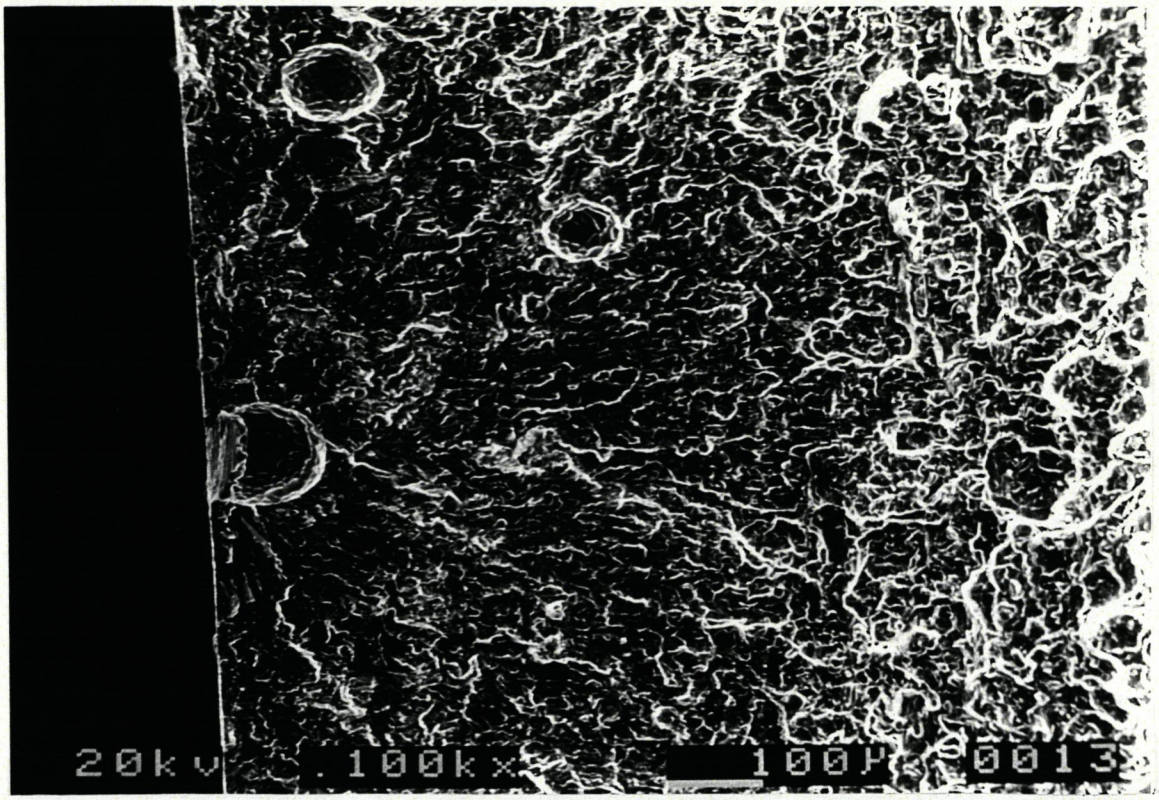

Figure 4.30a The initiation area in one of the skimmed plasma welded specimens ($\Delta\sigma$ = 212 MPa). The fatigue crack originated in correspondence of a circular defect next to the surface.

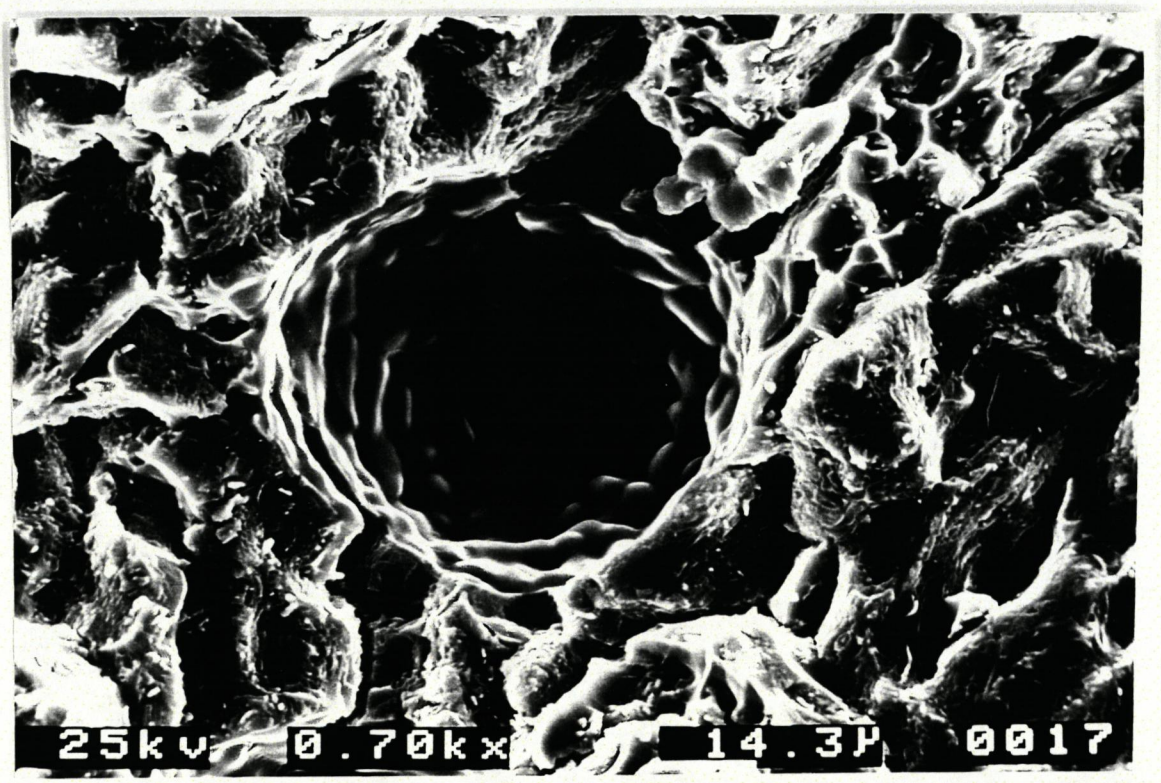

Figure 4.30b A closer view of the fracture surface in Figure 4.31a shows that the circular defects are pores. A secondary crack, crossing the pore from top left to bottom right, is visible.

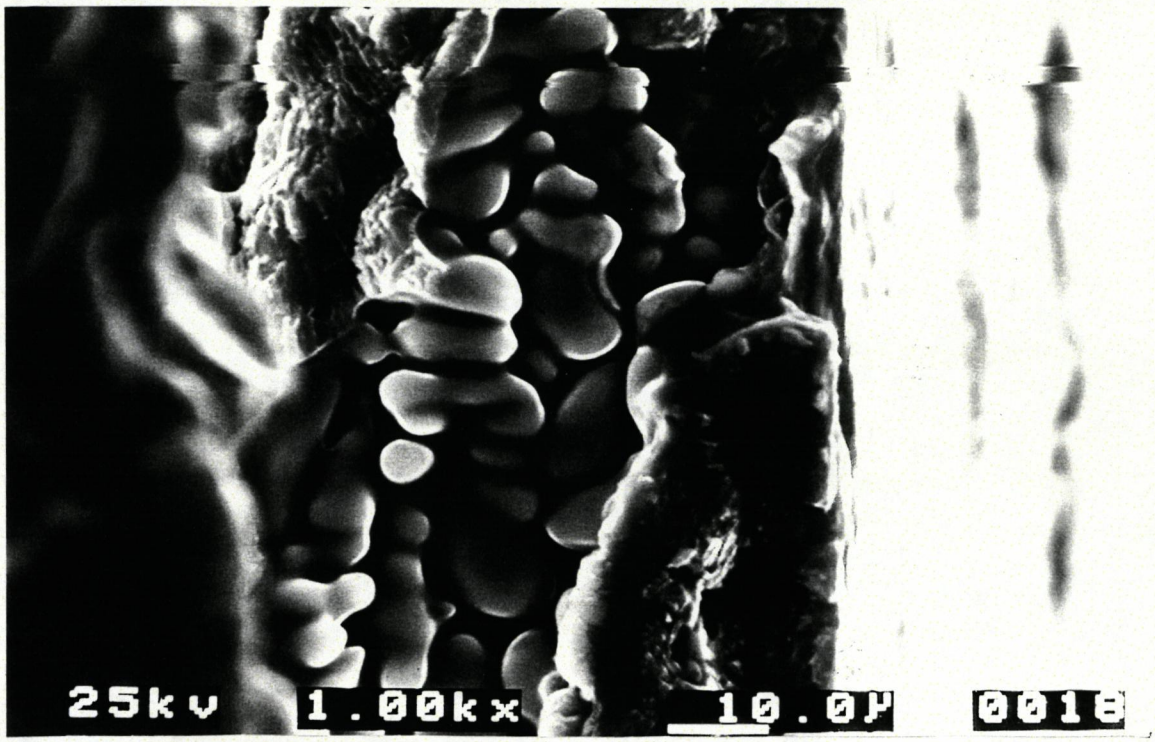

Figure 4.31 An example of defects in correspondence of the plate joint line in the transverse skimmed plasma welded joints ($\Delta\sigma = 313$ MPa). The defects, next to the specimen surface, were represented by cavities containing a complex structure.

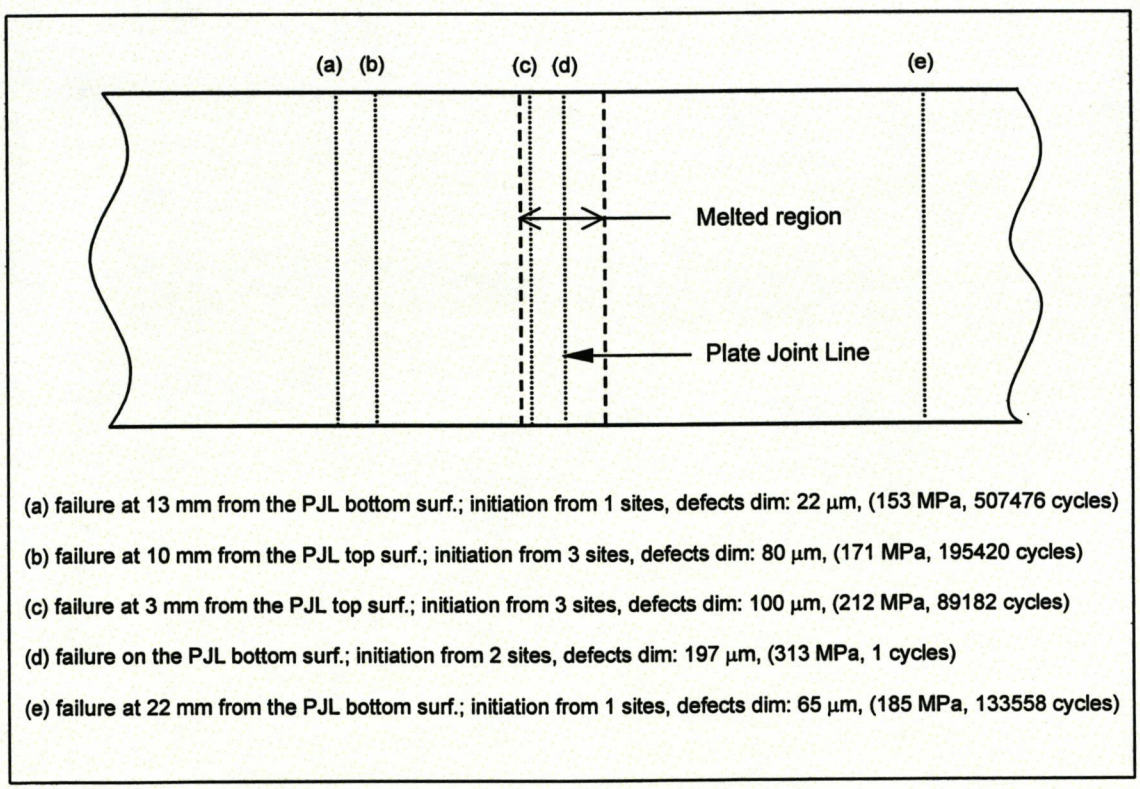

Figure 4.32 Locations of the fatigue initiation sites on the transverse skimmed plasma joints.

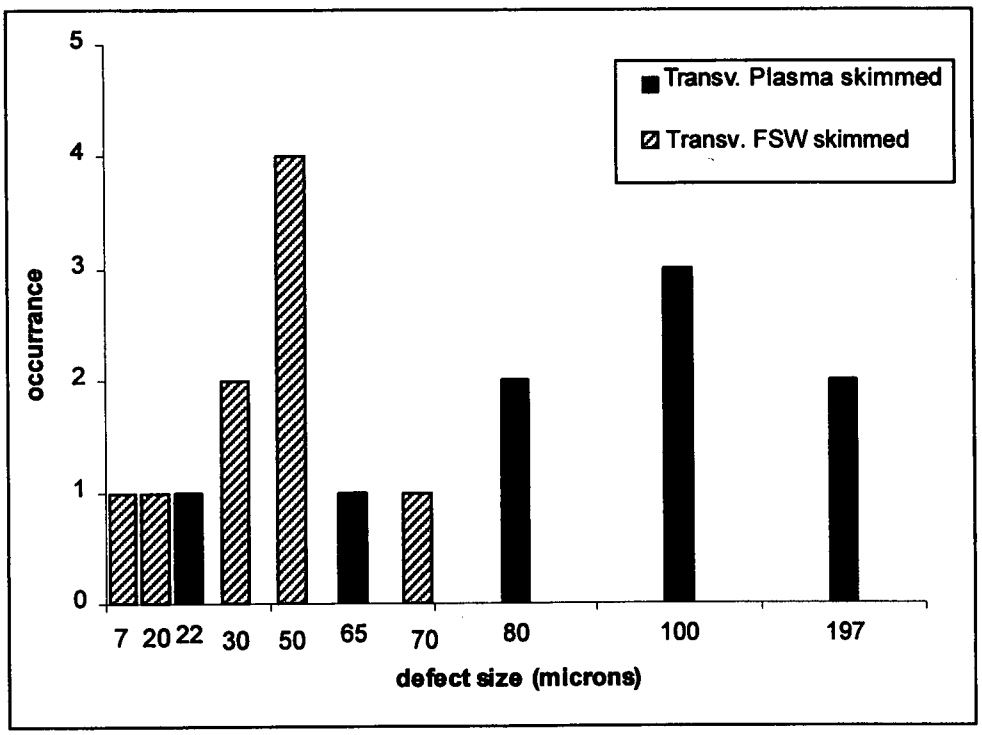

Figure 4.33 Defect size and distribution in the transverse skimmed FSW and plasma joints.

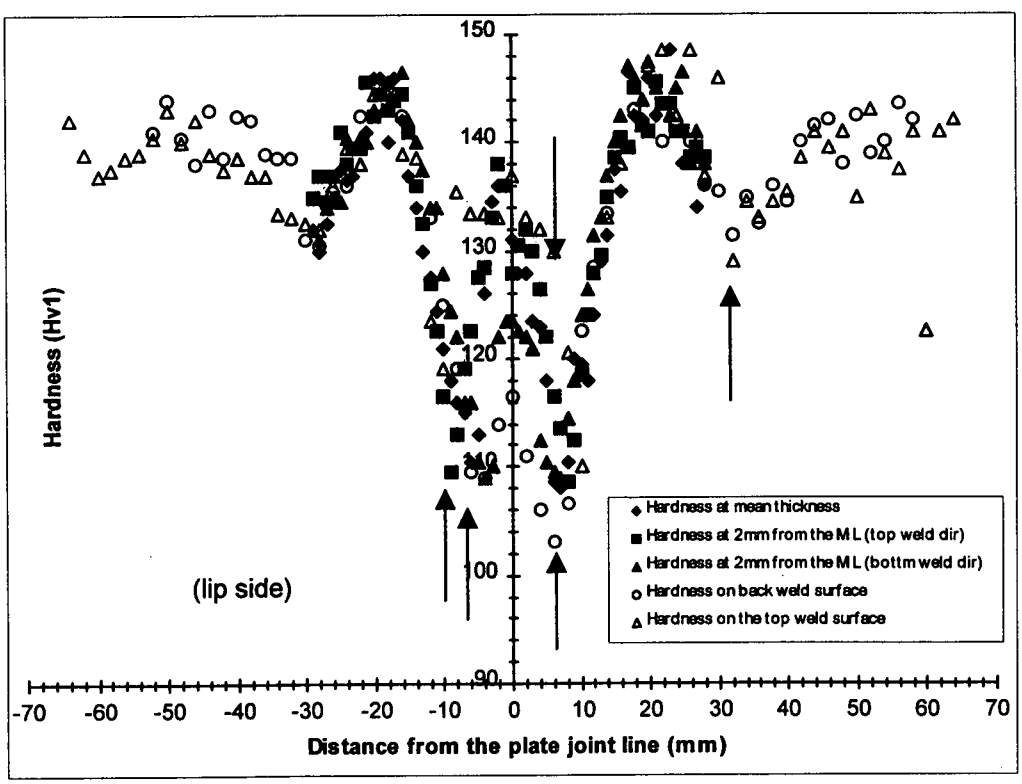

Figure 4.34 Positions of fatigue initiation sites (indicated by the arrows) are correlated with the hardness distribution in the transverse skimmed FSW joints.

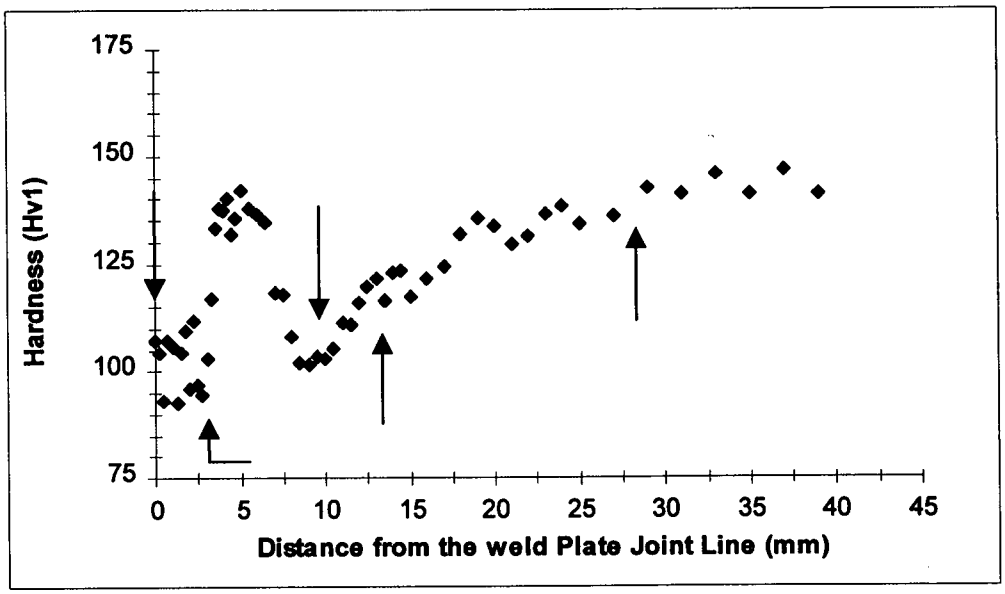

Figure 4.35 Positions of fatigue initiation sites (indicated by the arrows) are correlated with the hardness distribution in the transverse skimmed plasma welded joints.

4.3 Fatigue crack propagation

4.3.1 Parent plate Al 2024-T351

Figure 4.36 shows plots of crack growth rate versus stress intensity factor range observed for the parent plate in the LT and TL directions. The results are presented together with the crack propagation data published in ESDU 81031 for the same parent material (LT) and same stress ratio R = 0.1. The experimental results obtained in the tests were in good agreement with the EDSU 81031 data. The crack propagation tests carried out on the CT and SCT specimens in the LT and TL plate orientations showed similar behaviour. The differences in the near-threshold regime were less than 4% of the greatest of the values.

4.3.2 Propagation of cracks orthogonal to the weld

Figures 4.37a and 4.37b show the results of the crack propagation tests carried out on the SCT welded and parent plate (LT) specimens. Table 4.6 shows the stress intensity factor ranges measured for a crack growth rate of $5 \cdot 10^{-10}$ m/cycle. This "near-threshold" stress intensity factor (ΔK_{NT}) represents a good approximation of the threshold stress intensity factor range measured at da/dn = 10^{-11} m/cycle. The initial orientation of the cracks was 90° with respect to the weld direction. Two specimens were tested for each configuration in order to gain more information regarding the variation of the properties and the repeatability of the results. No more than two specimens per configuration could be tested because of the limitations in specimen availability. Differences in near-threshold stress intensity factor values (ΔK_{NT}) between the two repeated tests were 3, 7 and 9% (respectively for cracks on the plate joint line, at 11 and 25 mm from it) of the lowest of the two observed values.

Cracks that propagated from the surface flaws at 11 mm from the plate joint line (PJL) exhibited the lowest near-threshold stress intensity factor values (Tab. 4.6). At this location, high tensile longitudinal residual stresses were measured on similar specimens, as described in Section 4.1.4. The two plots exhibit a change in slope for $\Delta K \cong 3.3$ MPa $m^{1/2}$ and da/dn $\cong 3 \cdot 10^{-9}$ and $4 \cdot 10^{-9}$ m/cycle. The crack growth continued through the plate thickness, reaching and breaking through the back plate surface at values of ΔK of

7.8 and 8.0 MPa·m$^{1/2}$. Crack growth rates were approximately 10 times higher than in the parent plate. Figure 4.38 shows the positions of the crack front with respect to the microstructural regions of the weld. The thumbnail cracks grew mainly within the weld heat affected region. No change of slope in the crack propagation plots was observed when the cracks entered the thermo-mechanically affected region.

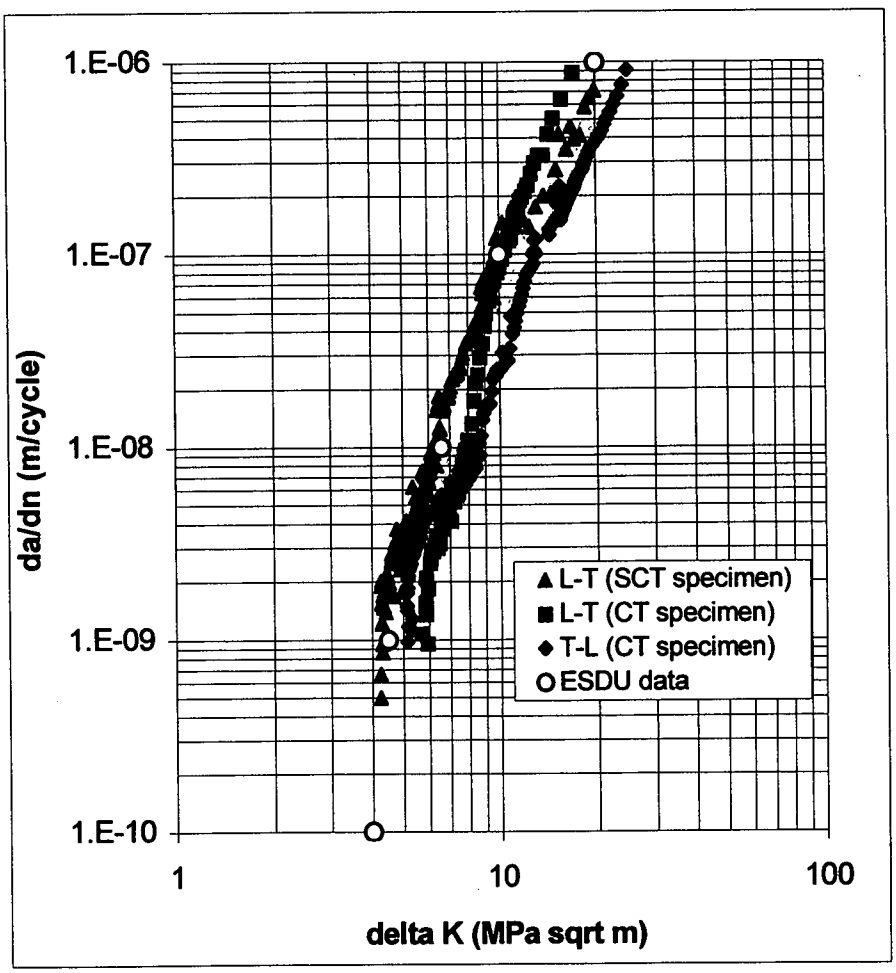

Figure 4.36 The results of the crack growth tests performed on the parent plate in the LT and TL directions.

The cracks that propagated at the plate joint line exhibited slightly higher ΔK_{NT} values (Tab. 4.6) and crack growth rates 4 times lower than those observed for the cracks growing at 11 mm from the PJL. Both of the two curves (Fig. 4.37a) exhibit changes in slope at a value of $\Delta K \cong 3.8$ MPa m$^{1/2}$ and crack growth rate of $1 \cdot 10^{-8}$ m/cycle. At a

value of ΔK of 4.6 MPa $m^{1/2}$ both of the curves show sudden increases in growth rates reaching peaks of $1.1 \cdot 10^{-7}$ m/cycle, at ΔK of 5.2 MPa $m^{1/2}$, and $4.3 \cdot 10^{-8}$ m/cycle at ΔK of 5.7 MPa $m^{1/2}$. Similar drastic changes in slope have been reported in crack propagation studies on aluminium and steel welded joints [24, 42, 110]. The thumbnail cracks reached the entire plate thickness at ΔK values of 8.5 and 8.7 MPa $m^{1/2}$. Figure 4.39 illustrates the crack front positions with respect to the weld microstructure. The cracks grew mainly within the weld nugget.

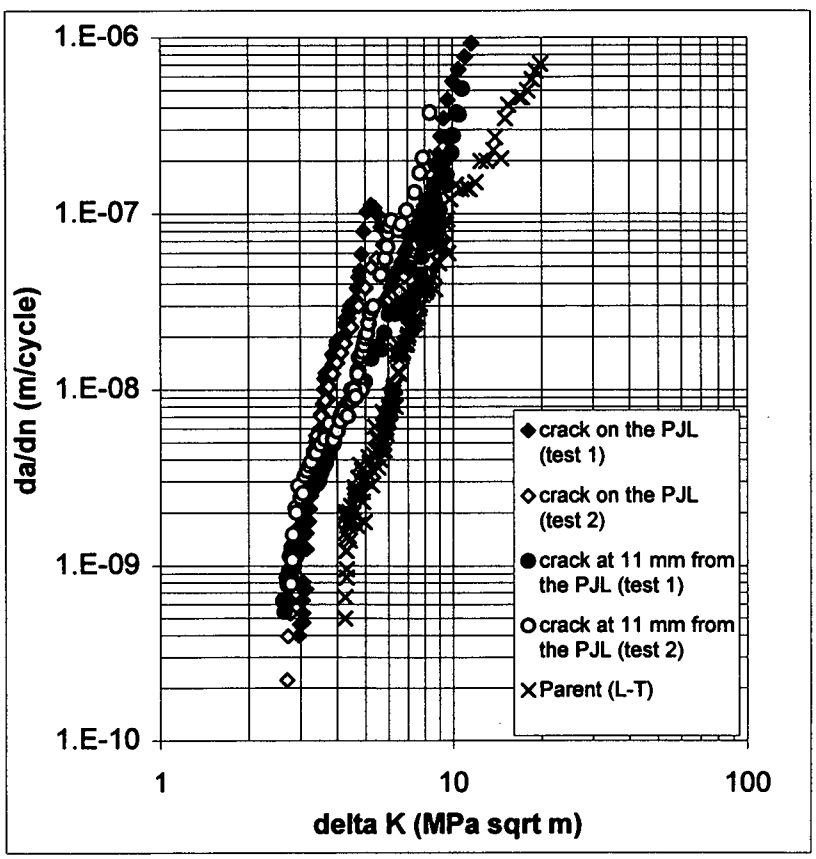

Figure 4.37a Results of the crack propagation test carried out on the SCT specimens (crack orthogonal to the weld propagating on the weld and at 11 mm form the PJL).

The cracks growing at 25 mm from the PJL exhibited the highest ΔK_{NT} values (Tab. 4.6) and the lowest crack growth rates. Crack growth rates were 4 times lower than in the unwelded plate and 15 times lower than in the weld. The crack growth curves of these two specimens exhibit pronounced slope changes at values of ΔK of 5.5 and 5.8

MPa $m^{1/2}$ and for a crack growth rate of $3 \cdot 10^{-9}$ and $4 \cdot 10^{-9}$ m/cycle (Fig. 4.37b). A second change in slope is exhibited at higher stress intensity factor values (9.8 and 9.6 MPa $m^{1/2}$) and crack growth rates between $8 \cdot 10^{-9}$ and $1 \cdot 10^{-8}$ m/cycle. The cracks reached the plate back surface at ΔK values of 14.8 and 15.4 MPa $m^{1/2}$. The cracks grew entirely within the heat affected region of the weld.

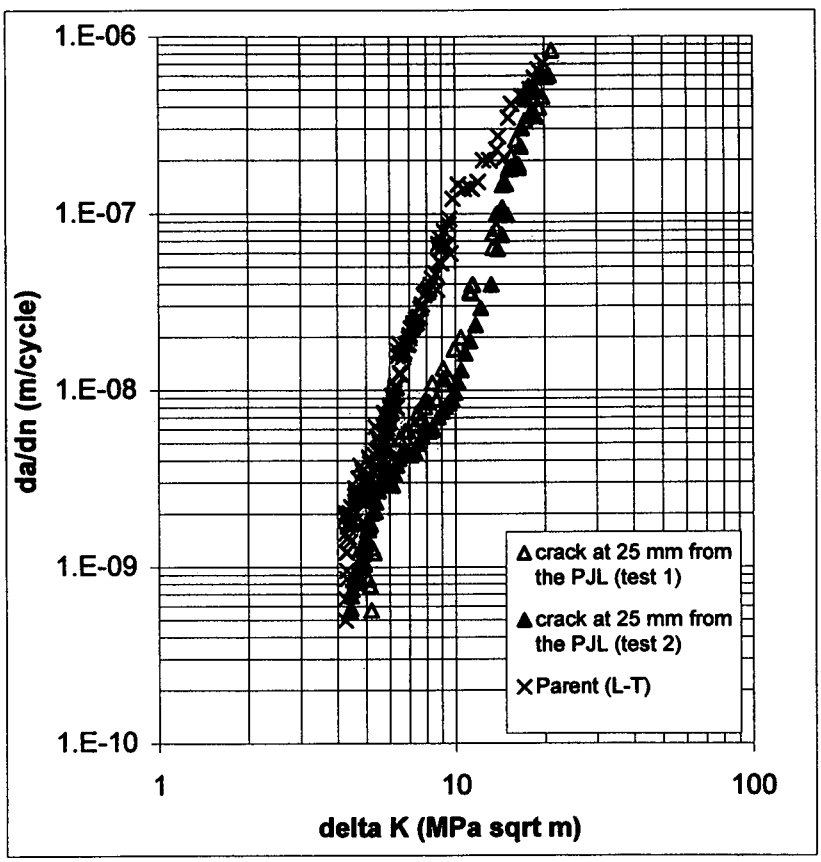

Figure 4.37b Results of the crack propagation test carried out on the SCT specimens (crack orthogonal to the weld at 25 mm form the PJL).

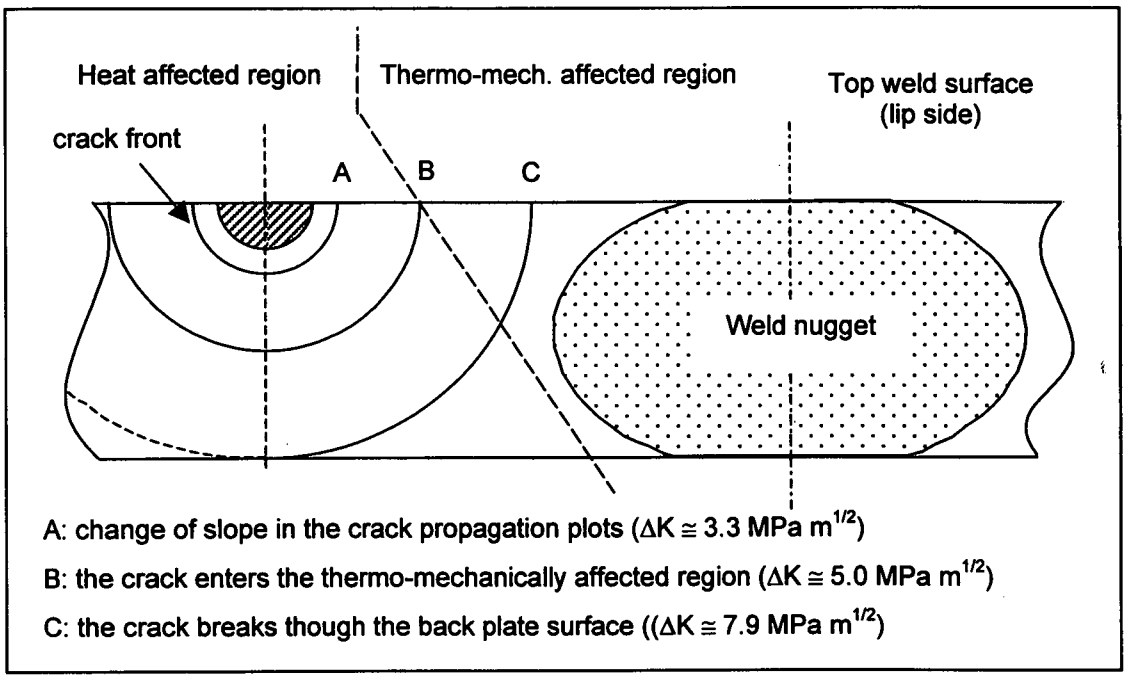

Figure 4.38 Positions of the crack front propagated from the flaw at 11 mm from the PJL (side opposite the lip) with respect to the weld microstructure.

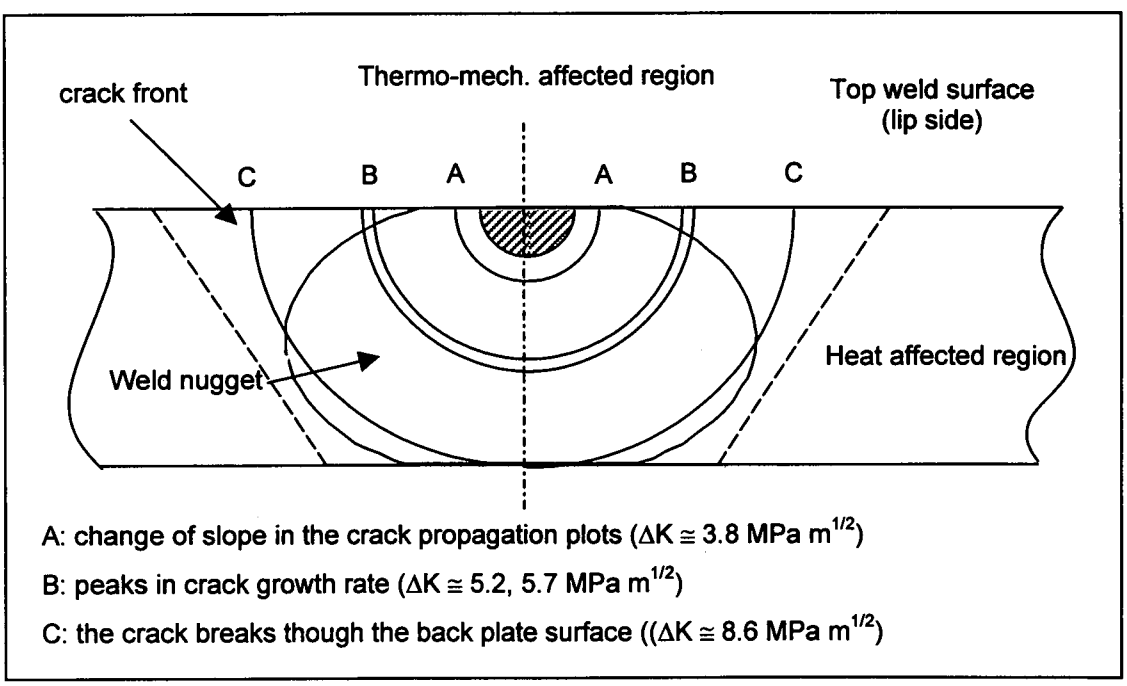

Figure 4.39 Positions of the crack front propagated from the flaw on the PJL with respect to the weld microstructure.

CRACK INIT. POSITION	ΔK_{NT} (*) – test no. 1	ΔK_{NT}(*) – test no. 2
On the plate joint line	2.8 MPa $m^{1/2}$	3.0 MPa $m^{1/2}$
At 11 mm from the plate joint line	2.7 MPa $m^{1/2}$	2.8 MPa $m^{1/2}$
At 25 mm from the plate joint line	4.4 MPa $m^{1/2}$	4.8 MPa $m^{1/2}$

(*) measured at $5 \cdot 10^{-10}$ m/cycle

Table 4.6 Near-threshold stress intensity factor values measured on cracks growing at 90° with respect to the weld direction (SCT specimens).

4.3.3 Propagation of cracks parallel to the weld

Figure 4.40 shows the results of the crack propagation tests carried out on the CT welded and parent (TL) specimens. Table 4.7 shows the near-threshold stress intensity factors measured for a crack growth rate of $5 \cdot 10^{-10}$ m/cycle. The cracks were initially oriented parallel to the weld direction. As for the SCT specimens, two specimens were tested for each configuration in order to gain more information regarding the variation of the properties and the repeatability of the results. Larger differences than those observed in the SCT specimens were measured between the two repeated tests. The stress intensity factor values at $5 \cdot 10^{-10}$ m/cycle of the repeated tests differed by 50, 44 and 3%, respectively for the cracks on the weld, at 6 and 28 mm from the PJL.

The lowest ΔK_{NT} values were exhibited by the cracks propagating at 28 mm from the plate joint line. These were approximately 2-3 times lower than those observed on the weld (Tab. 4.7). Crack propagation rates were generally higher than in the other cases. Residual stress measurements performed on a nominally identical CT specimen revealed the presence of moderate compressive residual stresses in the near crack tip area at the beginning of the test (Tab. 4.8). The two crack growth plots exhibit a change of slope for $\Delta K \cong 3.3$ MPa $m^{1/2}$ and growth rates of $2.4 \cdot 10^{-9}$ m/cycle. A second change of slope is observed in the two specimens at stress intensity factor values of 6.1 and 6.3 MPa $m^{1/2}$, and crack growth rates of $7.2 \cdot 10^{-9}$ and $1.1 \cdot 10^{-8}$ m/cycle. For higher crack growth rates, the crack growth plots show minor changes.

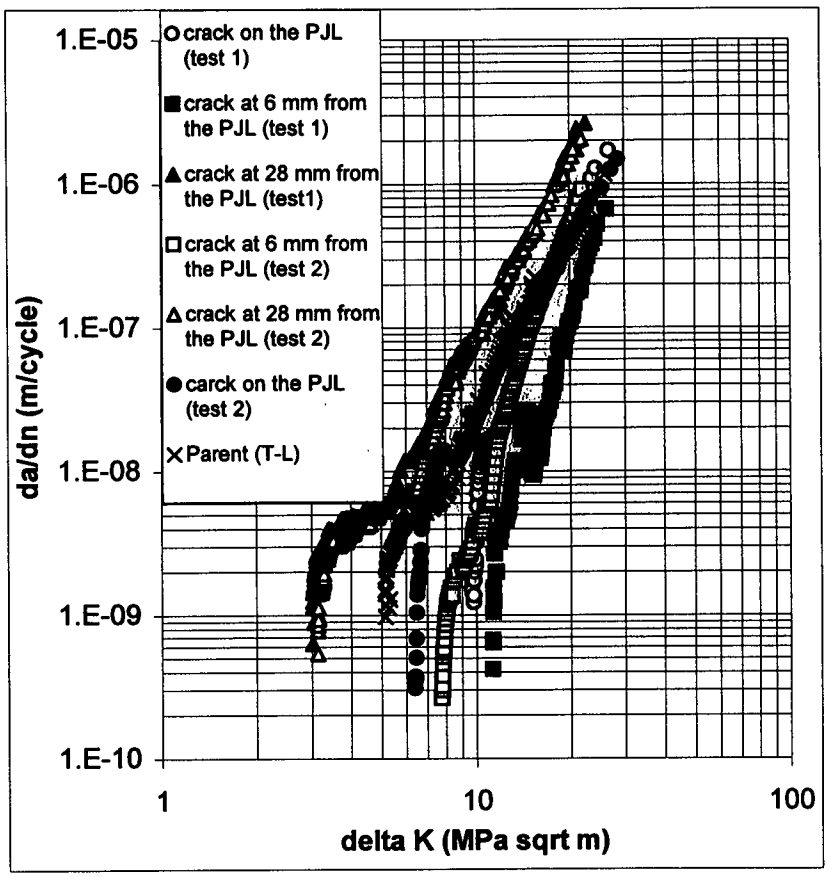

Figure 4.40 Results of the crack propagation tests carried out on the CT specimens (cracks parallel to the weld).

The CT specimens with cracks located on the plate joint line showed the largest difference between the measured ΔK_{NT} values (Tab. 4.7). Crack growth rates were 10 times lower than in the unwelded plate. At this location, the crack propagation plots exhibit change in slope at ΔK values of 6.9 and 9.7 MPa $m^{1/2}$, and $5.7 \cdot 10^{-9}$ and $4.4 \cdot 10^{-9}$ m/cycle. Both of the curves show sudden increases in growth rates. Maxima are reached at ΔK values of 8.0 MPa $m^{1/2}$ and at $1.4 \cdot 10^{-8}$ m/cycle, and 10.6 MPa $m^{1/2}$ and $1.6 \cdot 10^{-8}$ m/cycle.

The highest ΔK_{NT} values, up to 2 times higher than in the unwelded plate, were observed in the two specimens with the initial flaws located at 6 mm from the plate joint line (Tab. 4.7). At this location, crack propagation rates were approximately 15 times

lower than in the unwelded plate. The plots show change in slope for ΔK values of 8.3 (11.3) MPa $m^{1/2}$ and $1.4 \cdot 10^{-8}$ ($1.5 \cdot 10^{-8}$) m/cycle. Minor changes in slope are exhibited by the plots at higher stress intensity factor values. All the plots tend to converge at higher ΔK values in the region between 20 and 25 MPa $m^{1/2}$ at 10^{-6} m/cycle.

NOTCH POSITION	ΔK_{NT} (*) – test no. 1	ΔK_{NT} (*) – test no. 2
On the plate joint line	6.4 MPa $m^{1/2}$	9.6 MPa $m^{1/2}$
At 6 mm from the plate joint line	7.8 MPa $m^{1/2}$	11.2 MPa $m^{1/2}$
At 28 mm from the plate joint line	3.0 MPa $m^{1/2}$	3.1 MPa $m^{1/2}$

(*) measured at $5 \cdot 10^{-10}$ m/cycle

Table 4.7 Near-threshold stress intensity factor values measured in cracks growing parallel to the weld direction (CT specimens).

4.3.4 Effect of residual stress relief on crack propagation

In order to investigate the effect of residual stress on the observed crack growth behaviour, mechanical stress relief was performed by plastic deformation of the welded joints. The relief effect on the weld residual stress by plastic deformation is described in Section 2.8. SCT specimens were machined out from welded plates, as described in Section 3.7, and deformed achieving 2% of permanent deformation. Stretching was carried out before spark machining the surface defects. The SCT specimens were stretched using an Instron 8500 digitally controlled test machine of 250 kN load capacity. Displacements were monitored using a class 0.5 Instron 50 mm gauge length extensometer (±0.5% accuracy, 0.25% resolution) positioned at the midpoint of the specimen gauge length. The specimens were loaded up to a maximum load P_{max} of 155 kN to obtain a permanent plastic deformation of 2%. Figure 4.41 shows the method used to estimate P_{max}. P_{max} was estimated using the load-strain curve of the specimens and assuming a linear elastic unloading behaviour. Measurements of the achieved permanent deformations showed that in all the specimens the values were between 2.0 and 2.1% of the reference length of 50 mm.

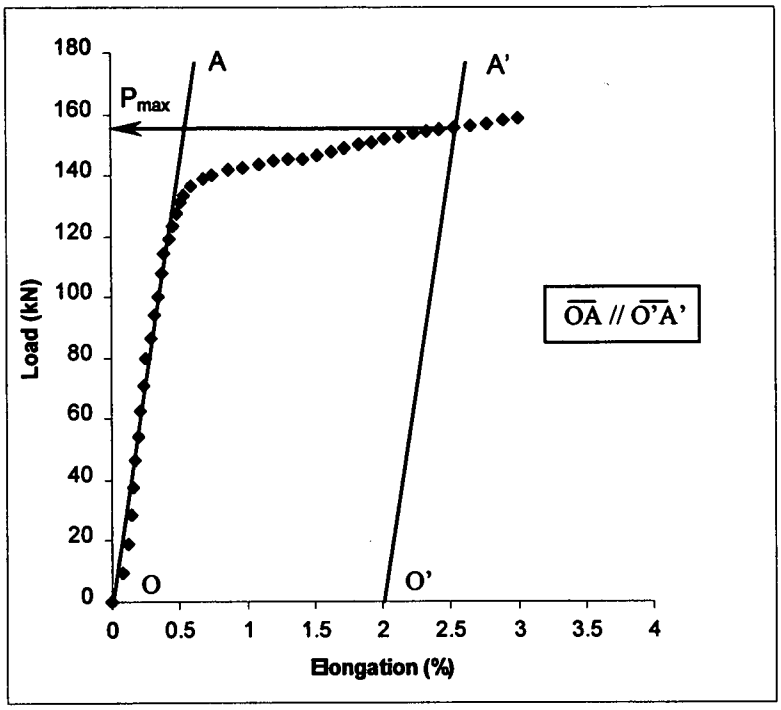

Figure 4.41 The procedure used to obtain 2% permanent deformation in the SCT specimens.

Three strips, with same width of the CT specimens (88 mm), were cut off from each welded plate in the direction orthogonal to the weld. The strips were stretched in the direction orthogonal to the weld up to a maximum load P_{max} of 90 kN chosen with the same procedure as that for the SCT specimens. Displacements were monitored using a class 0.5 Instron extensometer positioned with its midpoint on the PJL. The gauge length of 40 mm was used in order to be able to accommodate the extensometer between the grips during the test. The achieved permanent deformations in the stretched strips were between 2.0 and 2.1% of the reference length of 40 mm. One CT specimen was machined from each stretched strip according the specified distance from the weld. Figure 4.42a shows the typical microstructure, at 6 mm from the PJL on the side opposite the lip, of a transverse FSW joint which has been 2% plastically deformed. As Figure 4.16 suggests, this region of the joint is characterised by the maximum deformations introduced by stretching. Figure 4.42b shows the result of the hardness test carried out on the same joint with the same procedure described in Section 3.4. A comparison of Figure 4.42a and Figure 4.42b with Figure 4.8a and Figure 4.13,

respectively, indicates that no appreciable modifications in microstructure and hardness have been introduced by stretching.

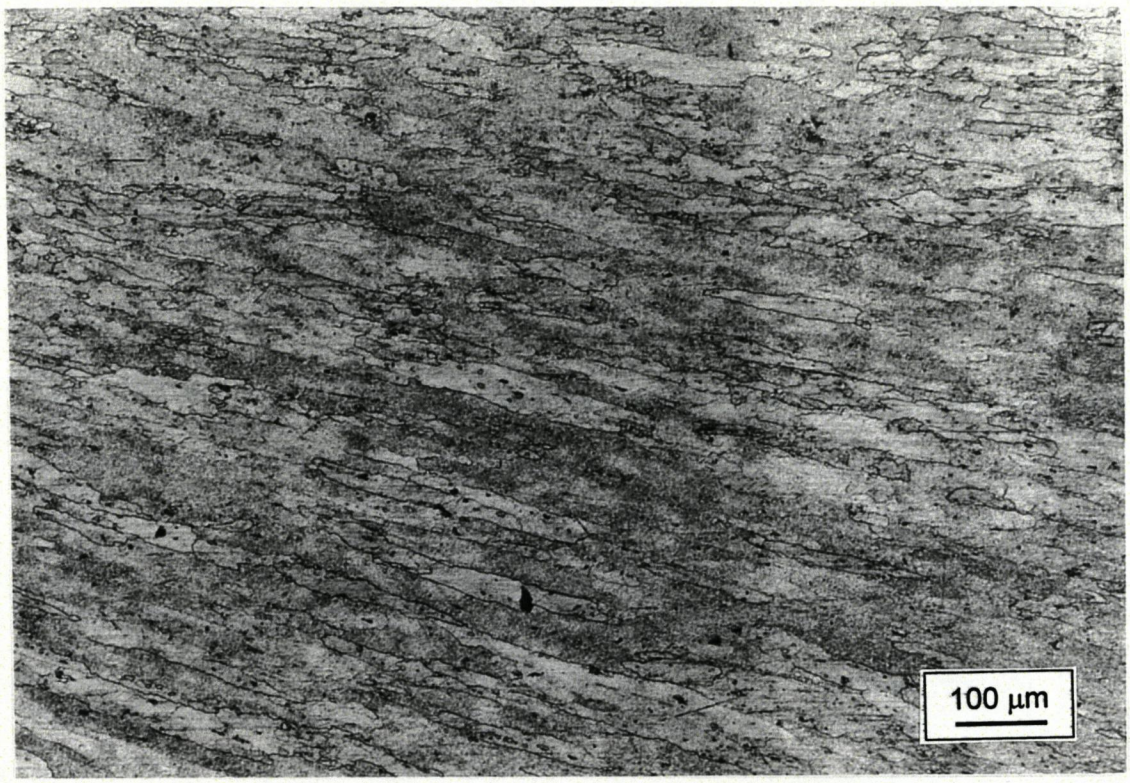

Figure 4.42a Typical microstructure of the thermo-mechanically affected region (at 6 mm from the PJL on a plane normal to the weld) in a 2% plastically deformed FSW skimmed joint. This region is characterised by maximum deformation values introduced by stretching.

Residual stresses were measured on the SCT and CT plastically deformed specimens in order to evaluate the effect of the mechanical stress relief. In the SCT specimen, the residual stress measurement was carried out 11 mm from the plate joint line on the side of the weld opposite the lip. The CT specimens had the notch at 6 mm from the plate joint line (Fig. 3.11). It was recognised that residual stresses in the CT specimens would have been likely to be affected by the pre-cracking sequence. For this reason, residual stresses were measured on the stretched CT specimen, after the pre-cracking sequence, 0.5 mm ahead of the crack tip. Residual stress measurements were repeated on a similar undeformed CT specimen. Table 4.8 shows the results of the residual stress measurements and a comparison with the residual stress values measured in the undeformed specimens at similar locations.

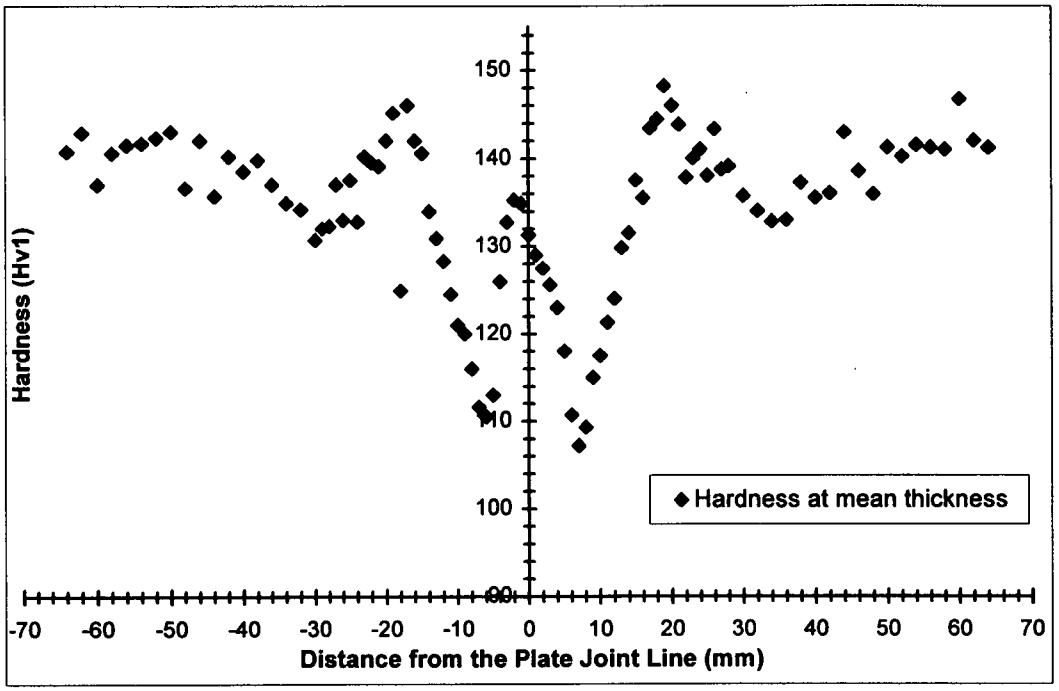

Figure 4.42b Typical mid-thickness hardness profile measured in a 2% plastically deformed FSW joint (skimmed).

The results in Table 4.8 indicate that, for SCT specimens, the longitudinal and transverse residual stresses are reduced by stretching. Large differences between the measurements carried out on two nominally similar SCT specimens can be noticed. The measured longitudinal residual stress exhibit a standard deviation values up to 141 MPa. For the CT specimens, stretching produced an increase in residual stress parallel to the weld and a decrease of the residual stress orthogonal to the weld. The latter variation was close to the experimental error of the residual stress measurement method. The mechanically stress-relieved specimens were tested in crack propagation. Figure 4.43 shows the test results for cracks orthogonal to the weld (SCT specimens).

It can be noticed that in all cases, with the initial flaw on the plate joint line, at 11 mm and at 25 mm, the crack growth rates exhibited similar crack growth rates. Crack growth rates at 11 mm and at 25 mm from the PJL decreased whereas crack growth rates on the weld increased to approach the growth rates of the unwelded plate (LT). Table 4.9 reports the near-threshold ΔK values measured at $5 \cdot 10^{-10}$ m/cycle in the three cases.

SPECIMEN CONFIG.	SPECIMEN #1 (undeformed)	SPECIMEN #2 (undeformed)	AFTER 2% DEFORMATION	$\frac{\sigma \text{ (def.)}}{\sigma \text{ (undef.)}}$
SCT (11mm from the PJL)	σ_{long} = 264 MPa	σ_{long} = 65 MPa	σ_{long} = 28 MPa	0.1 – 0.4
	σ_{transv} = 5 MPa	σ_{transv} = -21 MPa	σ_{transv} = 3 MPa	0.6 – -0.1
CT (28mm from the PJL)	σ_{long} = 6 MPa	—	σ_{long} = 33 MPa	55
	σ_{transv} = -15MPa	—	σ_{transv} = 0 MPa	0

Table 4.8 Results of the residual stress measurements on the plastically deformed specimens and a comparison with the residual stress values measured in the undeformed specimens at similar locations.

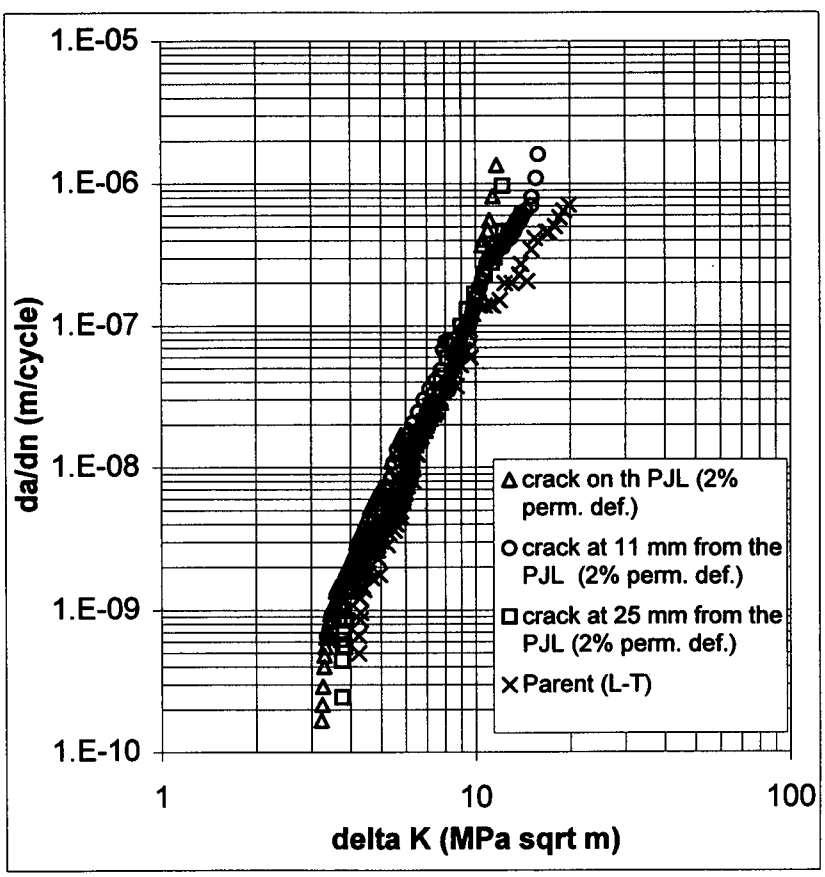

Figure 4.43 Results of the crack propagation test carried out on the 2% plastically deformed SCT specimens (crack orthogonal to the weld).

From Table 4.9, the ΔK_{NT} values observed in the stretched specimen were all between 3.4 and 3.8 MPa $m^{1/2}$ whereas for the unstretched specimens they varied between 2.7 and 4.8 MPa $m^{1/2}$. Larger variations (20%) in the ΔK_{NT} values were exhibited by the cracks at 11 mm and at 25 mm. The cracks in the stretched specimens exhibited near-threshold ΔK values generally close to the parent plate (LT) value (4.2 MPa $m^{1/2}$), Figure 4.43. The lowest ΔK_{NT} value among the stretched specimens was exhibited by the crack on the plate joint line (3.4 MPa $m^{1/2}$). The crack propagation plots of the cracks in the stretched specimens show a change in slope between 3.5 and 3.8 MPa $m^{1/2}$, and a crack growth rate of $5 \cdot 10^{-10}$ m/cycle.

CRACK INIT. POSITION	ΔK_{NT} (*) (2% pl. deform.)	ΔK_{NT} (*) (undeformed)	$\frac{\Delta K_{NT} \text{ (def.)}}{\Delta K_{NT} \text{ (undef.)}}$
On the plate joint line	3.4 MPa $m^{1/2}$	2.8 – 3.0 MPa $m^{1/2}$	1.2 – 1.1
At 11 mm from the plate joint line	3.6 MPa $m^{1/2}$	2.7 – 2.8 MPa $m^{1/2}$	1.3
At 25 mm from the plate joint line	3.8 MPa $m^{1/2}$	4.4 – 4.8 MPa $m^{1/2}$	0.9 – 0.8

(*) measured at $5 \cdot 10^{-10}$ m/cycle

Table 4.9 The near-threshold ΔK values measured in the 2% plastically deformed SCT specimens.

Figure 4.44 shows the results of the tests carried out on the stretched specimens with cracks parallel to the weld (CT specimens). As observed for the stretched SCT specimens, cracks on the weld and at 6 mm from the PJL exhibited similar crack growth rates. At these two locations crack growth rates increased to approach those in the unwelded plate (TL). Table 4.10 shows the ΔK_{NT} values measured for a crack growth rate of $5 \cdot 10^{-10}$ m/cycle. The cracks growing on the plate joint line and at 6 mm from it exhibited similar ΔK_{NT} values, between 6.0 and 6.4 MPa $m^{1/2}$. An exception to this general behaviour was exhibited by the cracks in the specimen with the notch at 28 mm from the PJL. In this case, stretching did not modify the crack propagation behaviour with respect to those observed in the corresponding unstretched specimens (Fig. 4.40).

Only for ΔK values greater than 7 MPa $m^{1/2}$ the crack propagation curve of the crack at 28 mm from the PJL approached the crack growth rates exhibited by the other stretched specimens.

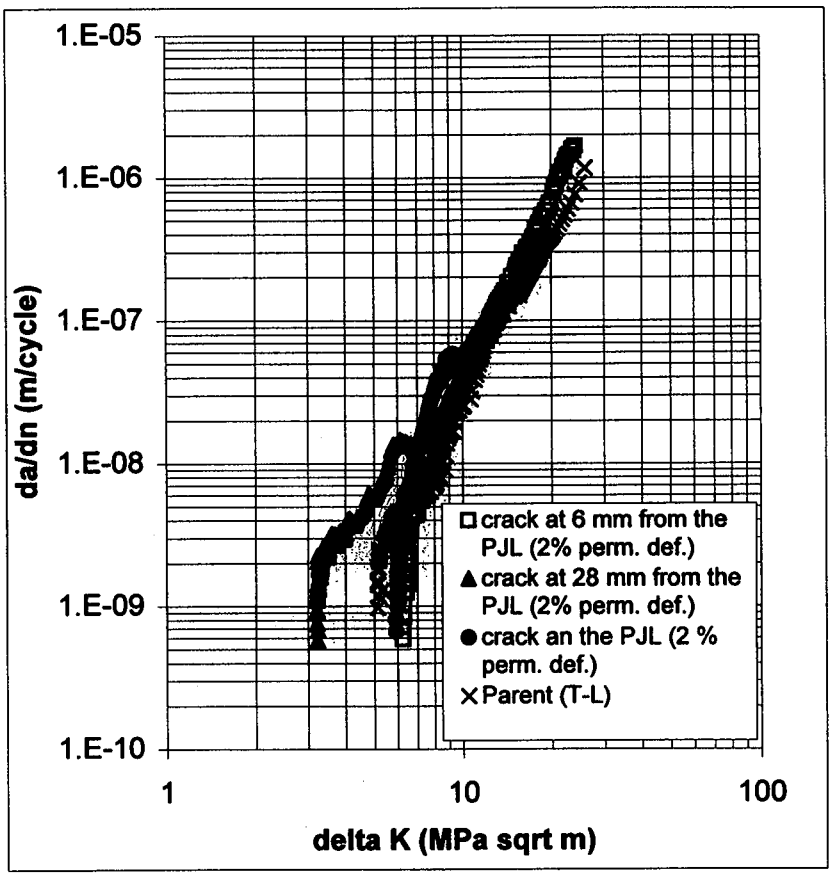

Figure 4.44 Results of the crack propagation test carried out on the 2% plastically deformed CT specimens (crack parallel to the weld).

4.3.5 SEM examination of cracks orthogonal to the weld

Figure 4.45 shows the locations at which the pictures were taken. Figure 4.46 shows the typical appearance of the fracture surface in the region next to the semicircular flaw exhibited by the cracks at 25 mm from the PJL (unstretched SCT specimens). The picture was taken on the crack growth region corresponding to the beginning of the test ($\Delta K \cong 4.9$ MPa $m^{1/2}$, $da/dn \cong 9.9 \cdot 10^{-10}$ m/cycle). Large smeared areas of material can be

noticed in proximity to ridges on the fracture surfaces. Metal debris was observed on the same region.

Figure 4.47 shows typical features observed on the fracture surface of the cracks at 25 mm from the PJL in the stretched SCT specimens. The picture was taken on the crack growth region corresponding to the beginning of the test ($\Delta K \cong 3.7$ MPa $m^{1/2}$, $da/dn \cong 8.5 \cdot 10^{-10}$ m/cycle). Figure 4.45 shows the location at which the picture was taken. Crack propagation occurred in the preferential direction of the crystallographic planes, similarly to that observed in the unstretched specimens. There was no evidence of smearing. However, local surface damage was observed, as indicated in the picture (Fig. 4.47). Fracture surfaces were characterised by parallel ridges at 3-5 μm of interval. Changes in plane orientation of the ridges could indicate grain boundaries (Section 4.1.2).

NOTCH POSITION	ΔK_{NT} (*) (2% pl. deform.)	ΔK_{NT} (*) (undeformed)	$\Delta K_{def.} / \Delta K_{undef.}$
On the plate joint line	6.0 MPa $m^{1/2}$	6.4 – 9.6 MPa $m^{1/2}$	0.95 – 0.60
At 6 mm from the plate joint line	6.4 MPa $m^{1/2}$	7.8 – 11.2 MPa $m^{1/2}$	0.80 – 0.60
At 28 mm from the plate joint line	3.2 MPa $m^{1/2}$	3.0 – 3.1 MPa $m^{1/2}$	1.05 – 1.0

(*) measured at $5 \cdot 10^{-10}$ m/cycle

Table 4.10 The near-threshold ΔK values measured in the 2% plastically deformed CT specimens.

Figure 4.48 shows typical appearance of the fracture surface at 11 mm from the PJL (unstretched SCT specimens). This picture was taken on the crack growth region corresponding to the beginning of the test ($\Delta K \cong 2.6$ MPa $m^{1/2}$, $da/dn \cong 6.3 \cdot 10^{-10}$ m/cycle). Figure 4.45 shows the location of the picture with respect to the weld. Crystallographically oriented fatigue fracture was observed. No evidence of smeared areas was found. Fragmentation caused by local crack branching was observed.

Figure 4.49 shows the fracture surfaces of the cracks at 11 mm from the PJL in the stretched SCT specimen. The picture was taken on the crack growth region corresponding to the beginning of the test ($\Delta K \cong 4.1$ MPa $m^{1/2}$, $da/dn \cong 1.7 \cdot 10^{-9}$ m/cycle). Figure 4.45 represents the location of the picture. The crack surface was quite similar to that observed on the unstretched specimens. Crack propagation took place still according to the crystallographic plane orientation. No evidence of surface damage was observed. Fragmentation caused by secondary cracks appeared to be more frequent than in the unstretched specimens.

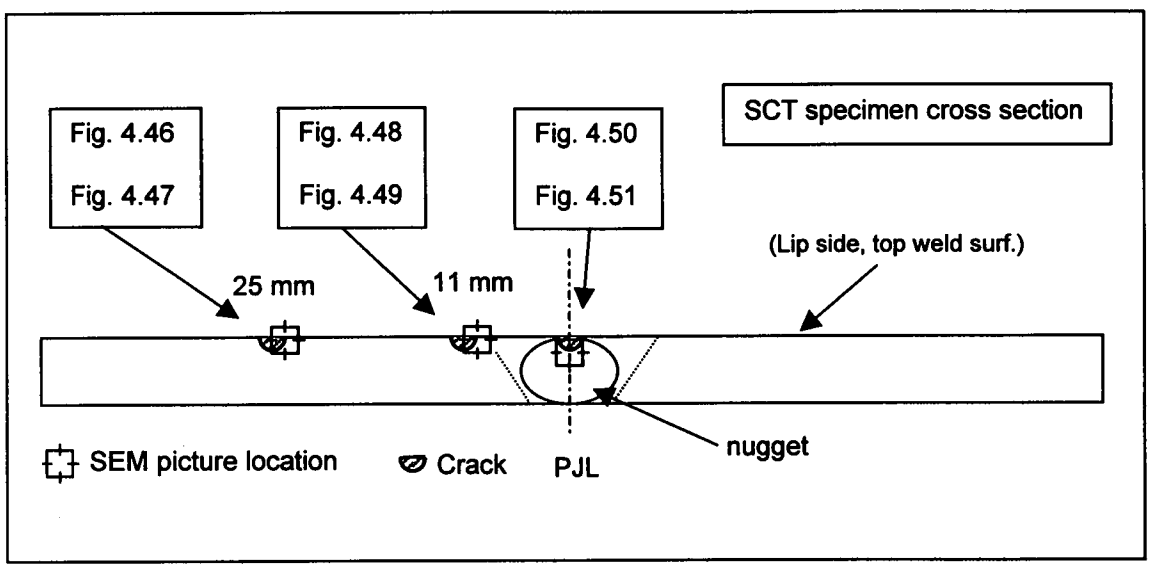

Figure 4.45 Schematic representation of the areas shown in the SEM pictures of the SCT specimens fracture surfaces.

Figure 4.50 shows the typical appearance of the fracture surfaces of the cracks in the centre of the weld (unstretched SCT specimens). This picture was taken on the crack growth region corresponding to the beginning of the test ($\Delta K \cong 2.7$ MPa $m^{1/2}$, $da/dn \cong 7.8 \cdot 10^{-11}$ m/cycle). Figure 4.45 shows the location of the picture. The crack propagated from the semicircular flaw thorough the 5-10 μm grains of the nugget (Section 4.1.2). The fracture surfaces were faceted on a much smaller scale. The crack planes followed the crystallographic orientation within the grains, as occurred during the near-threshold crack propagation in the other specimens. Local branching was observed.

Figure 4.51 shows the typical features of the fracture surface of the cracks in the centre of the weld of the stretched SCT specimen. The picture was taken on the crack growth region corresponding to the beginning of the test ($\Delta K \cong 3.2$ MPa $m^{1/2}$, $da/dn \cong 1.7 \cdot 10^{-10}$ m/cycle). Figure 4.45 shows the location of the picture. The fracture surface was faceted, although slip planes and grain boundaries were less well defined then in the unstretched specimens.

4.3.6 SEM examination of cracks parallel to the weld

Figure 4.52 shows a SEM picture of the typical fracture surface of the cracks 6 mm from the PJL (unstretched CT specimens). The picture was taken on the crack growth region at the beginning of the test ($\Delta K \cong 11.2$ MPa $m^{1/2}$, $da/dn \cong 4.2 \cdot 10^{-10}$ m/cycle). The fracture surfaces were characterised by series of ridges running parallel at 10-20 μm of distance. This characteristic was produced by the tendency of the fatigue cracks to grow following the crystallographic plane orientations within the individual grains (slip plane cracking). Grain boundaries running parallel to the direction of propagation and at 60 μm from each other, were evidenced by changes in the slip plane sequence (Fig. 4.52). These appeared elongated as the metallographic analysis showed in Section 4.1.2. Debris and smeared surfaces were frequently observed. The smearing was typically located at ridges on the fracture surface.

Figure 4.53 shows a SEM picture of the typical fracture surface of the cracks at 6 mm from the PJL in the stretched CT specimen. The picture was taken on the crack growth region corresponding to the beginning of the test ($\Delta K \cong 6.4$ MPa $m^{1/2}$, $da/dn \cong 3.0 \cdot 10^{-9}$ m/cycle). The fracture surface was smoother than the one observed in the unstretched specimens. Smeared areas and debris were observed on the crack surface. However, their presence was less frequent than in the fracture surfaces of the unstretched specimens.

Figure 4.54 shows the typical fracture surface of cracks in the centre of the weld (unstretched CT specimens). The picture was taken on the crack growth region corresponding to the beginning of the test ($\Delta K \cong 9.7$ MPa $m^{1/2}$, $da/dn \cong 2.6 \cdot 10^{-9}$ m/cycle). and at the mid-thickness line of the specimens. The crack grew thorough the

very fine grain region of the nugget (Section 4.1.2). The fracture surfaces were faceted. The crack paths followed the slip planes within the 5-10 μm grains (Section 4.1.2). This behaviour was similar to the case observed in the specimen with the crack 6 mm from the weld (Fig. 4.52). The picture shows the presence of isolated smeared areas associated with the presence of debris. The crack slip planes appeared to be crushed and plastically deformed. Figure 4.55 shows a macrograph of the specimens fracture surfaces. A pronounced deviation of the crack front characterised the propagation in the initial part of the tests (Fig. 4.55).

Figure 4.56 shows a picture of the fracture surface of the crack in the centre of the weld of the stretched CT specimen. The picture was taken on the crack growth region corresponding to the beginning of the test ($\Delta K \cong 6.0$ MPa $m^{1/2}$, $da/dn \cong 2.2 \cdot 10^{-9}$ m/cycle). The fracture surface appeared faceted, as in the unstretched specimens, but with more randomly orientated crack planes. No evident presence of debris or local crushing was observed on the crack surfaces. No evidence of crack front deviation was observed in the tested specimen, as shown in Figure 4.55.

Figure 4.57 shows a SEM picture of the fracture surface of the cracks at 28 mm from the PJL (unstretched CT specimens). The picture was taken on the crack growth region corresponding to the beginning of the test ($\Delta K \cong 3.1$ MPa $m^{1/2}$, $da/dn \cong 6.6 \cdot 10^{-10}$ m/cycle). This is a region characterised by large grains 40-60 μm wide, (Section 4.1.2). Grain boundaries have been indicated in the pictures for clarity. River patterns, cleavage-like faceted fracture surface and slip plane cracking at intervals of 5-8 μm were observed. No evidence of smeared areas or debris was observed.

Figure 4.58 shows a picture of the typical fracture surface of the crack at 28 mm from the PJL in the 2% stretched CT specimen. The picture was taken on the crack growth region corresponding to the beginning of the test ($\Delta K \cong 3.2$ MPa $m^{1/2}$, $da/dn \cong 5 \cdot 10^{-10}$ m/cycle). The fracture surfaces were quite similar to those of the unstretched specimens (Fig. 4.28). Slip plane cracking was frequently observed. Secondary cracking occurred too.

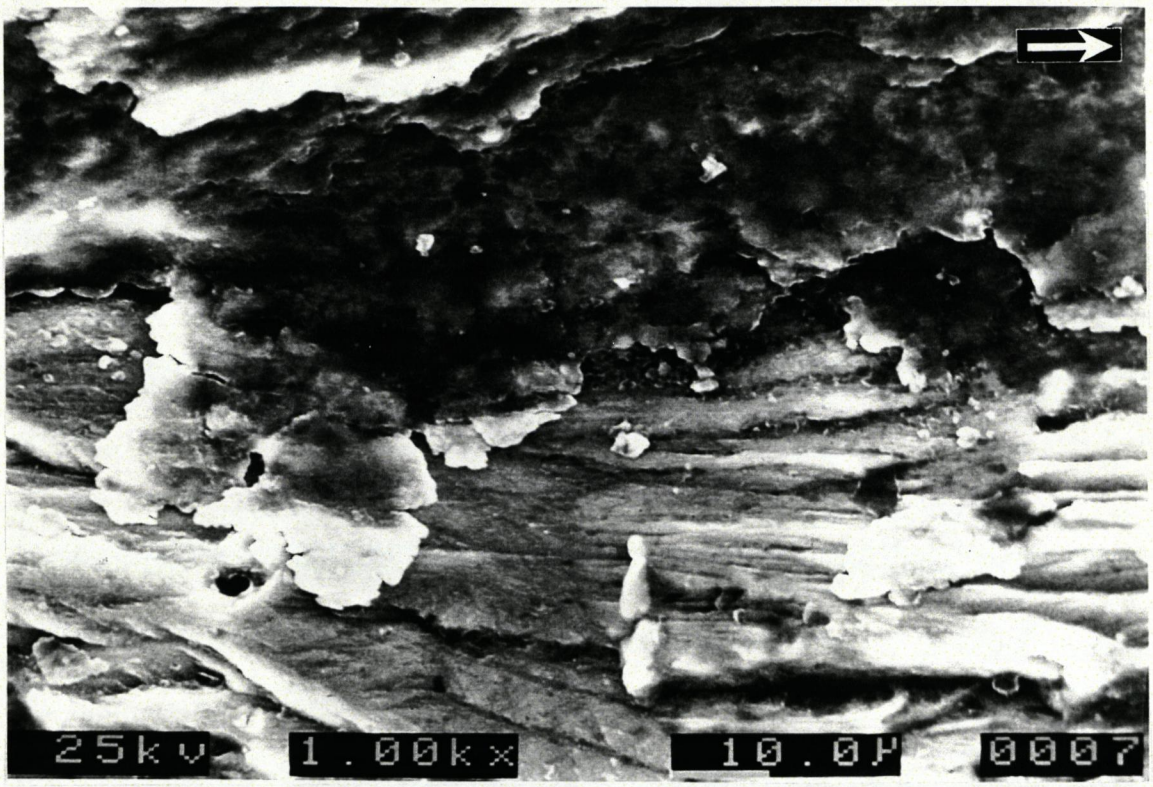

Figure 4.46 Fracture surface of the crack at 25 mm from the PJL in a tested SCT specimen (near-threshold regime). The smeared area of material is clearly visible in the upper part of the picture. The arrow indicates the direction of propagation.

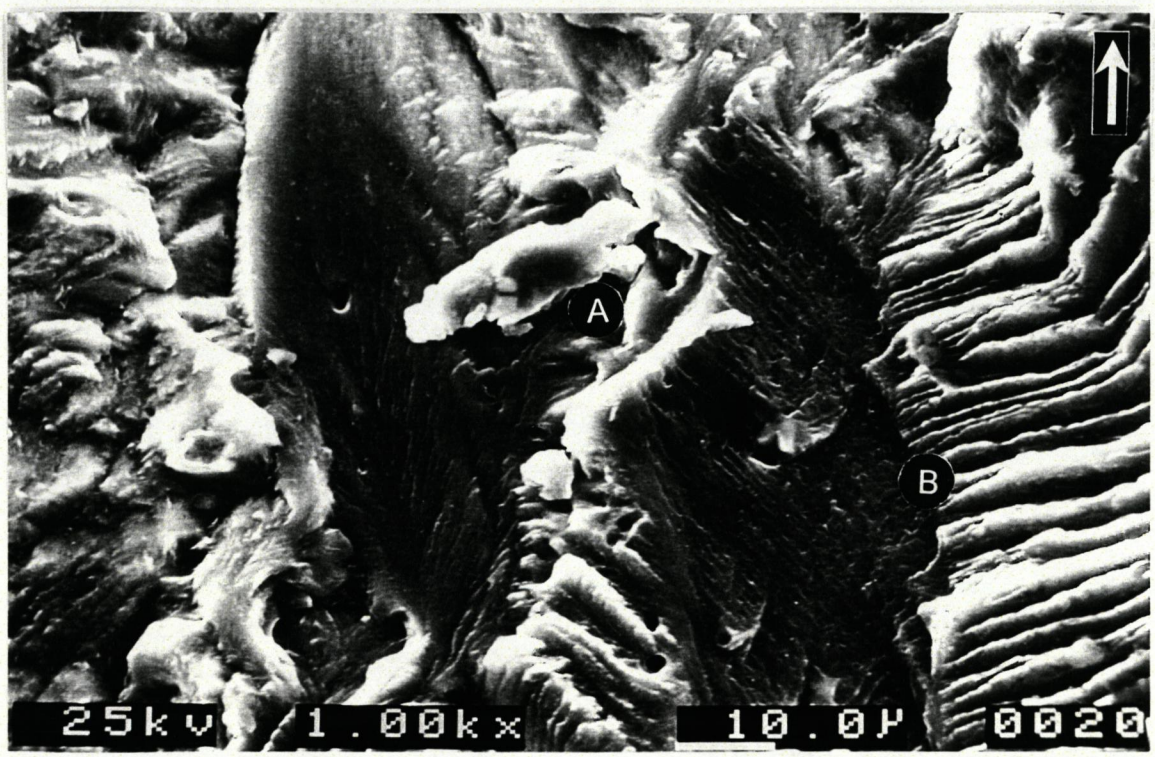

Figure 4.47 Fracture surface of the crack at 25 mm from the PJL in the 2% stretched SCT specimen (near-threshold regime). Evidence of a local surface damage (A) and grain boundaries (B) are indicated. The arrow indicates the direction of propagation.

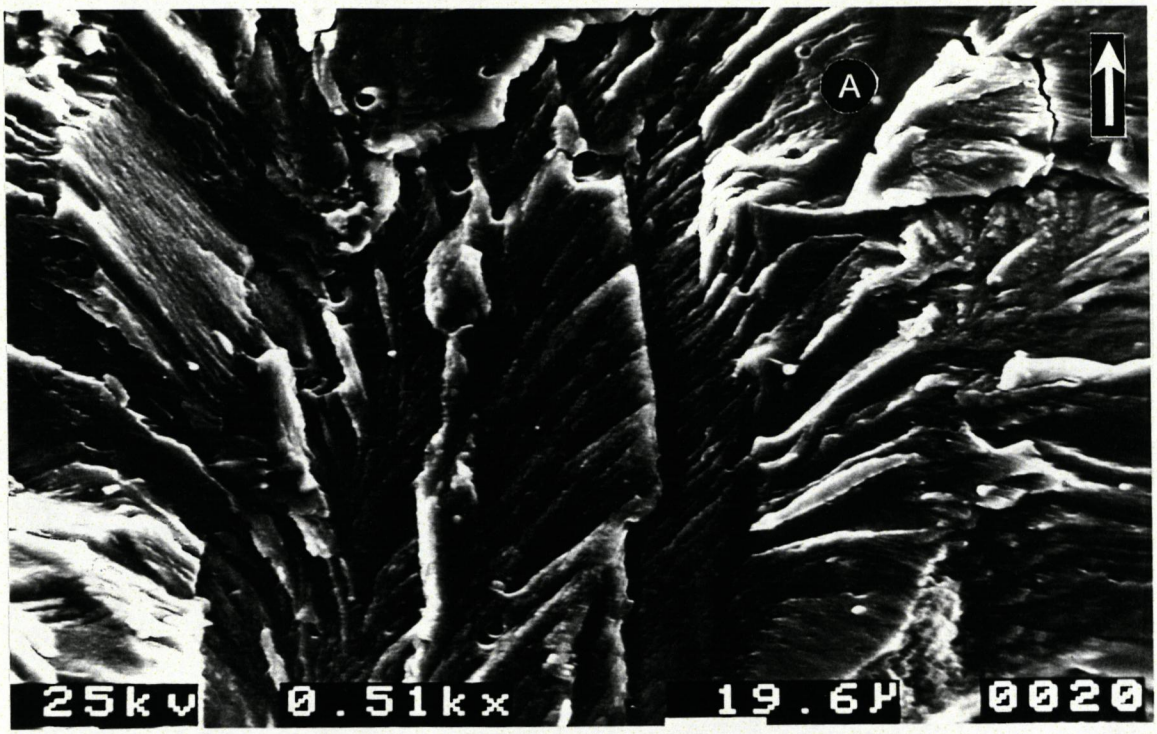

Figure 4.48 Fracture surface of the crack at 11 mm from the PJL in a tested SCT specimen (near-threshold regime). Local surface fragmentation caused by local crack branching is indicated (A) for clarity. The arrow indicates the direction of propagation.

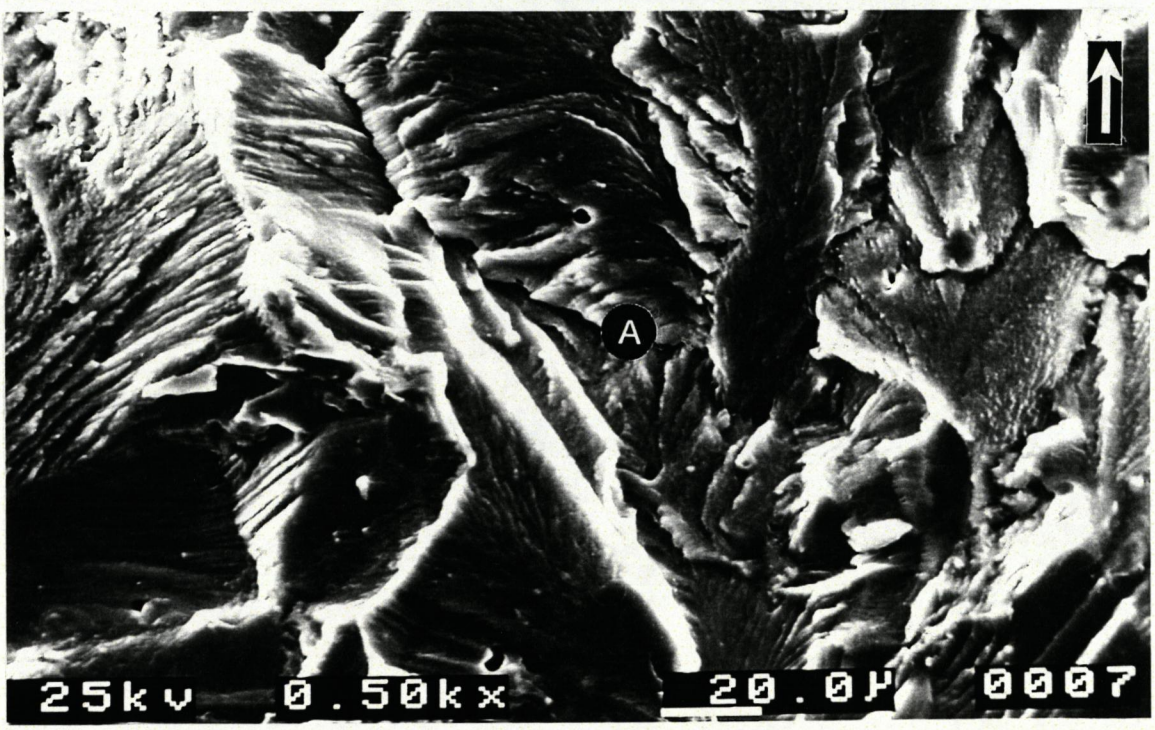

Figure 4.49 Fracture surface of the crack at 11 mm from the PJL in the 2% stretched SCT specimen (near-threshold regime). Evidence of secondary cracking is indicated (A) for clarity. The arrow indicates the direction of propagation.

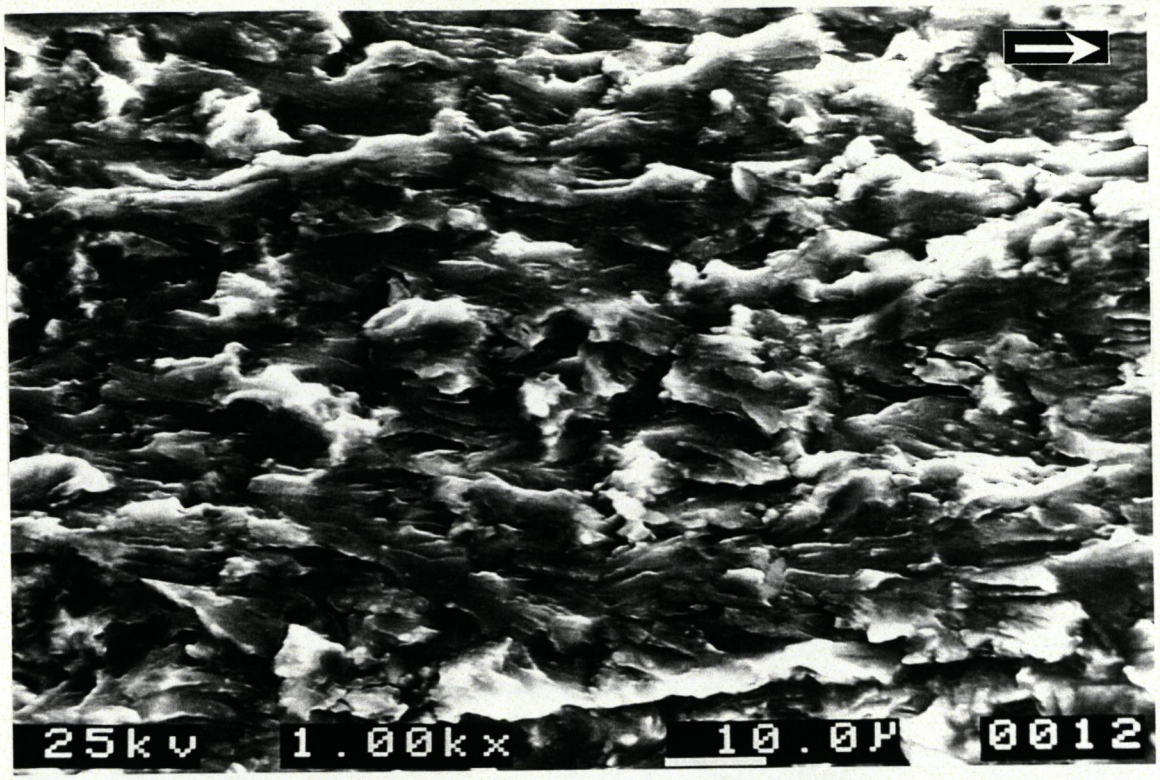

Figure 4.50 Fracture surface observed in the crack on the weld of a tested SCT specimens (near-threshold regime). The arrow indicates the direction of propagation.

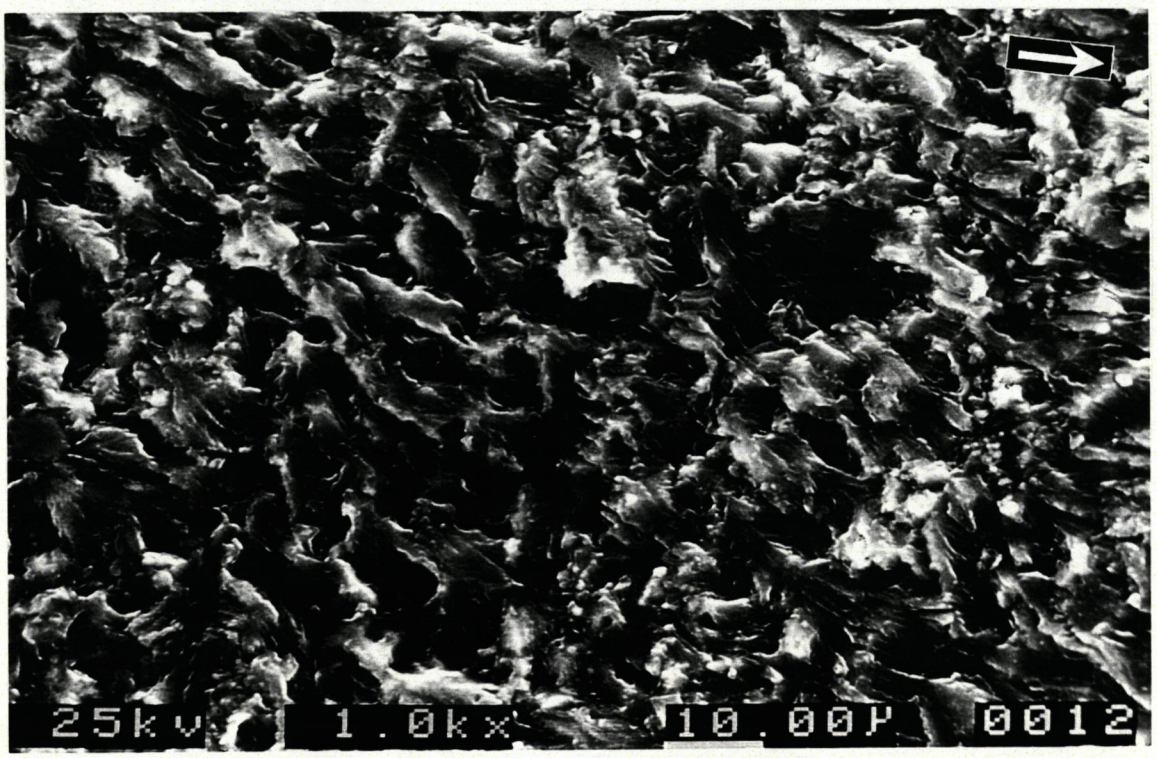

Figure 4.51 Fracture surface observed in the crack on the weld of the 2% stretched SCT specimens (near-threshold regime). The arrow indicates the direction of propagation.

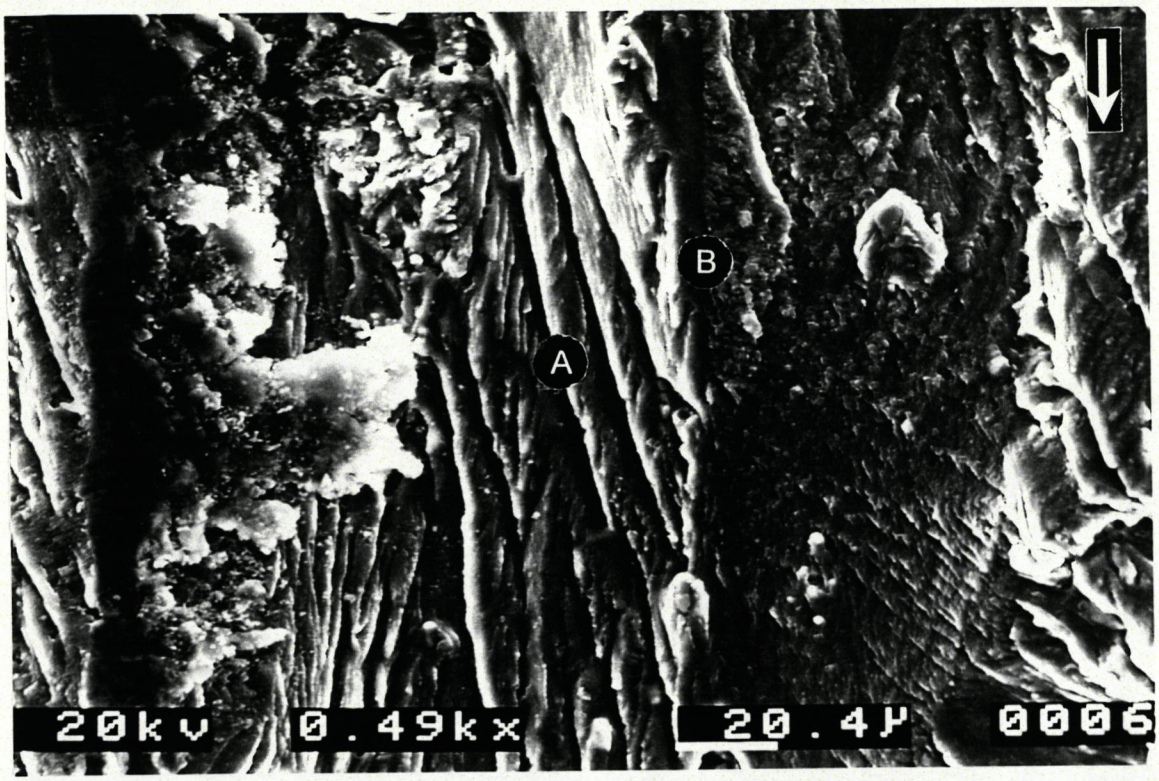

Figure 4.52 Fracture surface observed in the crack at 6 mm from the PJL on a tested CT specimen (near-threshold regime, plate mid-thickness). Crack slip planes (A) and grain boundaries (B) are indicated for clarity. The arrow indicates the direction of propagation.

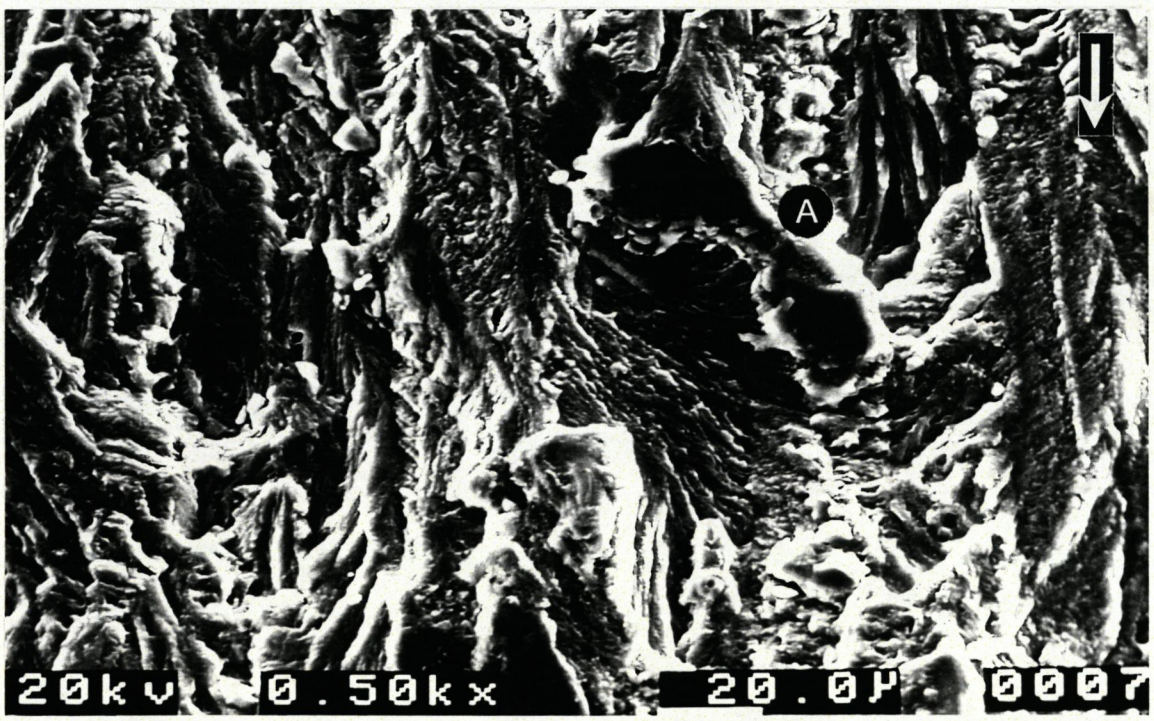

Figure 4.53 Fracture surface observed on the crack at 6 mm from the PJL in the 2% plastically deformed CT specimens (near-threshold regime, plate mid-thickness). Sporadic presence of smeared areas (A) are indicated for clarity. The arrow indicates the direction of propagation.

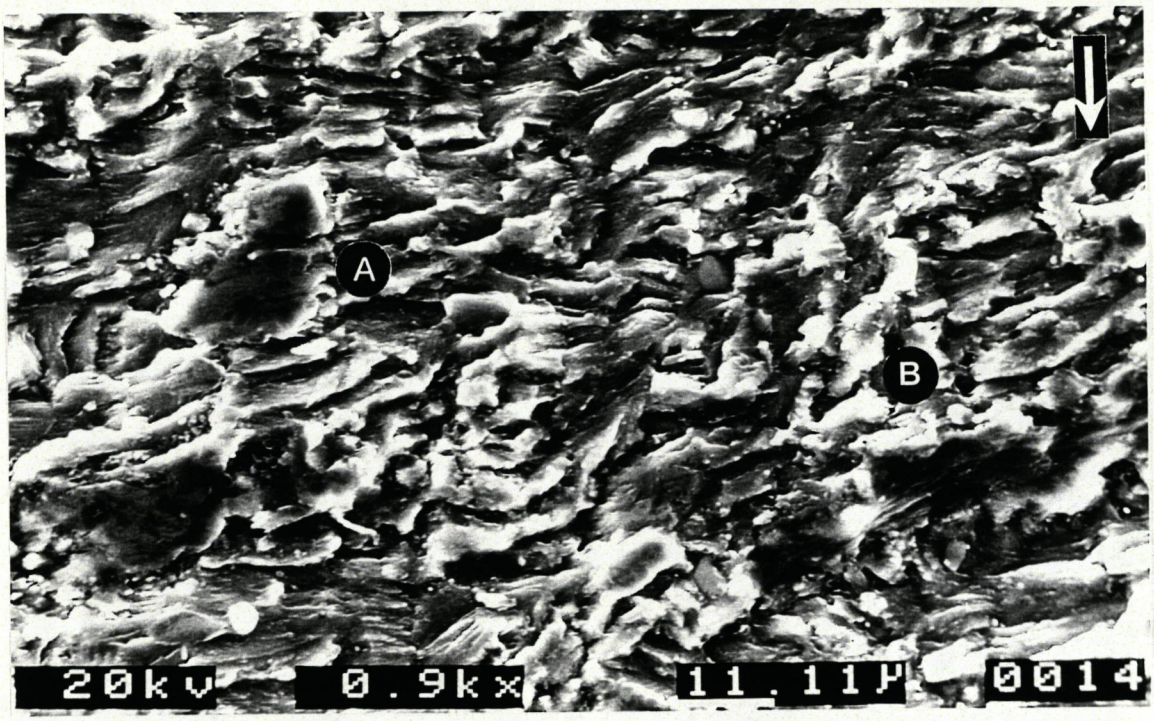

Figure 4.54 Fracture surface observed in the crack on the weld of a tested CT specimen (near-threshold regime, plate mid-thickness). Isolated smeared areas (A) and the presence of debris (B) on is indicated. The arrow indicates the direction of propagation.

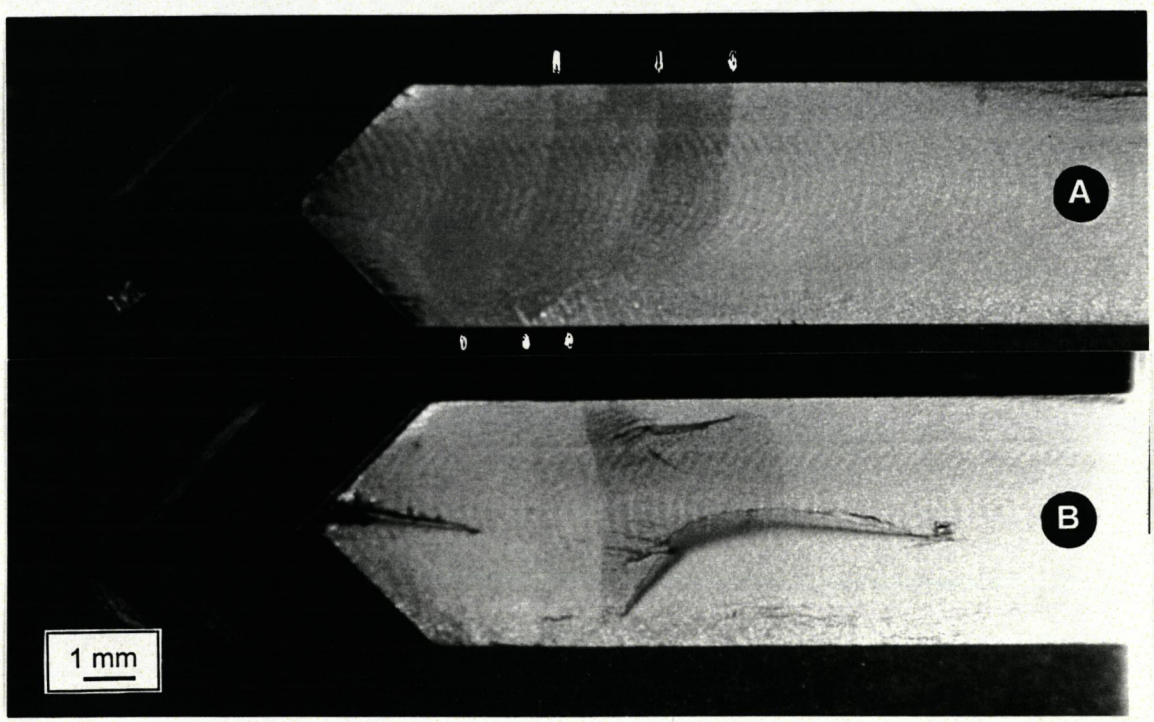

Figure 4.55 Optical picture of the tested CT specimens with the crack on the plate joint line. The crack front deviation (evidenced by marks) exhibited by the unstretched specimens (A) was sensibly reduced in the stretched specimen (B).

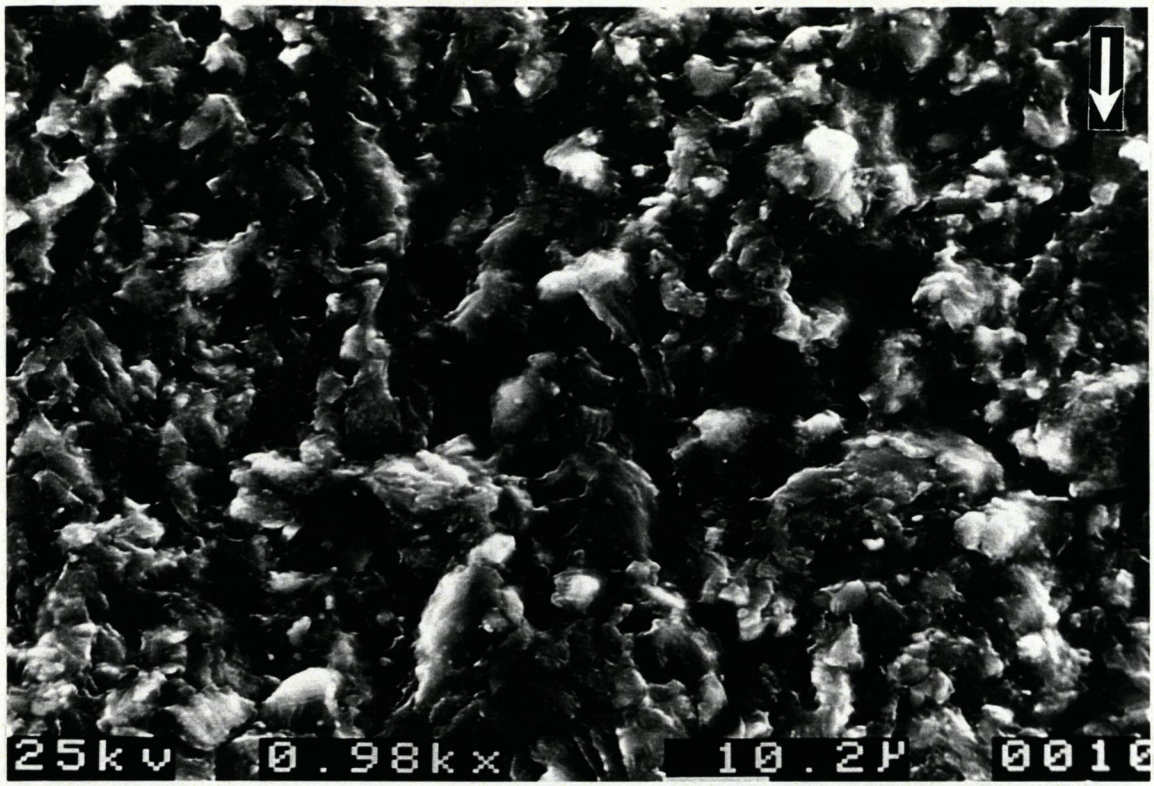

Figure 4.56 Fracture surface observed in the crack on the weld of the 2% plastically deformed CT specimens (near-threshold regime, plate mid-thickness). The arrow indicates the direction of propagation.

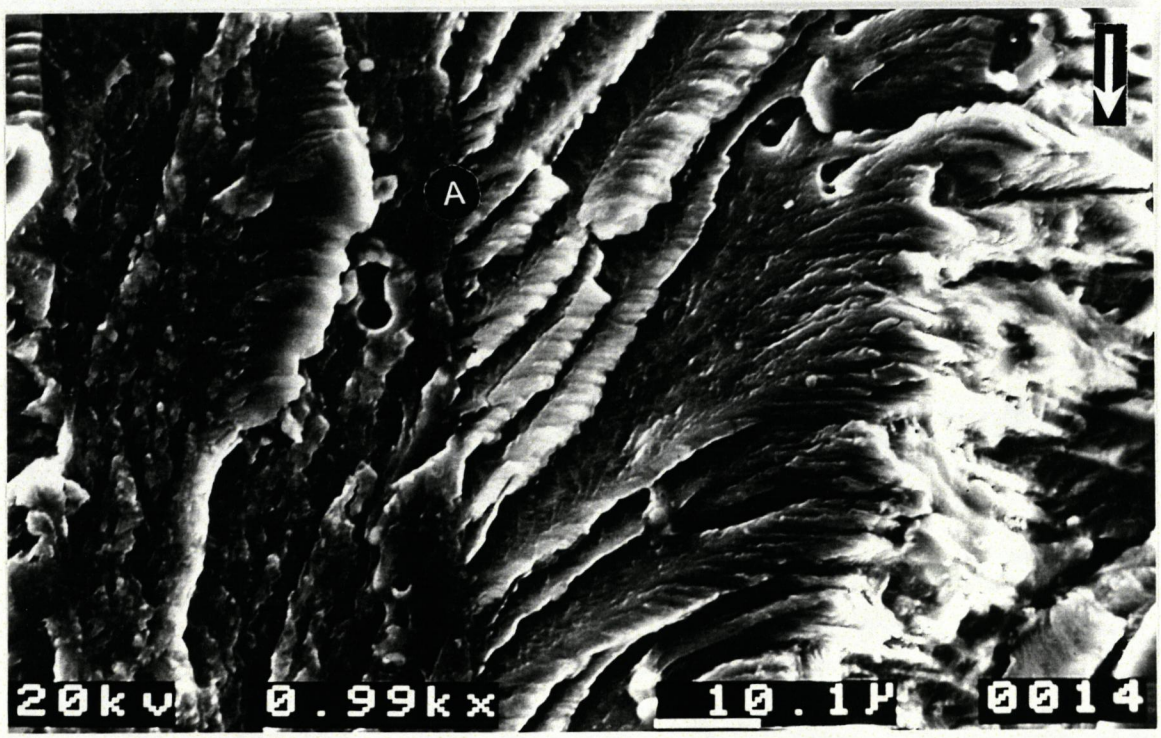

Figure 4.57 Fracture surface observed in the crack at 28 mm from the PJL on a tested CT specimen (near-threshold regime, plate mid-thickness). Grain boundaries (A) are indicated for clarity. The arrow indicates the direction of propagation.

Figure 4.58 Fracture surface observed on the crack at 28 mm from the PJL in the 2% plastically deformed CT specimens (near-threshold regime, plate mid-thickness). Presence of secondary cracking (A) is evidenced. The arrow indicates the direction of propagation.

The previous fractographic examination indicates that:

i) fracture surfaces of cracks parallel to the weld at 25 mm from the PJL, and orthogonal to the weld, propagating from the weld and at 6 mm from the PJL, were characterised by the large presence of smeared areas and debris.

ii) In nominally identical specimens, no smearing or debris was observed on the fracture surfaces after stretching.

iii) No smearing or debris was observed on the fracture surfaces of the SCT specimens with cracks on the weld and at 11 mm from the PJL.

iv) No appreciable difference was observed between the fracture surfaces of the unstretched and stretched CT specimens with cracks at 28 mm from the PLJ.

4.3.7 Measurement of crack opening loads during fatigue of welded specimens

Figures 4.59a and 4.59b show the stress intensity factor versus compliance offset plots obtained as described in Section 3.15 for the unstretched and stretched CT specimens with cracks at 6 mm and 28 mm from the PJL, respectively. Figure 4.59c shows the stress intensity factor versus compliance offset plot obtained for the stretched CT

specimen with the crack on the weld. Crack mouth displacements could not be measured in the unstretched CT specimen with the crack on the weld.

Table 4.11 shows the stress intensity factor values corresponding to the opening loads. The opening loads were measured at 2% offset of the open crack compliance value, as recommended in ASTM E 647 (1997). This is shown in Figures 4.59a, 4.59b and 4.59c.

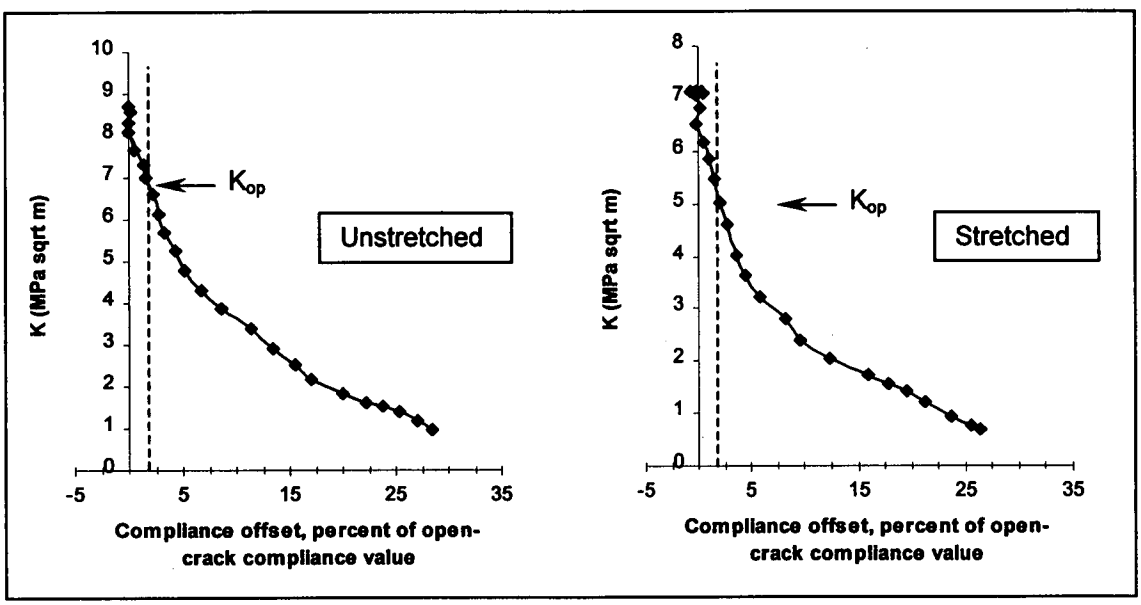

Figure 4.59a Stress intensity factor versus compliance offset curves for the CT specimens with cracks at 6 mm from the PJL.

From Table 4.11 it can be noticed that:

a) for cracks at 6 mm from the PJL, the ΔK_{NT} value was reduced by 20% by stretching, however the effective ΔK (ΔK_{eff}) measured in the stretched specimen was 5% higher than that in the unstretched specimen.

b) For cracks at 28 mm from the PJL, the ΔK_{NT} value was increased by 5% by stretching. No difference in the measured ΔK_{eff} values was noticed.

c) For the crack on the weld (stretched specimen), the ΔK_{NT} value was 5% greater than that measured in the stretched specimen with the crack at 6 mm from the PJL, and no difference in the measured ΔK_{eff} values was noticed.

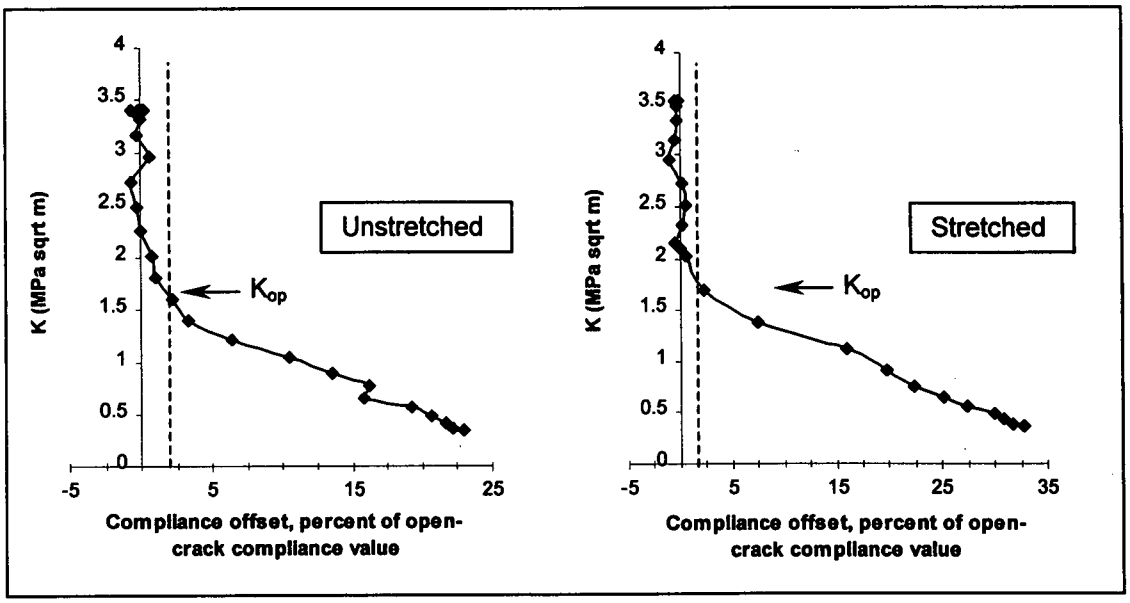

Figure 4.59b Stress intensity factor versus compliance offset curves for the CT specimens with cracks at 28 mm from the PJL.

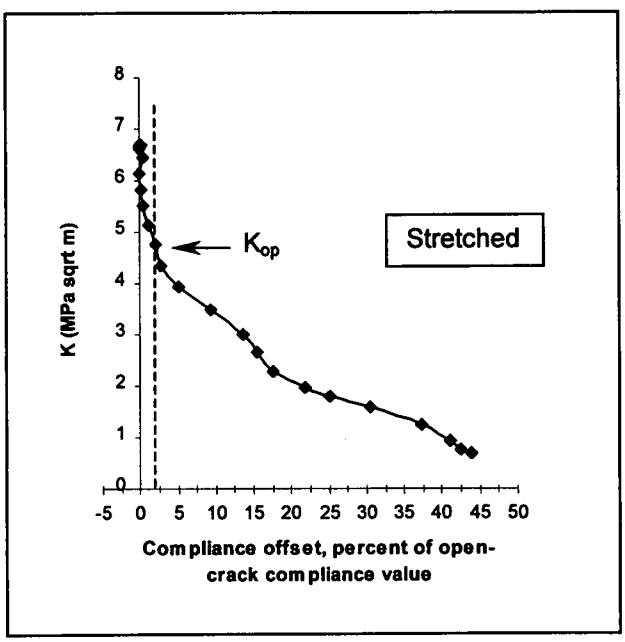

Figure 4.59c Stress intensity factor versus compliance offset curve for the CT specimen with crack on the weld (stretched).

SPEC. CONFIG.	K_{max} MPa $m^{1/2}$	K_{min} MPa $m^{1/2}$	ΔK_{NT} MPa $m^{1/2}$	K_{op} MPa $m^{1/2}$	ΔK_{eff} MPa $m^{1/2}$
on the PJL	—	—	—	—	—
	6.7	0.67	6.0	4.7	2.0
6 mm from the PJL	8.7	0.87	7.8	6.8	1.9
	7.1	0.71	6.4	5.1	2.0
28 mm from the PJL	3.4	0.34	3.0	1.7	1.7
	3.5	0.35	3.2	1.8	1.7

Table 4.11 The COL values for the CT specimens obtained from Figures 4.59a, 4,59b and 4.59c. The values reported on gray background refer to the 2% stretched specimens. Measurements of COL were taken at crack growth rates between $5 \cdot 10^{-10}$ and $2 \cdot 10^{-9}$ mm/cycle.

5. DISCUSSION OF RESULTS

5.1 Structure and hardness in friction stir and plasma welded joints

The macrostructure and microstructure observations in the FSW joints show that:

a) although FSW is a solid-state process, sharp changes in the grain structure as well as in the plasma welded joints have been observed in the weld region.
b) Within the thermo-mechanically affected region, the oval nugget (Fig. 4.1c) exhibits much finer grains (5-10 μm) than in the parent plate (400-600 μm), Figures 4.5a, 4.5b, 3.1b and 3.1c.
c) The region surrounding the nugget is characterised by highly elongated (approximately between 600 μm and 1 mm) and bent grains, Figures 4.7 and 4.8b.

Hardness measurements on FSW joints indicate that:

a) the nugget is characterised by a local maximum in the hardness profiles (138 Hv1)
b) Minimum hardness values (103 and 109 Hv1) have been observed within the thermo-mechanically affected region outside the nugget.
c) Maximum hardness values (148 and 146 Hv1) greater than in the parent plate have been observed in the HAZ.

During welding the material undergoes frictional heating and stirring by the welding tool acting from the top surface. In the nugget, maximum temperatures of 450-480 °C have been measured during welding of aluminium joints [52, 100]. These temperatures combined with the stirring action allow thermo-mechanically-induced recrystallisation of the material, as described in several works [36, 52, 100, 105]. This phenomenon would explain the presence of much finer grains observed in the nugget than in the parent material (Fig. 3.1b and 4.5a). In this region, hardness reaches a local maximum of 138 Hv1 on the PJL at 1 mm from the top surface (Fig. 4.13). The presence of the hardness peak suggests that solution heat treatment followed by reprecipitation takes place to a certain degree in the nugget, as observed in previous works [96, 105]. Moving from the top to the bottom weld surface on the PJL, hardness values gradually decrease to 117 Hv1 on the bottom surface (Fig. 4.13). This through-thickness hardness gradient (of approximately 4 Hv1/mm) within the nugget would indicate that the respective

regions of material through the weld thickness undergo different thermo-mechanical cycles.

The elongated and bent grains in the thermo-mechanically affected region external to the nugget (Fig. 4.7, 4.8a and 4.8b) indicate a large amount of plastic deformation. An estimate of the plastic strain can be obtained by comparing the grain dimensions in the thermo-mechanically affected region on the plane orthogonal and parallel to the weld (Fig. 4.7 and 4.8b) with those in the parent plate on the ST and LS planes, respectively (Fig. 3.1b and 3.1c). From this comparison, the plastic strain on the plane orthogonal to the weld is approximately 50% and on the plane parallel to the weld it is approximately 70%. These two values are broadly in agreement with those experimentally observed by Reynolds [83]. In the thermo-mechanically affected region the grains are deformed and bent by the forging action of the tool in the direction of the streamlines of material around the pin, as described in Ref. [17]. This is a region where recrystallisation does not take place. This is confirmed by the elongated grain structure (Fig. 4.1c), a typical result of a cold working process.

The boundary between the thermo-mechanically affected region and the heat affected region on both sides of the weld are the softest regions of the joint (Fig. 4.13 and 4.17b). The hardness profiles at these locations are asymmetric with respect to the PJL. Hardness is lower on the lip side (103 Hv1, 6 mm from the PJL) than on the opposite side (109 Hv1, 4 mm from the PJL). The asymmetry suggests that the regions of material on the two sides of the PJL undergo different thermo-mechanical cycles. Maximum temperatures of 330-350 °C are typically reached at these locations during welding [52, 100]. The fact that the temperatures are below the solvus temperature of the S' phase (Al_2CuMg) and above 200 °C suggests that precipitate coarsening takes place producing an overaged microstructure [81]. This was confirmed by observations carried out using Transmission Electron Microscopy (TEM) on fusion welded 2024-T3 joints in the regions characterised by similar maximum temperatures and hardness values [74].

At 18 mm (lip side) and at 22 mm (side opposite lip) from the PJL, hardness reaches the maximum values of 146 and 149 Hv1, respectively. At these regions, maximum temperatures between 180 and 200 °C are typically reached during welding [52, 100]. This is the temperature range typically required to allow further precipitation strengthening to take place [100]. Under these conditions, hardness could be increased above parent plate values.

Local hardness minima (130 Hv1) occur at 28 and 32 mm from the PJL (Fig. 4.13). The reason for these local hardness reductions is not entirely clear. Overageing, a possible cause for these reductions, is considered unlikely as the maximum temperature experienced during welding at these locations is presumably less than that occurring at the hardness maxima (18, 20 mm from the weld). Measurement of the local temperatures during the welding operation and TEM analysis would be required in order to establish the precipitate distribution and characteristics.

The central region of the plasma welds undergoes complete melting (maximum temperature above 640 °C) and subsequent re-solidification, as confirmed from the coarse segregated microstructure which typically characterises castings (Fig. 4.10). The hardness profile reaches its lowest values of 93 Hv1 in the weld centre (Fig. 4.14). This fact has been attributed in Ref. [100] to the redistribution of Cu within the re-solidified phases. Next to the fusion zone is a partially melted region, where the temperature causes localised fusion of the eutectic phase [74]. Hardness values in this region are comparable with those in the centre of the weld.

At 6 mm from the PJL the hardness reaches a maximum of 142 Hv1, equal to the hardness in the parent plate (Fig. 4.14). This has been explained in Ref. [100] as an effect of natural ageing. In fact, it is possible that the solvus temperature would have locally exceeded in a narrow region, and subsequent to a fast cooling rate, the solute would have diffused, and natural ageing taken place.

The hardness profile in the plasma joint exhibits a second minimum (102 Hv1) 9 mm from the weld (Fig. 4.14). Overageing of the alloy is considered a possible cause of this

reduction. The temperature conditions allow the precipitates present in the matrix to coarsen and their hardening effect to decrease consequently. This has been proven by TEM analysis carried out on similar joints [74]. The analysis has revealed the presence of S' precipitates that typically characterise an overaged microstructure. Etched surfaces appear darker in this region than in the surrounding ones (Fig. 4.12).

Comparing the hardness profile of the friction stir and plasma welds, it can be observed that plasma welds exhibit a narrower total HAZ (60 mm) than the friction stir welds (96 mm), (Fig. 4.13 and 4.14). Plasma welds show a lower hardness minimum value than the friction stir welds, however the difference is only marginal (65% of the parent plate in the former and 73% of the parent plate in the latter).

5.2 Residual stresses in friction stir welded joints

In the interpretation of the residual stress measurements it should be considered that:

i) measurements at three locations are not sufficient to provide a complete description of the residual stress distribution across the welded plate [38, 58, 106].

For this reason, no information about the effective residual stress maxima and minima (in terms of magnitude and position) can be obtained. Nevertheless, from the measurements a lower and an upper estimation respectively of the residual stress maximum and minimum values, and a lower estimation of the width of the residual stress affected area have been obtained.

ii) An accuracy of ±15 MPa in the measured values is expected [82].

Table 4.8 shows that residual stress measurements carried out at similar locations on two nominally identical SCT specimens differed by 199 MPa i.e. 64% of the parent plate 0.2% proof stress. This suggests that a large variability in residual stress is present from sample to sample.

In the light of these considerations, residual stress measurements in Tables 4.1a, 4.1b and 4.1c indicate that:

a) longitudinal tensile residual stress typically characterises the region of the joint close to the weld. Residual stress values measured at 11 mm from the PJL are always greater than those measured on the weld. This is in agreement with the residual stress distribution measured in aluminium and steel welded joints reported in other works [38, 42, 106].
b) Surface skimming increases transverse residual stresses. These are tensile in the weld and compressive in the surrounding regions.

In the as-machined plate, the longitudinal residual stress values on the weld and at 11 mm from it are tensile. In order to satisfy the internal equilibrium in the direction of the weld a further compressive residual stress area should exist in the plate. This implies that the residual stress affected area extends beyond the measurement location at 25 mm from the PJL. The maximum longitudinal residual stress value has been detected at 11 mm from the PJL. As previously mentioned, this represents a lower estimate of the maximum longitudinal residual stress in the plate. All the transverse residual stress values are relatively low and of the same order of magnitude as the experimental error associated with the method. This implies that the tensile and compressive stresses parallel to the PJL dominate the residual stress distribution in the plate.

During the machining of the dog-bone specimens, material is removed from the plate sides. As the material is machined, its restraint action on the rest of the plate is removed. This causes the residual stresses to be partially relieved and redistributed. This fact would explain the reduction in the corresponding measured values (Tab. 4.1a and Tab. 4.1b). At 25 mm from the PJL the longitudinal residual stress is negative, indicating the presence of a compressive residual stress area necessary in order to satisfy the internal equilibrium in the direction of the weld.

The transverse residual stress values in the dog-bone specimen are all low and within the experimental error (Tab. 4.1b). Transverse residual stresses arise in order to contrast the parent plate in-plane deformation by the offset action of the longitudinal tensile residual stress on the parent plates. This is shown in Figure 5.1. The transverse residual stresses depend on the in-plane moment of inertia of the parent plates, which is a

function of the third power of the parent plate width (W) [50]. This suggests that reductions in the plate width would lead to reductions in transverse residual stress.

Table 4.1c shows that transverse residual stresses in the weld and at 25 mm from the PJL are largely increased by the surface skimming operation. Although no evident explanation for this large increase in the transverse residual stresses was found, it is believed that factors such as through-thickness residual stress gradients and machining procedure could have played an important role. A more detailed analysis of the effects on residual stress distribution due to the changes in the specimen geometry by machining would require the use of finite element analysis.

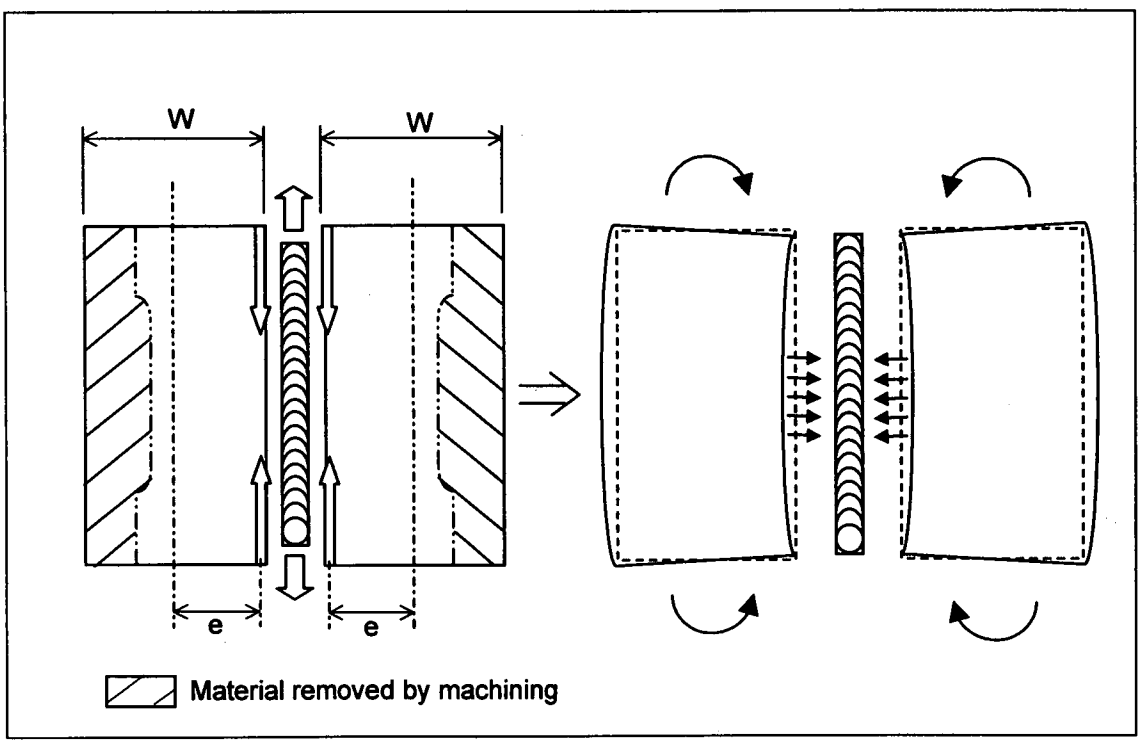

Figure 5.1 The mechanism of formation of transverse residual stress in the welded plate. The longitudinal residual stress can be represented as forces acting offset (e) to the parent plates.

5.3 Tensile testing of friction stir welded joints

The mechanical behaviour of the transverse joint (Fig. 4.15 and 4.16) can be represented by the stress-strain model shown in Figure 5.2(a). In this model three springs are connected in series. Each spring is defined by a linear-elastic, linear-plastic constitutive equation in terms of elastic modulus (k_i), yield stress (σ_{yi}) and work-hardening coefficient (k_{pi}). The two external springs represent the parent plate regions of the welded joint (k_p, σ_{yp}, k_{pp}) and the central one represents the weld (k_w, σ_{yw}, k_{wp}). For applied stress values (σ) less than σ_{yw} (σ_{yw} is lower than σ_{yp}) the joint behaves elastically, and $k_p = k_w = E$. From the curves of Figure 4.14, the mean value of E is approximately 77 GPa, with an experimental error of 7% with respect to the typical Young's modulus of aluminium alloys (72 GPa). Given that x_p and x_w are the strain along the main stress axis in the parent plate and in the weld respectively, and P is the applied load, from the model in Figure 5.2a:

$$k_p x_p = k_w x_w = E x_p = E x_w = P \qquad \textit{Eqn. 5.1}$$

and therefore $x_p = x_w$. This indicates that stress and strain in the weld and parent plates are the same, as Figure 4.14 shows. As the applied stress reaches σ_{yw} = 243 MPa (Tab. 4.2), yielding occurs in the weld. The stiffness of the spring representing the weld decreases from E to k_{wp} = 3 GPa. This is shown in Figure 4.15 by the reduction in slope of the weld stress-strain curve. Equation 5.1 becomes:

$$E x_p = k_{wp} x_w = P \qquad \textit{Eqn. 5.2}$$

Equation 5.2 indicates that, since $k_{wp} << E$, the strain within the weld becomes much larger than in the parent plates. For $\sigma = \sigma_{yp}$ = 330 MPa the stiffness in the springs representing the parent plate decreases from E to k_{pp} = 24 GPa, as indicated by the

reduction in gradient of the parent plate curve in Figure 4.15. At this stage, the entire welded joint is plasticised and:

$$k_{pp} x_p = k_{wp} x_w = P \qquad \textit{Eqn. 5.3}$$

This information can be used with the stress-strain model of Figure 5.2b to discuss the behaviour of the longitudinal FSW joint (Fig. 4.18).

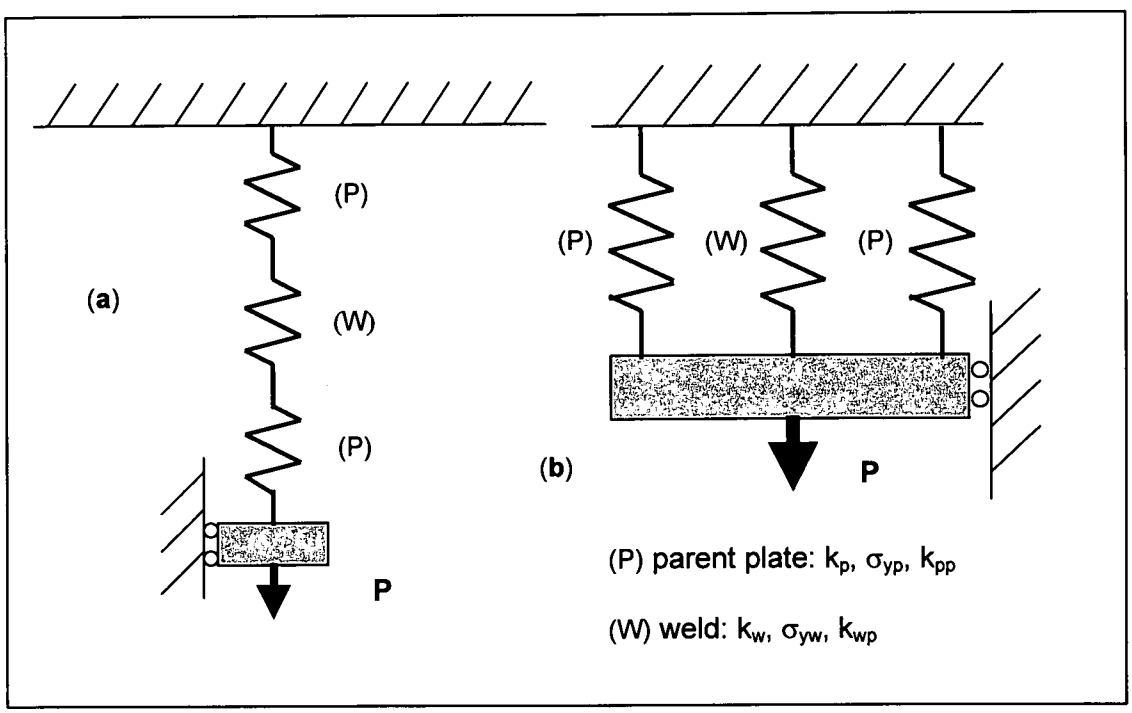

Figure 5.2 The stress-strain models representing the tensile behaviour of the transverse (a) and longitudinal (b) welded joints.

It is assumed that the constitutive equations of the springs are defined by the same constants as for the model of Figure 5.2a. Whereas in the model of Figure 5.2a the springs are subjected to equal stress, the springs in the model of Figure 5.2b are connected in parallel and therefore subjected to equal strain ($x_w = x_p = x$). This is

necessary in order to satisfy the boundary conditions imposed by the grips. At low load the joint behaves elastically and from the balance of the forces acting on the springs:

$$2\,(A_p\,E\,x + P_{res,\,p}) + A_w\,E\,x + P_{res,\,w} = P \qquad \textit{Eqn. 5.4}$$

where $P_{res,\,p}$ and $P_{res,\,w}$ are the forces in the elements associated with the presence of the longitudinal residual stresses. A_w and A_p are the cross sectional areas of the elements. Assuming that the weld element represents the tensile behaviour of the region of the joint with hardness value less than the hardness of the parent plate, A_w and A_p are then defined as in Figure 5.3.

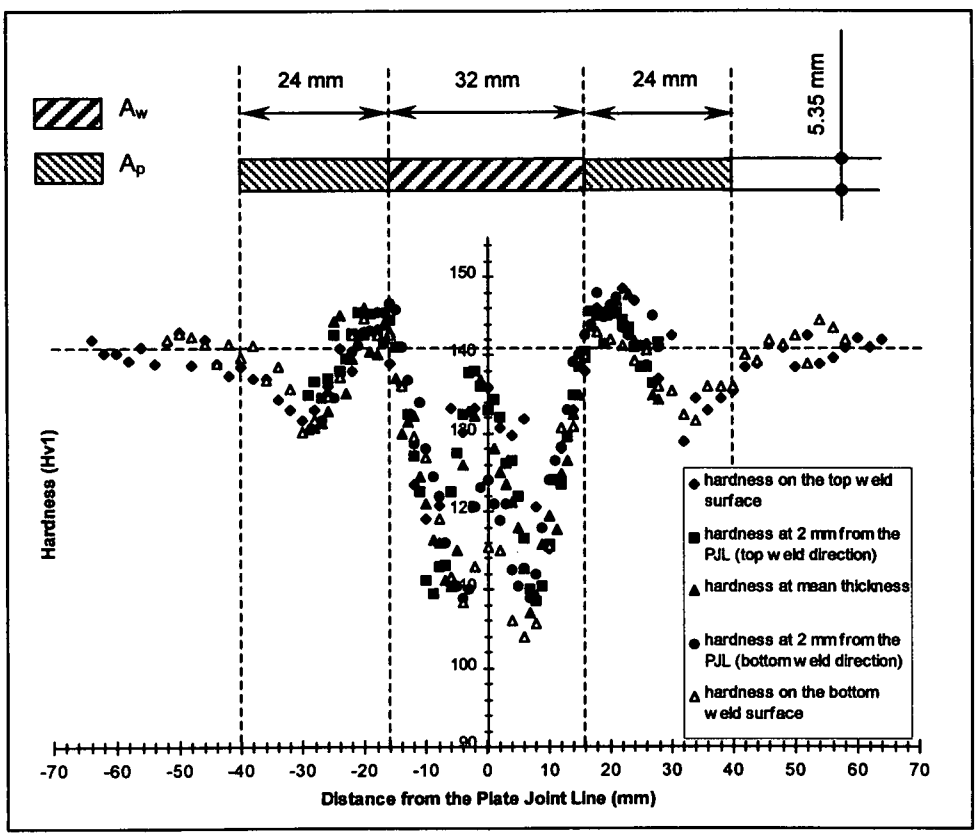

Figure 5.3 Definition of A_w and A_p with respect to the hardness profile of the joint.

For the internal balance $2\,P_{res,\,p} + P_{res,\,w} = 0$, therefore residual stresses do not contribute to the balance of Equation 5.4. However, it is possible to take into account the

contribution of the residual stresses considering the stress in the single elements. As the weld begins to yield, the stiffness of the joint gradually decreases from 2 A_p E + A_w E, as in Equation 5.4, to 2 A_p E + A_w k_{wp}. The joint gradually begins to deviate from linear behaviour when the proportional limit σ_{prop} is reached (Fig. 4.18). Therefore for the weld:

$$Ex + \frac{P_{res,w}}{A_w} = \sigma_{yw} \qquad \textit{Eqn 5.5}$$

where $P_{res,w}$ /A_w is the residual stress in the weld element. Equation 5.5 allows the estimation of the value of the residual stress in the weld element since σ_{yw} is known (243 MPa) and E x = σ_{prop} = 110 MPa, as measured from the tensile test carried out on the longitudinal joint (Tab. 4.2). This model assumes that the residual stress distribution within the weld element is constant and that yielding takes place in the weld at the softest location, 6 mm from the PJL. From Equation 5.5 the residual stress in the weld element is 133 MPa. This residual stress value is 2 times lower than the value initially measured at 11 mm from the weld (264 MPa, Tab. 4.1c) and 2 times higher than the value measured at the same location but on a similar specimen (84 MPa, Tab. 4.8).

As the applied stress increases, yielding gradually extends from the weld to the parent plates. As soon as the entire joint has yielded, the joint stiffness decreases to 2 A_p k_{yp} + A_w k_{wp} and the stress-strain curve exhibits a sudden reduction in slope (Fig. 4.18). This situation corresponds to the application of load 3 of Figure 2.14, for which the longitudinal residual stress of the joint has been completely relieved. Equation 5.4 becomes:

$$(2\ A_p\ k_{pp} + A_w\ k_{wp})\ x = P \qquad \textit{Eqn. 5.6}$$

with $P = \sigma_{0.2} (2 A_p + A_w)$, and $\sigma_{0.2} = 316$ MPa, obtained from the tensile test of the longitudinal joint (Tab. 4.2). Equation 5.6 allows the prediction of the strain value x at which the total yielding of the joint occurs. From Equation 5.6, x = 0.66%. Figure 5.4 shows that the strain value obtained with the model of Figure 5.2a, differs by 16% from the experimental value (0.57%).

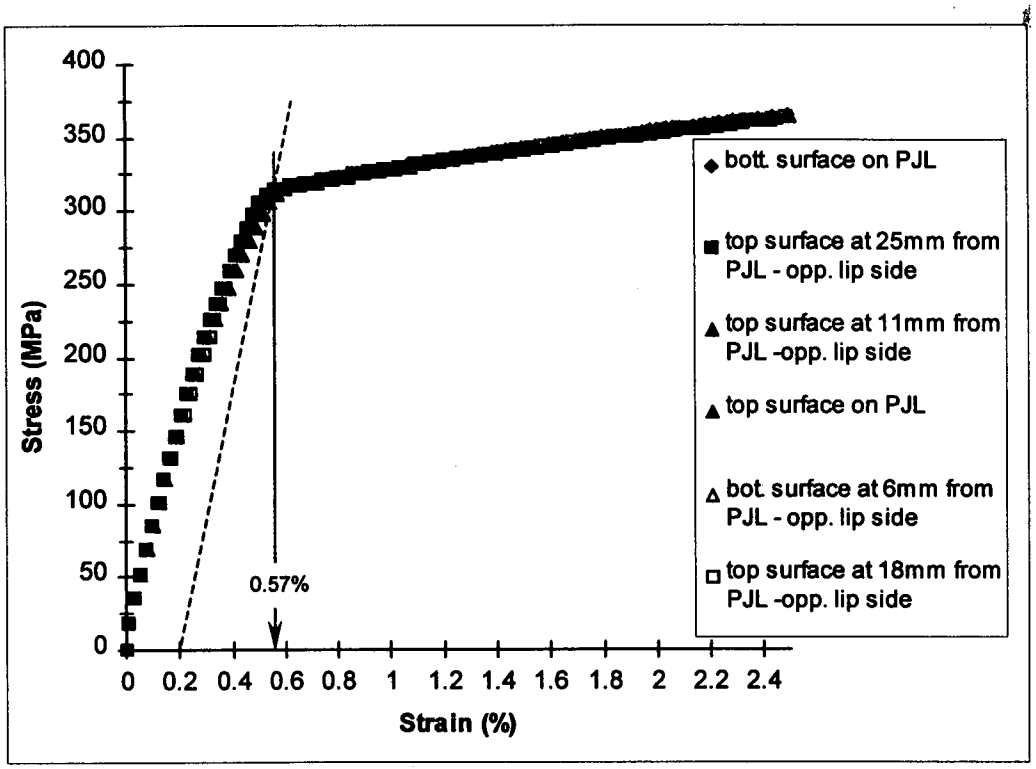

Figure 5.4 Predicted and measured yielding of the longitudinal welded joint.

5.4 Tensile properties - observations

The tensile test carried out on transverse FSW joints has shown that yielding takes place first at locations of minimum hardness, and failure occurs at the lowest hardness locations. Hardness measurements indicate that hardness minima are located in a planar region orientated at 45° with respect to the main stress axis (Fig. 4.17b). This location coincides with one of the maximum shear planes [50]. For this reason static failure occurs on the same plane. The area where static failure takes place is characterised by an elongated grain structure (Fig. 4.8a and 4.8b) in the direction of the main stress axis. This suggests that optimum orientation of the grain structure did not interfere with the static failure mechanism, which is clearly dominated by the minimum hardness. The

strain distribution measured in the transverse FSW joints (Fig. 4.16) has indicated that the deformation concentrates in a limited volume of material at the softest location of the joint. This suggests that hardness minima acted as a strain-concentrator in the joint.

It should be observed that the elongation values in the transverse joints (Tab. 4.2 and 4.4) are dependent on the respective gauge lengths. This dependence is due to the fact that the strain is not uniform within the gauge length but is concentrated at the regions of minimum hardness. Figure 5.5a shows a simplified strain distribution obtained with the strain values measured on the FSW transverse joint at 295 MPa during the tensile test (Fig. 4.15). The elongation values calculated from the strain distribution of Figure 5.5a are plotted in Figure 5.5b as a function of the gauge lengths. The elongation decreases as the reference gauge length increases. Elongation values tend asymptotically to the elongation in the parent plate. It can be noticed that for reference lengths greater than 100 mm the calculated elongation differs approximately by 10% from the asymptotic value.

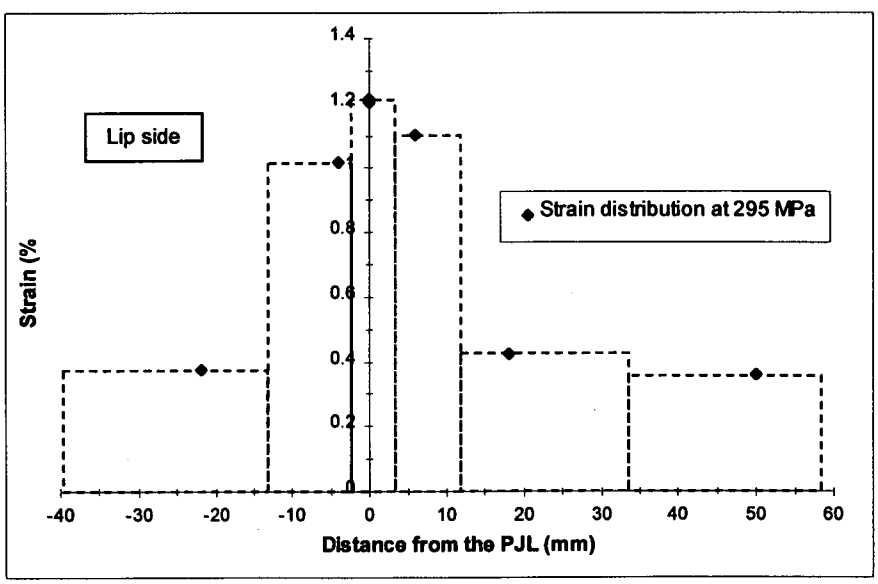

Figure 5.5a Simplified strain distribution in the transverse FSW joint. Data points have been measured at 295 MPa during the tensile test.

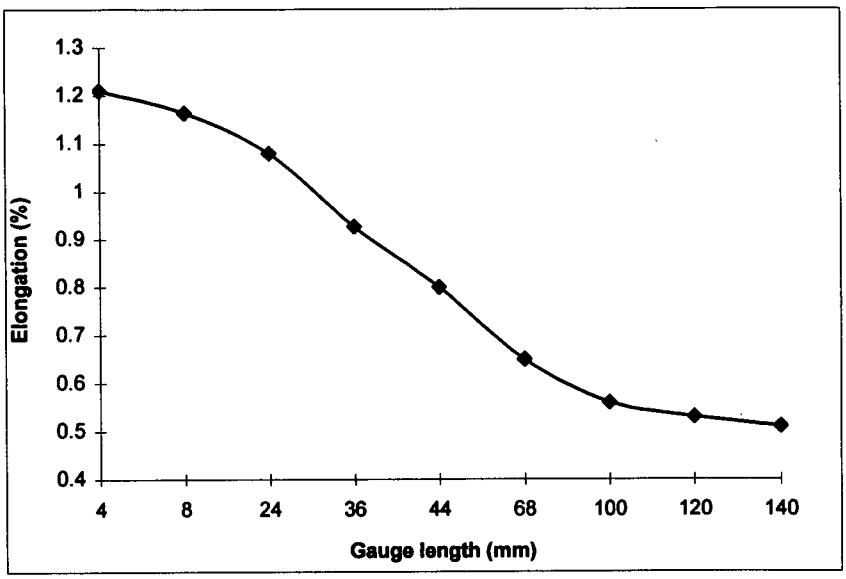

Figure 5.5b Calculated elongation plotted as a function of the gauge length in the transverse FSW joint.

Longitudinal FSW joints generally exhibited superior tensile properties than the transverse joints except for the proportional limit (Tab. 4.2). The proportional limit in the transverse joints was 40% higher than in the longitudinal joints. This fact has been explained in Section 5.3 as an effect of longitudinal residual stresses in the joint. As the results of Table 4.2 shows, the ultimate strength of the FSW joints is marginally influenced by the joint orientation in contrast with the dependence observed for the yield strength. However, it should be considered that in the longitudinal joints the ultimate strength depends on the ratio A_p/A_w. In fact, for $A_p/A_w >> 1$ the joint would be dominated by the parent plate properties, whereas for $A_p/A_w << 1$ the joint would be dominated by the weld properties.

Transverse plasma welded joints exhibit an ultimate tensile strength 12% lower than the transverse FSW joints (Tab. 4.4). This suggests that the plasma welding process produced a more severe degradation of the tensile properties as indicated from the fact that the minimum hardness value is 10% lower than that in the FSW joints. In this light, it is reasonable to believe that, as it has been found for the transverse FSW joints, hardness also dominates the tensile behaviour of the transverse plasma welded joints.

5.5 Fatigue endurance properties

The life to failure behaviour of FSW joints in the as-welded surface condition is clearly inferior to that of the parent plate. For both longitudinal and transverse joints the presence of surface irregularities is the source of fatigue cracking. In the case of the transverse joints, the removal of the lip causes the fatigue degradation to be reduced, in the region of long lives, from 50% to less than 10% of the parent fatigue strength (Fig. 4.19 and 4.20). On this basis, it is reasonable to believe that the lip, (transverse FSW joints) and the tool marks (longitudinal FSW joints) act as stress raisers allowing fatigue crack initiation from local defects. This behaviour has been observed and described in Ref. [8] as a result of investigations carried out on 2024-T3 as-welded FSW specimens.

The ratio between the stress ranges at 10^7 cycles of the skimmed and the as-welded transverse joints is an estimation of the effective fatigue stress concentration factor (K_f) [40, 98]. The fatigue stress concentration factor quantifies the effect of the stress concentration provided by the lip on the fatigue strength. From a comparison between Figures 4.19 and 4.20, for the transverse welded joints $K_f = 2.1$. As discussed in Section 2.1, because of the effect of plasticity in the region of material near the notch, generally $K_f \leq K_t$, and the fatigue stress concentration factor can be considered as a lower estimate for the stress concentration factor associated with the lip [50]. The estimation provided by this criterion is better for low stress fatigue failures, as the effect of plasticity is less than for high stress fatigue failures. Another estimate of K_t can be obtained by approximating the lip with a shoulder fillet under tensile stress. Figure 5.6 shows the dimensions of the shoulder fillet with respect to a representation of the lip cross section. The values of the notch radius and the step height have been estimated from Figure 4.3. From Ref. [78], the theoretical stress concentration factor associated with this geometry is 2.6. The fillet shoulder represents a more severe profile discontinuity than the lip, which is in simple terms a local outstanding portion of material (Fig. 4.1c). This suggests that the stress concentration associated with the effective lip geometry is between 2.1 and 2.6.

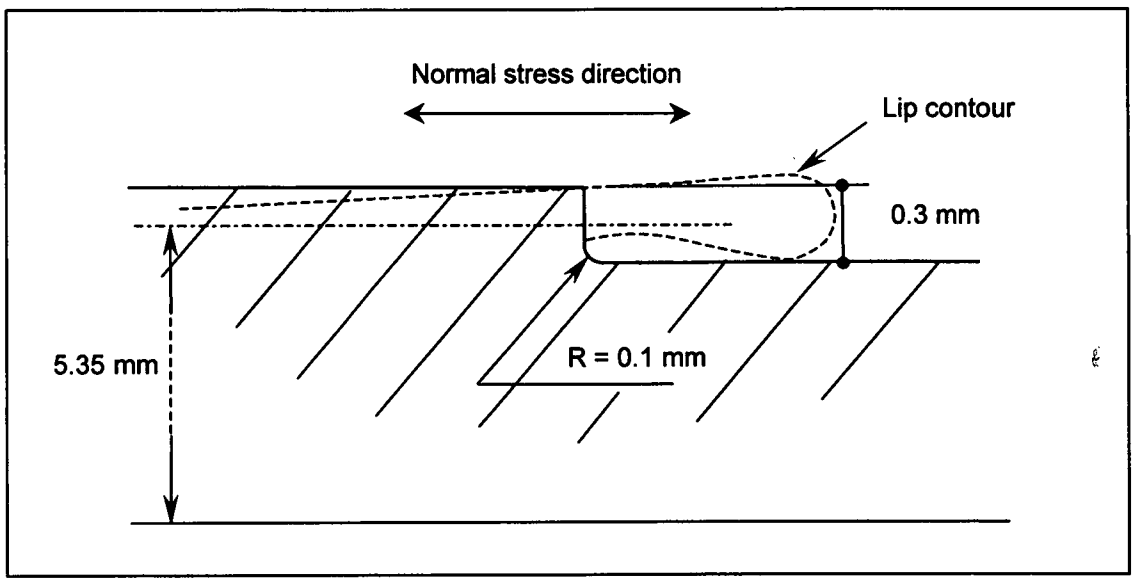

Figure 5.6 The dimensions of the shoulder fillet with respect to a representation of the lip cross section.

Fatigue initiation on transverse FSW joints has typically occurred at local defects present in the region underneath the lip (Fig. 4.23 and 4.24). Aluminium has been the only element to be detected in the initiation areas by EDX analysis. This suggests that the inclusions are composed of aluminium oxide (Al_2O_3) (oxygen is hardly detectable by EDX analysis because of its low energy X-ray emission). In the regions outside the nugget no mixing of material or melting occurs during welding. This suggests that oxide defects present in those regions are probably part of the defect distribution associated with the parent plate. Further defects could have been introduced in the nugget area by the crushing and embedding action of the tool on the oxide film, present on the plate surfaces before welding. Fatigue initiation in the transverse as-welded specimens occurred at multiple sites with the exception of the specimen tested at 155 MPa (Fig. 4.19). In this specimen, fatigue crack initiation took place from a single site in the region underneath the lip. This would explain the fact that the specimen exhibited a fatigue life approximately 3 times longer than that expected.

Once the lip is removed by surface skimming, the fatigue initiation mechanism in transverse joints changes and nucleation of fatigue cracks takes place still from oxide defects but at areas coincident with local minima in hardness transverses across the weld. The same correlation can be observed in the skimmed plasma welded joints. This

suggests a role of hardness in location of failures, as well as a role of oxide particles. The role can be applied to both FSW and plasma welded joints despite the difference in weld microstructure between the welds.

In the longitudinal joints fatigue initiation has taken place at the top surface tool marks (the lip is parallel to the normal stress axis, Fig. 4.25 and 4.26). Fatigue strength is better than in the transverse direction, but is still only 60% of the parent plate in the high cycle region (Fig. 4.19). As in the previous case fatigue cracks have initiated from local defects close to the tool marks, which the crack plane followed for some distance after initiation. This preferential growth direction suggests a possible correlation between crack morphology and material flow direction [52]. The removal of the tool marks and the defects in that area causes the degradation in fatigue strength to be reduced from 40% to 20% of the parent plate (L) at 10^7 cycles (Fig. 4.20). This indicates that the tool marks have a smaller K_f than the lip.

Skimming the longitudinal joints has modified the residual stress distribution in the specimens (Tab. 4.1b and 4.1c). Residual stress interaction with fatigue initiation depends on the applied stress level during testing [31, 38]. In fact, the application of high stress levels is more likely to produce a larger mechanical stress relief reducing the peaks of residual stresses and their effects on fatigue initiation. In contrast, such interaction would not be expected for the smaller transverse joints, since residual stress is supposed to be negligible.

The S-N curve of the longitudinal skimmed joints (Fig. 4.20) shows that the applied maximum stress levels are between 300 MPa (35526 cycles, 270 MPa) and 170 MPa (run-out at 10717932 cycles, 153 MPa). In the former case, the stress level is 5% lower than the $\sigma_{0.2}$ of the joint (Tab. 4.2). This indicates that the joint cross section has almost completely yielded during the first load cycle. The situation is that shown in Figure 2.7 for positive applied stresses, where the effective stress in the entire joint ranges between $\sigma_{0.2}$ and $\sigma_{0.2} - \Delta\sigma$, corresponding approximately to an effective stress ratio of 0.5. In the latter case, the maximum stress level (170 MPa) is 46% lower than the $\sigma_{0.2}$ of the joint. As discussed in Section 5.3, this situation corresponds to a partial yielding of the joint in

the weld region, whereas most of the parent plate still behaves elastically. This could be an explanation for the fact that skimmed longitudinal welded specimens perform as well as the skimmed transverse joints tested at higher stress levels, whereas at long lives fatigue strength is 13% lower than that in the transverse joints.

Fatigue failures in longitudinal skimmed joints have taken place from the edges of the specimens at the limits of the test gauge length in the fillet radius, (Fig. 3.6). The interpretation of these failures is not simple. A stress concentration of $K_t = 1.4$ is associated with this geometry [50]. Under the specified testing conditions the failure locations indicate that the weld performs in terms of initiation as good as or better than the parent plate.

Transverse skimmed plasma welded joints have always exhibited inferior fatigue strength to the corresponding FSW joints. This could be caused by the presence within the plasma welds of 2.8-3.0 times larger defects than the in FSW joints, as the SEM observation shows (Section 4.2.4). It has not been possible to test as-welded plasma joints in order to make a comparative evaluation of the influence of the surface skimming process on fatigue life. However, the scanning electron microscopy reveals that in the plasma welded specimens the skimming process has brought to the joint surface an internal distribution of pores (Fig. 4.30a and 4.30b). Therefore, those defects could cause crack initiation during the fatigue loading.

The data of Figure 4.34 indicate that initiation in transverse FSW joints occurs from smaller defects (7-70 μm) than in plasma joints (22-197 μm). In FSW joints, the thermo-mechanical affected region is characterised by defects as large as in the heat affected zone. In contrast, in the plasma welded joints, the largest defects are present within the melted region of the weld which is characterised by lower hardness. This combination could be responsible for the lower fatigue strength exhibited by the plasma welded joints.

5.6 Crack propagation in friction stir welded joints

Grain size, hardness, residual stress and ΔK_{NT} values are reported together in Tables 5.1a and 5.1b. ΔK_{NT} values represent an indication of fatigue crack behaviour at low crack propagation rates.

CONFIG.	Long. residual stress	Hardness (*)	Grain size (*)	Fracture appearance	ΔK_{NT} (MPa $m^{1/2}$)
Crack on the PJL	tensile area (8 MPa)	128 Hv1	fine equiaxed (5 -10 μm)	no smearing	2.8 – 3.0
Crack at 11 mm from the PJL	tensile area (246, 65 MPa)	124 Hv1	elongated (600 μm)	no smearing	2.7 – 2.8
Crack at 25 mm from the PJL	compr. area (-13 MPa)	141 Hv1	elongated (400 μm)	smeared	4.4 – 4.8

(*) At the beginning of the propagation test.

Table 5.1a Comparison of residual stress, hardness, grain size, fracture surface appearance and near-threshold stress intensity factor values in the skimmed SCT specimens.

CONFIG.	Transv. residual stress	Hardness (*) (top – bott. surf.)	Grain size (*)	Fracture appearance	ΔK_{NT} (MPa $m^{1/2}$)
Crack on the PJL	–	120 – 133 Hv1	fine equiaxed (5 -10 μm)	smeared	6.4 – 9.6
Crack at 6 mm from the PJL	–	106 – 123 Hv1	elongated (0.9 -1.0 mm)	smeared	7.8 – 11.2
Crack at 28 mm from the PJL	-15 MPa	137 Hv1	elongated (600 μm)	no smearing	3.0 – 3.1

(*) At the beginning of the propagation test.

Table 5.1b Comparison of residual stress, hardness, grain size, fracture surface appearance and near-threshold stress intensity factor values in the skimmed CT specimens.

The crack propagation tests conducted on the FSW joints show that:

a) cracks orthogonal to the weld, in the weld and at 11 mm from the PJL (opposite lip side) exhibit lower ΔK_{NT} values than the parent plate (i.e. cracks grow faster than in the parent plate); cracks at 25 mm from the PJL (opposite lip side) exhibit higher ΔK_{NT} values than the parent plate (i.e. cracks grow slower than in the parent plate).
b) Cracks parallel to the weld at 28 mm from the PJL (opposite lip side) exhibit lower ΔK_{NT} values than the parent plate; cracks in the weld and at 6 mm from the PJL (opposite lip side) exhibit higher ΔK_{NT} values than the parent plate (i.e. cracks grow slower than in the parent plate).
c) Stretching the longitudinal joints (cracks orthogonal to the weld) increases low ΔK_{NT} (reduces propagation rates) and reduces high ΔK_{NT} (increases propagation rates) to the parent plate values.
d) Stretching the transverse joints (cracks parallel to the weld) reduces ΔK_{NT} (increases propagation rates) of cracks in the weld and at 6 mm from the PJL to the parent plate values.
e) Stretching does not affect the crack propagation of cracks parallel to the weld at 28 mm from the PJL (opposite lip side).

5.6.1 Effect of residual stress on crack propagation

As discussed in Section 2.9, crack propagation in a tensile residual stress field is typically characterised by higher crack growth rates, whereas in a compressive residual stress field it is characterised by lower crack growth rates. The 2% permanent deformation has not introduced any appreciable modification either in the microstructure or in the hardness distribution of the joints (Fig. 4.42b and Fig. 4.42c). This implies that the stretched specimens differ from the unstretched ones only by the residual stress distribution.

In the direction orthogonal to the weld (Fig. 4.37a and 37b), cracks at 11 mm from the PJL (opposite lip side) have exhibited the lowest ΔK_{NT} value (2.7 MPa $m^{1/2}$) and crack growth rates 10 times faster than in the unwelded plate (LT). As the joint has been plastically deformed and the residual stresses relieved (Tab. 4.8), crack growth rates and ΔK_{NT} at 11 mm from the PJL have become similar to those in the parent plate (Fig.

4.43). This indicates that, in the unstretched specimens, the tensile residual stress present at 11 mm from the PJL is responsible for the high crack growth rates and low ΔK_{NT} value. Residual stress measurements have confirmed the presence of high tensile longitudinal residual stress (246 and 65 MPa) at 11 mm from the PJL on the unstretched specimens.

Cracks propagating on the weld have exhibited ΔK_{NT} values (2.8 MPa $m^{1/2}$) almost as low as those at 11 mm from the PJL and crack growth rates 4 times lower than those observed at 11 mm. As for the cracks at 11 mm from the PJL, stretching the specimen has resulted in an increase in the ΔK_{NT} value and a decrease in the crack growth rates to the respective values observed in the unwelded plate (LT), (Fig. 4.43). Although this indicates that such modifications are caused by the residual stress mechanical relief, and consequently that residual stress is responsible for the observed crack propagation behaviour in the unstretched specimen, it could not be confirmed by the residual stress measurements. In fact, residual stress measurements carried out on a nominally identical specimen have indicated a value of longitudinal residual stress (8 MPa) within the experimental error associated with the measurement technique.

Orthogonal cracks propagating at 25 mm from the PJL (opposite lip side) have exhibited ΔK_{NT} values (4.4 and 4.8 MPa $m^{1/2}$) higher and crack growth rates 4 times lower than those observed in the unwelded plate (LT), (Fig. 4.43). As the joint has been plastically deformed, crack propagation rates have increased and ΔK_{NT} values decreased to the corresponding values of the unwelded plate (LT), (Fig. 4.43). As observed for the cracks at 11 mm from the PJL, this strongly suggests that the crack propagation behaviour in the unstretched specimen is influenced by the presence of compressive longitudinal residual stress. As for the cracks at 11 mm, the presence of compressive residual stresses could not be confirmed by the residual stress measurements carried out on a nominally identical specimen at 25 mm from the PJL. These measurements have indicated a longitudinal residual stress (-13 MPa) within the experimental error of the measurement technique.

Two sets of residual stress measurements (Tab. 4.8) carried out on two nominally identical SCT specimens at the same location (11 mm from the PJL, opposite lip side) show that residual stress in the welded specimens is characterised by a large variation (up to 75% of the greatest of the values). This indicates that a large variability in the residual stress distribution exists from specimen to specimen. In this light, the fact that residual stress measurements, carried out on the weld and at 25 mm on nominally similar specimens, have not confirmed the presence of high longitudinal residual stresses could be explained as an effect of such a large variability.

For cracks parallel to the weld, in the weld and at 6 mm from the PJL (opposite lip side), (Fig. 4.40 and 4.44), the respective ΔK_{NT} values have shown that mechanical stress relief exerts an influence similar to that observed for the cracks orthogonal to the weld. Although no residual stress measurement has been performed on the CT specimens with the notch in the weld and at 6 mm from the PJL, the effect of the mechanical stress relief on crack growth indicates that crack propagation in the two locations is influenced by residual stress. Evidence of the presence of residual stresses in the unstretched CT specimens with the notch in the weld is indicated by the crack front deviations, as shown in Figure 4.55a. The crack front deviations have been substantially reduced after the stretching operation. This suggests that such deviations are associated with a through-thickness residual stress distribution responsible for local variations in crack growth rates.

SEM observations generally confirm the influence of residual stress on crack propagation. Observations of the fracture surface of cracks orthogonal to the weld at 25 mm from the PJL (Fig. 4.46) reveal frequent smeared areas indicating repeated contacts between the crack surfaces. This suggests that crack closure has occurred during propagation. The series of parallel ridges present on the fracture surface indicate that the crack has propagated following the slip planes within the grains. This mechanism of propagation (slip plane cracking) is typically associated with a crack closure effect owing to a combined mode I and mode II propagation [27]. The incidence of smeared areas is considerably reduced in the stretched specimens since longitudinal residual stresses are relieved. This suggests that crack closure, which has occurred in the

unstretched specimens during the early stages of the crack propagation at 25 mm from the PJL, is associated with the presence of compressive longitudinal residual stresses.

The frequent presence of smeared portions of surface and debris on the fracture surfaces of the cracks parallel to the weld at 6 mm from the PJL (Fig. 4.52), suggests that crack closure has taken place during the initial stage of the propagation. As residual stresses have been relieved by stretching their frequency has been reduced (Fig. 4.54). This suggests that crack closure, occurring during the propagation in the unstretched specimen, is caused by the presence of transverse compressive residual stress. The ridged pattern of the fracture surface also suggests that roughness-induced crack closure due to mixed mode I and mode II has probably occurred in the early stage of the propagation.

Cracks parallel to the weld at 28 mm from the PJL represent an exception to the effect of stretching on crack propagation. In fact, stretching has not caused large changes in the crack propagation behaviour: ΔK_{NT} in the stretched joint is less than 5% of the values measured in the unstretched joints (Fig. 4.40 and 4.44). Fractography carried out on the respective stretched and unstretched CT specimens does not reveal any appreciable difference (Fig. 4.57 and 4.58). Residual stress measurements on the unstretched and stretched CT specimens show in both cases low transverse residual stresses (Tab. 4.8). A possible explanation of this behaviour is based on the observation that the plastic deformation produced by stretching the joint in the direction orthogonal to the weld is mainly concentrated in the weld region, as the strain distribution observed during the tensile test shows (Fig. 4.16).

The effective deformation achieved at 28 mm from the PJL on the side opposite the lip after the 2% nominal deformation can be estimated using the stress-strain curves of the transverse joint obtained during the tensile test. In Figure 5.7, the horizontal line represents the maximum stress achieved during stretching (353 MPa). The arrows indicate the loading-unloading curves for the different regions of the joint.

The unloading lines corresponding to regions of the joint indicate that the effective permanent deformation of the region of the joint at 28 mm from the PJL is less than 0.6%, whereas in the weld it was approximately 3.0%. These considerations suggest that the residual stress relief at 28 mm from the PJL was less effective than on the weld.

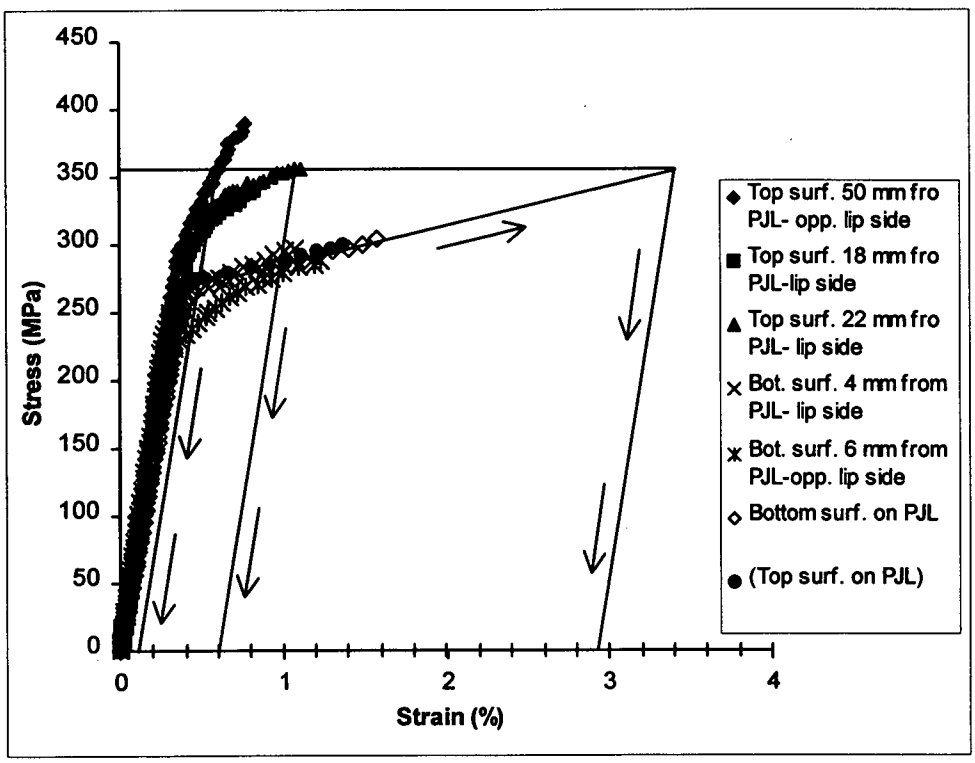

Figure 5.7 Stress-strain cycles in the transverse joint due to the 2% nominal stretching.

5.6.2 Residual stress and crack closure

The effect of residual stress and closure can be discussed in the light of the results from the COL measurements (Section 4.3.7). Cracks parallel to the weld exhibited different ΔK_{NT} values (between 3.0 and 11.2 MPa $m^{1/2}$) but similar ΔK_{eff} values (between 1.7 and 2.0 MPa $m^{1/2}$). This finding is in agreement with the observations conducted on welded joints in presence of residual stresses by several authors [5, 51, 73]. In these works, crack propagation curves obtained by growing cracks at different distances from the weld, i.e. at different residual stress values, coincided when plotted in terms of ΔK_{eff}. This suggests that the near-threshold behaviour of cracks parallel to the weld can be better described in terms of ΔK_{eff}. This consideration is in agreement with the

assumptions made in the crack closure model applied to crack propagation through a residual stress field, as discussed in Section 2.9.

Figure 5.8 shows the effect of the stretching operation on the propagation of the crack at 6 mm from the PJL interpreted through the crack closure model in the presence of residual stress.

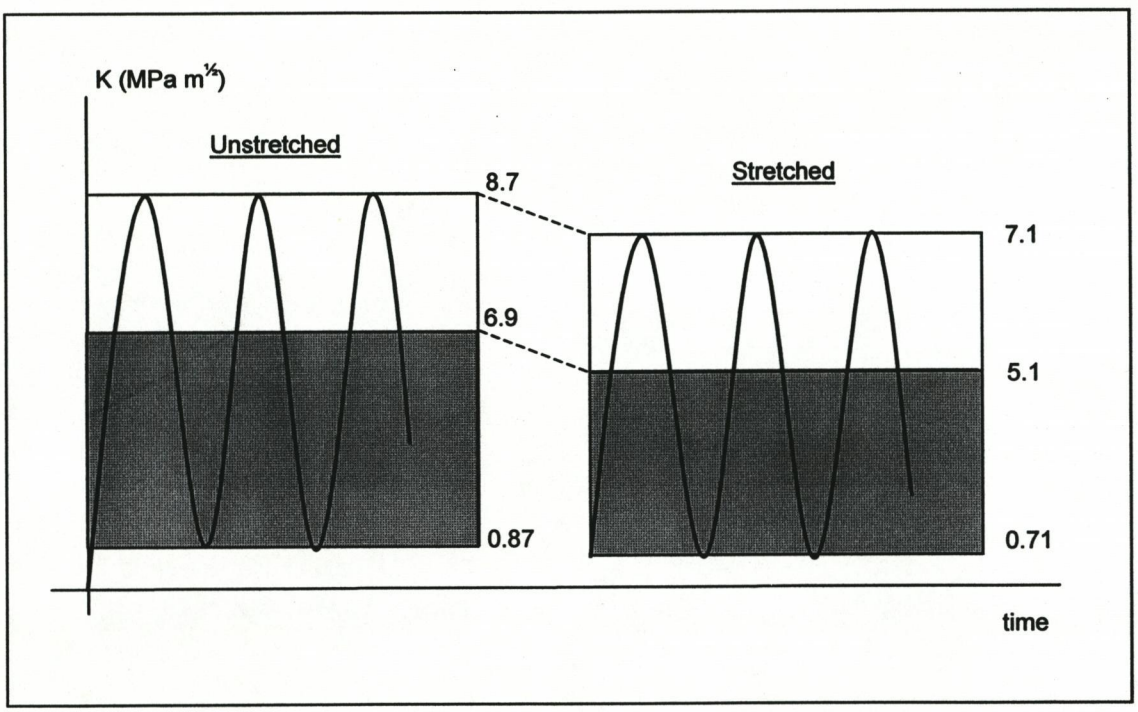

Figure 5.8 The effect of stretching on the propagation of the crack at 6 mm from the PJL interpreted applying the crack closure model.

The amount of crack closure can be estimated by the ratio $\Delta K_{eff}/\Delta K$. This is 0.23 for the unstretched specimen and 0.31 for the stretched specimen. This suggests that compressive residual stress, reduced by stretching, is responsible for the observed reduction in crack closure. The measured values of ΔK_{eff}, between 1.7 and 2.0 MPa $m^{1/2}$, are in general agreement with the values of ΔK_{eff} measured in 2024-T351 base metal in Ref. [79, 34]. These were between 1.33 and 2.0 MPa $m^{1/2}$. This indicates that crack propagation in the near-threshold regime for both welded and base metal can be well correlated by the effective stress intensity factor range ΔK_{eff}, based on measured K_{op} values. Stretched and unstretched CT specimens with the cracks at 28 mm from PJL

exhibit similar K_{op} values. This fact is in agreement with the supposition that at that location residual stress was marginally affected by the 2% nominal stretching.

As discussed in Section 2.9, the application of the crack closure model to crack propagation in a residual stress field does not require any calculation of the stress intensity factor associated with the residual stress distribution K_{res} (although measurements of K_{op} are needed). However, a correlation between closure and weld residual stress can only be established via a quantitative evaluation of K_{res}. This requires the application of numerical methods [51, 70, 73] and a detailed knowledge of the residual stress distribution present in the specimens at the beginning of the propagation test.

5.6.3 Effect of microstructure and hardness on crack propagation

As discussed earlier, the effects of residual stress on crack propagation have been generally reduced in the stretched specimens. For this reason, the effects of microstructure and hardness will be principally discussed in the light of the propagation test results of the stretched specimens.

SEM observations show that for cracks that have propagated through large grains, both parallel and orthogonal to the weld, fracture surfaces are characterised by patterns of parallel ridges as a result of slip plane cracking. The presence of these features is typically associated with roughness-induced crack closure which is responsible for an increase in ΔK_{NT} in coarser microstructures [98]. The effect on ΔK_{NT} of roughness-induced crack closure would be in good agreement with the fact that, among the stretched specimens, cracks that have propagated in coarser microstructure (thermo-mechanically affected regions external to the nugget and heat affected zone) exhibited slightly higher ΔK_{NT} values and slightly lower crack growth rates than in regions with fine microstructure (weld nugget), (Tab. 5.1b). However, it should be observed that the measured differences in the ΔK_{NT} values are in the order of 5% and it is not known if they are greater than the level of error associated with the results.

A comparison between hardness values, which characterises crack propagation in the near-threshold regime, and ΔK_{NT} values in the stretched specimens seems to indicate that regions with lower hardness generally exhibit a superior fatigue crack growth threshold and slower growth rates. This is always true for cracks parallel to the weld but not for orthogonal cracks. Among the latter ones, cracks at 25 mm from the PJL exhibited the opposite behaviour with hardness similar to the parent plate (141 Hv1) and high ΔK_{NT} values (up to 4.8 MPa $m^{1/2}$). It should be observed that cracks parallel to the weld have always propagated through regions of constant hardness (in the direction of propagation) whereas cracks orthogonal to the weld crossed regions of different hardness. It also should be observed that the differences are in the order of 5% of the measured values and it is unknown if they are again greater than the level of error associated with the results.

5.6.4 Crack propagation at higher crack growth rates

Figure 4.40 shows that for crack growth rates greater than 10^{-8} m/cycle, the propagation curves of the cracks parallel to the weld tend to converge. It is reasonable to believe that as the cracks propagate in the specimen, the internal restraints are gradually removed and residual stress gradually redistributed and relieved [24, 110]. It is found that the behaviour exhibited by the orthogonal cracks in the weld, for ΔK values between 5.5 and 6.5 MPa $m^{1/2}$ (Fig. 4.37), is related to the redistribution mechanism and relief of the tensile longitudinal residual stress due to crack propagation [24, 42, 110]. The first phase, for $\Delta K \leq 5.5$ MPa $m^{1/2}$, is typically dominated by the effect of tensile residual stresses which produce an increase in the crack growth rate. As the tensile residual stress is locally relieved by the crack propagation, crack growth rates are consequently reduced (ΔK between 5.5 and 6.5 MPa $m^{1/2}$). From Figure 4.39, it can be observed that these variations in crack growth rate do not correspond to any significant microstructural change along the crack front.

The transition from the near-threshold regime to the intermediate stage of crack growth is characterised by pronounced changes in slope of the crack propagation curves (Fig. 4.37a, 4.37b and 4.40). Table 5.2 shows the ΔK values corresponding to the transition near-threshold regime to the intermediate stage for orthogonal and parallel cracks at

different positions with respect to the weld. An estimate of the cyclic plastic zone at the crack tip has been made according to the expression reported in Ref. [27]. The estimate has indicated that during the transition the cyclic plastic zone sizes have been between 4 and 10 μm for the cracks orthogonal to the weld, and between 4 and 70 μm for the cracks parallel to it. These estimated cyclic plastic zones are generally smaller than the local grain dimensions and do not explain the changes in slope. TEM analysis would be required to establish if the cyclic plastic zone at the crack tip could be correlated with some other characteristic microstructural dimension such as the spacing between the dispersoid particles in the region of propagation [27].

Crack orientation	Distance from the weld	ΔK transition (MPa sqrt m)	Crack orientation	Distance from the weld	ΔK transition (MPa sqrt m)
ORTHOGONAL	in the weld	2.8 - 3.2	PARALLEL	in the weld	6.8 – 10.0
	11 mm	2.9		6 mm	8.3 – 11.4
	25 mm	4.7 – 5.0		28 mm	3.4

Table 5. 2 ΔK values corresponding to the transition near-threshold regime to the intermediate stage for orthogonal and parallel cracks.

6. DESIGN CONSIDERATIONS

6.1 Have FSW joints the right fatigue lives for aircraft structures?

Fatigue requirements in aircraft applications are quite severe. It is therefore of fundamental importance that FSW joints exhibit fatigue performance not inferior to the traditional riveted joints. A significant comparison can be made in terms of S-N data between transverse (skimmed) FSW joints and high-transfer riveted joints. Longitudinal (skimmed) FSW can be compared with low load transfer bolted joints. This latter comparison is based on design considerations.

As discussed in Section 2.11, wing skins can be manufactured welding together, parallel to the wing span direction and therefore to the main normal stress direction, skin components such as integrally stiffened panels. Figure 6.1 shows a longitudinal bolted wing skin joint. In the bolted joint solution, rivets transmit shear flows that arise within the skin panels and stringer web. The rivet action prevents skin panels and splices sliding along the joint direction. At the same time, skin panels and (stringer) splice cross sectional areas are subjected to normal stress associated with the wing bending moment [13, 85]. This action exerted by the rivets and the jointed elements can be represented by a low load transfer bolted joint [25].

Fatigue performance of riveted joints depends on several factors such as plate material properties and thickness, joint geometry, rivet characteristics and riveting procedures [72]. Figure 6.2 shows a comparison in terms of S-N data of longitudinal and transverse FSW skimmed joints with high load and low load transfer riveted joints. The riveted joints data refer to transverse double-row single lap and to low load transfer joints of 1.0 mm 2024-T3 Alclad and 9.5 mm 7010-T7 aluminium plates, respectively [25, 35]. The double-row single lap joints were manufactured with solid countersunk rivets. The low load transfer joints were manufactured using Hi-Lok bolts. The rivet holes were cold worked and the bolts fitted with interference in order to improve fatigue endurance.

Most of the fatigue data for riveted joints have been generated at constant mean stress instead of at constant stress-ratio. In order to be able to compare the riveted joint endurance data with the friction stir welded data at constant R = 0.1, the riveted joint data were corrected for the mean stress effect using Goodman curves [92]. Previous studies have shown that Goodman curves can be used to correlate fatigue data of riveted joints obtained for different stress ratios [77]. The fatigue data obtained using the Goodman correction are in good agreement with experimental results presented by other authors [77].

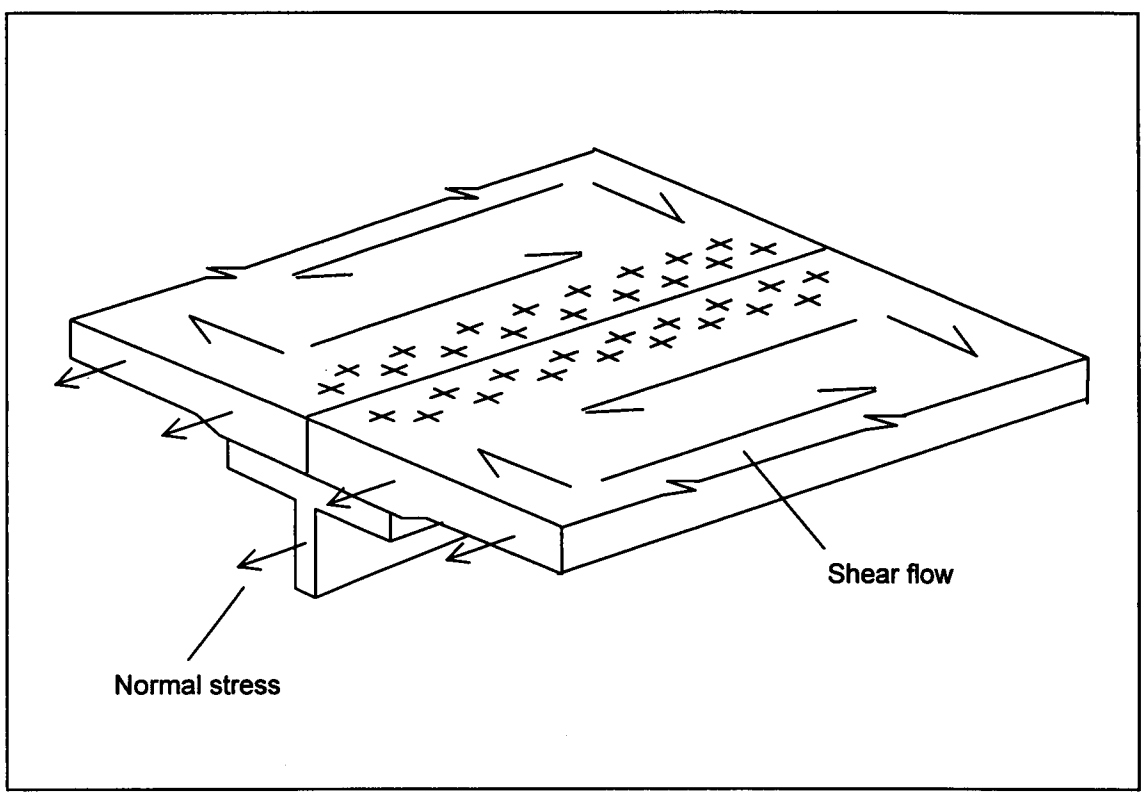

Figure 6.1 Longitudinal splice stringer bolted wing skin joint.

As Figure 6.2 shows, the low load transfer riveted joints exhibit higher fatigue strength than the single lap riveted joints. Longitudinal and transverse FSW (skimmed) joints exhibit equal or better fatigue performance than the riveted joints. In the region between 10^5 and 10^6 cycles, fatigue performance of the longitudinal and transverse welded joints is comparable with that exhibited by the low load transfer bolted joints. At 10^7 cycles,

the transverse FSW joints exhibit a fatigue strength 4 times higher than that of the single lap riveted joints. For the same number of cycles, the fatigue strength of the longitudinal FSW joints is more than 2 times higher than that of the low load transfer bolted joints.

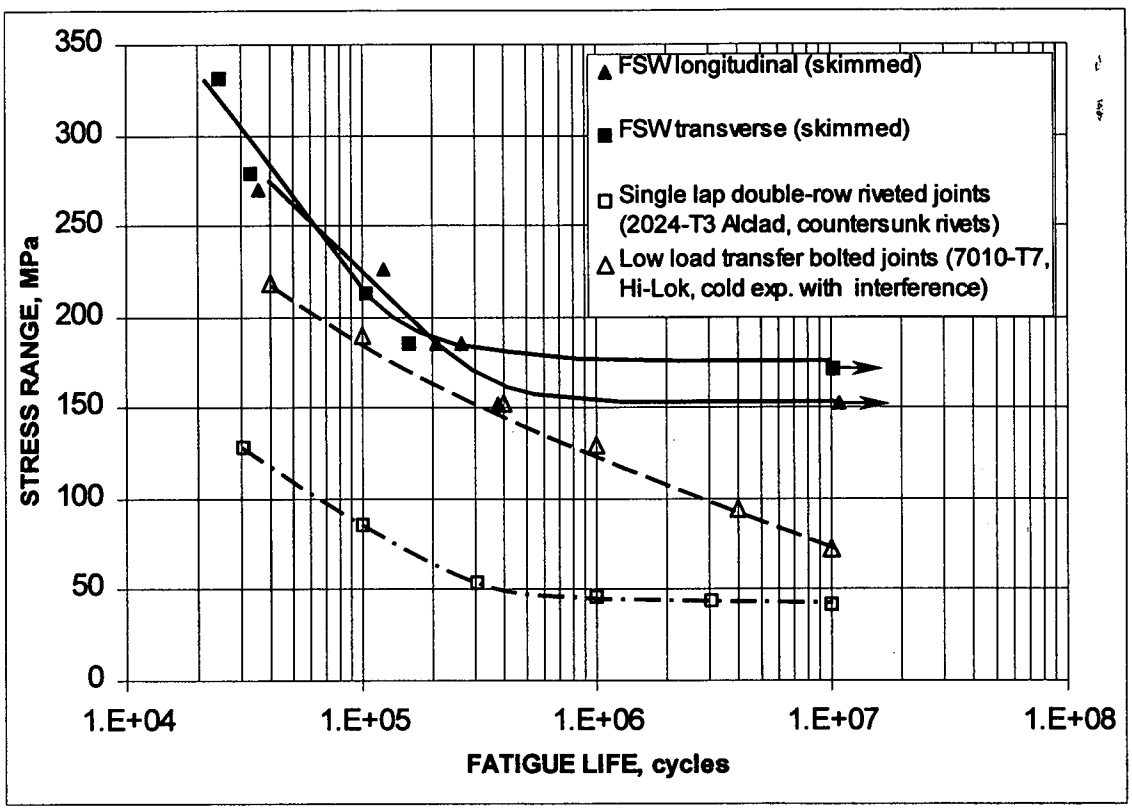

Figure 6.2 Fatigue test results on friction stir welded skimmed joints compared with riveted joint endurance data (R = 0.1).

This comparison shows that, under constant load amplitude, FSW skimmed joints have better fatigue performance than the traditional riveted joints. This indicates that FSW joints could fulfil the severe fatigue requirements for aircraft applications. However, a complete evaluation of the fatigue performance of FSW joints requires a more detailed investigation. Fatigue performance of FSW joints under variable loading spectra and environmental effects on fatigue behaviour, such as corrosion-fatigue, need to be evaluated and failure mechanisms understood.

6.2 FSW joint S-N data: the durability aspect

Aircraft structures, designed to be safe i.e. damage tolerant, have to provide a durable service life in order to be economically affordable for the aircraft operators. In other words, while designing for damage tolerance consists in guaranteeing the structure to be safe from any critical propagation of cracks, designing for durability consists in guaranteeing the structure to be highly resistant to the nucleation of cracks. A durable structure is therefore a structure characterised by high in-service availability and low maintenance costs during the whole operative life [95].

In this light, fatigue data in the form of S-N curves and typical initial defect size and origin, as have been investigated for FSW joints, are essential information in order to design a durable structure. As discussed in Section 2.8, S-N curves indicate the time (cycles)-to-failure at given stress levels. This period includes both the time-to-initiate and the time-to-propagate the cracks. An experimental evaluation of these intervals requires more complex testing, during which most likely crack initiation sites are continuously monitored and first crack detection recorded. Although for welded joints propagation can cover a larger portion of the total life than that in the unwelded material, for long lives (10^6-10^7 cycles) S-N curves can be considered as estimates of the number of cycles to initiate fatigue cracks.

In the light of the previous approximation, Figure 6.2 shows that at 10^7 cycles FSW joints generally exhibit higher number of cycles to initiate fatigue cracks than riveted joints. These observations indicate that the initiation behaviour in FSW joints could lead to a higher in-service durability than that of traditional riveted structures. It should be observed that the evaluation process of the durability of aircraft structures requires much more information and the initiation behaviour under constant amplitude loads of simple joints is just the first step.

6.3 Damage tolerance considerations on FSW joint initial defects

Information about initial flaw size and distribution is extremely important for the design of damage tolerant structures. Fatigue life prediction is based on the typical initial defect

size and distribution. Inspection intervals are also influenced by the initial defect size from which the propagation will begin. For these reasons aircraft structures are certified considering the assumptions made on the initial flaw sizes and locations [101].

The actual damage tolerance requirements for the certification of aircraft structures do not prescribe any initial flaw size, either of the initial manufacturing defects or in-service inspectable flaws, to be considered in the crack growth calculations. Nevertheless, it is required to provide evidence that none of them will grow catastrophically within an established minimum period of repair service [48]. The reason for this consists in the fact that manufacturers are encouraged to improve their manufacturing processes and design skills.

Figure 6.3 compares the initial manufacturing defect size and distribution measured in the welded joints (Section 4.2.5) with the size and statistical distribution of the typical manufacturing defects in riveted joints [90]. Manufacturing defects in riveted joints are typically located on rivet hole surfaces and edges. Their origin is generally related to the hole drilling process, i.e. tool marking, to the presence of inclusions and to other forms of damage. Fractography, both by optical and electron microscopy, has shown the average size of initial defects in riveted joints to be in the order of 20 μm [95, 30].

Although the number of cases reported for the riveted joints in Figure 6.3 is greater than the number of cases observed for the FSW and plasma skimmed joints, the comparison suggests a number of observations. In FSW joints initial defects had the same origin, usually oxide fragments, with their size varying between 7 and 70 μm but more likely to be between 20 and 50 μm. In plasma welded joints, the initial defects had instead various origins (pores, different forms of solidification defects or oxide fragments). As a consequence of this, sizes varied between 7 and 197 μm, being more likely to be between 80 and 100 μm. In riveted joints (Fig. 6.3), the initial defect size typically varies between 9 and 30 μm, being more likely to be between 16 and 24 μm. These data indicate that riveted joints are characterised by a smaller initial defect size than FSW skimmed joints, whereas plasma skimmed joints exhibit the largest initial defect size.

As it was previously observed, cracks in riveted joints initiated from larger defects typically located at the rivet holes. The highly localised stress concentrations associated with the rivet holes are additional detrimental factors influencing crack initiation, propagation and fatigue life. Whereas in welded joints fatigue cracks initiate from defects which are typically located on the two external surfaces of the joints (mainly on the weld area), in riveted joints, cracks can initiate from defects located at rivet holes and be hidden by rivet heads. This suggests that in welded joints crack locations can be more easily accessible for inspections than in riveted joints. On the other hand, whereas in riveted joints defects are concentrated at rivet holes, welds potentially represent an area of continuous distribution of defects from which cracks could initiate. These aspects, influencing the level of defect detectability, should be take into account in the calculation of the initial flaw sizes of damage tolerant FSW components.

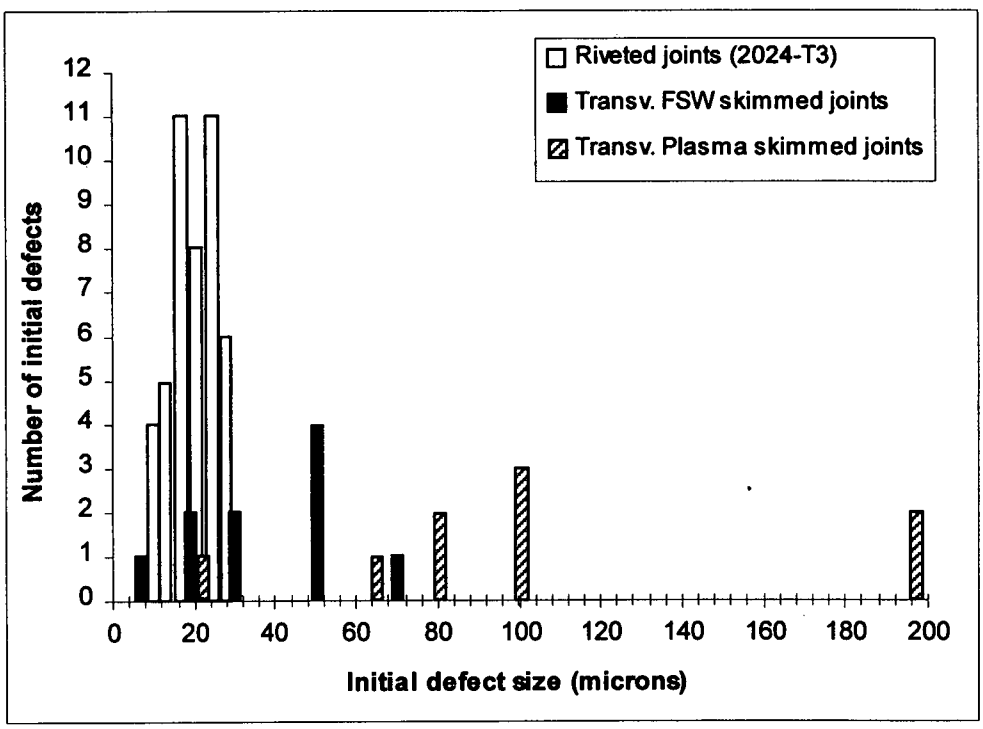

Figure 6.3 The defect size and distribution measured in the FSW and plasma skimmed joints (Section 4.2.5) compared with the defect size and statistical distribution in riveted joints.

6.4 Damage tolerant aircraft welded structures: which design philosophy?

Damage tolerant structures are designed to operate safely until possible existing damages are not detected during inspections and damaged components are replaced [101, 95]. Damage tolerant structures can be designed as fail-safe or slow crack growth structures. The former relies on the mechanism according to which the reduction in stiffness of a damaged structural component causes stresses to be redistributed through alternative load paths. This allows the structure to withstand operative loads until the damage is not detected and the component replaced [48, 101]. Fail-safe structures can be designed as multiple load path or crack arrest structures. A typical example of a multiple load path structure is the riveted skin stringer panel where stress redistribution from the skin to the stringers causes a crack propagating through the skin to be arrested (crack arrest structures) before reaching a critical length [91].

Slow crack growth structures are typically single-load path structures. In these structures, stress redistribution is limited by the fact that no alternative load paths are available. Damage tolerance (in this case more appropriately "crack tolerance") is achieved by an optimum choice of materials and design stress levels in order to guarantee that fatigue propagation of cracks present in the structure is slow enough to allow safe detection within the specified inspection intervals. An example of damage tolerant single load path structure is the single plank lower wing stiffened panel of integrally machined construction. Failure of the entire plank would cause failure of the wing. Thus, the panel is classified as single load path slow crack growth if the extent of damage from detectability to criticality is readily detectable [101].

It clearly appears that fail-safe structures can only be obtained by assembling different structural components and that an integral or monolithic structure (i.e. typically a welded structure) can only be classified as a slow crack growth structure. Regulators classify damage tolerance structures as either single or multiple load path [48]. However, single load path structures are allowed, but not recommended, provided that partial damage can be shown to be obvious before it becomes critical. In this light, it is of fundamental importance for the certification of single load path structures to

guarantee a high level of inspectability and to develop a solid understanding of the crack initiation and propagation behaviour.

6.5 Welded wing structure: proposed solutions

The stress distribution in a wing box is generally studied using simplified approaches depending on the level of accuracy required. The Elementary Theory [13] assigns to each structural element well defined roles: stringers and spar caps are subjected to normal stress due to the wing bending moment. Skin, spar webs and ribs carry the shear flows due to the wing torsion. A more refined model can be obtained correcting stress flows obtained with the Elementary Theory with stresses calculated applying the Shear Lag Theory or the Hyperstatic Model approach [85]. In the present analysis, the torsional contribution to the wing stress distribution is neglected. This simplified approach is based on the fact that the most significant contribution to the stress distribution in a wing structure is due to the wing bending moment. The error introduced applying this simplified model is generally considered acceptable for a preliminary analysis of the stress distribution in a wing structure [72].

The fundamental problem in designing a welded wing structure consists in defining the position and orientation of welds with respect to the stress distribution in the structure. In principle, welded joints should be located and orientated in order to minimise weld stresses. This would allow using higher design stress levels in order to maximise the strength to weight ratio, i.e. the structural efficiency. Static strength requirements prescribe that the structure must be able to withstand the limit load (defined as the maximum load expected in service) without any detrimental permanent deformation [47]. In design terms this translates to the condition that under the limit load the structure shall not yield. From these considerations, it follows that longitudinal welded joints, exhibiting a superior yield strength (Tab. 4.2), should be preferred to transverse welded joints in the design of a welded wing structure.

From a damage tolerance point of view, the design of welded structural components should be focused on maximising the level of inspectability of welded joints. Cracks

that originate from welds should be readily detectable in order to allow the component to be replaced before critical crack lengths are achieved. Design should consider the important manufacturing aspects typical of welded components such as allowing accessibility for welding and assembly, weld deformation and residual stresses. Design should also consider the use of large extruded components in order to reduce machining operations and number of parts.

6.5.1 The outer wing stiffened panel

Possible solutions for a lower wing panel have been examined. Figure 6.4 shows two skin-skin longitudinal welded joint solutions: the single load path solution (Fig 6.4, a) and the fail-safe solution (Fig. 6.4, b). In both solutions a welded joint is produced in the skin along the span wise direction. Welds are subjected to a normal stress parallel to their axis. This stress is typically tensile during flight and compressive during ground manoeuvers. In the former solution (Fig 6.4, a), integrally stiffened panels are joined by welding the skin. This is a monolithic structure and it can only be designed for damage tolerance as a slow crack growth structure. In the latter solution (Fig. 6.4, b), stringers are fastened to the welded skin as in the traditional riveted wing panels. This allows redistribution of stresses from the skin to the stiffeners if a crack propagates through the skin. In this case crack arrest design criteria can be applied. Stringers fastened next to the welded joints could benefit in terms of crack propagation resistance from the weld compressive residual stress distribution.

As discussed earlier, fatigue cracks are more likely to initiate at rivet holes and welds. In the single load path solution (Fig 6.4, a), cracks that initiate from the welds can be easily detected as soon as they break through the outer skin surface. In the fail-safe solution (Fig. 6.4, b), cracks can initiate at the stiffener rivet holes. Early detection of these rivet hole cracks requires internal inspections. For this reason, the single load path solution (Fig. 6.4, a) presents a higher level of inspectability than the fail-safe solution (Fig. 6.4, b). Longitudinal tensile residual stresses would tend to increase crack propagation rates and to reduce ΔK_{th} values (Sections 2.9, 4.3.2, 4.3.3 and 4.3.4). For this reason, enhancing early detection of cracks in welds is particularly important.

The skin-skin welded solutions in Figure 6.4 allow several potential manufacturing advantages. Furthermore, in the single load path solution, the integrally stiffened panels could be produced by extrusion in order to minimise machining operations and scraping of material. Skin thickness could be increased at the welded joints obtaining a local reinforcement. This would also allow skimming of the weld surfaces, obtaining considerable improvement in fatigue strength (Section 4.2.3).

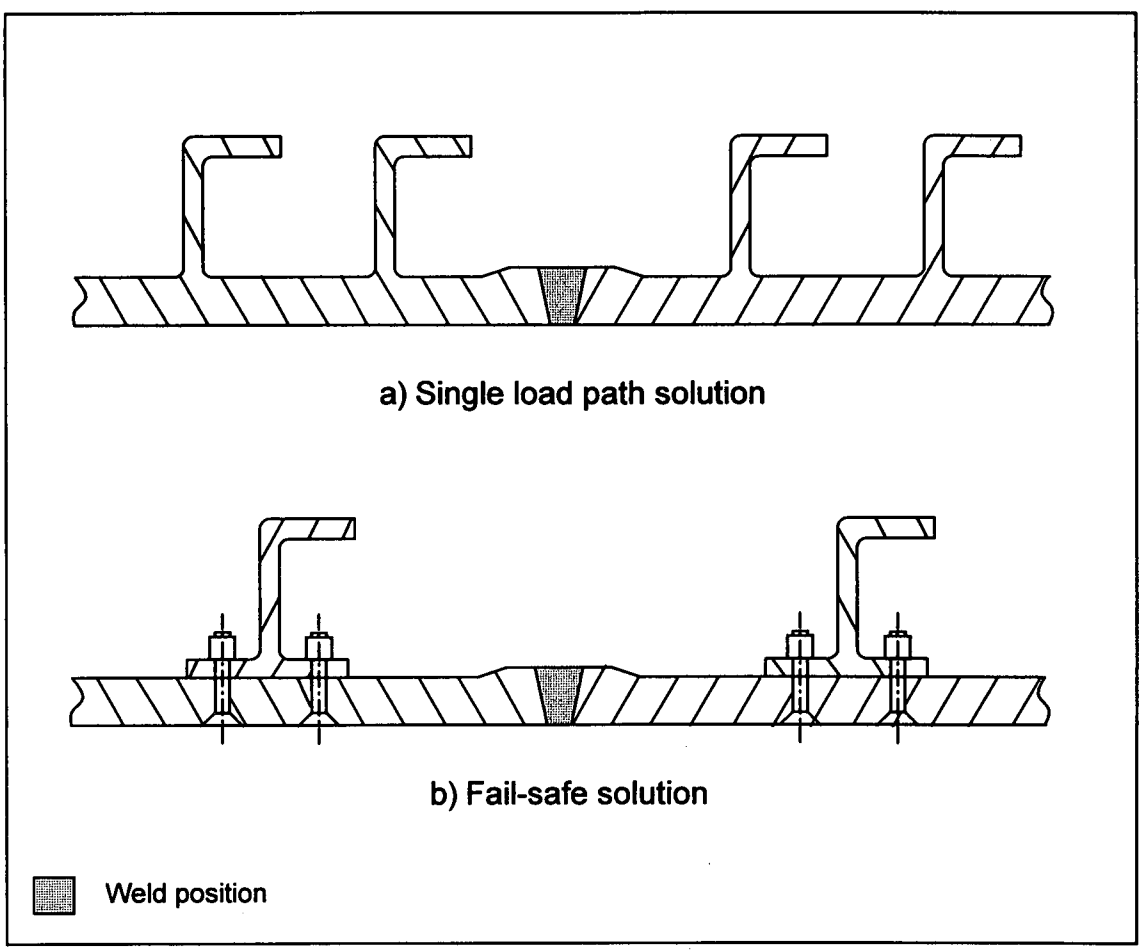

Figure 6.4 Two skin-skin welded joint solutions for a lower wing panel.

Figure 6.5 shows the skin-stringer web welded solution. Stringer webs are butt welded to integral outstanding supports present on the skin panel. In this case the skin panel is weld-free limiting the degradation of mechanical properties due to welding to the stringer web metal only. The thickness of stringer webs is generally lower than the skin

thickness. This allows applying this solution also in the inner region of the wing box where the skin thickness typically exceeds the maximum weldable thickness. Both stringers and panels can be either machined or extruded with integral outstanding supports.

Fatigue cracks propagating from weld defects would not be detected before growing through the stringer cross section and breaking through the entire skin thickness. For this reason, the skin-stringer web welded solution presents a lower level of inspectability than the skin-skin welded solutions. The structure could be classified as damage tolerance fail-safe (multiple load path) if following the failure of one welded panel the load redistributes on the adjacent panels and the structure is able to withstand the operative loads until damage detection and repair.

6.5.2 Spars

As Figure 6.6 shows, spars are subjected to a normal stress distribution due to the wing bending moment. It can be noticed that part of the spar cross section is under normal tensile stress and part under compressive stress. A neutral bending axis, where the normal stress associated with the wing bending moment is zero, can be localised between the tensile and compressive areas. In order to minimise the stress acting on the weld, spars could be manufactured in two parts and joined by welding the web along the neutral bending axis (Fig. 6.6). It should be observed that welds positioned along the neutral bending axis would still be subjected to spar web shear stress and to the normal stress associated with the spar out-of-plane bending moment. The presence of these stress components is likely to influence the weld mechanical behaviour. The investigation of this behaviour would require testing of welded components under representative stress distributions.

Integral web-cap semi-spars could be extruded and machined to final dimension and shape. This would eliminate traditional spar web-cap bolted connections obtaining a sensible reduction in weight and number of parts. Cracks initiating from weld defects under the effect of weld tensile residual stress would propagate through the lower part of

the spar where normal stresses are expected to be tensile for most of the operative conditions. Internal inspections should be required in order to ensure ready detection of possible cracks.

6.5.3 Ribs

A more refined stress model is required in order to analyse the stress field present in a rib. In the elementary theory of wing structures rib frames are subjected to normal stresses and rib webs to shear flows [72]. Figure 6.7 (a) shows a possible welded rib solution. Welds can be positioned along the lower or upper rib profiles at the ends of the rib web. The welds are mainly subjected to the normal stress parallel to the weld direction present on the rib frame.

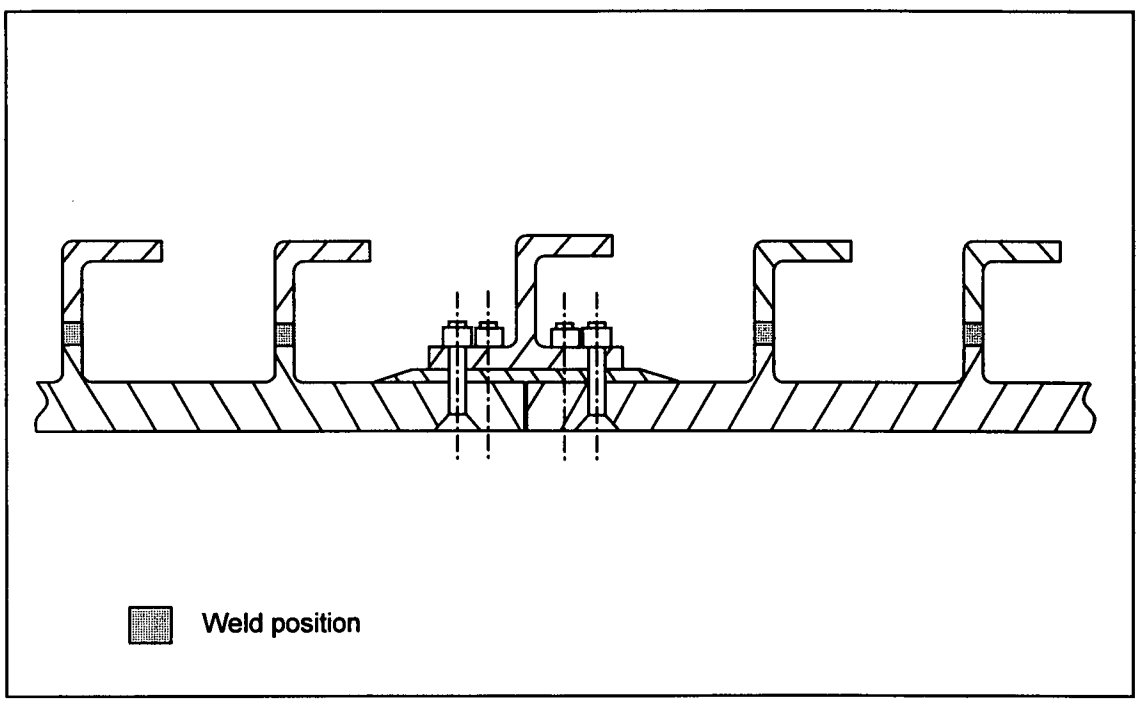

Figure 6.5 Possible design for a welded lower wing panel: skin-stringer web welded solution.

Figure 6.7 (b) shows the manufacturing benefits of the proposed solution. Spars could be machined from bulk plates. Welding rib webs to rib frames would sensibly reduce machining operations and scrapping of material. From a damage tolerance point of view, fatigue cracks initiated in the welds are expected to propagate through the rib

frame cross section under the influence of weld tensile residual stresses and applied loads. Cracks would be readily detectable only during internal inspections.

6.6 Damage tolerance evaluation of aircraft welded structures

Figure 6.8 shows a procedure that can be applied for the evaluation of the damage tolerance characteristics of a welded aircraft structure. Critical locations where cracks are more likely to initiate and propagate should be selected. For a welded structure, these are typically welds, HAZ and locations characterised by high stress concentration.

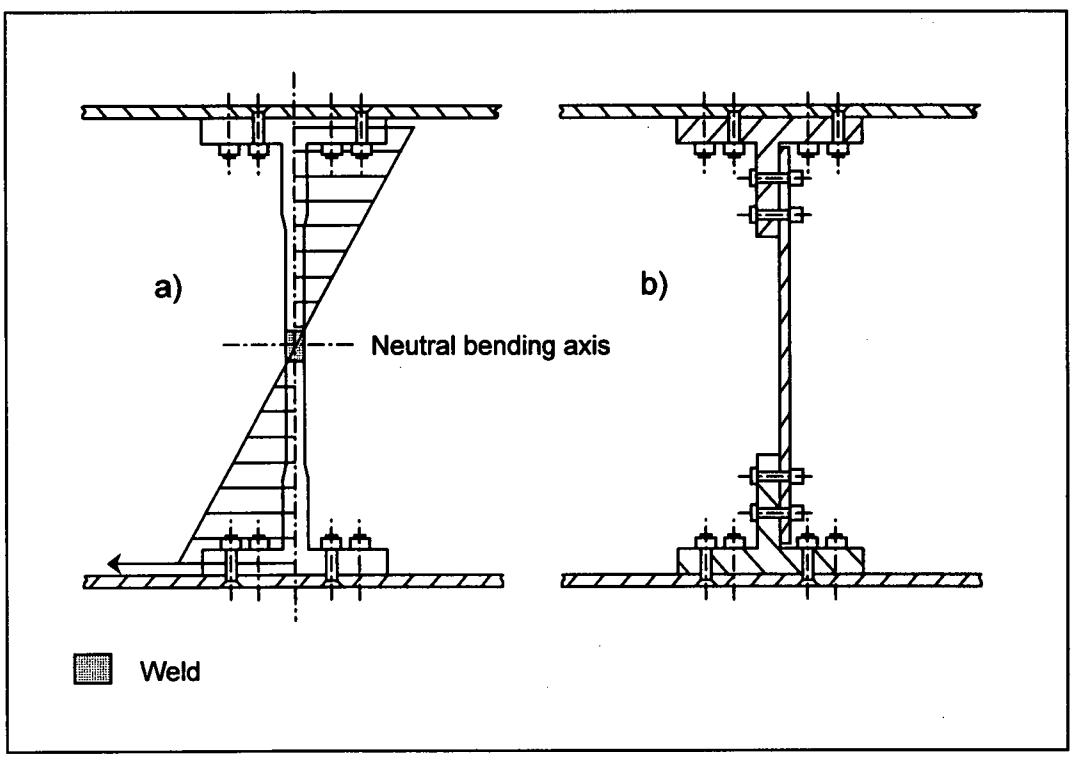

Figure 6.6 Welded spar solution (a) compared with a traditional mechanically fastened solution, (b).

For each critical location stress spectra based on the aircraft typical utilisation should be developed. This is typically obtained by converting the load factor spectrum into stress using a stress structural model [13]. Constant amplitude crack propagation data, as those obtained in Sections 4.2.1 and 4.2.3 and testing full scale welded components,

should be developed taking into account weld residual stress effects and environmental conditions. Particularly high humidity, high temperature and salt spray can cause crack propagation rates in welds and parent material to increase considerably [24].

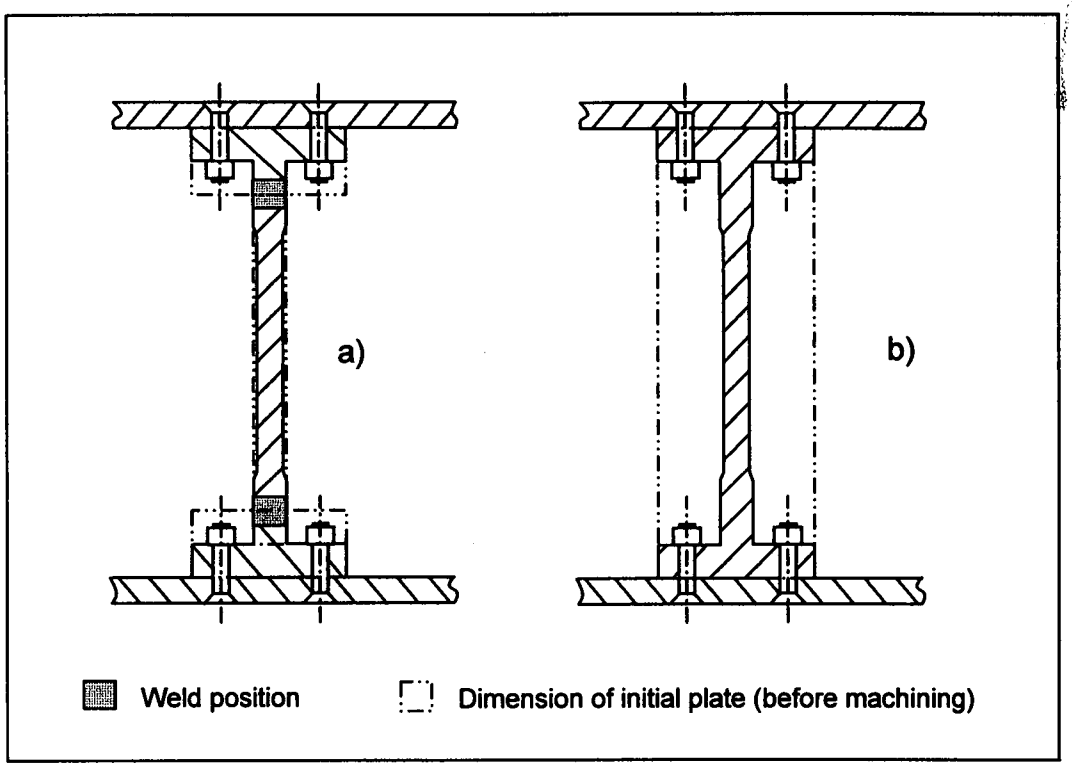

Figure 6.7 A possible welded rib solution (a) is compared with the traditional machined rib solution (b). The amount of machined material is indicated.

Stress intensity factor solutions should be developed for each location as functions of the crack length. At this stage, crack growth curves for cracks at each critical location can be obtained by integrating the material crack growth data. The crack growth analysis is carried out using specific software packages and fundamentally consists of solving the following equation:

$$n = \int_{a_i}^{a_f} \frac{da}{f(\Delta K, C)} \qquad \textit{Eq. 6.1}$$

where n is the number of cycles from initial crack size a_i to final crack size a_f, and C a factor representing the influence of material.

Crack growth retardation due to tensile overloads and acceleration due to compression loads should be accounted for by suitable analysis models such as yield zone or crack closure models [27, 98]. Crack growth testing should be conducted on welded joints representative of structural elements under flight-by-flight spectrum loading in order to validate the analysis model.

Critical crack lengths and residual strength of the structure in terms of damage extent at limit load should be estimated considering the fracture toughness values of the weld, HAZ and the parent material for the full range of thickness used. Inspection methods should be developed at this stage of the analysis. This should take into account the accessibility, the geometry of the welded component and typical characteristics of the weld initiation behaviour such as those discussed in Section 6.3. Calculation of the inspection intervals is the final part of the damage tolerance analysis. The safe period for inspections is defined as the period from detectable to critical at limit load, Figure 6.9.

The inspection interval is typically obtained by dividing the safe period into three intervals so that if an inspection is made just before the crack reaches a detectable size, then one possibility of missing a detectable crack size is allowed before failure at limit load is imminent [101]. The determination of the detectable crack size depends on the selected inspection method, defect locations, distribution and typical size. Accidental damage and corrosion should be considered in addition to typical manufacturing defects.

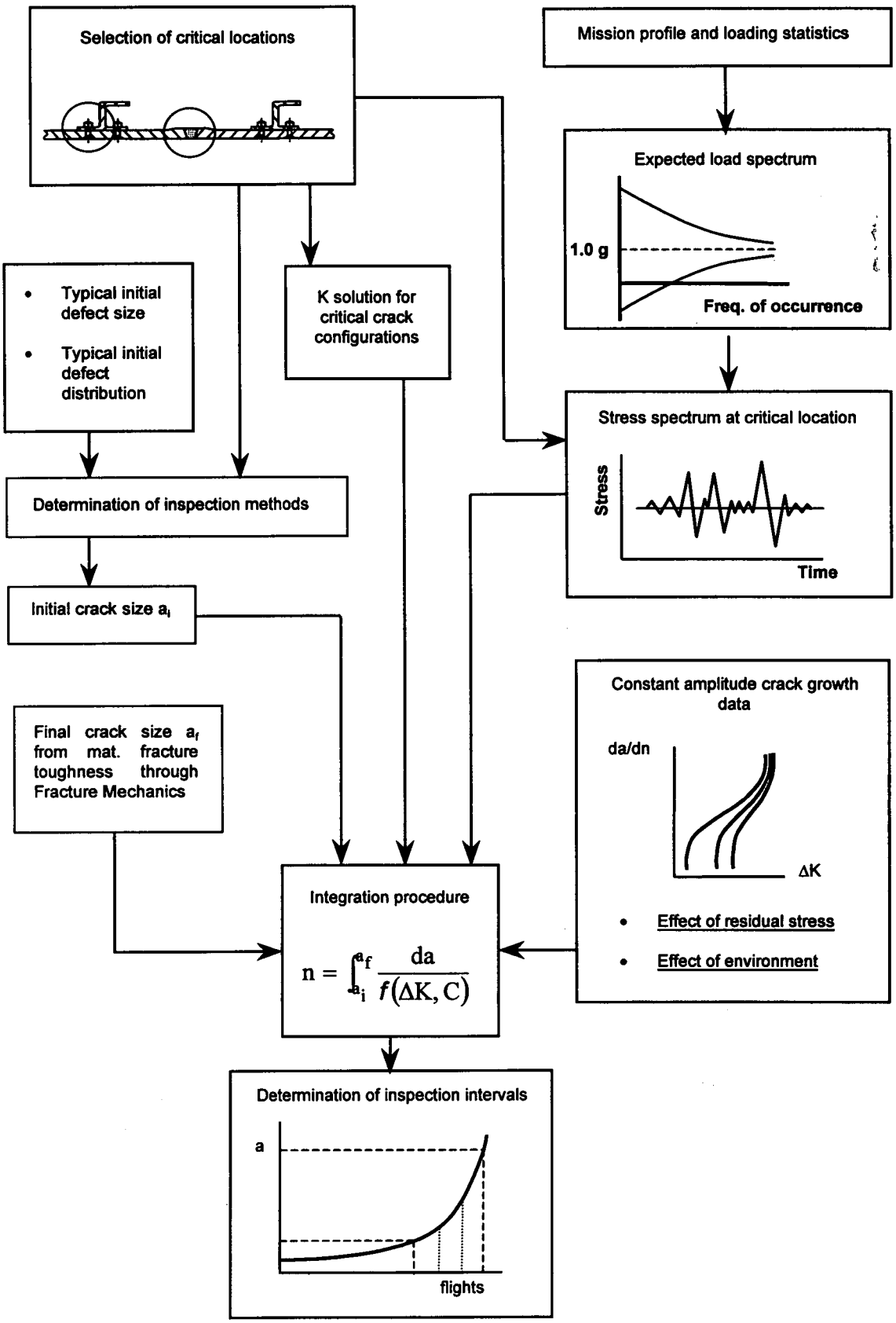

Figure 6.8 Damage tolerance evaluation of aircraft welded structures.

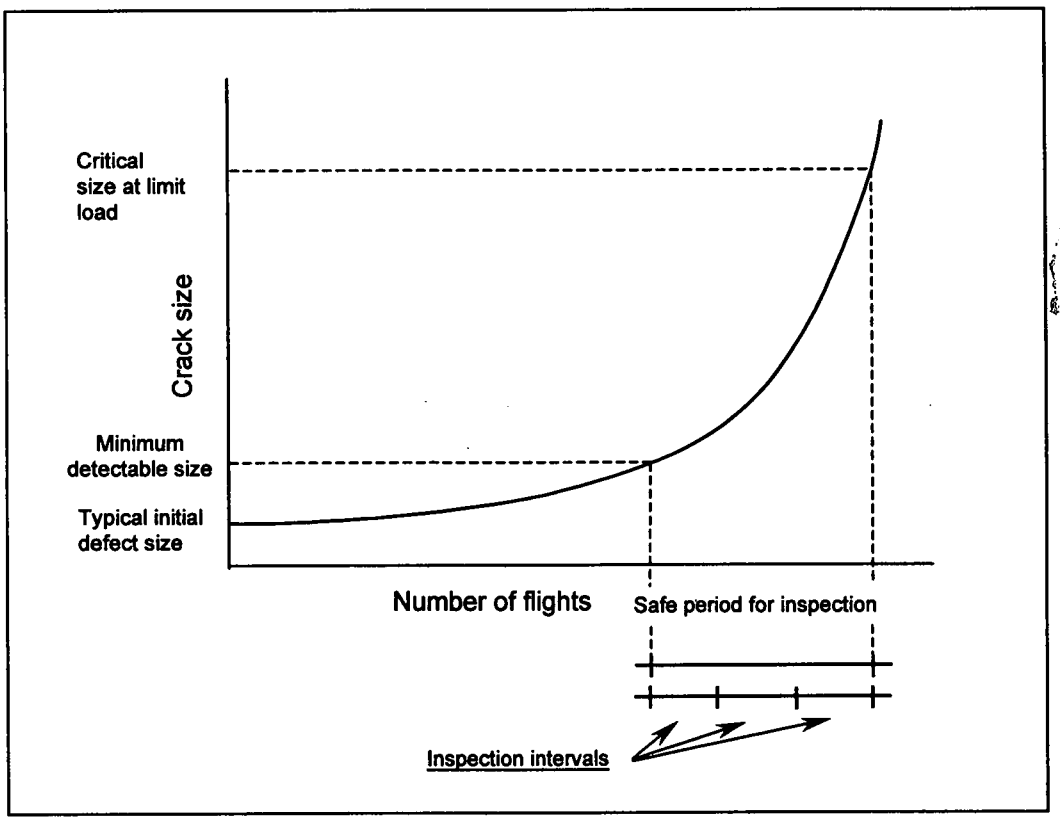

Figure 6.9 Determination of inspection intervals in damage tolerant structures.

7. CONCLUSIONS AND RECOMMENDATIONS FOR FUTURE WORK

7.1 Welded joint characterization

1) FSW structures are asymmetric with respect to the PJL, with hardness and structure also changing through the plate thickness. On the top weld surface, a sharp notch (lip) is formed on one side of the PJL, parallel with the weld, caused by flow of metal over the top surface of the original plate during the welding process.

2) Butt FSW structures in 6.35 mm thick 2024 T-351 plates consist of three regions: a) a central oval nugget of 10 mm diameter, containing 5-10 μm equiaxed re-crystallized grains; b) a thermo-mechanically affected region of elongated and distorted grains (600-1000 μm in size), 5-13 mm from the plate PJL; c) a heat affected region of similar grain structure to the parent plate but with different hardness values, extending to 44 mm (lip side) and 50 mm (side opposite lip) from the plate joint line.

3) Hardness minima occur 6 mm from the PJL in the direction opposite to the lip (103 Hv1) and 4 mm from the PJL on the lip side (109 Hv1) in region (b). Within the central region (a), hardness increases to 138 Hv1 on the top weld surface and to 117 Hv1 on the bottom weld surface. At 22 mm (19 mm) from the PJL on the side opposite the lip (on the lip side), the hardness profiles show a maximum value of 149 Hv1 (142 Hv1). Hardness decreases again to 129 Hv1 on the side opposite the lip (132 Hv1 on the lip side) before reaching the parent plate value (142 Hv1).

4) Plasma butt welds in 6.35 mm thick 2024-T351 plates show a central fusion zone (7 mm across) surrounded by a HAZ extending to 30 mm on each side from the PJL. The hardness exhibits its minimum value in the fusion zone on the PJL (93-110 Hv1) and a peak (142 Hv1) at 6 mm from the weld. A point of local minimum (102 Hv1) is exhibited at 11 mm from the PJL.

5) The HAZ in FSW joints was 1.6 times the width of that in the plasma welded joints. Hardness minima and maxima in FSW were 1.1 times the value measured in the plasma welded joints.

6) Residual stress measurements made on FSW dog-bone specimens (as-welded surface state) using hole-drilling showed that the weld contained longitudinal tensile residual stress of 33 MPa on the PJL and 73 MPa at 11 mm on the side opposite the lip. Moving out from the PJL, the longitudinal residual stress became compressive with –51 MPa at 25 mm from the PJL. Transverse residual stresses were between 3 and 20% of the longitudinal values.

7) The process of surface skimming to remove 0.5 mm from each side of the welded plate significantly changed the residual stresses. Surface skimming produced a complex response, increasing the longitudinal tensile stress 11 mm from the PJL from 73 to 264 MPa and transverse residual stresses 25 mm from the PJL from –2 to –192 MPa. It is not known how the surface skimming process would affect the weld residual stress distribution in a real structure. The evaluation of the effects of surface skimming on weld residual stresses in a real structure would require the extensive use of finite element analysis and residual stress measurements.

8) Tensile testing on specimens with transverse welds showed that the softest parts of the HAZ yielded first at 243 MPa (88% of the parent plate value), reaching an ultimate stress of 409 MPa (84% of the parent plate value). Tensile failures occurred in shear in a through thickness plane at 45° to the tensile axis. The location of the failure plane was coincident with the softest areas of the HAZ (104-109 Hv1).

9) Tensile testing on longitudinal welded specimens showed tensile properties to be generally superior to those for transverse welds. 0.2% proof stress increased by 30% and ultimate stress by 4% when orientating the weld parallel to the normal stress axis. These results depended on the specimen test section width (HAZ-parent metal ratio) and

therefore they are to be considered as a lower estimate of the tensile properties of wider welded joints.

7.2 Fatigue properties

1) Fatigue (S-N) tests on longitudinal FSW in the as-welded surface state showed an endurance limit at 10^7 cycles of between 121 and 105 MPa. This was approximately 58% of the parent plate (L) value (between 185 and 203 MPa). Samples containing transverse welds in the as-welded condition were 30% lower than those with longitudinal welds. Fatigue cracks always initiated from local defects (oxide inclusions 20-70 μm in diameter) at irregularities on the top weld surface: these were the ripples due to the tool marks in the longitudinal welds and the "lip" in the transverse welds. The stress concentration value associated with the lip was estimated to be between 2.1 and 2.6.

2) Surface skimming the longitudinal FSW samples to remove 0.5 mm from each surface increased the endurance limits to values around 80% of those for the parent plate (L). In the transverse FSW joints, the removal of the lip by surface skimming increased the fatigue strength to values higher than 90% of those for the parent plate (LT). Crack initiation in the transverse skimmed specimens occurred at oxide inclusions 7-70 μm in diameter. The cracks always initiated at the softest regions of the HAZ; the inclusions were present in the original microstructure of the parent plate. Crack initiation in the longitudinal skimmed specimens always took place from the edge of the specimens at the end of the gauge test length.

3) The S-N curve for plasma welded joints in the skimmed condition showed a fatigue endurance limit at 10^7 cycles 20% lower than those for friction stir welds. Cracks initiated at pores and at solidification defects in the fused regions of the weld. These were 20-200 μm in diameter, therefore larger than the oxide defects in friction stir welds. Fatigue initiation locations corresponded to the softest regions of the HAZ.

7.3 Crack propagation

1) Fatigue crack growth measurements performed on 2024-T351 parent plate (LT and TL crack orientations) showed good agreement with published ESDU data for this material.

2) Crack propagation tests were carried out on longitudinal FSW specimens. Cracks orthogonal to the weld were started at artificial thumbnail defects in the weld, 11 mm and 25 mm from the PJL (opposite lip). Cracks starting from the weld and 11 mm from the PJL exhibited faster growth rates (up to a factor of 50) than the parent plate (LT). Cracks 25 mm from the PJL (opposite lip) exhibited slower propagation rates (up to a factor of 10) than the parent plate (LT).

3) Cracks growing parallel to the weld 28 mm from the PJL (opposite lip) exhibited 40% lower ΔK_{NT} values and about 6 times faster growth rates than the parent plate (TL); cracks in the weld and 6 mm from the PJL (opposite lip) exhibited higher ΔK_{NT} values (up to 2 times the parent plate value) and 14 times lower growth rates than the parent plate (TL).

4) Stretching the welded panels by 2% nominal plastic strain had dramatic effects on crack growth rates and ΔK_{NT} values. Cracks orthogonal to the weld had similar growth rates and ΔK_{NT} values, irrespective of their location. The growth rates were almost identical to those found in the parent plate material (LT). Cracks parallel to the weld 6 mm from it and in the PJL after stretching exhibited similar growth rates and ΔK_{NT} values to the parent plate (TL). Crack growth rates 28 mm from the weld line were unaffected by the stretching operation. This different response is attributed to the non-uniform plastic strain distribution in the joint obtained during the 2% nominal stretching.

5) The stretching operation was found to reduce residual stresses orthogonal to the direction of crack propagation significantly. Stretching did not cause any significant changes in the joint hardness and microstructure. This indicates that the differences in

fatigue crack growth rate and ΔK_{NT} values observed in each specimen are a consequence of residual stress differences rather than hardness or microstructural differences. The conclusion is further confirmed by the crack closure measurements. ΔK_{eff} values for cracks were all similar for the same values of growth rate despite great differences in nominal values of ΔK as generally observed in previous works.

7.4 Design considerations

1) FSW transverse skimmed joints exhibited (under constant load amplitude) fatigue strength equal or better than mechanically fastened joints. This suggests that FSW aircraft structures could have equal or better in-service durability than riveted structures.

2) Typical initial defect sizes in FSW skimmed joints (7-70 μm) were larger than in the riveted joints (between 9 and 30 μm, being more likely to be between 16 and 24 μm). In contrast to the welded skimmed joints, in riveted joints cracks initiated from defects at rivet holes where high stress concentrations were present. These differences are likely to produce a strong impact on the determination of inspection intervals.

3) Design of aircraft structures should consider the use of longitudinal welded joints in order to maximise structural strength. Fail-safe can be only achieved with hybrid structures (welded-riveted) whereas welded structures could be certified as damage tolerant slow crack growth.

4) Weld residual stress in real structures can be larger than that in smaller test specimens. For this reason, the effects of weld residual stress on crack propagation observed in test specimens may be amplified in the real structure. In this light, damage tolerance evaluation of large welded structures should consider test results obtained from welded specimens as well as from full scale components.

7.5 Recommendations for future work

1) Control of residual stress is a major requirement for effective prediction of fatigue crack growth rates in welded structures. Quantitative models able to predict crack

propagation behaviour based on information on residual stress and applied loads need to be developed. This can be fully achieved provided that a detailed description of the residual stress distribution around FSW joints is available.

2) Developing a statistical database of mechanical properties is essential to any in-service application. FSW mechanical properties (tensile, fatigue and crack propagation) should be described on the basis of results obtained on a large population of specimens.

3) The present research does not address the prediction of fatigue crack growth rates in welded aircraft structures. Areas where further research is required include:

- A detailed study of the interaction of short cracks with weld microstructures and residual stress levels
- Testing under compressive mean loads representative of the upper wing loading
- Testing under variable amplitude loading
- Assessment of models to obtain fatigue crack growth lives under variable amplitude loading
- Testing of full scale welded structural components.
- Testing of welded structural elements under flight-by-flight loading spectra.

8. REFERENCES

1. Aluminium Federation, The properties of aluminium and its alloys, Alfed, 1983
2. Askeland, D. R, The science and engineering of materials, VNR International, 1984
3. ASTM E 647 Appendix X2, Recommended practice for determination of fatigue crack opening load from compliance, American Society for Testing and Materials, 1997
4. Backlund, J. et al, friction stir welding: weld properties and manufacturing techniques, 7th International Conference: joints in aluminium, INALCO 98, Cambridge, UK, 16 April 1998
5. Beghini, M, et al, Fatigue crack propagation through residual stress fields with closure phenomena, *Engineering Fracture Mechanics*, Vol. 36, No. 3, 1990, pp. 379-387
6. Bertini, M. at al, Fatigue crack growth in residual stress fields: experimental results and modelling, *Fatigue and Fracture of Engineering Materials and Structures*, Vol. 17, No. 12, 1994, pp. 1433-1444
7. Bhuyan, G. and Vosikovsky, O, Prediction of fatigue crack initiation lives for welded plate T-joints based on the local stress-strain approach, *International Journal of Fatigue*, Vol. 11, No. 3, 1989, pp. 153-159
8. Biallas, G. at al, Mechanical properties and corrosion behaviour of friction stir welded 2024-T3, First International Symposium on Friction Stir Welding, Thousand Oaks, CA, 14-16 June 1999
9. Booth, G. S. and Maddox, S, Correlation of fatigue crack growth data obtained at different stress ratios, ASTM STP 982, Mechanisms of Fatigue Crack Closure, 1988
10. Brandon, D. et al, Microstructural characterization of materials, John Wiley & Sons, 1999
11. Bratukhin, A. G. et al, Problems in fabricating welded structures for aviation systems, *Welding International*, Vol. 9, No. 5, 1995, pp. 390-393
12. Bratukhin, A. G. et al, Prospects for using aluminium-lithium alloys for stamped-welded aviation structures, *Welding International*, Vol. 11, No. 1, 1997, pp. 70-74
13. Bruhn, E. F, Analysis and design of flight vehicle structures, Tri-State Offset Co. Cincinnati,1965
14. British Standard BS 8118: Part 1 and 2, July 1991

15. Bussu, G. and Irving, P.E, Fatigue performance of friction stir welded 2024-T351 aluminium alloys, First International Symposium on Friction Stir Welding, 14-16 June 1999, Thousand Oaks, CA
16. Chien, P, Welding the Space Shuttle's Al-Li external tank presents a challenge, *The Welding Journal*, Vol. 77, No. 6, June 1998
17. Colligan, K, Dynamic material deformation during friction stir welding of alumnium, First International Symposium on Friction Stir Welding, Thousand Oaks, CA, 14-16 June 1999
18. Cost effective manufacture: welding aerospace materials, Proposal to IMI for CEMWAM I and II, 1995
19. Dawes, C. J. et al, Friction stir joining of aluminium alloys, TWI Bulletin (6), November/December 1995
20. Dawes, C. J. et al, Friction stir process welds aluminium alloys, the Welding Journal, Vol. 75, No. 3, March 1996
21. Dickerson, P.B. et al, Welding aluminum: it's not as difficult as it sounds, *The Welding Journal*, April, 1992
22. Ding, R. J. et al, Mechanical properties analysis in the retracted pin-tool (RPT) region of friction stir welded (FSW) aluminum-lithium 2195, First International Symposium on Friction Stir Welding, Thousand Oaks, CA, 14-16 June, 1999
23. Elber, W, The significance of fatigue crack closure, Damage tolerance in aircraft structures, ASTM STP 486, American Society for Testing and Materials, 1971
24. El-Soudani, S. M, and Pelloux, R. M, Anisotropy of fatigue crack propagation in aluminum alloy butt welded joints, *The Welding Journal*, 54, 5, 1979, pp.1445-1555
25. Engineering Science Data, ESDU 81301, Issue 3, April 1998
26. Engel, L. and Klingele, M, An atlas of metal damage, Carl Hanser Verlag, 1981
27. Ewalds, H. L. and Wanhill, R. J. H, Fracture Mechanics, Arnold Publications, 1989
28. Gallagher, J. P. et al, USAF Damage Tolerant Design Handbook: Guidelines for the Analysis and Design of Damage Tolerant Aircraft Structures, AFWAL-TR-82-3073, May 1984

29. Gangloff, R. P. et al, Direct current electrical potential measurement of the growth of small cracks, Small crack test methods, ASTM STP 1149, American Society for Testing and Materials, 1992
30. Golden, J. P et al, A comparison of fatigue crack formation at holes in 2024-T3 and 2524-T3 aluminium alloy specimens, *International journal of Fatigue*, 21, December 1999, S211-219
31. Gray, T. G. F, Spence, J. and North, T. H, Rational welding design, Newnes-Butterworths, London, 1975
32. Guidelines for electrical potential difference determination of crack size, ASTM E 647 Annex A3, American Society for Testing and Materials, 1997
33. Gurney, T. R and Maddox, S. J, A re-analysis of fatigue data for welded joints in steel, *Welding Research International*, 1973, 3(4), pp. 1-54
34. Hallyday, M. D. et al, In situ measurements of crack closure for small fatigue cracks in aluminium 2024-T351, *Fatigue and Fracture of Engineering Materials and Structures*, Vol. 18, No. 6, 1995, pp. 717-729
35. Hartman, A. and Schijve, J, The effect of secondary bending on the fatigue strength of 2024-T3 Alclad riveted joints, NLR TR 69116 U, December 1969
36. Hashimoto, T. et al, Mechanical properties of joints for aluminium alloys with friction stir welding process, 7th International Conference: Joints in Aluminium, INALCO 98, Cambridge, UK, 16 April 1998
37. Henderson, I, Exploiting friction stir welding in explosively-formed aluminium boat hull construction, 7th International Conference: Joints in Aluminium, INALCO 98, Cambridge, UK, 16 April 1998
38. Hill, H. N, Residual welding stresses in aluminum alloys, *Metal Progress,* August 1961,pp. 92-96
39. Hori, H. et al, Friction stir welding of rolling stock for subway, First International Symposium on Friction Stir Welding, Thousand Oaks, CA, 14-16 June, 1999
40. Horne, D. F, Aircraft production technology, Cambridge University Press, 1986
41. Hou, C. Y. and Lawrence, F. V, Crack closure in weldments, *Fatigue and Fracture of Engineering Materials and Structures*, Vol. 19, No. 6, 1996, pp. 683-693

42. Ignat'eva, V. S. and Kulakhmet'ev, R. R, Effect of residual stress on the development of fatigue cracks in the region of butt welds, *Automatic welding*, Vol. 38, No. 1, January 1995

43. Irving, B, Why aren't airplanes welded ?, *Welding Journal*, Vol. 75 No. 1, January 1997

44. Isida, M, Stress intensity factors for the tension of an eccentrically cracked strip, *Journal of Applied Mechanics*, 33, 674, 1966

45. Joint Aviation Authorities, JAR 25, Large Aeroplanes, para 25-301, 301, Change 14, October 1989

46. Joint Aviation Authorities, JAR 25, Large Aeroplanes, para 25-301, 303, Change 14, October 1989

47. Joint Aviation Authorities, JAR 25, Large Aeroplanes, para 25-301, 305, Change 14, October 1989

48. Joint Aviation Authorities, JAR 25, Large Aeroplanes, para 25.571, Change 13, January 1993

49. Jones, C. et al, Assembly of a full-scale external tank barrel section using friction stir welding, First International Symposium on Friction Stir Welding, Thousand Oaks, CA, 14-16 June, 1999

50. Juvinall, R. C. et al, Fundamentals of machine component design, John Wiley & Sons, second edit. 1991

51. Kang, K. J. et al, Fatigue crack growth through a tensile residual stress field under compressive applied loading, *Fatigue and Fracture of Engineering Materials and Structures*, Vol. 12, No. 5, 1989, pp. 363-376

52. Karlsson, J. et al, Microstructure and properties of friction stir welded aluminium alloys, 7th International Conference: joints in aluminium, INALCO 98, Cambridge, UK, 16 April 1998

53. Kelsey, R. A. et al, Effect of residual stresses on fatigue properties of aluminum alloy butt welds, weldments: physical metallurgy and failure phenomena, Fifth Bolton Landing Conference, August 1978

54. Kinchen, D. G. et al, Properties of friction stir welds in Al-Li 2196 T8, First International Symposium on Friction Stir Welding, Thousand Oaks, CA, 14-16 June, 1999

55. Knipstrom, P. et al, a novel joining process-friction stir welding, Svetsaren V52, No. 1-2, 1997, pp. 49-52

56. Kumagai, M. et al, Properties of aluminium wide panels by friction stir welding, First International Symposium on Friction Stir Welding, Thousand Oaks, CA, 14-16 June, 1999

57. Lee, Y. B. et al, Effects of redistributing residual stress on the fatigue behavior of SS330 weldment, *International Journal of Fatigue*, Vol. 20, No. 8, 1998, pp. 565-573

58. Leggatt, R. H, Residual stress in MIG aluminium alloy panels, The Welding Institute, 7913.01/86/539.3, July 1987

59. Linert, T. J, Microstructural evolution in friction stir welds on 6061 T-651, First International Symposium on Friction Stir Welding, Thousand Oaks, CA, 14-16 June, 1999

60. Lowak, H. et al, MINITWIST: a shortened version of TWIST, NLR Miscellaneous Publication MP 79018 U, National Aerospace Laboratory NLR, Amsterdam, May 1979

61. Maddox, S. J, Fatigue strength of welded structures, Second Edition, Abbington Publishing, 1991

62. Maddox, S. J, Recent advances in the fatigue assessment of weld imperfections, *Welding Journal*, Vol. 72, No. 7, July 1993, pp. 42-51

63. Mahoney, M. W. et al, Properties of friction stir welded 7075 T-651 aluminum, *Metal Transactions*, Vol. 29A, July 1998

64. Marchetti, M. et al, Tecnologie aeronautiche, Vol. 1, ESA, 1989

65. Mastuoka, K. et al, Fatigue strength of welded joints in 61N01 aluminium alloy extrusions, Welding International, Vol. 11, No. 8, 1994, pp. 856-862

66. Meneghetti, G. et al, Stress gradient effects on fatigue strength of light alloy welds, 7th International Conference: joints in aluminium, INALCO 98, Cambridge, UK, 16 April 1998

67. Midling, O. T. et al, Friction stir welding aluminium: process and applications, 7th International Conference: joints in aluminium, INALCO 98, Cambridge, UK, 16 April 1998

68. Model 488-PC2 IEEE 488.2 Bus Interface Card User's Manual, ICS Electronics Corporation, USA, 1994

69. National Strategic Technology Acquisition plan for Aeronautics Aviation Committee, DTI report, 1 Air CB.110, 1993

70. Nelson, D. V, Effects of residual stress on fatigue crack propagation, Residual stress effects in fatigue, ASTM STP 776, American Society for Testing and Materials, 1981

71. Nguyen, N. T. et al, The effect of undercut, misalignment and residual stress on the fatigue behaviour of butt welded joints, *Fatigue Fracture of Engineering Materials and Structures*, Vol. 19, No. 6, 1996, pp. 769-778

72. Niu, M. C. Y, Airframe stress analysis and sizing, Hong Kong Conmilit Press, October, 1997

73. Nordmark, G. E, et al, Effect of residual stress on fatigue crack growth rates in weldments of aluminum alloy 5456 plate, Residual stress effects in fatigue, ASTM STP 776, American Society for Testing and Materials, 1981

74. Norman, A. F. et al, Effect of welding parameters on the microstructure of Al-Cu-Mg autogenous TIG welds, 7th International Conference: joints in aluminium, INALCO 98, Cambridge, UK, 16 April 1998

75. Nunes, A. C. et al, Variable polarity plasma welding on the Space Shuttle external fuel tank, *The Welding Journal*, Vol. 63, No. 9, September 1984

76. Otegui, J. L, Fatigue crack initiation from defects at weld toes in steel, International Journal of pressure vessels and piping, Vol. 38, pp. 385-417, 1989

77. Pedwell, R. et al, The application of friction stir welding to aircraft wing strictures, First International Symposium on Friction Stir Welding, Thousand Oaks, CA, 14-16 June, 1999

78. Peterson, R. E, Stress concentration design factors, John Wiley & Sons, 1966

79. Phillips, E. P, The influence of crack closure on fatigue crack growth threshold in 2024-T3 aluminum alloy, Mechanisms of fatigue crack closure, ASTM STP 982, 1988

80. Pisarski, H. G, et al. Fatigue propagation in an aluminium alloy weldment, *Welding Research international*, No. 4, Vol. 6, 1976

81. Polmear, I. J, Light alloys: metallurgy of light metals, Arnold, 1995

82. Private conversation with Gawthorpe, P, Stress Engineering Technologies, Somerset, England, September 1999

83. Reynolds, A. P. et al, Visualization of material flow in an autogenous friction stir weld, First International Symposium on Friction Stir Welding, Thousand Oaks, CA, 14-16 June 1999

84. Ritchie, R. O, Near-threshold fatigue: an overview of the role of microstructure and environment, Conference Fatigue '84, 1984, pp. 1833-1863, Vol. 111

85. Rivello R. M, Theory and analysis of flight structures, Mc Graw-Hill, 1969

86. Rooke, D. P. and Cartwright, D. J, Compendium of stress intensity factors, Her Majesty's Stationary Office, MoD, 1976

87. Sanders, W. W, et al, Fatigue behaviour of aluminium alloy weldments, Welding Research Council Bulletin No. 286, August 1983

88. Scott, M. H. and Gittos, M. F, Tensile and toughness properties of arc-welded 5083 and 6082 aluminum alloys, *Welding Research Supplement*, September 1983, 243s-252s

89. Schijve, J, Fatigue crack closure, observations and technical significance, Report LR-485, Delft University of Technology, April 1986

90. J.Schijve, Fatigue life until small cracks in aircraft structures. Durability and Damage Tolerance, FAA/NASA International Symposium on Advanced Structural Integrity Methods for Airframe Durability and Damage Tolerance, Hampton, Virginia, 1994, pp. 665-681

91. Schijve, J, Multiple-site damage in aircraft fuselage structures, Fatigue and Fracture of Engineering Materials and Structures, Vol. 18, No. 3, 1995, pp. 329-344

92. Schijve, J, The fatigue strength of riveted joints and lugs, NACA TM 1395, August 1956

93. Shih, H-C. et al, Precipitation behaviors in Al-Cu-Mg and 2024 aluminum alloys, *Metallurgical and materials transactions*, Vol. 27A, September 1996, pp. 2479-2494

94. Shonin, V. A, The effects of residual stresses on the fatigue strength of a supporting member of AMg6 alloy at a point where transverse stiffeners are welded to it, *Automatic Welding*, Vol. 31, No. 1, 1978, pp. 48-49

95. Stone, M. and Swift, T, Future damage tolerance approach to airworthiness certification, 10th ICAF Symposium, Brussels, 1979, paper 2.9

96. Strangwood, M. et al, Characterization of thermo-mechanical effects on microstructural development in friction stir welded age hardening aluminium-based alloys, First International Symposium on Friction Stir Welding, Thousand Oaks, CA, 14-16 June 1999

97. Strawberry Tree data acquisition systems user manual, Strawberry Tree, 160 South Wolfe road, Sunnyvale, CA, 1993

98. Suresh, S, Fatigue of materials, Cambridge Solid State Science Series, Second edition, 1998

99. Sutton, G. R, An improved electrical potential method for crack length measurement, RAE TR 83063, August 1983

100. Svensson, L. E. et al, Microstructure, hardness and fracture in friction stir welded AA 6082, First International Symposium on Friction Stir Welding, Thousand Oaks, CA, 14-16 June 1999

101. Swift, T, Application of damage tolerance to type certification, SAE technical paper, No. R 59961, Aerospace congress and exhibition, Anaheim 1981.

102. Technology Foresight Report No 12, Defence and Aerospace section, May 1995

103. Thomas, W. M. et al, Friction stir butt welding. International Patent Application No. PCT/GB92/02203 and GB Patent Application No. 9125978.8, Dec. 1991

104. Thomas, W. M, Friction stir welding and related friction process characteristics, 7th International Conference: joints in aluminium, INALCO 98, Cambridge, UK, 16 April 1998

105. Threadgill, P, Friction stir welds in aluminium alloys: preliminary microstructural assessment, TWI bulletin, March/April 1997

106. Trufyakov, V. I. et al, Effect of residual stress on the fatigue strength of welded joints in aluminium alloys, *Automatic Welding*, Vol. 28-29, No. 5, 1976

107. Tsay, L. W, et al, Microstructure and fatigue crack growth of EH36 TMCP steel weldments, International Journal of fatigue, No. 21, 1999, pp. 857-864

108. Van Cleave, B. P. et al, Keyhole plasma arc welding of aluminum, Welding Technology for the Aerospace Industry, American Welding Society, October 1980

109. Von Strombeck, A. et al, Fracture toughness behaviour of FSW joints on aluminium alloys, First International Symposium on Friction Stir Welding, Thousand Oaks, CA, 14-16 June 1999

110. Wang, G. S. et al, A strip model for fatigue crack growth predictions under general load conditions, *Engineering Fracture Mechanics*, Vol. 40, No. 3, 1999, pp. 507-533

111. Woodward, N. J, Richardson, I. M. and Thomas, A, Variable polarity plasma arc welding of 6.35mm aluminium alloys, *Science and Technology of Welding and Joining*, Vol. 5, No. 1, 2000, pp. 21-25

112. Woodward, N. J. et al, Process enhancement for automated GTA and plasma welding of aluminium alloys, 7th International Conference: joints in aluminium, INALCO 98, Cambridge, UK, 16 April 1998

APPENDIX

Design of high load capacity grips

During a fatigue crack propagation test in which the DCPD technique is used to measure the crack length, the specimen is electrically insulated from the frame of the test machine. In fact, during measurements, it is essential that no portion of the applied current is shunted in a parallel circuit through the test machine [1]. In addition, the high current input if even partially flowing through the test machine might cause damage or interference with the test machine control systems. Figure 1A shows the high load capacity grips designed *ad hoc* to allow the use of the DCPD technique. The specimen electrical insulation was achieved using non-conductive Tufnol™ elements interposed between the grip body and the gripping pads (Fig. 1A).

The grips were designed using a safe-life design approach. The grip components were initially sized to fulfil the static requirements. The simultaneous presence of tensile stresses due to the test loads and bending due to the clamping action by the screws were taken into account. A safety factor of 2.0 was applied to the estimated maximum load condition. The most critical locations for fatigue initiation were identified and the relative stress intensity factors estimated. S-N curves and endurance limits for the selected material (EN24T high resistance steel), for a stress ratio of 0.1 and for each Kt value were obtained [2]. A safety factor of 2.0 was then applied to the endurance limit corresponding to the most critical location [3].

The fatigue strength verification of the values initially estimated in the above procedure demonstrated that the dimensions fulfilled the fatigue requirements by a factor of 3.0. The gripping pads were designed so that the centre of pressure was slightly offset with respect to the geometrical centre of the gripping surface allowing a progressive distribution of the gripping pressure applied to the specimen. This was obtained by reducing locally the gripping pad thickness, i.e. stiffness. Flanges and bolted connections, designed considering both static and fatigue strength requirements, were assembled using calculated maximum allowable torque values.

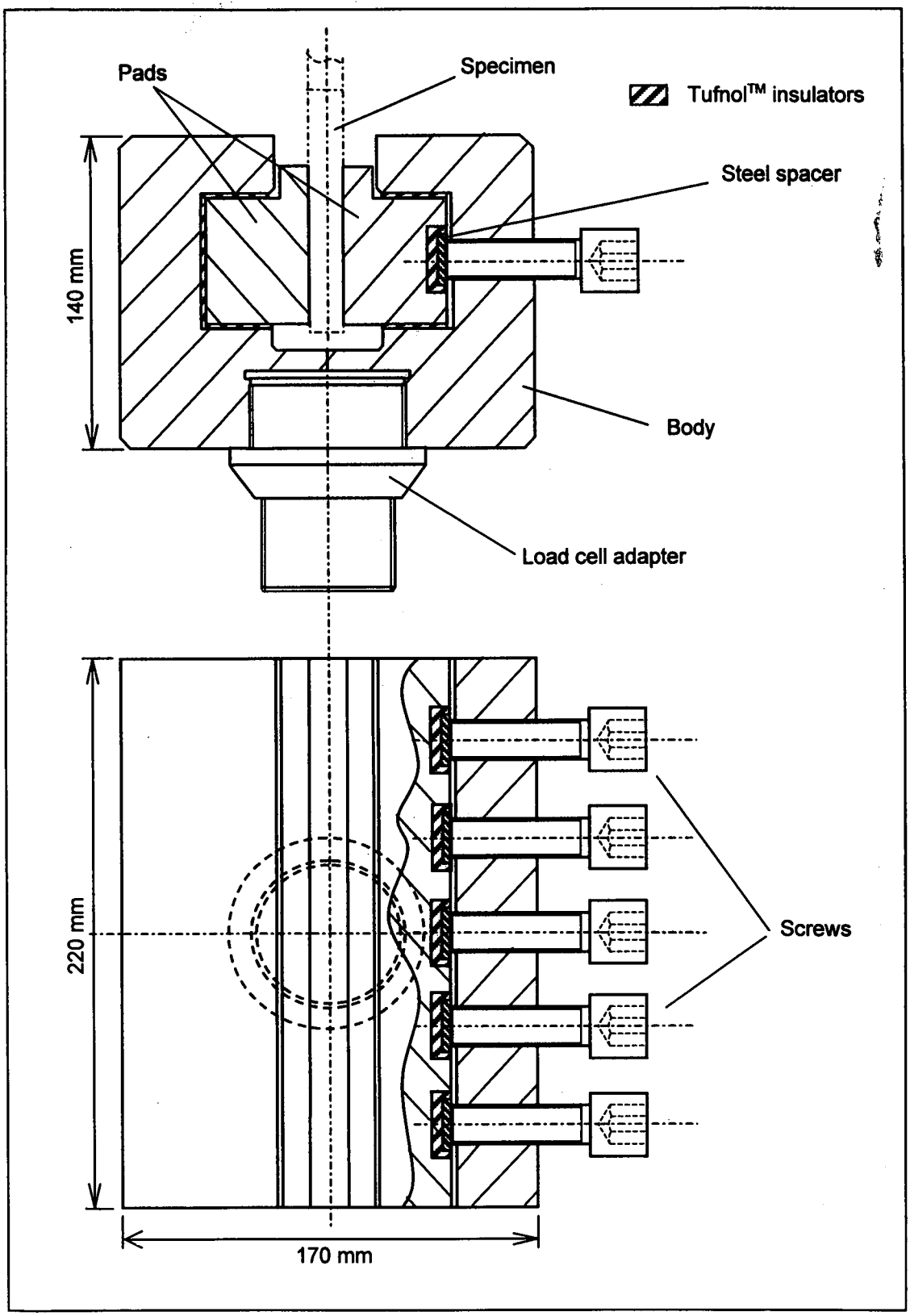

Figure 1A Schematic of the high load capacity grips designed for the crack propagation tests.

References:

1. Gangloff, R. P. et al, Direct current electrical potential measurement of the growth of small cracks, Small crack test methods, ASTM STP 1149, American Society for Testing and Materials, 1992
2. Military Handbook MIL-HDBK-5D, Change Notice 2, May 1985
3. Juvinall, R. C. et al, Fundamentals of machine component design, John Wiley, II edit. 1991